ARISTOTLE UNIVERSITY OF THESSALONIKI
FACULTY OF SCIENCES
SCHOOL OF GEOLOGY

PANAGIOTIS S. KOLLIAS
MSc Sustainable Energy Engineering

ATMOSPHERIC DISPERSION OF PARTICLES AND THEIR CHEMICAL AND MINERALOGICAL ANALYSIS IN THE GREATER AREA OF THESSALONIKI

DOCTORAL DISSERTATION THESIS

THESSALONIKI
2020

ΑΡΙΣΤΟΤΕΛΕΙΟ ΠΑΝΕΠΙΣΤΗΜΙΟ ΘΕΣΣΑΛΟΝΙΚΗΣ
ΣΧΟΛΗ ΘΕΤΙΚΩΝ ΕΠΙΣΤΗΜΩΝ
ΤΜΗΜΑ ΓΕΩΛΟΓΙΑΣ

ΠΑΝΑΓΙΩΤΗΣ Σ. ΚΟΛΛΙΑΣ
MSc Μηχανολόγος Μηχανικός Βιώσιμης Ενέργειας

ΑΤΜΟΣΦΑΙΡΙΚΗ ΔΙΑΣΠΟΡΑ ΣΩΜΑΤΙΔΙΩΝ ΚΑΙ ΧΗΜΙΚΗ, ΟΡΥΚΤΟΛΟΓΙΚΗ ΑΝΑΛΥΣΗ ΤΟΥΣ ΣΤΗΝ ΕΥΡΥΤΕΡΗ ΠΕΡΙΟΧΗ ΤΗΣ ΘΕΣΣΑΛΟΝΙΚΗΣ

ΔΙΔΑΚΤΟΡΙΚΗ ΔΙΑΤΡΙΒΗ

ΘΕΣΣΑΛΟΝΙΚΗ
2020

ΠΑΝΑΓΙΩΤΗΣ Σ. ΚΟΛΛΙΑΣ
MSc Μηχανολόγος Μηχανικός Βιώσιμης Ενέργειας

ΑΤΜΟΣΦΑΙΡΙΚΗ ΔΙΑΣΠΟΡΑ ΣΩΜΑΤΙΔΙΩΝ ΚΑΙ ΧΗΜΙΚΗ, ΟΡΥΚΤΟΛΟΓΙΚΗ ΑΝΑΛΥΣΗ ΤΟΥΣ ΣΤΗΝ ΕΥΡΥΤΕΡΗ ΠΕΡΙΟΧΗ ΤΗΣ ΘΕΣΣΑΛΟΝΙΚΗΣ

Εκπονήθηκε στον Τομέα Μετεωρολογίας και Κλιματολογίας του Τμήματος Γεωλογίας Α.Π.Θ.
Υποβλήθηκε στο Τμήμα Γεωλογίας Α.Π.Θ. τον Μάρτιο του 2020

Ημερομηνία Προφορικής Εξέτασης: 30/04/2020

Αριθμός Παραρτήματος Επιστημονικής Επετηρίδας Τμήματος Γεωλογίας N°: 199
[λαμβάνεται από τη Γραμματεία]

Τριμελής Συμβουλευτική Επιτροπή

Καθηγητής Πρόδρομος Ζάνης, Επιβλέπων
Αν. Καθηγητής Ιωάννης Πυθαρούλης, Μέλος Τριμελούς Συμβουλευτικής Επιτροπής
Αν. Καθηγητής Νικόλαος Καντηράνης, Μέλος Τριμελούς Συμβουλευτικής Επιτροπής

Εξεταστική Επιτροπή

Καθηγητής Πρόδρομος Ζάνης, Τμήμα Γεωλογίας Α.Π.Θ.
Αν. Καθηγητής Ιωάννης Πυθαρούλης, Τμήμα Γεωλογίας Α.Π.Θ.
Αν. Καθηγητής Νικόλαος Καντηράνης, Τμήμα Γεωλογίας Α.Π.Θ.
Καθηγητής Χαράλαμπος Φείδας, Τμήμα Γεωλογίας ΑΠΘ
Καθηγητής Δημήτριος Μελάς, Τμήμα Φυσικής Α.Π.Θ.
Αναπλ. Καθηγήτρια Λαμπρινή Παπαδοπούλου, Τμήμα Γεωλογίας Α.Π.Θ.
Διευθυντής Ερευνών Βασίλειος Αμοιρίδης, Εθνικό Αστεροσκοπείο Αθηνών

ΑΤΜΟΣΦΑΙΡΙΚΗ ΔΙΑΣΠΟΡΑ ΣΩΜΑΤΙΔΙΩΝ ΚΑΙ ΧΗΜΙΚΗ, ΟΡΥΚΤΟΛΟΓΙΚΗ ΑΝΑΛΥΣΗ ΤΟΥΣ ΣΤΗΝ ΕΥΡΥΤΕΡΗ ΠΕΡΙΟΧΗ ΤΗΣ ΘΕΣΣΑΛΟΝΙΚΗΣ. – *Διδακτορική Διατριβή*

ATMOSPHERIC DISPERSION OF PARTICLES AND THEIR CHEMICAL AND MINERALOGICAL ANALYSIS IN THE GREATER AREA OF THESSALONIKI .– *Ph.D. Thesis*

Citation:

Κόλλιας Π. Σ., 2020. – Ατμοσφαιρική διασπορά σωματιδίων και χημική, ορυκτολογική ανάλυση τους στην ευθύτερη περιοχή της Θεσσαλονίκης. Διδακτορική Διατριβή, Τμήμα Γεωλογίας Α.Π.Θ., Αριθμός Παραρτήματος Επιστημονικής Επετηρίδας Τμ. Γεωλογίας Νο XXX, 200 σελ.

Kollias P. S., 2020. – Atmospheric dispersion of particles and their chemical and mineralogical analysis in the greater area of Thessaloniki. Ph.D. Thesis, School of Geology, Aristotle University of Thessaloniki, Annex Number of Scientific Annals of the School of Geology No XXX, 200 pp.

Εικόνα Εξωφύλλου: www.hdwallpapers.in , "flying colorful particles" modified by PANAGIOTIS KOLLIAS, 03/2020

With gratitude to God!

Contents

Prologue

This PhD thesis has been conducted at the School of Geology, Aristotle University of Thessaloniki, Department of Meteorology and Climatology and Department of Mineralogy-Petrology-Economic Geology.

The completion of this PhD thesis would not have been possible without the support, tolerance and guidance from important people who contributed to its completion. Thus, I would like to specially mention and express my gratitude to each one of them.

Starting from my supervisor Professor Prodromos Zanis, I would like to thank him for the assignment of the extremely interesting subject of the present research and for his guidance, support and willingness to provide me with knowledge throughout my PhD studies I would like to thank Assoc. Professor Ioannis Pytharoulis for his constructive and to the point guidelines, advices and direct assistance regarding my studies. Many special thanks I would like to give to Assoc. Professor Nikolaos Kantiranis for his provision of vast knowledge, patience, faith, continuous guidance and non-stop support till the very end that he showed at me all this time.

I would also like to specially thank Ioannis Tegoulias for his direct solutions and immediate assistance and knowledge that he kindly offered me and shared without hesitation.

Additionally, I would like to specially thank Emeritus Professor Theodor Karakostas for his unwavering trust and his unceasing support giving me strength to carry on and enlightening me with his expertise to advance and complete my studies.

Furthermore, I would also like to specially thank Professor Anestis Filippidis for his kind and thoughtful support and important guidance on the journey of education providing me with his know-how in the science-research field during all this time of my PhD research.

I would also like to express my thanks to Professor Constantini Samara for trusting me as a researcher, and for her kind words and guidance.

Also, Stavros Solomos for his kind support when I asked for his assistance.

Additionally, I would like to thank Professor Andreas Georgakopoulos for helping me to start this educational journey many years ago when I was a bachelor student in France by helping me and sending me fly ash notes and instructions without even knowing me.

I need to express my sincere thanks to Jerrome Brioude for sharing knowledge and guiding me through this journey of Flexpart dispersion modelling.

I would also like to thank my Professor Anders Nordstrand from Royal Institute of Technology KTH, Stockholm for his inspirational words and knowledge than he kindly shared with me.

From the environmental department of municipality of Thessaloniki, I would like to express my deepest thanks to Professors Maximos Petrakakis and Apostolis Kelessis for their faith in me all these years and for the guidance they gave me.

Also, I would like to express my thanks to all the members of the examination committee for reading my thesis.

Through my heart I would like to express my deepest gratitude to my grandmother Eftychia, my father and my mother and all my family for their continuous support that they gave me all these years.

Many thanks to all my friends for their tolerance and support.

Finally, I would like to thank from the depths of my heart the person that had more faith in me than my own self and continues to believe in me till this day.

"This PhD Thesis is dedicated to all beloved ones that I lost hoping that I shall meet them soon in Paradise."

Specially dedicated to my Grandfather ***Demetrios Vatzias***
and to the most ***NOBLE*** *and* ***RARE*** *soul* ***E.*** *!!!*

Panagiotis Kollias,
Thessaloniki 2020

CHAPTER 1: INTRODUCTION

1.1. Introducing Atmospheric Particle Dispersion

Atmospheric pollution from air particle dispersion is nowadays consider an aspect of our daily life. Efforts are being held on local and global scale to reduce the increased levels of air-pollutants by setting alert and alarm limits in accordance with European Union rules - legislations and directives. Air pollution emissions and concentrations have increased in many areas worldwide, largely impacting health and ecosystems. Regarding EU state members, air quality is still not adequately utilized in many areas, despite reductions in emissions and ambient concentrations.

In order to reduce air pollution and its impacts a good understanding of its causes is necessary, how air particle pollutants are transported and transformed in the atmosphere, how the chemical composition of the atmosphere changes over time, and how pollutants impact on human health, ecosystems, climate and consequently economy and society. Next most important environmental factor after climate change for EU citizens is air pollution (European Commission 2017).

1.2. Air pollution and EU legislation

To prevent, protect and improve the air quality European Union is integrating environmental protection standards by implementing systematic control of harmful substances emissions into the atmosphere, improving fuel quality, transportation, industrial and energy sectors (Figure 1.1, Tables 1.1., 1.2).

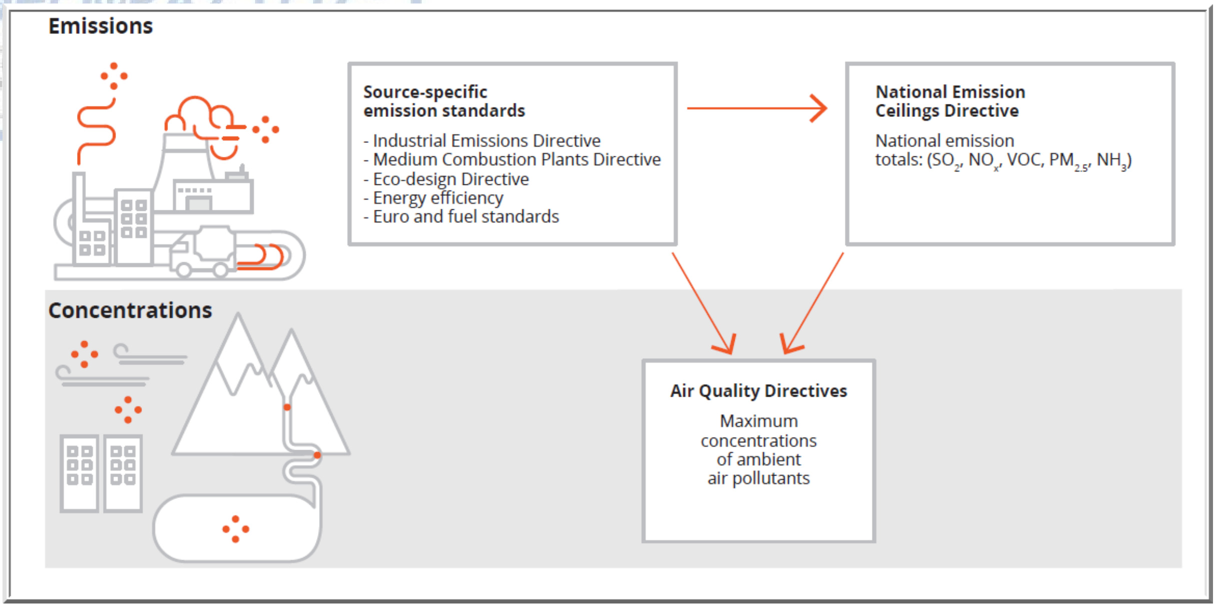

Figure 1.1. EU's clean air policy framework, based on three main pillars (European Commission 2018)

Table 1.1. Air quality standards for the protection of health, as given in the EU ambient air quality Directives (EU 2004, 2008)

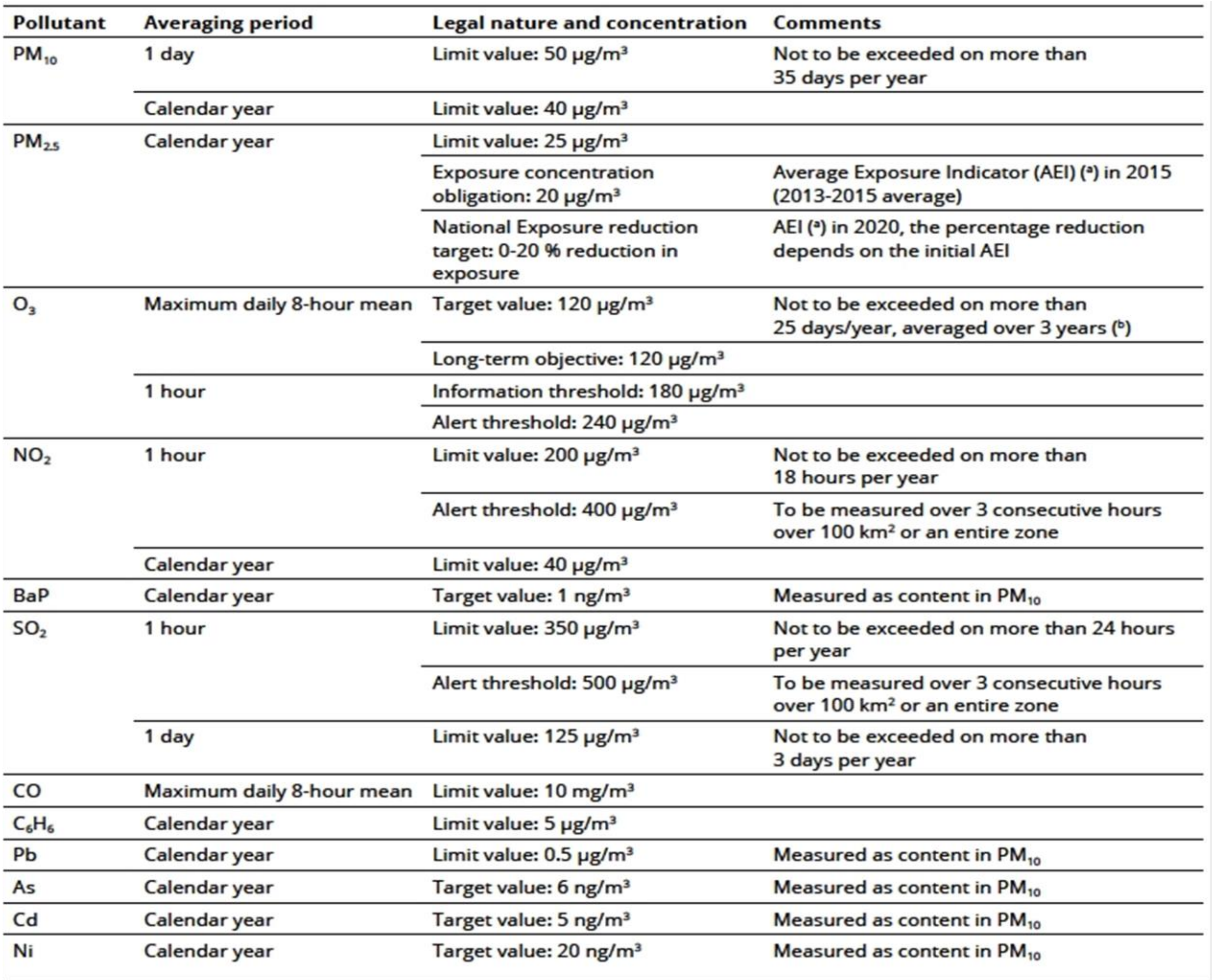

Pollutant	Averaging period	Legal nature and concentration	Comments
PM_{10}	1 day	Limit value: 50 μg/m³	Not to be exceeded on more than 35 days per year
	Calendar year	Limit value: 40 μg/m³	
$PM_{2.5}$	Calendar year	Limit value: 25 μg/m³	
		Exposure concentration obligation: 20 μg/m³	Average Exposure Indicator (AEI) (ᵃ) in 2015 (2013-2015 average)
		National Exposure reduction target: 0-20 % reduction in exposure	AEI (ᵃ) in 2020, the percentage reduction depends on the initial AEI
O_3	Maximum daily 8-hour mean	Target value: 120 μg/m³	Not to be exceeded on more than 25 days/year, averaged over 3 years (ᵇ)
		Long-term objective: 120 μg/m³	
	1 hour	Information threshold: 180 μg/m³	
		Alert threshold: 240 μg/m³	
NO_2	1 hour	Limit value: 200 μg/m³	Not to be exceeded on more than 18 hours per year
		Alert threshold: 400 μg/m³	To be measured over 3 consecutive hours over 100 km² or an entire zone
	Calendar year	Limit value: 40 μg/m³	
BaP	Calendar year	Target value: 1 ng/m³	Measured as content in PM_{10}
SO_2	1 hour	Limit value: 350 μg/m³	Not to be exceeded on more than 24 hours per year
		Alert threshold: 500 μg/m³	To be measured over 3 consecutive hours over 100 km² or an entire zone
	1 day	Limit value: 125 μg/m³	Not to be exceeded on more than 3 days per year
CO	Maximum daily 8-hour mean	Limit value: 10 mg/m³	
C_6H_6	Calendar year	Limit value: 5 μg/m³	
Pb	Calendar year	Limit value: 0.5 μg/m³	Measured as content in PM_{10}
As	Calendar year	Target value: 6 ng/m³	Measured as content in PM_{10}
Cd	Calendar year	Target value: 5 ng/m³	Measured as content in PM_{10}
Ni	Calendar year	Target value: 20 ng/m³	Measured as content in PM_{10}

European Union focusing on the protection of the environment and of human health as natural outcome has set ambient Air Quality Directives (EU 2004, 2008) (Tables 1.1 and 1.2), calling for all the member states to embrace and implement air quality plans. Member states are thus required to develop National Air Pollution Control Programs BY 2019 following the directive of 2016 (EU 2016) in order to comply with their emission reduction commitments.

Table 1.2. WHO air quality guidelines and estimated reference levels (WHO 2000, 2006)

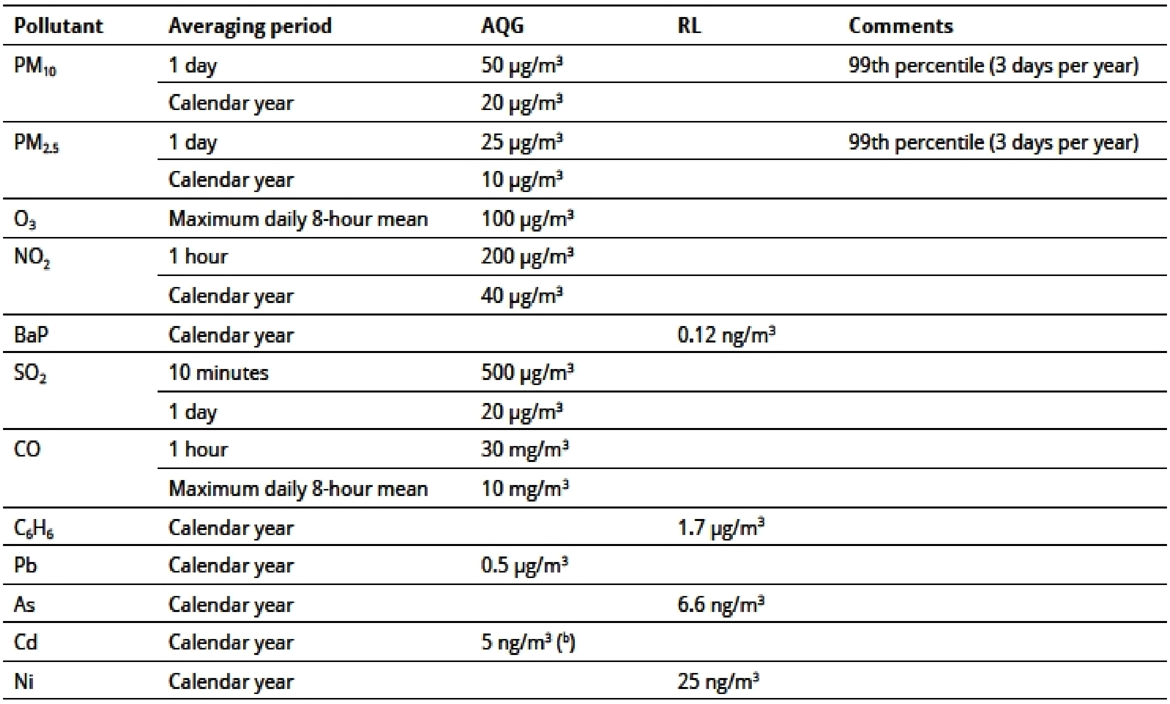

Pollutant	Averaging period	AQG	RL	Comments
PM_{10}	1 day	50 µg/m^3		99th percentile (3 days per year)
	Calendar year	20 µg/m^3		
$PM_{2.5}$	1 day	25 µg/m^3		99th percentile (3 days per year)
	Calendar year	10 µg/m^3		
O_3	Maximum daily 8-hour mean	100 µg/m^3		
NO_2	1 hour	200 µg/m^3		
	Calendar year	40 µg/m^3		
BaP	Calendar year		0.12 ng/m^3	
SO_2	10 minutes	500 µg/m^3		
	1 day	20 µg/m^3		
CO	1 hour	30 mg/m^3		
	Maximum daily 8-hour mean	10 mg/m^3		
C_6H_6	Calendar year		1.7 µg/m^3	
Pb	Calendar year	0.5 µg/m^3		
As	Calendar year		6.6 ng/m^3	
Cd	Calendar year	5 ng/m^3 (b)		
Ni	Calendar year		25 ng/m^3	

In addition, European Union is setting out key source standards of air pollution emissions and energy efficiency standards which cover from vehicle emissions to products and industrial emissions. These standards focus on industrial emissions, power plants emissions, vehicles and transportation fuels, energy performance of products and non-road mobile machinery. Long-term planning of the Clean Air Program for Europe (CAPE), published by the European Commission (2013), is to improve air quality to such an extent so that by 2030 there shall be a 50% reduction of pre-mature deaths compared to those of 2005, ensuring full compliance with existing legislation.

1.3. Air pollution and health

Air pollution and its health risks are an aspect that must be taken under serious consideration. The consequences are vast and at such an extent that approx. 400.000 premature deaths per year are caused by it as it is considered the largest environmental health risk in Europe (Lim et al., 2012, WHO 2014, 2016a, HEI, 2018). Most commonly occurring cause of premature deaths are heart diseases, followed by lung infections and lung cancer (WHO 2014). Particulate Matter (PM) particles air pollution is classified as carcinogenic by the International Agency for Research on Cancer (IARC 2013). Adverse effects of short and long-term exposure for children and adults to air pollution may lead to reduced lung function, respiratory infections and aggravated asthma. Also, there have been evident impacts on fertility, pregnancy, infants and children as well, from exposure to ambient air pollution (WHO 2013). Latest researches tend to associate exposure to air pollution with new-onset type 2 diabetes in adults, and it may be linked to obesity, systemic inflammation, ageing, Alzheimer's disease and dementia (WHO 2016b).

1.4. Air pollution and Climate change

Air pollution and climate change are connected since a large number of air pollutants have a potential impact on climate and global warming affecting one another as climate forcers. Direct effect on global warming is an issue that occurs by a constituent of PM, tropospheric O_3 and black carbon (BC), are short-lived climate. Other PM constituents, such as organic carbon, ammonium (NH_4^+), sulphate (SO_4^{2-}) and nitrate (NO_3^-), have a cooling effect (IPCC 2013). Furthermore, weather patterns tend to change and vary due to climate change. This may alter the dispersion, deposition, transport and formation of air pollutants in the atmosphere. Volatile organic compounds (VOCs), which are O_3 precursors, and emissions from wildfires and dust events tend to increase when temperature increases. The O_3 impairs vegetation growth by reducing vegetation's uptake of carbon dioxide (CO_2). Adverse environmental effects of pollutants, including O_3, toxic metals and persistent organic pollutants (POPs) may be magnified by Climate change (Hansen and Hoffman 2011, Staudt et al. 2013) which in turn may alter environmental conditions (e.g. temperature, pH) that modify the bioavailability of pollutants (e.g. metals), the exposure, uptake and sensitivity of species to pollutants (Noyes et al. 2009). Furthermore, impacts of air pollution concerning damage caused to materials, properties, buildings and artworks, including each Europeans cities cultural heritage is of serious concern for it may lead to the loss of fundamental parts of our cultural-social history. Damage effects include corrosion (caused by acidifying compounds), biodegradation, soiling (caused by particles), and weathering and colors fading (EEA 2018a).

1.5 Air pollution Guidelines

WHO (World Health Organization) committed to protect and promote people's health and well-being by improving air quality to such an extent that follows WHO air quality guidelines (WHO 2000, 2006), set to assist in the reduction of health impacts from air pollution based on evaluation analyzed from scientific evidence. The United Nations Environment Program requested that UN Environment supports each nation and their efforts to implement the resolution through activities raising awareness and strengthening cooperation on air pollution. Also, to utilize air quality monitoring and assessment of global, regional and sub-regional focus urging state members to implement policies and measures to prevent and reduce air pollution from significant sources (UNEP 2014, 2017). Air quality is linked to the Sustainable Development Goals concerning health, welfare and urbanization focusing at the substantial reduction of deaths and illnesses caused by air pollution till 2030.

1.6 Sources and emissions of air pollutants

Airborne particles are emitted, primary and suspended directly in the atmosphere in particulate form or produced secondarily in the atmosphere varying in terms of concentration, and physical, chemical and morphological characteristics (Figure 1.2).

Primary air pollutants contain particulate matter (PM), black carbon (BC), sulphur oxides (SOx), nitrogen oxides (NOx) (which includes both nitrogen oxide-NO and nitrogen dioxide-NO_2), ammonia (NH_3), carbon monoxide (CO), methane (CH_4), non-methane volatile organic compounds (NMVOCs) including benzene (C_6H_6), certain metals and polycyclic aromatic hydrocarbons (PAHs), including benzo(a)pyrene (BaP). Secondary air pollutants are particulate matter formed in the atmosphere, ozone (O_3), nitrogen dioxide NO_2 and a number of oxidized volatile organic compounds (VOCs). Key precursor gases for secondary PM are sulphur dioxide (SO_2), nitrogen oxides (NOx), ammonia (NH_3) and volatile organic compounds (VOCs). The gases NH_3, SO_2 and NOx react in the atmosphere to form ammonium ion (NH_4^+), sulphate (SO_4^{2-}) and nitrate (NO_3^-) compounds. Secondary PM is formed by these compounds that form new particles in the air or condense onto those already existent. Specific non-methane volatile organic compounds (NMVOCs) are oxidized to form less volatile compounds that generate secondary organic aerosols. Ground-level tropospheric ozone (O_3) is formed from chemical reactions via the sunlight, following emissions of precursor gases, mainly NOx, NMVOCs and CH_4. These precursors can be of natural (biogenic) and anthropogenic origin. NOx depletes tropospheric O_3 as a result of the titration reaction with the emitted NO to form NO_2 and O_2.

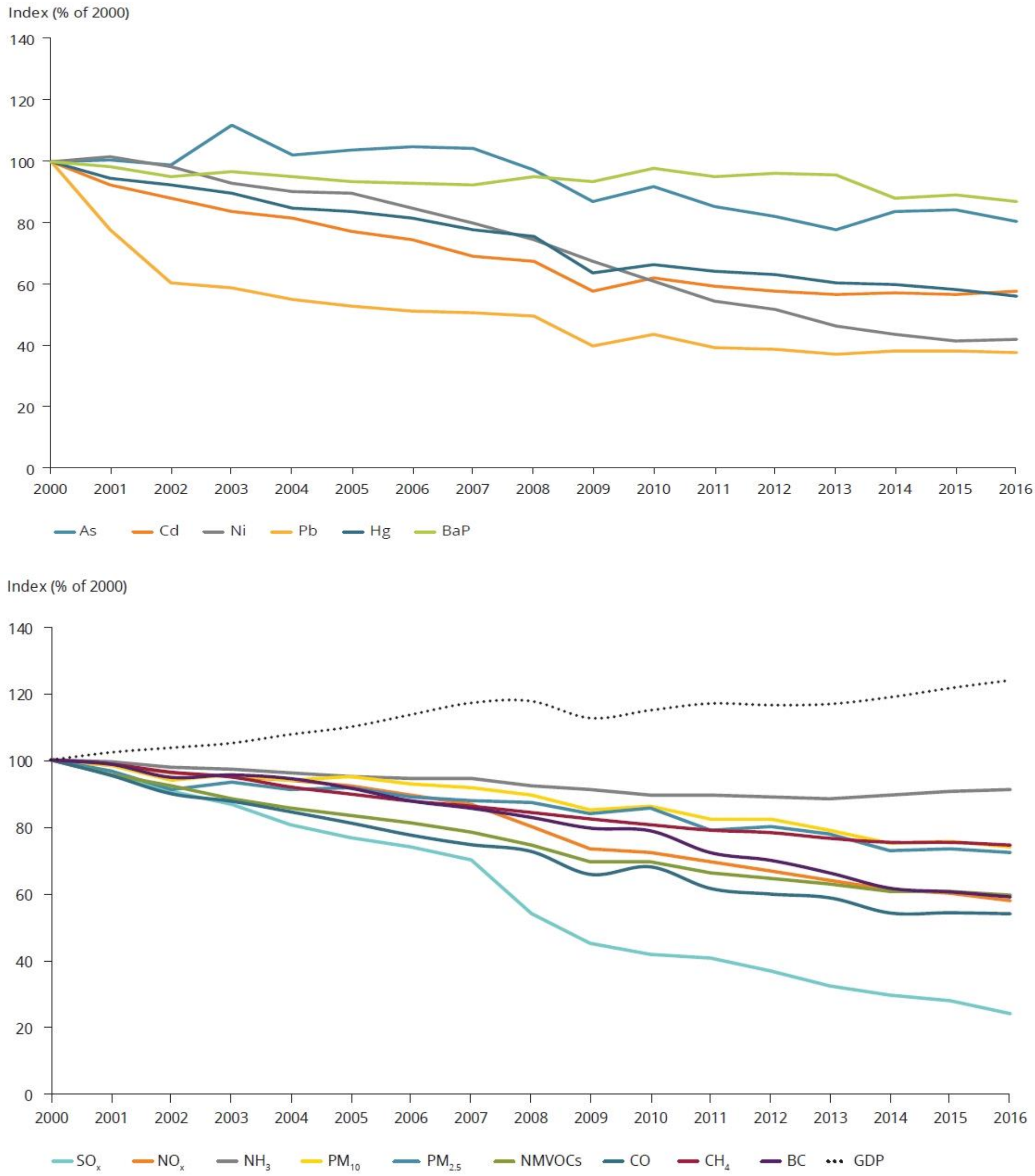

Figure 1.2. Decrease in emissions of primary and precursor pollutants contributing to ambient air concentrations of PM_{10}, $PM_{2.5}$, O_3 and NO_2 (bottom), as well as As, Cd, Ni, Pb, Hg and BaP (top), between 2000 and 2016 in the EU-28 also shown for comparison is gross domestic product (GDP) (EEA 2018a).

As can be seen in Figure 1.2, emissions of all primary and precursor pollutants contributing to ambient air concentrations of PM, O_3 and NO_2, as well as As, Cd, Ni, Pb, Hg and BaP , decreased between 2000 and 2016 in the EU-28 (EEA 2018a).

1.7. Sources of regulated pollutants by emissions sector

Main contributing emitting sectors of air pollutants are: Transportation, road and non-road (air, rail, sea and inland water transport), commercial, institutional and households, energy production and distribution, energy use in industry, industrial processes and product use, agriculture and waste (which includes landfill, waste incineration with heat recovery and open burning of waste). For primary air pollutants (e.g. NOx, SOx, PM, BaP, CO, C_6H_6 and toxic metals) stationary and mobile combustion processes are the main source. SOx and NOx are primarily emitted from fuel combustion in the form of SO_2 and NO, respectively. BaP, CO and C_6H_6 are emitted as a result of the incomplete combustion of fossil fuels and biofuels. Road transport was once a major source of CO emissions, but this has changed since the use of catalytic convertors assisted in the reduction of emission. Primary PM is classified as PM_{10} and $PM_{2.5}$, is mainly derived from fuel combustion for domestic heating, power generation, etc. BC (Black carbon) is a constituent of $PM_{2.5}$ formed from incomplete fuel combustion, with the main sources including domestic heating and transport. Agriculture contributes to important emissions of primary pollutants which is the main source of CH_4 (ruminant animals in particular), followed by waste management. Industrial activity (e.g. metal processing) and energy production are key sources of toxic metal emissions to the air, which tend to originate from a small number of facilities (EEA 2018b).

1.8 Particulate matter concentrations EU

European Environment Agency (EEA) received PM_{10} data for 2016, with sufficient valid measurements from approx. 2,900 stations located in all the EEA-39 countries except Liechtenstein and Andorra. From all those stations 174 monitored concentrations above the PM_{10} (Fig. 1.3) annual limit value while the stricter value of the world health organization for PM_{10} annual mean was exceeded by 1932 of the stations and in all the reporting countries, except Estonia, Iceland, Ireland and Switzerland.

$PM_{2.5}$ concentrations for 2016 (Figure 1.4) were higher than the annual limit value in four EU member states and four other reporting countries. These values above the limit value were registered in around 5 % of all the reporting stations and also occurred primarily (97 % of cases) in urban or suburban areas.

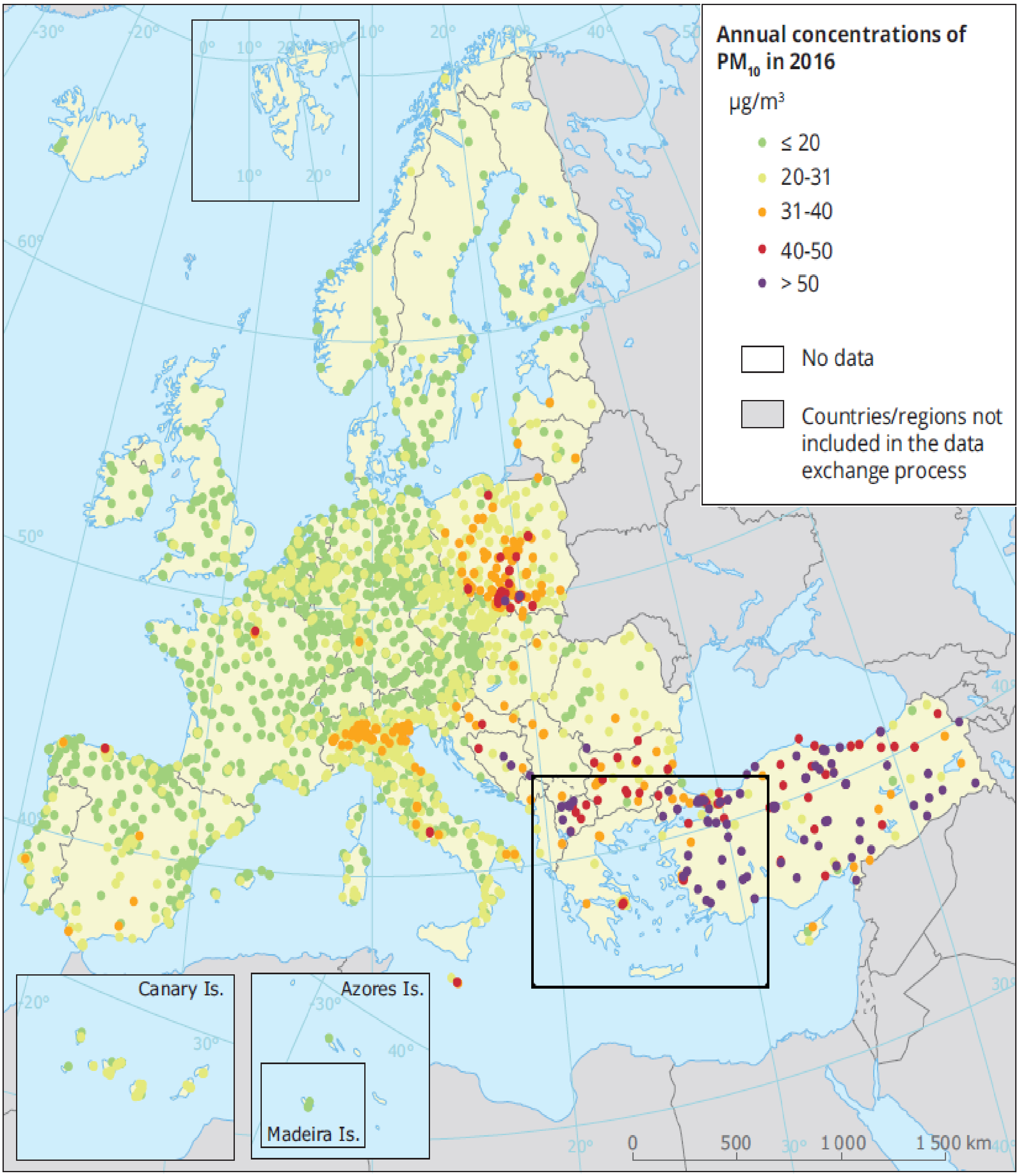

Figure 1.3. Annual concentrations of PM_{10}, 2016 (EEA 2018a)

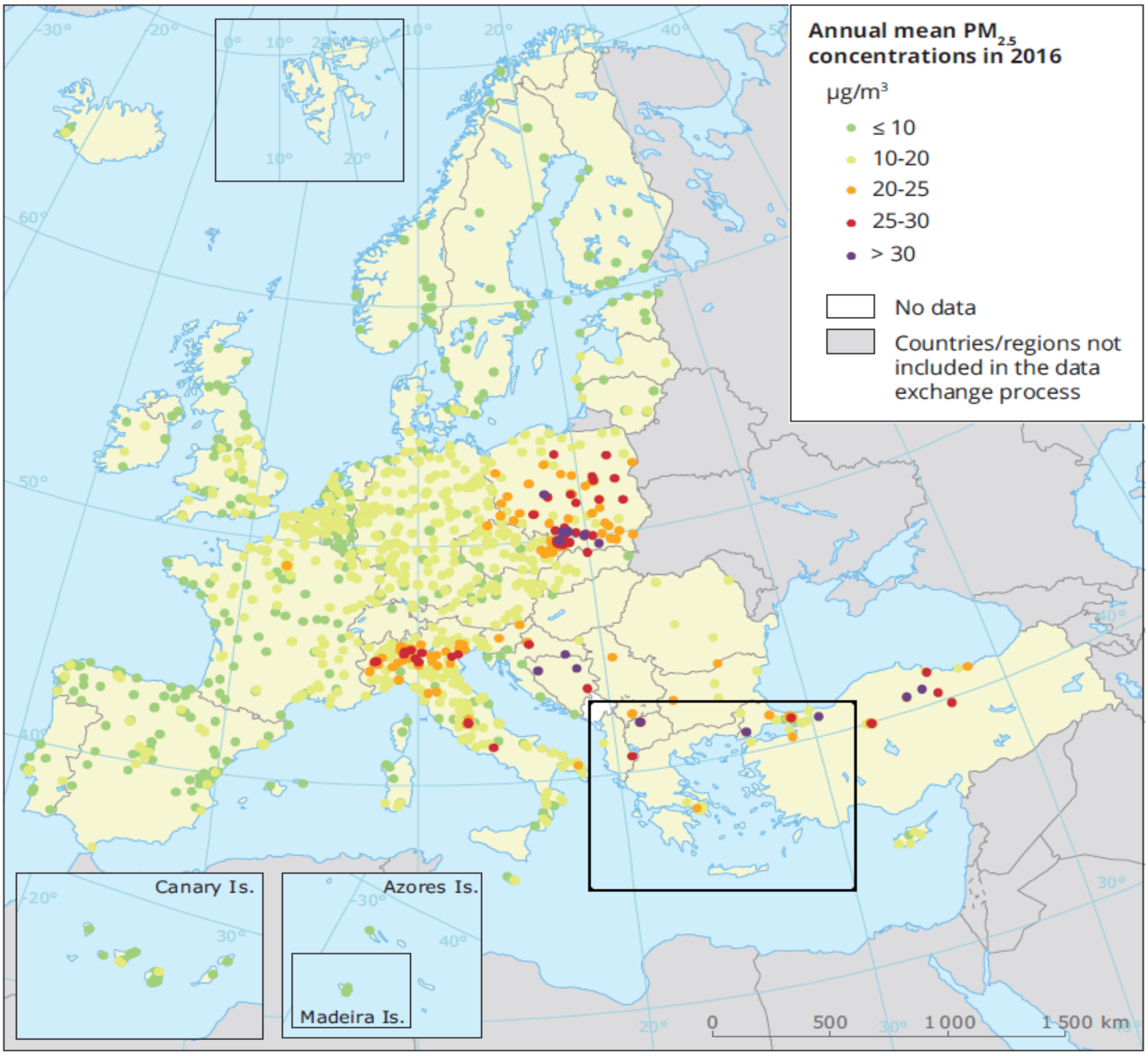

Figure 1.4. Annual mean concentrations of $PM_{2.5}$, 2016 (EEA 2018a)

1.9 Toxic metals concentrations EU

Toxic metals monitoring is not adequate since it does not cover all parts of Europe probably because concentrations are generally low and below the lower assessment thresholds, making assessments by modeling or objective estimates. The air pollution problems caused by toxic metals such as arsenic (As), cadmium (Cd), lead (Pb) and nickel (Ni) in terms of ambient air concentrations seem to be highly localized for each EU state. Increased emissions levels seem to be typically related specifically to industrial plants. According to European Environment Agency air quality report for 2018 results from the 2016 data from 28 EU state members, indicated that from the 678 participating stations, seven stations located in urban and industrial areas reported arsenic concentrations above the target value. The rest were below the lower assessment thresholds. For cadmium from the 698 stations only three showed concentrations above target values.

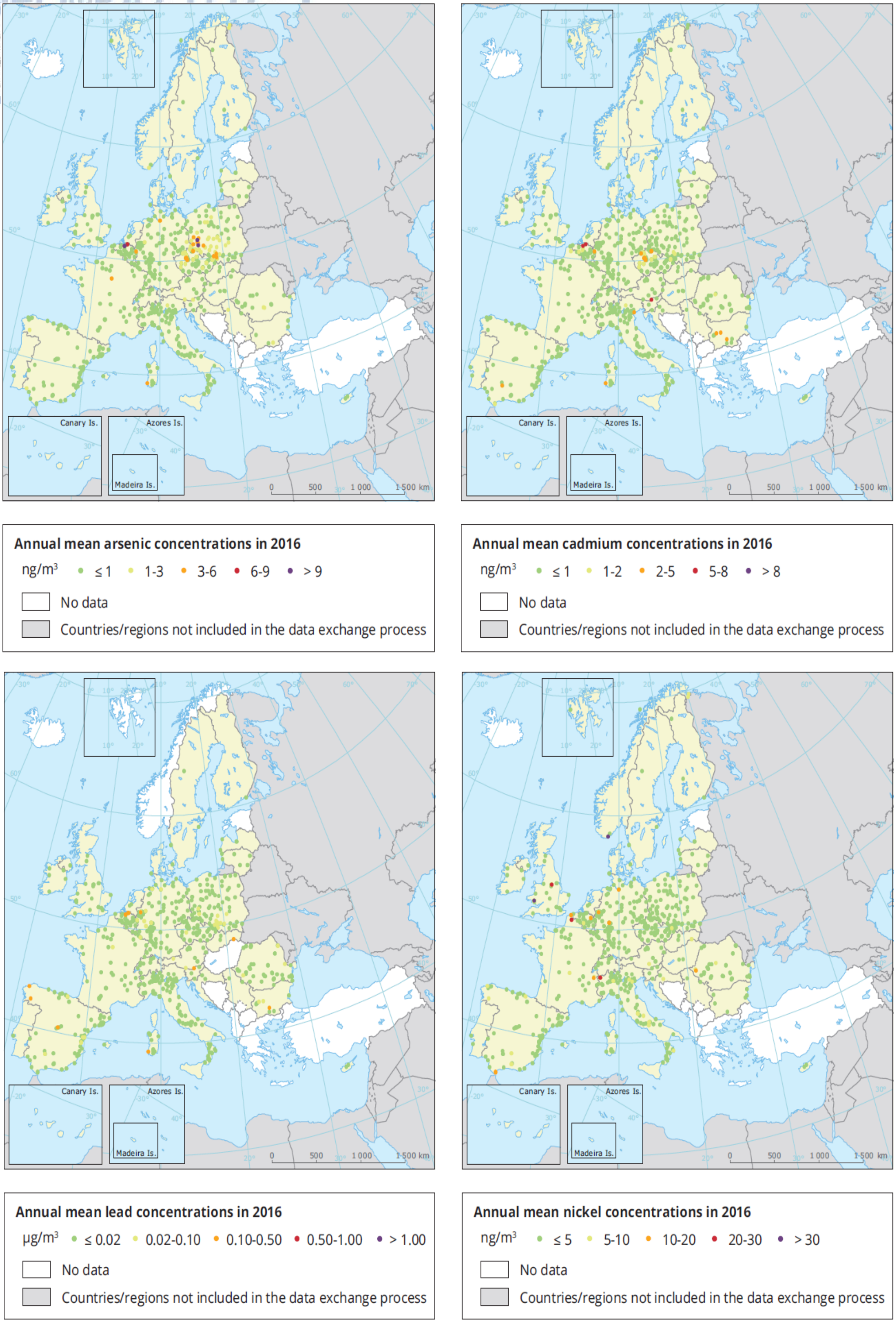

Figure 1.5. Annual mean concentrations of As, Cd, Pb and Ni 2016 (EEA 2018a)

For lead from 647 stations there was no report for concentrations above limit values. Finally, for nickel from 679 stations five stations showed concentrations above limit values with four of the located in industrial areas.

Heavy metals are considered one of the most dangerous environmental pollutants mainly because they do not degrade and accumulate in the environment for a long time. This gives rise to the immediate need to control-restrict heavy metal emissions to the environment (Barakat 2010).

1.10 Location of the study area - Thessaloniki city

Thessaloniki (40° 62′ E, 22° 95′ N) is the second largest city of Greece and one of the most densely populated city in Europe accounting for approximately 16,000 inhabitants km^{2} (Samara et al. 2003). Built at the innermost point of Thermaikos gulf and having the second largest major commercial port in Greece. The city is surrounded by hills to the north and mount Hortiatis (1,200 m height) to the east (Figure 1.6).

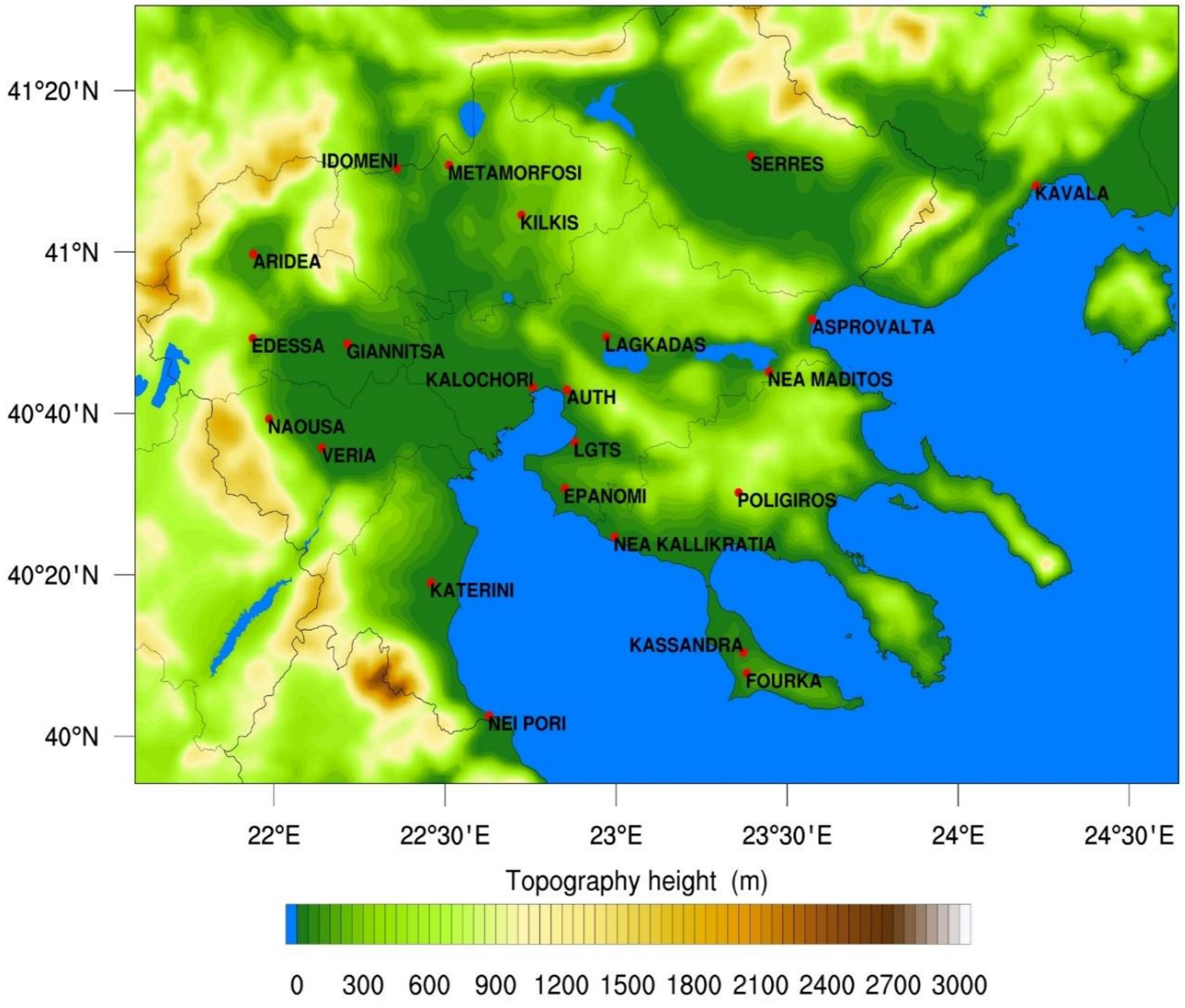

Figure 1.6. Topography of Thessaloniki, Dept. of Meteorology and Climatology, AUTH.

Numerous residential suburbs surround the city and several industrial activities (oil refining and petrochemical facilities, metal scrap incineration, iron and steel manufacturing, electrolytic MnO_2 production, cement and lime production, quarry works) are located at variable distances to the West, Northwest and North. According to Manoli et al. (2002), the climate of Thessaloniki is typically Mediterranean: mild, strongly influenced by the sea breeze. Mean monthly values of relative humidity vary between 47% and 80% (mean annual rainfall is 490 mm), while temperature varies between 5.5 °C (in January) and 28 °C (in August). The prevailing synoptic conditions are characterized by calms (wind speed by 0.5 m s^{-1}) and weak northerly and southern winds during the cold period, while a local circulating system of sea/land breezes is developed mainly in the warm period and transient months (Flocas et al. 2009).

1.11 Aim of the study

The aim of the present study is to analyze the atmospheric particles dispersion and their chemical and mineralogical impact in the wider area of Thessaloniki during the yearly period of 2012-2013. Falling dust samples were collected at street-level and rooftop building level from three selected urban sampling sites according to prevailing meteorological conditions such as wind speed and precipitation. This was made in order to identify the pollution levels of the examined urban sites, the species of heavy metals detected and the of possible emitting sources, both from broader area of the Thessaloniki or/and remote areas. To achieve this goal, dates of increased heavy metals concentrations were selected and the atmospheric particles dispersion model, Flexpart-WRF with high resolution data feedback from the Weather Research and Forecasting Model (WRF) ruining at high analysis of 0.6 km x 0.6 km (with the advanced research dynamic solver-AWR) and with analysis data from the European Centre for Medium-Range Weather Forecasts (ECMWF) were applied.

CHAPTER 2: DATA AND METHODOLOGY

2.1 Sampling

The data that were utilized in this research consist, of analyzed dust samples concentrations from three (3) selected sampling sites separating properly the city of Thessaloniki in north, central and south area, in order to chemically, morphologically and mineralogical analyze the samples for consistency of hazardous pollutants. The results showed increased amounts of heavy metals, organic matter etc. These results were implemented to the dispersion model Flexpart-WRF in order to identify the origin that contributed to the polluted sampling sites of the city.

2.2 Atmospheric Particle Dispersion Models

The utilization of atmospheric transport and dispersion modeling, is of vital importance to both life and environment. Based on gridded meteorological data the numerical dispersion models can provide accurate dispersion simulations to forecast anthropogenic, natural and accidental chemical releases, explosions of hazardous material, volcanic eruptions and fire emissions of hazardous air pollutants (Figure 2.1). The Flexible Particle model (FLEXPART) a Lagrangian dispersion model that relies on meteorological data to drive simulations, combined with the high resolution Weather Research and Forecasting model (WRF) are integrated within a part of this study. This integration is made to provide high resolution modeling in order to improve the dispersion simulations leading to an overall better forecast of air pollutant migration, from the findings of the annual collected dust samples, measured at selected sampling site locations in Thessaloniki and thus FLEXPART-WRF is utilized in this research.

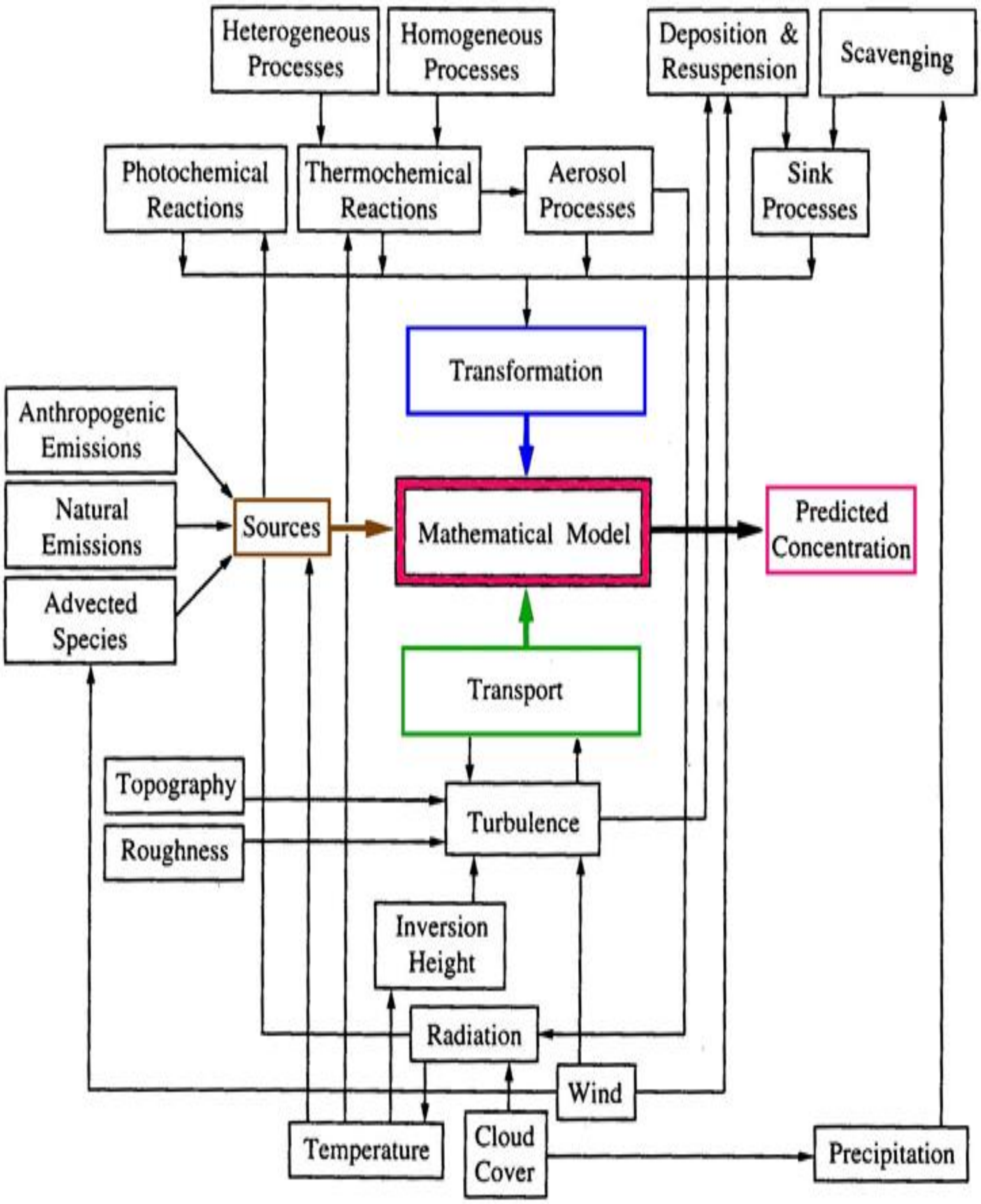

Figure 2.1. Dispersion modeling scheme (Seinfeld and Pandis 1998)

2.3 Lagrangian dispersion model FLEXPART

The Lagrangian particle dispersion model FLEXPART was originally (first release in 1998) designed for calculating the long-range and mesoscale dispersion of air pollutants from point sources, such as after an accident in a nuclear power plant. In the meantime, FLEXPART has evolved into a comprehensive tool for atmospheric transport modeling and analysis. Its application fields were extended from air pollution studies to other topics where atmospheric transport plays a role (e.g., exchange between the stratosphere and troposphere, or the global water cycle). It has evolved into a true community model that is now being used by at least 35 groups from 14 different countries and is seeing both operational and research applications (Stohl et al. 2005).

How it works: FLEXPART, simulates long-range and mesoscale transport, diffusion, dry and wet deposition, and radioactive decay of tracers released from point, line, and area or volume sources. Also, it can be used in a domain-filling mode where the entire atmosphere is represented by particles of equal mass. FLEXPART can be used either forward in time to simulate the dispersion of tracers from their sources, or backward in time for given receptors to determine potential source contributions. FLEXPART's first version was developed during the first author's military service at the nuclear-biological- chemical school of the Austrian Forces, the management of input data was mainly taken from FLEXTRA, a kinematic trajectory model (Stohl et al. 1995), the deposition code was added later (version 2), and was validated using data from three large tracer experiments (Stohl et al. 1998). Version 3 implemented performance optimizations and the development of a density correction (Stohl and Thomson 1999). Further updates included the addition of a convection scheme (Seibert et al. 2001) (version 4), and better backward calculation capabilities (Seibert and Frank 2004), and also improvements in the input/output handling (version 5). Validation of the model was made during intercontinental air pollution transport studies (Stohl and Trickl 1999, Spichtinger et al. 2001), in order to extend the models forecasting capabilities, special developments for FLEXPART were applied (Stohl et al. 2004), a domain-filling options was applied, and the possibility to use output nests and corrections to the numeric in the convection schemes, unification of the ECMWF and GFS model versions in one source package. GFS data in GRIB2 format can be read, using ECMWF's grib-api library. Each species got its own definition file. Output can be written individually for multiple species in backward runs. The output format was changed to a compressed sparse matrix format while memory is partly allocated dynamically. Furthermore, dry and wet deposition algorithms were updated and new, global land use inventory introduced. The OH^{-} reaction based on a monthly averaged 3 dimensional OH- field is available as an option. FLEXPART is coded following the Fortran 95 standard and tested with several compilers (gfortran, Absoft, Portland Group) under a number of operating systems (Linux, Solaris, Mac OS X, etc.). FLEXPART is based on model level data of the numerical weather prediction model of the European Centre for Medium-Range Weather Forecasts (ECMWF 1995).

FLEXPART is an offline model that uses meteorological fields (analytical or forecast data) in Gridded Binary (GRIB) format in version 1 or 2 from the ECMWF numerical weather prediction model (ECMWF 1995) on native ECMWF model levels as input and on a latitude/longitude grid. GRIB data from NCEP's GFS model, available on pressure levels, can also be utilized. Data is provided by the ECMWF archives using a pre-processor and can be global or only covering a limited area. Furthermore, higher-resolution domains can be nested into a mother domain. ECMWF parameters consist of: five(5) 3-D fields: horizontal and vertical wind components, temperature and specific humidity and 2-D fields: sfc pressure, total cloud cover, 10 m horizontal wind components, 2 m temperature and dew point temperature, large scale and convective precipitation, sensible heat flux, east/west and north/south surface stress, topography, land- sea-mask and subgrid standard deviation of topography and calculate surface stress and sensible heat flux (in case they are missing and using the profile method) and friction velocity. The includepar file contains all settings related to FLEXPART the physical constants and maximum field size limits dimensions. The file includecom specifies all FLEXPART global variables and fields, i.e., those shared between most subroutines.

The input data is provided at the vertical plane (n) of the ECMWF model which is determined by a hybrid coordinate system (Table 2.1). Converting to pressure coordinates is done through the relationship:

$$p_k = A_k + B_k \cdot p_s$$

while the heights of n surfaces are determined by the relation:

$$n_k = A_k / p_0 + B_k$$

where n_k is the n value at k level of the model, p_s is surface pressure and p_0 = 101325 Pa. A_k and B_k are coefficients, selected in such way that the levels closest to the ground follow the topography, while the higher levels align with the pressure surfaces.

Boundary layer parameterization from ECMWF forecasts, flow and surface tension data are available. The total surface tension is calculated by means of the relation

$$T = \sqrt{T_1^2 + T_1^2}$$

where T_1 and T_2 are the surface stresses in east/west and north/south direction, respectively.

Table 2.1. Input data variables utilized at the lagrangian model FLEXPART.

	Grib data code	**Input data variables**	**units**
1	131	u wind	m/s
2	132	v wind	m/s
3	135	ω	Pa/s
4	130	temperature	K
5	134	surface pressure	Pa
6	133	specific humidity	Kgr/Kgr
7	141	snow depth	m
8	151	m.s.l pressure	Pa
9	164	total cloud cover	%
10	165	u wind 10 m	m/s
11	166	v wind 10 m	m/s
12	167	temperature 10 m	K
13	168	dew point 2 m	K
14	142	large scale precipitation	m
15	143	convective precipitation	m
16	146	surface flux of sensible heat	W/m^2
17	176	surface solar radiation	$W/m^2/s$
18	180	u wind stress	Pa
19	181	v wind stress	Pa
20	129	surface geopotential height	m^2/s^2
21	172	land-sea mask	
22	160	standard deviation of topography	

Friction velocity is then calculated from

$$u_* = \sqrt{T/\rho}$$

where ρ is the air density (Wotawa et al. 1996). Most accurate method to calculate friction velocities and heat fluxes (Wotawa and Stohl 1997). However, if de-accumulated surface stresses and surface sensible heat fluxes are not available, the profile method after Berkowicz and Prahm (1982) (subroutine pbl_profile.f) is applied to wind and temperature data at the second model level and at 10 m (for wind) and 2 m (for temperature). The following three equations are solved iteratively:

$$u_* = \frac{\kappa \Delta u}{\ln\frac{z_l}{10} - \Psi_m\left(\frac{z_l}{L}\right) + \Psi_m(\frac{10}{L})}$$

$$\Theta_* = \frac{\kappa \Delta \Theta}{0.74\ [\ln\frac{z_l}{2} - \Psi_h\left(\frac{z_l}{L}\right) + \Psi_h(\frac{2}{L})]}$$

$$L = \frac{\bar{T} u_*^2}{g \kappa \Theta_*}$$

L is the Obukhov length (m) and can be interpreted as the height where the absolute value of the shear production term and the buoyant term have the same absolute value, κ is the von Karman constant (0.4), z_l is the height of the second model level, Δu is the difference between wind speed at the second model level and at 10m, ΔΘ is the difference between potential temperature at the second model level and at 2m, Ψ_m and Ψ_h are the stability correction functions for momentum and heat (Businger et al. 1971, Beljaars and Holtslag 1991), g is the gravitational acceleration , Θ_* is the temperature scale and $\bar{T}$ is the average surface layer temperature (taken as T at the first model level). The heat flux is then computed by

$$(\overline{\omega'\Theta'_\upsilon})_0 = \rho c_p \Theta_*$$

where ρc_p is the specific heat capacity of air at constant pressure. ABL heights are calculated according to Vogelezang and Holtslag (1996) using the critical Richardson number concept. The ABL height h_{mix} is set to the height of the first model level l for which the Richardson number exceeds the critical value of 0.25.

$$Ri_l = \frac{(\frac{g}{\Theta_{\upsilon 1}})(\Theta_{\upsilon l} - \Theta_{\upsilon 1})(z_l - z_1)}{(u_l - u_1)^2 + (u_l - u_1)^2 + 100u_*^2}$$

Θ_u and Θ_{ul} are the virtual potential temperatures, z_1 and z_l are the heights and (u_1, v_1), and (u_l, v_l) are the wind components at the 1st and lth model level, respectively (Figure 2.2).

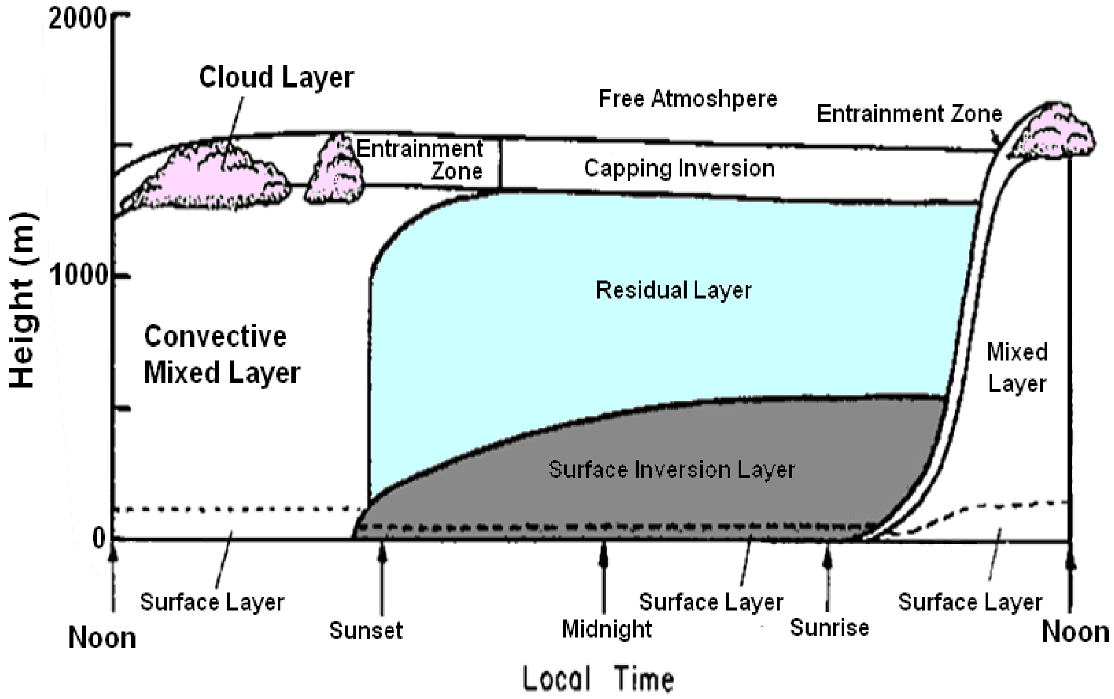

Figure 2.2. The Boundary Layer, troposphere bottom layer that is in contact and affected by the surface of the earth (Sull 1988).

For Particle trajectory calculations FLEXPART generally uses the simple “zero acceleration” scheme

$$X(t + \Delta t) = X(t) + u(X,t)\Delta t$$

which is accurate to the first order, to integrate the trajectory equation (Stohl 1998)

$$\frac{dX}{dt} = u[X(t)]$$

with t being the time, Δt being the time increment, X the position vector, and u = $\bar{u}$ + ut + um the wind vector that is composed of the grid scale wind $\bar{u}$, the turbulent wind fluctuations ut and the mesoscale wind fluctuations um. The transport and dispersion due to particle turbulence is controlled by the advance.f subroutine where wind and other data are interposed at the particle location. It also solves the Langevin equation, which is a parameterization of the turbulent motions ut for i components of the wind:

$$du_{t_l} = ai(x, u_t t, t)dt + bij(x, u_t, t)dW_j$$

where the drift term a and the diffusion term b are functions of the position, the turbulent velocity and time. dWj are incremental components of a Wiener process with mean zero and variance dt, which are uncorrelated in time (Legg and Raupach 1982). With the above assumptions, the Langevin equation for the vertical wind component ω can be written as

$$d\omega = -\omega\left(\frac{dt}{T_{L_\omega}}\right) + \left(\frac{\delta\sigma_\omega^2}{\delta z}\right)dt + \left(\frac{\sigma_\omega^2\,\delta\rho}{\rho\,\delta z}\right)dt + \left(\frac{2}{T_{L_\omega}}\right)^{\frac{1}{2}}\ \sigma\omega\, dW$$

where ω and σω are the turbulent vertical wind component and its standard deviation, TLω is the Lagrangian timescale for the vertical velocity autocorrelation and ρ is density. The second and the third term on the right hand side are the drift correction (McNider et al. 1988) and the density correction (Stohl and Thomson 1999), respectively.

Regarding timestep there are two possibilities either with, a fixed time step without adaptation to the lagrangian timescales which may be faster but less accurate (COMMAND ctl <0) and may be useful for long range applications if computational resources are limited or with time step adapting to the vertical lagrangian time scales where turbulence is described in a more accurate way (COMMAND ctl >0, ifine) and thus needed for any BL studies. Time step for the horizontal will be defined as:

$$\Delta t_i = \frac{1}{c_{tl}}\min(TL_\omega, \frac{h}{2\omega}, \frac{0.5}{\frac{\delta\sigma_\omega}{\delta z}})$$

Time step in the vertical is splitted:

$$\Delta t_\omega = \frac{\Delta t_i}{ifine}$$

The minimum value of Δti is 1 second. Δti is used for solving the Langevin equations for the horizontal turbulent wind components.

An important transport mechanism is upward movements in vertical transport clouds, which are not included in the ECMWF vertical velocity data. To represent this vertical transport in a particle dispersion model, it is necessary to redistribute the particles in entire vertical column. In FLEXPART the parameterization method of Emanuel and Zivkovic-Rothman (1999) is selected. The upward shift is activated when

$$T_{up}^{LCL+1} \geq T_{u}^{LCL+1} + T_{thres}$$

with T_{up}^{LCL+1} the virtual temperature of a surface air parcel lifted to the level above the LCL (lifting condensation level), T_{u}^{LCL+1} the virtual temperature of the environment there, and Tthres = 0.9 K a threshold temperature value. Then a matrix MA of the saturated upward and downward mass fluxes within clouds is calculated by accounting for entrainment and detrainment:

$$MA^{i,j} = \frac{M^{i}\left(\left|\sigma^{i,j+1} - \sigma^{i,j}\right| + \left|\sigma^{i,j} - \sigma^{i,j-1}\right|\right)}{(1 - \sigma^{i,j}) \sum_{j=LCL}^{LNB}(|\sigma^{i,j+1} - \sigma^{i,j}| + |\sigma^{i,j} - \sigma^{i,j-1}|)}$$

Here $MA^{i,j}$ are the mass fractions displaced from level i to level j, M^{i} the mass fraction displaced from the surface to level i, LNB the level of neutral buoyancy of a surface air parcel and $0 < \sigma^{i,j} < 1$ the mixing fraction between level i and level j.

During the initial dispersion phase from a point source in the atmosphere, particles normally form a compact cloud. Relatively few particles suffice to simulate this initial phase correctly. However, the particle cloud gets distorted after some time, and particles spread over a much larger area, more particles are now needed. FLEXPART allows the user to specify a time constant Δt_s. Particles are split into two (each of which receives half of the mass of the original particle) after travel times of Δt_s, 2 Δt_s, 4 Δt_s, 8 Δt_s, and so on.

Table 2.2. Physical units of the input and output data for forward and backward simulation runs for different command settings (ind_source and ind_receptor).

Direction	ind_source	ind_receptor	input unit	output unit
Forward	1	1	Kg	ng m^{-3}
Forward	1	2	Kg	ppt by mass
Forward	2	1	1	ng m^{-3}
Forward	2	2	1	ppt by mass
Backward	1	1	1	s
Backward	1	2	1	s m3 kg^{-1}
Backward	2	1	1	s kg m^{-3}
Backward	2	2	1	s

When FLEXPART performs forward in time simulations, particles are released from one or more sources and their concentrations in various grids are calculated. FLEXPART can perform backward simulations as well, which are more effective in calculating the relationship between the recipient and the potential source (Table 2.2).

The calculation of the relationship between source and receiver has been generalized for both front and rear time simulations of the units of measurement used. Through the ind_source and ind_receptor commands in the COMMAND folder, the units of mass are rotated in a mixture ratio for the source and the recipient respectively. It is noteworthy that by the term source we always mean the natural source and not the point at which the particles can be released, which for the forward time simulations is the source while for the backward simulations is the receiver.

Stohl et al. (2002) proposed a method designed to simplify the complex and numerous model output data using cluster analysis (Dorling et al. 1992). The main principle of the above method is to group and monitor, at each time step, the locations of all particles released from a point source, as well as other additional information (ex. percentage of particles in the ABL). The resulting file (plumetraj.f) contains the data required to construct the particle orbits of each cluster. The number of clusters is selected by the ncluster command in the includepar folder.

FLEXPART takes into account processes leading to the reduction of particulate matter such as radioactive decay and wet and dry deposition. During radioactive decay the particle mass decreases according to

$$m(t + \Delta\tau) = m(t)exp(-\frac{\Delta t}{\beta})$$

where m is particle mass, and the time constant $\beta = T_{1/2} = \ln(2)$ is determined from the half-life $T_{1/2}$. Deposited pollutant mass decays at the same rate .Wet deposition removes aerosols and gas particles from the atmosphere, a process described by exponential mass reduction

$$m(t + \Delta\tau) = m(t)exp(-\Lambda\Delta t)$$

m is the particle mass and Λ increases with the precipitation rate I according to

$$\Lambda = AI^{B}$$

where I is the rainfall rate in mm / hour, A the coefficient of removal for I = 1 mm / hour and B expresses the dependence on the rainfall rate. A and B are defined by the user in the SPECIES folder. Dry deposition, this is described by a deposition velocity which for the gases is described by the relation

$$|u^d(z)| = [r_a(z) + r_{ab}(z) + r_c(z)]^{-1}$$

where r_a is the aerodynamic resistance between z and the surface, r_b is the quasilaminar sublayer resistance, and r_c is the bulk surface resistance and

Finally, the deposition of particulates is calculated in subroutine according to

$$u_d(z) = [r_a(z) + r_{ab}(z) + r_c(z)]^{-1} + u_g$$

where u_g is the gravitational settling velocity calculated from (Slinn, 1982)

$$u_g = \frac{g\rho_p d_p^2 C_{cun}}{18\mu}$$

where ρ_p and d_p are the particle density and diameter, μ the dynamic viscosity of air (0.000018 kg $m^{-1}s^{-1}$) and C_{cun} the Cunningham slip-flow correction.

Regarding particle mass reduction via deposition by dry deposition, a reference level is set at href = 15 m and for the particles below that level this reduction is calculated by

$$\Delta m(t) m(t)[1 - \exp\left(-\frac{u_d(h_{ref})\Delta t}{2h_{ref}}\right)]$$

2.4 Dispersion model Flexpart –WRF

The applications of FLEXPART include fire emissions (Solomos et al. 2015, Kasischke et al. 2005, Wotawa and Trainer 2000), emergency response (Pechinger et al. 2001, Wenig et al. 2003) urban dispersion (Fast and Easter 2006) and most recently pathogen transport. Stohl (1998) validated the FLEXPART dispersion model by applying it to large field campaigns. Each experiment had its own unique feature that challenged the dispersion model such as terrain, weather patterns and spatial and temporal sampling and release locations. Many of the concentration results were comparable to the observed values. However, frontal passages and underestimation of the air concentration led to FLEXPART's poor performance during some of the experiments. In response to these limitations, a new convective algorithm was added, and high resolution meteorological model can now be ingested into the model. A modified version of FLEXPART (based on version 6.2) was produced to ingest the WRF model, now referred to as FLEXPART-WRF (Pagano et al. 2010).

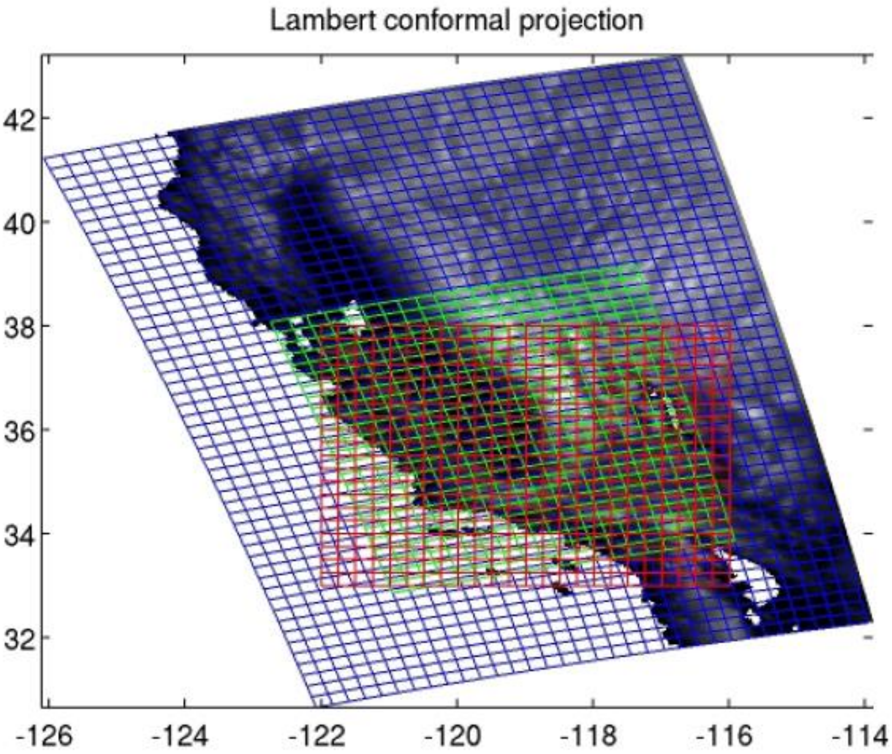

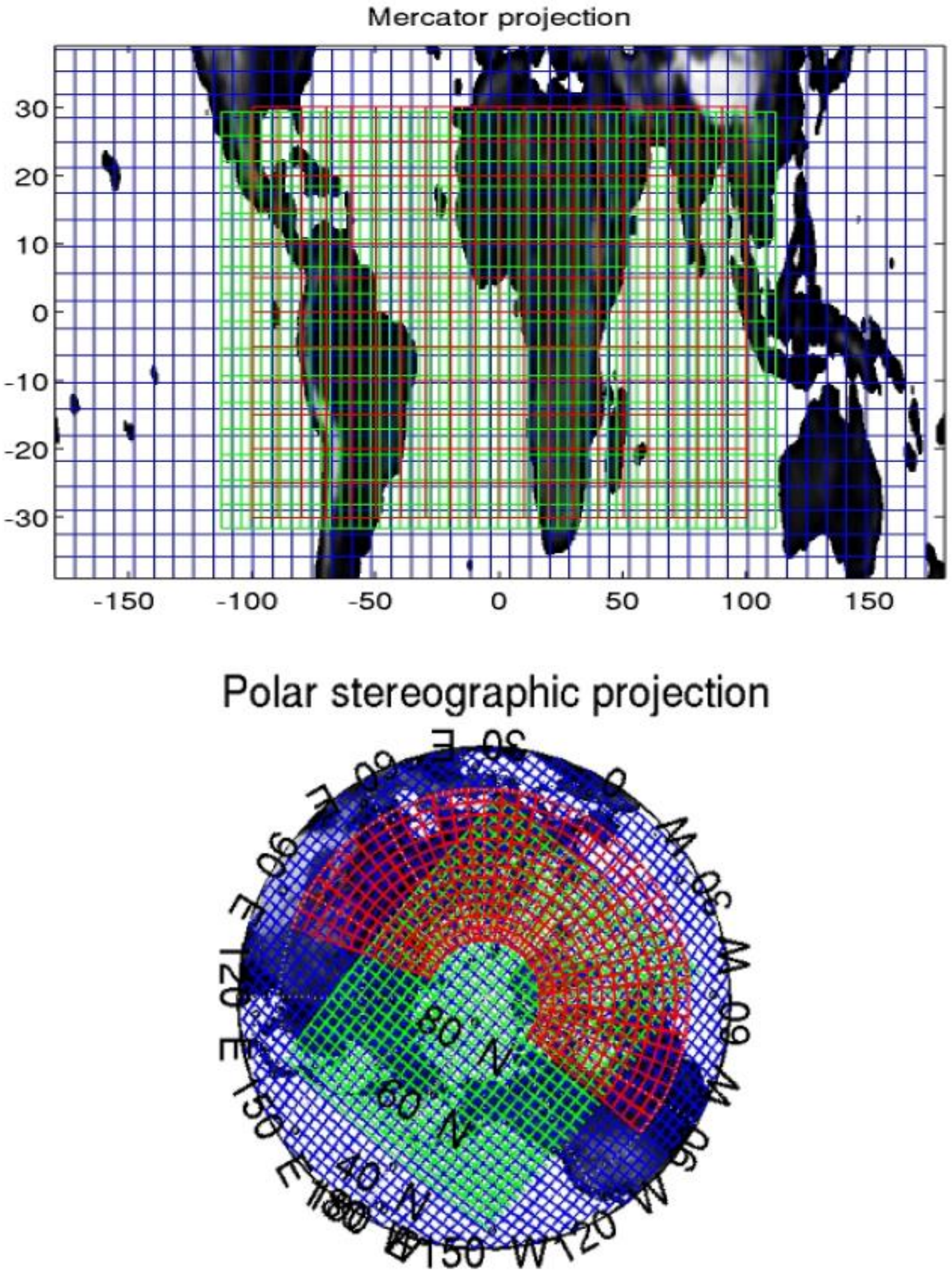

Figure 2.3. Lambert conformal, Mercator and polar stereographic projections from WRF (blue grid). Flexpart output can define two types of projections : The irregular output grid (green grid) that follows the WRF projection, and the regular grid (reg grid) based on latitude/longitude coordinates (Brioude et al. 2013).

FLEXPART-WRF can handle different map projections that WRF is able to work with. Figure shows the Lambert conformal, stereographic and mercator projections that are commonly used in WRF. The blue grid cells represent the center grid the Arakawa C-grid used in WRF (Fig 2.3). The green and red grids represent the two different FLEXPART output projections.

To conduct a FLEXPART run, different meteorological fields from WRF are needed Tab.2.3. presents the list of variables needed to run FLEXPART-WRF. Horizontal and vertical wind 3-D fields are the most important meteorological fields in order to calculate the advection of air by resolved winds. Latitude and longitude 2-D fields are used to validate the projection calculation in FLEXPART. The map factor field is utilized to correct the displacement of the trajectories. For density calculations and vertical coordinate transformations the pressure 3-D field is used. To interpolate the WRF vertical coordinate onto the FLEXPART vertical coordinate, geopotential is used. The specific humidity and temperature 3-D fields are used for calculating air density and different parameters used in PBL parameterizations. The surface pressure, horizontal winds at 10ma.g.l, the temperature and dew point at 2ma.g.l., are used to calculate different parameters used in PBL schemes. Variables, RAINNC and RAINC are needed to calculate wet deposition. The output time interval of WRF output provided to FLEXPART should in general be as short as practical, time interval of 1h is reasonable in complex terrain (Brioude et al. 2012).

Table 2.3. List of variables needed from the WRF output to run FLEXPART-WRF.

WRF variable	dimension	description
ZNW	1-D	sigma value of full levels
ZNU	1-D	sigma value of half levels
PB	3-D	base value of pressure
P	3-D	perturbation of pressure
PHB	3-D	base value of geopotential
PH	3-D	perturbation of geopotential
T	3-D	temperature
QVAPOR	3-D	specific humidity
TKE	3-D	turbulent kinetic energy (optional)
XLAT	2-D	Latitude
XLONG	2-D	Longitude
MAPFAC_M	2-D	Map factor
PSFC	2-D	surface pressure
*U*10	2-D	10 m wind along x-axis
*V*10	2-D	10 m wind along y-axis
*T*2	2-D	2 m temperature
*Q*2	2-D	2 m dew point
SWDOWN	2-D	surface solar radiation (optional)
RAINNC	2-D	large scale precipitation (optional)
RAINC	2-D	convective precipitation (optional)
HFX	2-D	surface sensible heat flux (optional)
UST	2-D	friction velocity (optional)
PBLH	2-D	PBL height (optional)
	if WIND_OPTION $\leq$ 0 is used	
U	3-D	wind along x-axis
V	3-D	wind along y-axis
W	3-D	Cartesian vertical velocity[1]

The FLEXPART-WRF model has different structure than the FLEXPART ECMWF version. All the input files have been merged into a single control namelist file. The format of the input file assist the experienced FLEXPART users to easily identify the PATHNAMES (the path name of the directory where the meteorological data and FLEXPART output are located), COMMAND (the list of options), AGECLASSES (the ageclasses used in the experiment), OUTGRID (the coordinates and vertical levels of the FLEXPART output domain), RECEPTORS (the coordinates of the receptors), SPECIES (a list of species that include molar weight, wet and dry deposition parameters), RELEASES (coordinates of the release boxes). The rationale behind this consolidation of the input files is that instead of duplicating the FLEXPART binary or directories that include the input files, a single binary and a single directory can be used for any number of FLEXPART-WRF experiments, which improves its flexibility and helps automatic scripting.

Lagrangian particle dispersion models compute trajectories of a large number of infinitesimally small air parcels, also called particles, to describe the transport of air in the atmosphere. Unlike Eulerian models that suffer from the numerical diffusion that is inherent to discrete Eulerian grid-point models, Lagrangian models can accurately represent the emissions from point or line sources and advect accurately narrow plumes and filaments (Rastigejev et al. 2010). Additional benefits of Lagrangian models are their flexibility and small computational cost compared to Eulerian models (Brioude et al. 2013) (Figure 2.4).

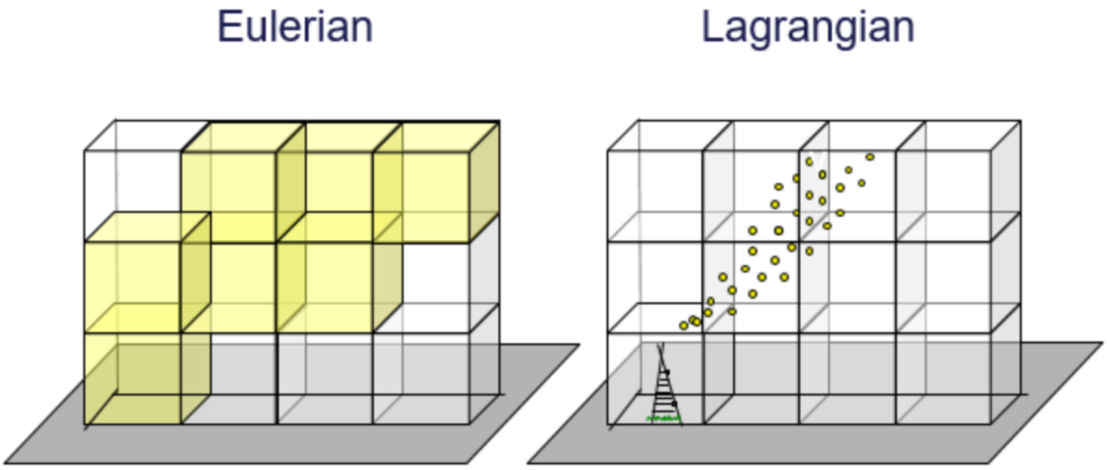

Figure 2.4. Eulerian and Lagrangian advection methods (Flexpart training course 2013)

FLEXPART has been designed to use a large number of particles, while keeping computational costs acceptable taking less than 1 s to calculate the transport of 100 thousand trajectories per time step. This aptitude is mostly important when dispersion from pollution of large areas or from numerous sources need to be simulated. The number of particles needed in a FLEXPART experiment will depend on the size of the domain, the resolution (in space and time) of the meteorological data and the FLEXPART output, and the distribution of the sources. It is suggested using at least 1000 particles per FLEXPART release location in order to achieve a bias of about 0.1% or less in the random term used in the trajectories,

FLEXPART-WRF defines the computational domain, characteristics and grid specifications from the input meteorological data with the same way as FLEXPART-ECMWF/GFS. In the case of a nested input configuration, the coarsest and largest domain will be the one defining the geographical extent of the computational domain. Using the same horizontal coordinates as WRF, x and y coordinates are in meters from the lower left corner of the WRF output domain moreover it reads the projection information to convert the WRF coordinates given in meters into latitude/longitude coordinates if necessary. Also, it tests the uncertainty in the projection transformation before beginning the experiment using latitude and longitude 2-D fields from WRF and terminates if the error is larger than 2% of the horizontal grid spacing. It should be noted that while the grid distances Δx and Δy within the WRF domain are constant, the corresponding distances on Earth are not. Therefore, in order to calculate the true horizontal distance on Earth at any point in the WRF domain 2-D map factors are utilized. Since the Lambert conformal, polar stereographic and mercator projections in WRF are isotropic, the map factors along x and dy directions are identical. However, map factors along x and y directions differ for the latitude/longitude projection used for a WRF run at global scale.

The WRF model output is on a Arakawa C-grid with terrain-following pressure based sigma levels, where the horizontal and vertical wind components are defined on a staggered grid. In FLEXPART-WRF, there is no need of preprocessing the WRF output since the winds are interpolated onto the grid cell center so that all the meteorological data are on the same grid. Wind data from WRF output is on sigma levels. The subroutine verttransform.f90 interpolates the 3-D data onto the FLEXPART-WRF Cartesian terrain following coordinates applying the appropriate correction factors (Figure 2.5).

To achieve better performance and reduced computational time FLEXPART-WRF uses a Cartesian terrain following coordinate system, since the PBL turbulence parameterization is done in this coordinate system. In addition, an option (ADD_SFC_LAYER) is given to add a near surface level with the wind speed at 10ma.g.l., the 2m temperature and the 2m specific humidity read in from the WRF output. In case the first sigma level of a WRF run is below 10m in altitude, this option should not be utilized. Enormous uncertainties can arise from using W, according to Brioude et al. (2012), from the vertical wind in Cartesian coordinates that is output from WRF by default, when significant orography is encountered in the domain. This version of FLEXPART-WRF therefore gives the possibility to use different vertical velocities and allows choosing options between time-average and instantaneous winds. This results in FLEXPART-WRF to require additional output fields from WRF. By default, the WRF output includes instantaneous horizontal wind along x- and y axes on sigma levels (U and V , in m s^{-1}) and a geometric Cartesian vertical velocity (W, in m s^{-1}). In order to convert W from a geometric vertical coordinate onto a terrain following coordinate (either Cartesian or coordinate), a correction factor based on the gradient of orography has to be applied.

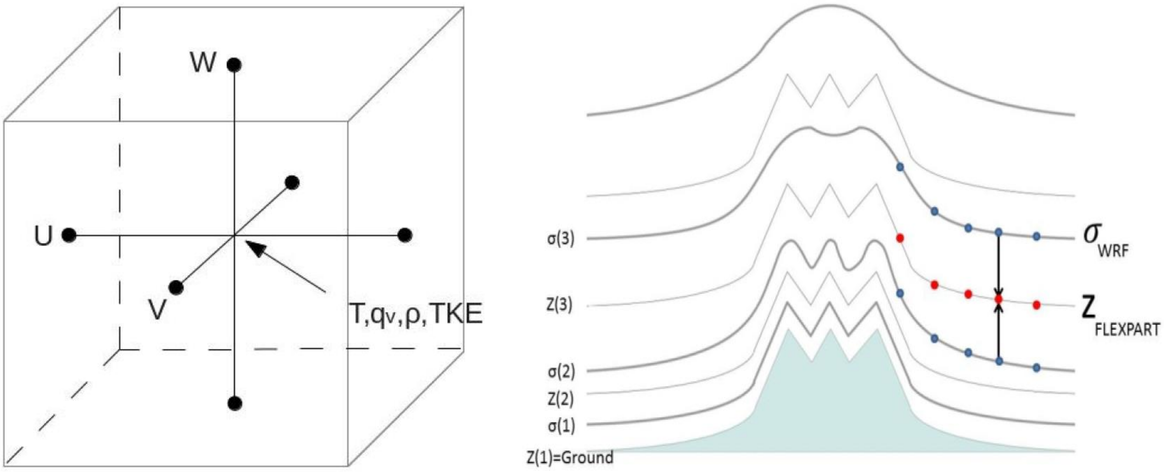

Figure 2.5. On the left, Arakawa C grid representing the staggering of the wind field (U,V ,W) and T, qv, TKE at the center of the grid. On the right, terrain following coordinates used in WRF (σ) and FLEXPART (z). WRF fields are interpolated vertically onto the terrain following Cartesian coordinate z (Brioude et al. 2013).

Flexpart-WRF was implemented in order to utilize it for backwards modelling to track down the origin of the increased concentrations of heavy metals that we measured from the dust samples we collected and chemically, morphologically and mineralogically analyzed, moreover forward simulations from the identified source emitting areas were also made to validate the models predictability. Normally, when FLEXPART is run forward in time (ldirect=1 in file COMMAND), particles are released from one or a number of sources and concentrations are determined downwind on a grid. However, FLEXPART can also run backward in time (ldirect=-1), which is more efficient than forward modeling for calculating source-receptor relationships if the number of receptors is smaller than the number of (potential) sources. In the backward mode, particles are released from a receptor location (e.g., a measurement site) and a four-dimensional (3 space dimensions plus time) response function (sensitivity) to emission input is calculated. To increase accuracy WRF was utilized to feed the output data to Flexpar-WRF running at 0.6km x 0.6km for the selected research domain.

2.5 The numerical weather prediction model WRF-ARW

Weather Research and Forecasting (WRF) Model is a next-generation non-hydrostatic mesoscale numerical weather prediction model designed for both operational forecasting and atmospheric research. It can be utilized for various forecast and analysis applications varying from microscale to synoptic and even global scales. Having a vast number of available parameterizations such as: boundary layer processes, convection, microphysics, radiation and land surface processes and several options for numerical schemes (Skamarock et al. 2008). To operate as a limited-area model, WRF must be provided with boundary conditions from another meteorological analysis system. The effort to develop WRF has been a collaborative partnership among the National Center for Atmospheric Research (NCAR), the National Oceanic and Atmospheric Administration (the National Centers for Environmental Prediction (NCEP) and the Forecast Systems Laboratory (FSL), the Air Force Weather Agency (AFWA), the Naval Research Laboratory, Oklahoma University, and the Federal Aviation Administration (FAA).

WRF model uses perturbation equations with respect to a dry hydrostatic base state and pressure based terrain following coordinates. The mass-weighted prognostic variables in WRF help to conserve mass. The WRF pre-processing module, WPS, sets the computational domain, the geographical projection and resolutions both in the horizontal and in the vertical, and interpolates the meteorological fields (from forecast or from global model analysis) used as initial and boundary conditions. WPS also prepares and re-projects the static data for the runs usually coming from satellite information, including land use and elevation. The choice of meteorological data for the initialization, the land surface model, boundary layer scheme, and convection scheme are all important for an accurate WRF and therefore FLEXPART-WRF simulation.

A WRF simulation consists of three steps pre-processing, run and post-processing. The initialization of the models pre-processing stage consists primary of the definition of geographic data of the domain height, sea-land boundary, interpolation of the initial and boundary conditions of the domain grid provided by a global model. Run, the second step of the model consists of numerical integration of the model equations utilizing initial and boundary conditions assigned in the preprocessing stage where values of equations variables at each domain grid points are calculated. Finally, the post processing is the step in which meteorological fields are calculated.

The non-hydrostatic Weather Research and Forecasting model with the Advanced Research dynamic solver (WRF-ARW Version 3.7.1) was utilized in the numerical experiments. It is a flexible, state-of-the-art numerical weather prediction system, designed to operate in both research and operational mode (Skamarock et al. 2008, Wang et al. 2010).

2.6 X-ray diffraction (XRD)

2.6.1. Introduction

X-ray diffraction (XRD) is one of the most important analytical tools in characterization of crystalline or very fine-grained materials or even amorphous materials. The method is based on diffraction of monochromatic X-rays by the repeating crystal structure of a solid material. The position of peaks in the XRD pattern are determined by the symmetry and size of the unit cell (and the wavelength of the incident radiation), and the relative intensity of the peaks are determined by the crystal structure (the nature of the atoms and their locations) of the investigated material. Both peak positions and intensities provide powerful information for qualitative and quantitative analysis of crystalline substances.

Qualitative phase analysis is carried out based on the positions (d-spacings) and relative intensities of the peaks in an X-ray diffraction pattern in comparison with patterns of known compounds (a so-called search/match procedure). These databases can be customized collections of patterns of pure phases, specialized databases, most commonly the Powder Diffraction File (PDF) maintained by the International Centre for Diffraction Data (ICDD). Due to the relation of the results to the position of the peaks in an XRD pattern, systematic errors that affect peak positions can seriously impact the search/match procedure in qualitative analyses. Shifts in peak positions can occur for several reasons, such as a poorly aligned diffractometer (an error in the zero-2θ position), poor sample packing, and specimen displacement, in addition to the possibility that solid solutions involving cation or anion substitutions can significantly modify peak positions. Internal peak-position standards can be used to correct peak shifts caused by the sample displacement error (e.g., quartz, silicon, talc, zincite, corundum).

There are several approaches to phase identification, ranging from manual to sophisticated computer-automated methods. Manual search/match procedures can be carried out alphabetically (if a material is suspected or known) or according to the most intense peaks in a diffraction pattern (i.e., the Hanawalt search method, Hanawalt & Rinn, 1936). Automatic search/match procedures using a complete peak list or even a complete digital diffraction pattern are possible with a variety of different computer programs, usually included in the software suite provided with a modern diffractometer. With any search/match procedure, the results should be considered as a list of suggestions. Ultimately, it is up to the analyst to determine the correct solution(s) that are reasonable.

Quantitative analysis provides information about the composition of multiphase mixtures e.g., for raw material analysis. There are two families of quantification methods. The first one relates to extracted intensities of distinct (single) lines in the XRD pattern. Different approaches include the addition/dilution method, the use of standards or the direct Reference Intensity Ratio (RIR) method. The second method relates in full-pattern fitting to the whole pattern phase intensities without refinement of structural parameters of the contained phases or even with their refinement in the Rietveld method. With proper methodology, high precision quantitative analyses can be obtained, with very low detection limits.

Most conventional methods of quantitative analysis today are based on the familiar equation given in Klug and Alexander (1974) that relates the intensity of a reflection from a phase in a mixture (I_i) to its concentration and density and to the mass absorption coefficient of the unknown mixture:

$$I_i = K_i \frac{X_i}{\rho_i \, \mu_m}$$

where X_i is the weight fraction of component i, K_i is a constant depending on the diffractometer and component i, ρ_i is the density of component i, and μ_m is the mass absorption coefficient of the mixture.

Amorphous components occur in many materials and in some instances can comprise most of the mixture. Thus, although amorphous components are not usually quantified by X-ray powder diffraction, it is often useful to be able to determine, at least semi-quantitatively, the amount of amorphous material in a sample. Because amorphous materials present problems different than those encountered with crystalline minerals, their analysis deserves special mention.

With the general availability of automated X-ray powder diffractometers in the 1980’s, digital diffraction data are now routinely available on computers and can be analyzed by a variety of numerical techniques. Complete digital diffraction patterns provide the opportunity to perform quantitative phase analysis using all data in a given pattern rather than considering only one or a few of the strongest reflections. As the name implies, full pattern methods involve fitting the entire diffraction pattern, often including the background, with a synthetic diffraction pattern.

The Rietveld method of analysis provides numerous advantages over conventional quantitative analysis methods for mixtures of crystalline phases. Because the method uses a pattern-fitting algorithm, all lines for each phase are explicitly considered, and even severely overlapped lines are not problematic. The use of all lines in a pattern minimizes the uncertainty in the derived weight fractions and the effects of nonlinear detection systems. The effects of primary extinction are also minimized, as all reflections from each phase are used in the analysis rather than just the strongest ones. Because each phase in a mixture must be explicitly included in the analysis, failure to consider a phase will yield obvious differences between the observed and calculated diffraction patterns in the so-called different plot. The Rietveld quantitative analysis method can also be used in the traditional manner for refining the structural parameters of each phase in the mixture. Thus, information obtained by this method can include atom positions, site occupancies, and precise unit-cell parameters, in addition to information on the nature of peak broadening.

2.6.2. Sample Preparation for X-ray Powder Diffraction

As with many analytical methods, the preparation of samples for X-ray powder diffraction analysis is one of the most critical steps. The primary results desired are accurate and precise (i.e., reproducible) intensities, and minimizing systematic sample related effects is probably more important than accounting for instrumental systematic errors in the collection of accurate and precise diffraction data. X-ray powder diffraction has at its heart two primary assumptions, namely (1) that we present to the beam essentially an infinite number of crystallites in (2) a random orientation. Thus, the “ideal” powder consists of material with a grain size of about 1 – 3 μm, although this restriction depends greatly on the interplay between sample and radiation. Klug and Alexander (1974) showed that reproducible intensities could only be obtained from quartz powders with $Cu_{K\alpha}$ radiation when size fractions <15 μm were used. It is important to note that although good results can be obtained using 5 – 15 μm powders of typical silicate minerals, the required sizes for powders of more highly absorbing materials, such as Fe oxides, are considerably smaller due to the fact that a smaller volume of crystallites is bathed in the X-ray beam.

The powder should be mounted with randomly oriented grains with a flat and smooth sample surface forming an "infinitely" large specimen to avoid beam overflow and transmission. However, real materials consist of large crystals together with fine-grained material often containing phases with different properties in hardness, cleavage, density and sensitivity against mechanical and thermal influence. Thus, several sample preparation problems are commonly encountered. Some of these concerns the preparation of the powdered material and others arise during mounting of the powders in a suitable holder. In order to fulfill the requirement of having a representative subsample, grinding, homogenization, and splitting must be carried out without loss of material, contamination, phase separation, phase transformation, or destruction/ modification of crystal structures. Due to the large differences in material physical properties, there is no one standard method for preparation of powdered samples. The best strategy must be adapted to the material and the needs of analysis.

Representative particle size of the <63μm fraction of the studied samples was grounded further and used for qualitative and semi-quantitative determination of their mineralogical composition adsorbent materials by the X-ray diffraction method. Random orientated preparations were used for determination of the total percentage of clay minerals, as well as of the other minerals involved in the formation of natural clays. Samples were also tested in parallel-oriented preparations for identification of clay minerals, as well as their parallel orientation of chain silicate minerals causes the intensities of their reflections to be enhanced, as well as after treatment with ethylene glycol, in order to determine whether or not swelling minerals are involved. The examination was held in the laboratories of the Department of Mineralogy-Petrology-Economic Geology, School of Geology, Aristotle University of Thessaloniki.

A Philips PW1820/00 diffractometer with $Cu_{K\alpha}$ radiation (λ=1.5418 Å) and Ni filter (0.0170 mm) under 35 kV and 25 mA conditions were used for the measurements. Counting statistics, i.e., "step size" and "time per step" parameters were determined according to the requirements of each analysis, and in particular for random and orientated preparations, a scan step of 2θ 0.02 degrees and a time per step of 1.5 sec in the range of 3-63° 2theta were selected (measuring time ~1 hour and 25 minutes), as proposed by Moore and Reynolds (1997). For samples which were treated with ethylene glycol, the 2θ range of 3-33 degrees was selected (duration ~42 minutes), while the rest of the parameters remained unchanged. Prior to the diffraction, the sensitivity and accuracy of the diffractometer was checked with a special standard of pure silicon. Values of differences were for d ±0.0002 and for 2theta ±0.006.

In the present work, the identification of the various mineral phases was made based on the characteristic reflections of the resulting X-ray patterns, while its semi-quantitative determination of the mineralogical composition was carried out based on measurements of intensities at specific reflections of the phases identified, taking into account the density and mass absorption coefficient of the minerals determined for $Cu_{K\alpha}$ radiation. Corrections were made using external standard of mixtures of the major phase identified in the studied samples.

2.7 Scanning Electron Microscopy - SEM

Scanning Electron Microscopy - SEM - is a powerful technique in the examination of materials. It is used widely in metallurgy, geology, biology and medicine, to name just a few.

The user can obtain high magnification images, with a good field depth, and can also analyze individual crystals or other features. A high-resolution SEM image can show detail down to 25 Angstroms, or better. When used in conjunction with the closely related technique of energy-dispersive X-ray microanalysis (EDX, EDS, EDAX), the composition of individual crystals or features can be determined.

A normal scanning electron microscope operates at a high vacuum. The basic principle is that a beam of electrons is generated by a suitable source, typically a tungsten filament or a field emission gun. The electron beam is accelerated through a high voltage (e.g.: 30 kV), passes through a system of apertures and electromagnetic lenses to produce a thin beam of electrons and then scans the surface of the specimen by means of scan coils.

Electrons are emitted from the specimen by the action of the scanning beam and collected by a suitably positioned detector. The microscope operator is watching the image on a screen. The key to how the scanning electron microscope works (and this is the clever bit) is that the beam scanning the specimen surface is exactly synchronized with the spot in the screen that the operator is watching. The electron detector controls the brightness of the spot on the screen - as the detector "sees" more electrons from a particular feature, the screen brightness is increased. When there are fewer electrons, the spot on the screen gets darker. These days, the screen is generally a digital monitor, not a glass cart, but the principle is the same.

The magnification of the image is the ratio of the size of the screen to the size of the area scanned on the specimen. If the screen is 300 mm across and the scanned area on the specimen is 3 mm across, the magnification is x100. To go to a higher magnification, the operator scans a smaller area; if the scanned area is 0.3 mm across, the magnification is x 1000, and so on.

There are different types of electron image. The two most common are the secondary electron image (SEC) and the backscattered electron image (BACK). The SEC is used mainly to image fractured surfaces and gives a high-resolution image. The BACK is used typically to image a polished section; the brightness of the BACK is dependent on the atomic number of the specimen (or, for compounds, the average atomic number). For example, lead will appear brighter than iron and calcium oxide will appear brighter than calcium carbonate. The BACK is an atomic number map of the specimen surface. All SEM images are in black-and-white, although they may subsequently have false colors applied to them for aesthetic reasons or to aid interpretation.

A development of the normal high-vacuum scanning electron microscope is the ESEM, or Environmental SEM. The ESEM can operate with air in the specimen chamber - the pressure is lower than atmospheric pressure but higher that the high-vacuum of a normal SEM. This has the advantage that wet specimens can be examined without them dehydrating and is especially useful for biological specimens and other specimens containing water, such as freshly mixed cement paste.

2.8 Energy-dispersive X-ray microanalysis (EDX)

Energy-dispersive X-ray microanalysis (EDX) is complementary to SEM. It enables the operator to determine the composition of the features in the SEM image. The principle of EDX is that the electron beam generates X-rays within the specimen. Many of these X-rays have energies characteristic of the elements that emitted them. So, if you can measure the energy of the X-rays, you know what elements are present in the specimen. If you control the instrumental conditions carefully you can determine not only what elements are present but their concentrations.

There are three principal components to a basic EDX system: The X-ray detector that measures the voltage pulses corresponding to the X-ray energies, and a computer. The X-ray detector is positioned to intercept X-rays emitted from the specimen. On entering the detector, an X-ray generates a small current, which is then converted into a voltage pulse. The size of the voltage pulse is proportional to the energy of the X-ray. A computer measures the voltage pulses over a time period, e.g. 60 seconds and plots them as a histogram. The histogram shows a spectrum of the X-ray energies that were measured; by examining the spectrum, the elements present can be determined. The EDX system may also be able to take control of the SEM scanning system in order to collect elemental distribution maps ("dot maps") or elemental line profiles. The samples studied under a JEOL JSM-840A scanning electron microscope at the electron microscopy laboratory of Aristotle University of Thessaloniki, equipped with an energy dispersive analysis system INCA 250. The instruments operating conditions were voltage 15kV, electron beam intensity <3nA and 1mm diameter, while the measurement time was 60sec.

CHAPTER 3: CASE STUDY 1

3.1 Introduction

In this chapter the case study of the impact of uncontrollable burning of biomass for residential heating in the atmosphere of the city of Thessaloniki during December 2012, is presented. The difficult economic effects on urban economy in the last two years in Greece resulted in the almost tripling of oil prices which lead the majority of people to turn to alternative forms for domestic heating such as the uncontrolled consumption of biomass (firewood and any other form of artificial substitutes). The particles released from burning wood contain organic toxic ingredients such as methylphenol (Kjällstrand et al. 2001) and polycyclic aromatic hydrocarbons (PAHs) (Barregard et al. 2006). Numerous studies have certified that biomass burning contributes as a release source of fine particles $PM_{2.5}$ (Daher et al 2012, Verma et al. 2007, Zheng et al. 2005, Saffari et al. 2013). Exposure to emissions from biomass combustion leads to particular adverse health effects such as cardiorespiratory problems, increased blood pressure, increased mortality / decrease of life expectancy, lung disorders and lung cancer, systemic inflammation and oxidative stress etc. (Barregard et al. 2006, Saffari et al. 2013, Orozco-Levi et al. 2006, McCracken et al. 2007, Mousiopoulos 2013).

One of the biggest problems of air pollution in the city of Thessaloniki is the high concentrations of suspended particles. Airborne particles vary in terms of their concentration, and physical, chemical and morphological characteristics (Samara et al. 2011). They are emitted primary (anthropogenic processes, soil erosion, sea droplets) and suspended directly in the atmosphere in particulate form, either produced secondarily in the atmosphere (condensation, nucleation, chemical conversion). Suspended particles with equivalent aerodynamic diameter less than 10mm (PM_{10}, respirable suspended particulates) can act as carriers for various chemical compounds that serve as biological contaminants adsorbed or adhered on them, as well as catalysts of chemical reactions that occur in the atmosphere, which mainly contribute to air pollution. These particles are separated into particles having diameter less than 2.5 microns and with a diameter greater than 2.5 microns. Airborne particles of diameter less than 2.5 microns and 1micron, $PM_{2.5}$ and PM_1, are able to enter in the respiratory system and then via the lungs into the bloodstream (respirable suspended particulate matter).

The suspended particulate contaminants in ground level are responsible for the formation of smog. The most intense incidents of smog formation occur in urban areas, where light winds and a shallow boundary layer act combined resulting in concentration of pollutants in a relatively small volume of air. The weather-meteorological conditions enhance the formation of this kind of cloud that usually occurs during the winter period in early morning hours, while the type of smog is characterized by high aerosol loads and high levels of sulfur dioxide (Kourtidis et al. 2002, Marley et al. 2008).

The present study examines the impact of air pollutants in the atmosphere of Thessaloniki during December 2012. Mineralogical, morphological and chemical analysis was implemented by falling dust collected at rooftop level from multi-storey buildings from three sampling location areas, Kalamaria District, Aristotle University and Seaport. These samples were compared with the same dust sampling locations from earlier sampling periods (September 2012 and December 2011) in order to assess their organic load. Furthermore, we investigated and evaluated the influence of meteorological conditions of the study period (December 2012) to the accumulation of pollutants.

3.2 Methodology

3.2.1 Sampling and sample preparation

Falling-dust samples collected at rooftop building levels from three selected sampling sites (Figure 3.1) in Kalamaria district (multi-storey building), Aristotle University (building roof Faculty of Science) and Seaport (multi-storey parking lot station). Sampling was carried out during the period December 2011 - September 2012 between 23:00 to 00:00, twice a month every 15 days. From each sample 50-150 g of powder was collected, wiping total area of 1m^2 using sterilized collectible instruments. The samples were dried in an oven at 35 °C for

3 days. After that they were passed through a bronchi sieve section of 63mm and received the fraction diameter <63 mm for further investigation.

Figure 3.1. Sampling locations (1: AUTH 2: Port 3: Kalamaria) of the dust testing samples ©2006 Yahoo! Inc - Imagery © 2006 i-cubed, GeoEye).

A total number of over 140 samples (3 sampling locations × 2 samples per month × 12 months × 2 years = 144 samples) was collected from the three sampling sites. For this study 9 samples were utilized, 3 from each sampling area that were collected on 21-12-12 (wide extent of uncontrolled burning of biomass phenomenon, overcrowded repletion of the atmosphere with smog) on 22-09-12 (smog-free atmosphere) and 20.12.11 (small extent of uncontrolled burning of biomass, atmosphere with little or no encumbrance of smog).

3.2.2 Analytical Methods

The evaluation of the mineralogical composition of the falling-dust samples was conducted by the method of X-ray diffractometry (XRD) using a Philips PW1820/00 diffractometer equipped with a microprocessor and software PW1710/00 PCAPD v3.6 for automatically sampling and processing of scanned data into digital format. Cu tube and Ni filter were utilized to obtain Cu_{Ka} radiation at 35kV voltage conditions and current 25mA and scan area angle 2θ 3-63^{o}. The semi-quantitative determination of the minerals was based on counts of specific reflections, taking under consideration the density and the mass absorption coefficient of minerals identified for Cu_{Ka} radiation. The amorphous material of a sample is comprised of two components, the organic material and the amorphous inorganic phases, both of which are recognized as a background hump on the XRD pattern starting approximately from 10° 2θ. The proportion of amorphous material (organic and inorganic origin) was calculated according to the methodology described by Kantiranis et al. (2004).

The calculation of the contained organic material was made with the effect of an aqueous solution 30% H_2O_2 in a representative sample of <63mm fraction for each of the examined dust samples (Jackson 1974). The atomic oxygen released during the decomposition of H_2O_2 ($H_2O_2 \rightarrow H_2O + ½O_2$) is one which destroys organic matter without affecting the other components of the samples. The content of organic material is calculated as the difference in weight before and after treatment expressed as a percentage (%).

The study of the morphology and chemistry of the dust grains was performed by the method of electron microscopy. The study of the samples was made by a scanning electron microscope of JEOL JSM-840A type at the electron microscopy laboratory of Aristotle University of Thessaloniki, equipped with an energy dispersive analysis system INCA 250. The instruments operating conditions were voltage 15kV, electron beam intensity <3nA and 1mm diameter, while the measurement time was 60sec.

3.3. Results and discussion

3.3.1. Mineralogical analysis and organic material

Samples of <63mm fraction (Table 3.1) were found in all cases significantly higher in Kalamaria region. Specifically, during December 2012, falling dust quantity of <63mm equal to 1,78g / m^2 was measured in Kalamaria, while at the same time period the measured values were 1,33 and 0,48g / m^2 for AUTH and Port respectively. Compared with the period of December 2011, an incensement in the amount of <63mm fraction of falling dust is observed for December 2012 in all sampling sites, with most important noted in the sampling position of Kalamaria (19.1%), while less increased was in AUTH (10.5%) and the Port (by 8.3%).

Representative diffractograms of the falling dust for Kalamaria sampling region on 12/21/2012, are given in Figure 3.2. As shown, a background hump in the XRD pattern of the initial material occurs between 10-18 °2θ which is attributed to amorphous organic and inorganic phases, disappears completely in the treated sample. No other reflection disappears, an indication that the processing method is particularly effective in organic matter removal.

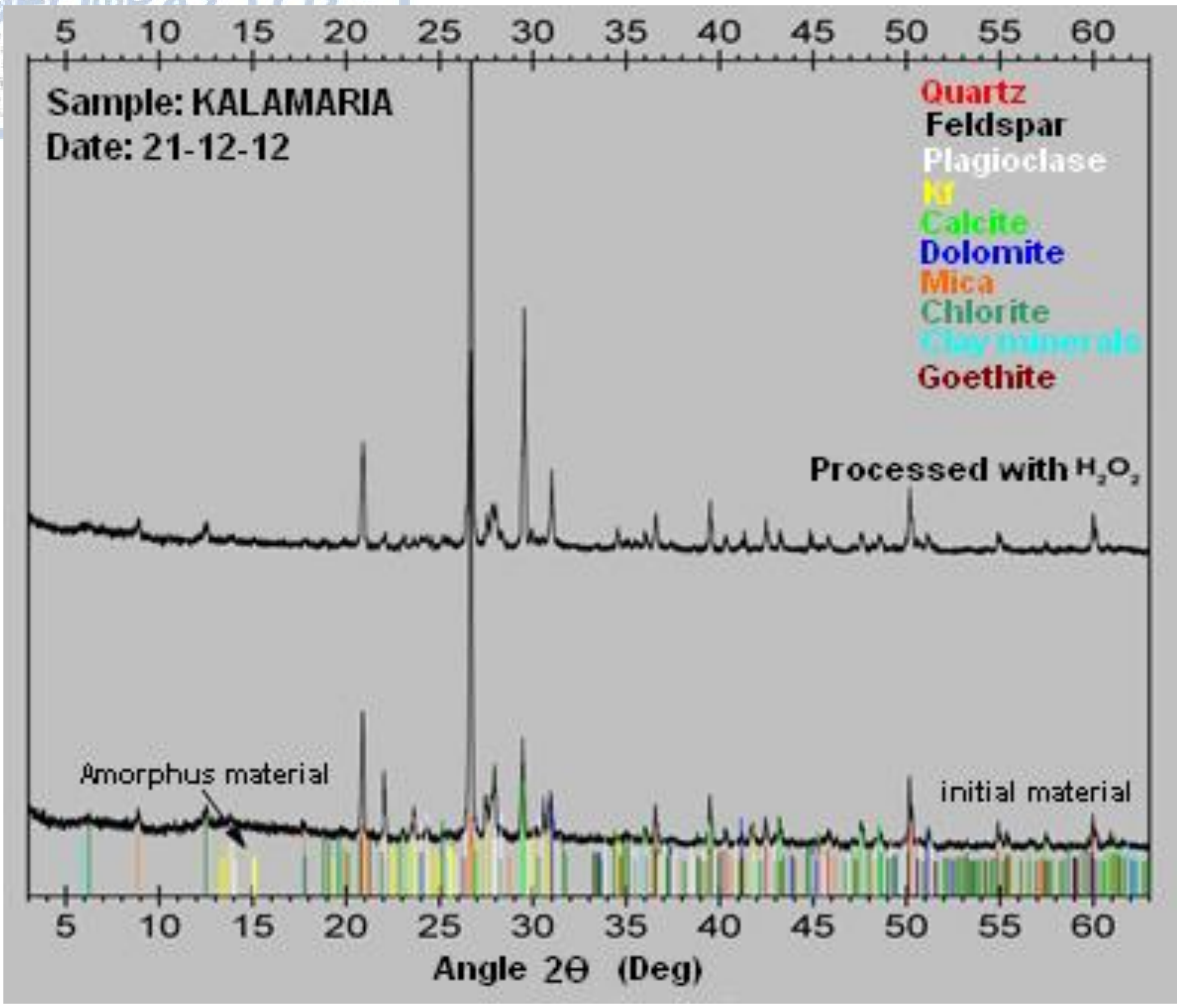

Figure 3.2. Representative diffractogram of falling dust from Kalamaria District (21-12-012) before and after sample treatment for organic matter removal process.

According to the results of the mineralogical analysis (Table 3.1), the samples of falling dust primarily consist of quartz (40-45 % w/w) and calcite (15-23 % w/w) as major phases, feldspars and dolomite in lesser percentages, while mica, chlorite and clay minerals were detected in very small quantities. Goethite was measured at low rates in two sites (Kalamaria and AUTH). Furthermore, significant amounts of amorphous phases were identified (8-15% w/w).

Quartz (SiO_2) is one of the most resistant minerals to physical and chemical erosion. The possible effects of the crystalline forms of silica (most common quartz) on health, are of particular interest (Ikeda et al. 1986), while the International Agency for Research on Cancer (IARC 1997) classifies them as carcinogenic to humans (Category I). However, these results do not allow the assessment of the potential risk to the population, as the health risk depends largely on the morphology of quartz. However, calcite, dolomite and feldspar, derive mainly from building materials erosion (Tossavainen et al. 1999). The phyllosilicate minerals (mica, chlorite, and clay minerals) may possibly be derived from the corrosion of construction materials and deposited directly on the ground, but it is probably due to their sheet-like structure and low specific weight, that can be carried out by re-suspending from other regions. Goethite derives from the oxidation of metallic elements located on building's rooftops (e.g., antennas). The amorphous phases derive from the incomplete combustion of organic material origin (mainly solid and liquid fuels) and from the corrosion of inorganic aluminosilicate phases of buildings structural components.

Table 3.1. Weight of <63mm fraction, organic material and semi-quantitative determination of the mineralogical composition (% w/w) of examined falling dust samples.

Sample	**Weight (g/m^2) of <63μm fraction**	**Organic Matter**	**Q**	**Pl**	**Kf**	**C**	**D**	**M**	**Ch**	**Cl**	**Go**	**Am**
K1_21-12-12	1.78	9.4	44	7	6	15	5	2	3	1	2	15
K2_22-09-12	6.26	2.3	42	9	5	18	3	4	5	3	1	13
K3_20-12-11	1.44	4.1	40	8	7	20	4	3	4	2	2	10
A1_21-12-12	1.33	7.1	43	5	3	22	3	4	3	3	1	13
A2_22-09-12	0.47	2.2	45	5	5	23	2	3	2	4	1	10
A3_20-12-11	1.19	3.6	44	4	4	22	4	4	3	4	1	10
Π1_21-12-12	0.48	5.2	43	9	6	19	3	4	4	3	-	9
Π2_22-09-12	0.15	1.9	44	8	6	20	5	3	3	3	-	8
Π3_20-12-11	0.44	2.8	43	7	7	18	4	5	4	3	-	9

K1-K3: Kalamaria Samples, A1-A3: A.U.TH. Samples, Π1-Π3: Seaport multi-storey parking lot station, Q: Quartz, Pl: Plagioclase, Kf: Kf Feldspar, C: Calcite, D: Dolomite, M: Mica, Ch: Chlorite, Cl: Clay minerals, Go: Goethite, Am: Amorphous phase.

The organic material was measured at concentrations of between 1.9% (sample P2_22-09-12) and 9.4 % w/w (sample K1_21-12-12) showing significant differences between periods and between sampling areas. Specifically, in the samples collected on 12/21/2012 a higher participation of organic material was found between 5.2% (sample P1_21-12-12) and 9.4 % w/w (sample K1_21-12-12). On the contrary in the samples of September 2012 and in those of December 2011, there is less impact of falling dust of organic material origin. Between the same sampling sites a significant impact can be observed in December 2012. More specifically, an increase of ≈129% in Kalamaria, of ≈100% at the Aristotle University and ≈86% in multi-storey car parking station at the port was measured comparing prices with those of December 2011. Comparing the results with the summer sampling period (September 2012) an increase of ≈309% in Kalamaria, ≈223% at the Aristotle University and ≈174% in port can be observed. The differentiation between the three sampling sites is caused due to their placement in the conurbation. The region of Kalamaria is characterized by a densely built environment with buildings and many household heaters, the position in AUTH is severely influenced of the built environment of the city center, and finally the position of the parking station near port is not significantly affected by housing since the surrounding area is comprised of professional building premises.

Increases of the concentration of falling dust in organic material found in this study agrees with the increased concentrations of particulate matter observed in Thessaloniki during the winter period after 2010 attributed to the burning of wood and other types of biomass (Petrakakis et al. 2013). According to Moussiopoulos (2013), the burning of biomass and wood led to a rapid increase in the average monthly concentration of fine particles in the winter period (Nov 2012-January 2013), with this increase being more pronounced in afternoon hours. Moreover, Saffari et al. (2013) found that in the urban background of Thessaloniki’s region concentrations of $PM_{2.5}$ in the winter of 2013 were 30% higher compared to the same period in 2012 and 2-5 times higher concentrations of the biomass combustion indicators such as water-soluble K, anhydride sugars, organic carbon and PAHs.

3.3.2. Morphological examination

The observation by electron microscopy (Figure 3.3) showed that the test samples composed mainly of silica and aluminosilicate particles and of particles rich in Ca.

The silica and aluminosilicate dust particles are shown with angular or irregular shapes that are characteristic of their origin. Ca-rich particles are mainly calcite particles or appear as irregular aggregates and derived from erosion of building materials on the building’s rooftops. Finally, the identified Fe-rich particles are corrosion products of the metal materials located on the roofs of buildings and presented as irregular aggregates. Furthermore, particles of various morphologies were recognized as carbon rich (Figure 3.3). Specifically, spheroidal dust particles identified consisting almost exclusively of carbon and derive from domestic and industrial heating systems emissions, as well as flattened or spongy particles deriving from household heaters emissions. Domestic heaters (fireplaces and stoves) emitting mainly lamp-black and / or flattened (microscopic chips of unburned wood) particles in comparison to diesel boiler burners that produce predominantly in all cases spherical and carbon-rich particles.

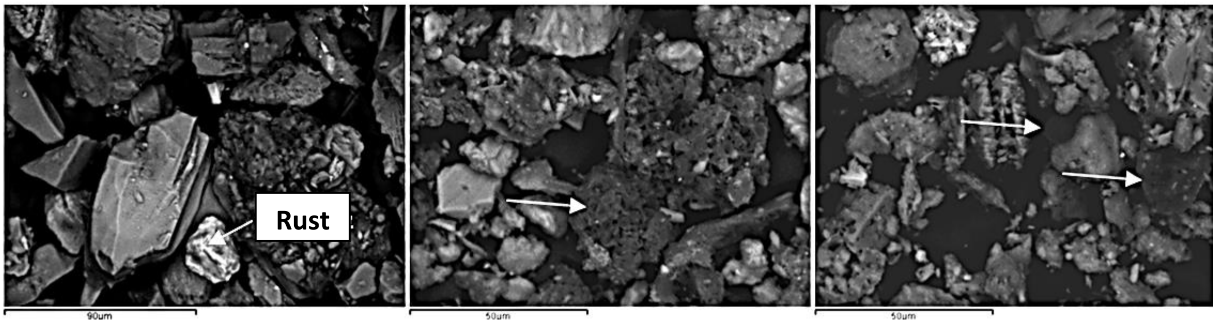

Particle/Element	C	Mg	Al	Si	P	S	K	Ca	Mn	Fe
Rust			5.78	11.5				1.50		81.3
Spongy (center)	68.9		7.68	16.32			1.6	5.92		
Spherical (right)	95.2			0.94	0.75	1.01	0.94	1.07		
Flattened (right)	73.6	2.03	3.71	6.02		2.59	0.84	4.97	1.36	4.48

Figure 3.3. Backscatter photomicrographs dust particles and microanalysis (left) irregularly shaped silicates, aluminosilicates components and rust, (center) sponge particles agglomerate and (right) a spherical particle and carbon-rich flattened piece

3.3.3 Meteorological conditions

In Figure 3.4 the meteorological measurements of AUTH observatory during 21 to 22 December 2012 are shown.

The measurements show a decrease in wind speed during 21 December 2012 with the lowest rates (about 1 m/s, i.e. almost apnea) occurring during the afternoon and nocturnal hours. These low wind speeds were maintained throughout the night from 21 to 22 December. The transition to lower wind speeds is generally associated to relatively higher temperatures and higher relative humidity values compared to the previous day, as well as drop of air pressure. The fact of the shift of meteorological observations during the day of 21 December is linked to the change of the short wind direction from northwest to southwest in the lower layers of the atmosphere due to the approach of a low barometric system over Southern Italy, Adriatic Sea and Western Greece. The study of the thermodynamic state of the atmosphere indicates stable conditions. Therefore, meteorological data analysis with low wind speeds and stability favors high concentrations of pollutants.

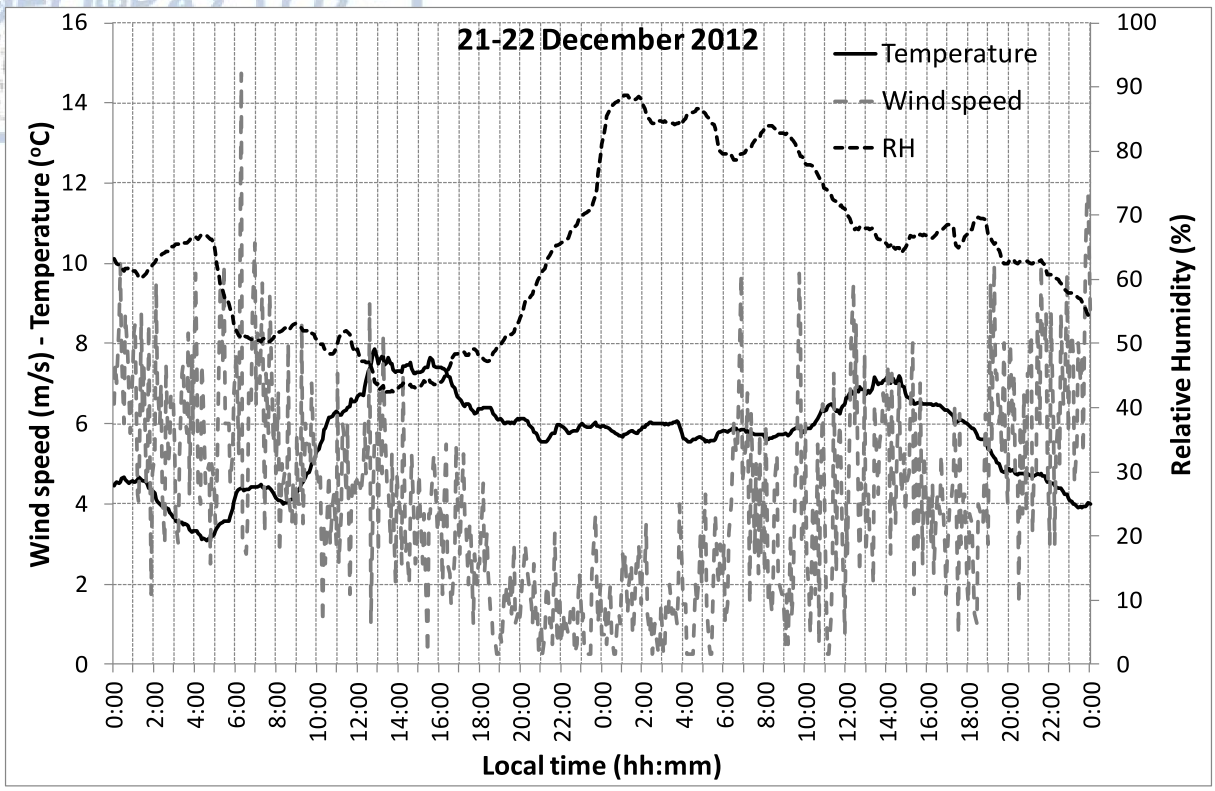

Figure 3.4. Meteorological observations of wind speed, temperature and relative humidity in Thessaloniki (Dept. of Meteorology and Climatology, A.U.TH.) during 21-22 December 2012.

3.4. Conclusions

Mineralogical, chemical and morphological analysis of falling dust samples collected from rooftops level in three selected sampling sites in the wider conurbation of Thessaloniki found that: The fallen dust mainly consists of inorganic origin components from the corrosion of building materials without excluding material contribution from air suspending fumes. During December 2012 a significant increase in the organic load of dust samples had been observed compared to previous winter and summer sampling periods (by 86-129% compared to December 2011, at 174-309% compared to September 2012). The pollution impact of the atmosphere of Thessaloniki with pollutants of organic origin during the period of December 2012 attributed to the extensive and uncontrolled burning of biomass for domestic heating. Meteorological conditions in December 2012 favored the high pollutant concentrations and the occurrence of smog.

CHAPTER 4: CASE STUDY 2

4.1. Introduction

In chapter 4 the case study of seasonal variations of the mineralogical composition and the organic matter content of falling dust in Thessaloniki during 2012-13, is presented. The severe economic crisis that struck Greece the last six years affected greatly its urban economy. These economic parameters lead the majority of people in search of alternative forms for domestic heating in order to withstand the winter period and the increased fuel prices. This resulted in the uncontrolled consumption of biomass, i.e. firewood and any other form of artificial substitutes (Kollias et al. 2014). Biomass burning contributes as a release source of fine particles PM2.5 (e.g. Zheng et al. 2005, Verma et al. 2007, Daher et al. 2012, Saffari et al. 2013), the particles released from burning wood contain organic toxic ingredients such as methylphenol (Kjällstrand and Petersson 2001) and polycyclic aromatic hydrocarbons (Barregard et al. 2006).

Increased concentrations of suspended particles causing air pollution is a major problem occurring in the city of Thessaloniki. Airborne particles can be categorized according to their concentration, physical, chemical and morphological characteristics (Samara et al. 2016). Emitted primary (anthropogenic processes, soil erosion, sea droplets) and suspended directly in the atmosphere in particulate form, either produced secondarily in the atmosphere (condensation, nucleation, chemical conversion). Suspended particles with equivalent aerodynamic diameter less than 10μm (PM10, respirable suspended particulates) can affect air pollution since they act as carriers for various chemical compounds for biological contaminants adsorbed or adhered on them. Also they can act as catalysts of chemical reactions that occur in the atmosphere. They can be further separated into coarse particles having a diameter greater than 2.5μm and fine particles with a diameter less than 2.5μm capable of entering the respiratory system and then via the lungs into the bloodstream.

Exposure to emissions from biomass combustion leads to particular adverse health effects such as cardiorespiratory problems, increased blood pressure, increased mortality/decrease of life expectancy, lung disorders and lung cancer, systemic inflammation and oxidative stress (Barregard et al. 2006, Orozco -Levi et al. 2006, Mc Cracken et al. 2007, Mousiopoulos 2013, Saffari et al. 2013).

High concentrations of suspended particles at ground level occur during smog conditions, in association with high levels of sulfur dioxide, or with photochemical pollutants such as O_3, NO_2, PAN, etc. The most intense incidents of smog formation occur in urban areas, where light winds and a shallow boundary layer air act combined resulting to concentration of pollutants in a relatively small volume of air. The weather-meteorological conditions enhance the formation of this kind of cloud that usually occurs during the winter period in early morning hours (Kourtidis et al. 2002, Marley and Frederick 2008).

The present study examines the impact of air pollutants in the atmosphere of Thessaloniki during years 2012-13. Mineralogical and organic material analysis was implemented on falling dust collected at building rooftop level from three sampling location areas that are Kalamaria (East Thessaloniki), Aristotle University (center of Thessaloniki) and Seaport (West Thessaloniki). The methods and techniques used for the analysis of the studied samples were mentioned in Chapter 3.

4.2. Methodology

4.2.1 Sampling and sample preparation

Falling-dust samples collected at rooftop building level from three selected sampling sites in Kalamaria district (multi-storey building), Aristotle University (building roof of the Faculty of Sciences) and Seaport (multi-storey parking lot station). Sampling was carried out during the period June 2012 - May 2013 between 23:00 to 00:00, twice a month every 15 days. From each sample 50-150g of powder was collected, wiping an area of $1m^2$ using sterilized collectible instruments. The samples were dried in an oven at 35^oC for 3 days. After that the <63μm fraction was separated by sieving for further investigation. A total number of over 70 samples (3 sampling locations × 2 samples per month × 12 months = 72 samples) were collected between June 2012 and May 2013.

4.3. Results and discussion

4.3.1. Mineralogical analysis and organic material

In Table 4.1 the mean value, standard variation, minimum and maximum amounts of the minerals and the amorphous content determined in the <63μm sample fraction are shown. Also, the weight and the organic material of the <63μm fraction are given. More specifically, the <63 μm fraction of the total amount of falling dust during 2012-13 ranged from 10.3% (Autumn 2012) to 27.5% (Spring 2013). It is clear from Figure 4.1 that the mean weight of the <63μm fraction is progressively increasing from autumn 2012 to spring 2013. Kollias et al. (2014), comparing the periods of December 2011 and December 2012, found an incensement in the amount of <63μm fraction of falling dust during December 2012 in the same sampling sites and attributed this observation to favorable meteorological conditions with atmospheric stability and low winds.

According to the results of the mineralogical analysis (Table 4.1), the samples of falling dust primarily consist of calcite (35-45 wt.%) and quartz (29-35 wt.%) as major phases, feldspars and dolomite in lesser percentages, while mica, clay minerals and amphibole were detected in very small quantities. Gypsum was measured at low amounts in spring 2013. Furthermore, significant amounts of amorphous phases were identified (7-15 wt.%).

Quartz (SiO_2) is one of the most resistant minerals to physical and chemical erosion. The possible effects of the crystalline forms of silica (most common quartz) on health are of particular interest (Ikeda et al. 1986), while the International Agency for Research on Cancer (1997) classifies them as carcinogenic to humans (Category I). Also, calcite, dolomite, feldspars and gypsum derived probably from the erosion of building materials (Tossavainen and Forrssberg 1999).

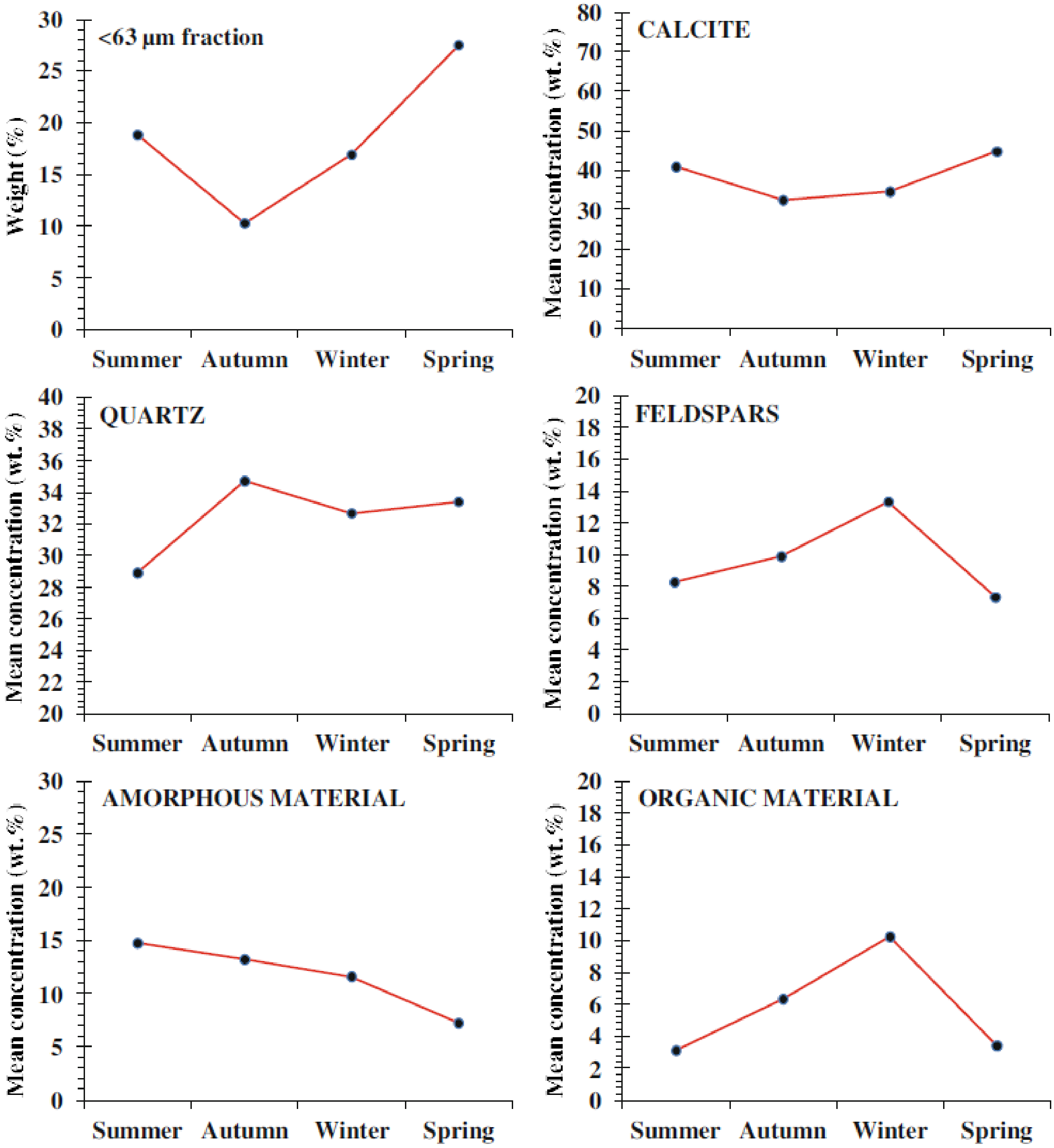

Figure 4.1. Annual variation (wt.%) of weights and amounts of calcite, quarts, feldspar, amorphous and organic material of the < 63 μm fraction of the examined samples.

The phyllosilicate minerals (mica and clay minerals) may possibly derive from the corrosion of construction materials and deposited directly on the ground, but it is probably due to their sheet-like structure and low specific weight can be carried out by re-suspending from other regions. The amorphous phases derive from the incomplete combustion of organic material (mainly solid and liquid fuels) and from the corrosion of inorganic aluminosilicate phases of buildings components.

Table 4.1. Weight (%) of the <63μm fraction, semi-quantitative mineralogical composition (wt.%) and organic matter (wt.%) of the studied samples.

		Summer 2012				Autumn 2012			
		MV	*SD*	Min	Max	MV	*SD*	Min	Max
Weight of the <63μm fraction	g/m^2	0.74	*0.43*	0.24	1.52	0.81	*0.22*	0.56	0.99
	%	18.8	*13.2*	6.7	48.7	10.3	*6*	6.1	17.2
Quartz		29	*7*	21	44	35	*9*	24	40
Micas		1	*0.5*	1	2	1	*0*	1	2
Clay minerals		2	*1*	1	3	3	*1*	1	3
Feldspar		8	*4*	3	13	10	*1*	9	11
Calcite		41	*4*	33	46	32	*12*	24	46
Dolomite		4	*1*	2	7	5	*2*	4	7
Amphibole		2	*1*	1	2	2		2	2
Gypsum		-	-	-	-	-	-	-	-
Amorphous		15	*6*	8	27	13	*4*	9	16
Organic matter		3	*1*	2	5	6	*2*	4	8
		Winter 2012-13				Spring 2013			
		MV	*SD*	Min	Max	MV	*SD*	Min	Max
Weight of the <63μm fraction	g/m^2	0.94	*0.63*	0.42	1.82	2.69	*2.81*	0.71	7.6
	%	16.9	*11.9*	6.9	34.1	27.5	*28.6*	5.2	69.9
Quartz		33	*11*	24	47	33	*6*	23	41
Micas		1	*0*	1	1	1	*1*	1	2
Clay minerals		2	*1*	1	2	2	*1*	1	4
Feldspar		13	*7*	8	24	7	*5*	3	13
Calcite		35	*12*	22	48	45	*9*	31	59
Dolomite		4	*1*	3	5	3	*1*	3	4
Amphibole		2	*1*	1	2	1	*0.5*	1	2
Gypsum		-	-	-	-	1	*0*	1	1
Amorphous		12	*3*	8	16	7	*2*	3	9
Organic matter		10	*3*	7	14	3	*1*	2	4

MV: Mean value, SD: Standard deviation, Min: Minimum value, Max: Maximum value

The organic material was measured at concentrations between 3 wt.% (summer 2012 and spring 2013) and 10 wt.% (winter 2012-13) showing significant differences between seasons. Specifically, in the samples collected during winter higher participation of organic material was found. During winter 2012-13, the mean amount of organic matter is more than 3 times higher compared with summer 2012 and spring 2013 and more than 1.5 times higher compared with autumn 2012. Kollias et al. (2014) found higher amounts of organic material comparing December 2012 with December 2011 and September 2012 and conclude that this can be attributed to the extensive and uncontrolled burning of biomass for domestic heating. Petrakakis et al. (2013) found increased concentrations of particulate matter in Thessaloniki during the winter period after 2010 which attributed to the burning of wood and other types of biomass. According to Moussiopoulos (2013) the burning of biomass and wood led to a rapid increase in the average monthly concentration of fine particles in the winter period (Nov 2012-January 2013), with this increase being more pronounced in afternoon hours. Moreover, Saffari et al. (2013) found that in the urban background of Thessaloniki's region concentrations of $PM_{2.5}$ in the winter of 2013 were 30% higher compared to the same period in 2012 and 2-5 times higher concentrations of the biomass combustion indicators such as water-soluble K, anhydrides sugars, organic carbon and PAHs.

4.4. Conclusions

Mineralogical analysis and organic material of the falling dust samples collected from rooftops in three sampling sites during summer 2012-spring 2013 in the wider conurbation of Thessaloniki found that:

The fallen dust mainly consists of inorganic origin components from the corrosion of building materials without excluding material contribution from air suspending fumes.

Calcite and quartz are the major inorganic crystalline phases determined with the latter to be potentially dangerous for public health.

A significant increase in the organic load of dust samples had been observed for winter 2012-13 compared to the other seasonal sampling periods and to previous winter and autumn monthly periods

The pollution impact of the atmosphere of Thessaloniki with pollutants of organic origin during the winter 2012-13 is attributed to the extensive and uncontrolled burning of biomass for domestic heating as a consequence of the economic crisis in Greece and the high value of petroleum fuel during this period.

CHAPTER 5: CASE STUDY 3

5.1. Introduction

In chapter 5 the implementing case studies of seasonal variations of falling dust in Thessaloniki during 2012-13 for further in detail application with atmospheric particles dispersion models to justify the dispersion on monitored sampling locations, are presented. Regarding air pollutants, road dust nowadays plays one of the most important roles in many parts of Europe, since it is an air pollution factor related to traffic levels not controlled by rules and legislation, therefore it is difficult to control and reduce. More specifically on local scale the relatively coarse road dust particles play an important role for PM concentrations while the directive is based on mass concentrations. Road dust is a complex dust mix with a divergence of space and time sources. Regarding Mediterranean countries road dust sources are mainly from local building sites and wear from pavements, tyres and braking systems with an additional contribution of Saharan dust. Under dry conditions road dust emission can occur by wear particles that are either emitted directly in the air or they are suspended on road dust surface depot by passing vehicles. Even though road dust is coarser than the inhalable fraction passing vehicles can further disintegrate it into finer fractions. Mineral particles are an important component of road dust. Road pavements wear dust has an inhalable fraction that peaks around 4-5μm and goes down to approximately 0.5μm in size. Another important road dust component derives from braking systems and tyre wear. Traffic flow characteristics are time and space dependent as well as on other sources, On the contrary to the bulk mineral particles, these are dominated by organic species and metals such as copper, antimony, zinc etc. Size distribution from tyre wear data varies but there seems to be an inhalable fraction ranging from a few μm or even smaller. The inhalable dust fraction of braking system wear peaks around a few μm.

5.2. Methodology

5.2.1 Sampling and sample preparation

Samples were taken from the selected sites weakly for a period of one year (2012-13), according to prevailing meteorological conditions such as wind speed and precipitation. After the completion of sampling the number of samples collected were 264. It was decided to merge the samples in groups according to meteorological conditions (precipitation, wind). It was decided to group the samples that were deposited under dry conditions that mediated between 2 rain episodes. According to these criteria, 14 bulk samples for sampling location Kalamaria in the east part of Thessaloniki, 18 bulk samples for sampling location AUTH campus in the center part of Thessaloniki, and 16 bulk samples for sampling location PORT in the west part of Thessaloniki.

5.3. Results and discussion

5.3.1. Mineralogical analysis of examined samples

The mineralogical composition (wt. %) of the 14 samples collected from the east part of Thessaloniki, i.e. KALAMARIA location, is given in Table 5.1. Also, the mineral statistics (mean value, standard deviation, median value, maximum and minimum values) are calculated and shown at the end of this table. According to table 5.1, quartz and calcite are the major minerals phases detected in the studied samples, while minor amounts of feldspars (K-feldspar and plagioclase), amphibole, dolomite, micas, clays and hematite were also present. More specific, quartz was detected in all samples and its amount varied from 2 (sample N12Π26) to 27 wt.% (sample J13Π28) with a mean value of 19±6.4 wt.% and a median value of 20 wt.%. Calcite was detected in all samples and its amount varied from 44 (J13Π14) to 67 wt.% (J13Π10) with a mean value of 58±5.4 wt.% and a median value of 59 wt.%. Dolomite was also detected in all samples and its amount varied from 2 (samples A13Π1, J13Π14, J13Π1721, M13Π5 and A13Π1926) to 5 wt.% (samples M2129Π and N12Π919) with a mean value of 3±1.1 wt.% and a median value of 3 wt.%.

Table 5.1. Mineralogical composition (wt.%) and mineral statistics of the examined samples collected for the KALAMARIA location in the east part of Thessaloniki.

Year	Month	Day	Sample code	Q	Kf	Pl	A	C	Do	M	Cl	Ht	Am
2012	MAY	07-12	M712Π	17	-	4	-	62	4	1	-	-	12
2012	MAY	21-29	M2129Π	19	4	**3**	**1**	59	**5**	-	-	-	9
2012	JUNE	01-14	J12ΠA	16	2	5	-	62	4	1	1	-	9
2012	NOV	26	N12Π26	**2**	**15**	5	**1**	58	4	1	-	-	**14**
2012	NOV	9-19	N12Π919	18	3	-	**1**	61	**5**	1	1	-	10
2013	APRIL	01	A13Π1	23	3	4	-	55	**2**	-	1	-	12
2013	JAN	10	J13Π10	12	-	**3**	2	**67**	3	1	1	**6**	5
2013	JAN	14	J13Π14	22	-	**20**	-	**44**	**2**	1	1	-	10
2013	JAN	28	J13Π28	**27**	5	4	**3**	54	3	-	-	-	4
2013	JAN	17-21	J13Π1721	26	5	7	-	55	**2**	1	1	-	**3**
2013	FEB	01	F13Π1	24	-	4	-	58	3	1	-	-	10
2013	MARCH	05	M13Π5	23	9	**3**	-	54	**2**	1	-	**3**	5
2013	APRIL	19-26	A13Π1926	17	4	**3**	-	59	**2**	1	-	**6**	8
2013	APRIL	5-12	A13Π512	20	**1**	7	**1**	60	3	-	-	-	8
			n	***14***	***10***	***13***	***6***	***14***	***14***	***10***	***6***	***3***	***14***
			MEAN	19	5	6	2	58	3	1	1	5	9
			SD	6,4	4,1	4,6	0,8	5,4	1,1	-	-	1,7	3,3
			MEDIAN	20	4	4	1	59	3	1	1	6	9
			MAX	27	15	20	3	67	5	1	1	6	14
			MIN	2	1	3	1	44	2	1	1	3	3

Q: Quartz, Kf: K-feldspar, Pl: Plagioclase, A: Amphibole, probably tremolite, C: Calcite, Do: Dolomite, M: Mica, Cl: Clay minerals, Ht: Hematite, Am: Amorphous phases.

K-feldspar was detected in 10 samples and its amount varied from 1 (sample A13Π512) to 15 wt.% (sample N12Π26) with a mean value of 5±4.1 wt.% and a median value of 4 wt.%. Plagioclase was detected in 13 samples and its amount varied from 3 (samples M2129Π, J13Π10, M13Π5 and A13Π1926) to 20 wt.% (sample J13Π14) with a mean value of 6±4.6 wt.% and a median value of 4 wt.%. Amphibole was detected in 6 samples and its amount varied from 1 (samples M2129Π, N12Π26, N12Π919 and A13Π512) to 3 wt.% (sample J13Π28) with a mean value of 2±0.8 wt.% and a median value of 1 wt.%. Mica was detected in 10 samples and its amount is 1 wt.% in all samples, while clay minerals were detected in 6 samples and their amount is also 1 wt.% in all samples. Hematite was detected in 3 samples and its amount varied from 3 (sample M13Π5) to 6 wt.% (samples J13Π10 and A13Π1926) with a mean value of 5±1.7 wt.% and a median value of 6 wt.%. Finally, amorphous material was detected in all samples and its amount varied from 3 (sample J13Π1721) to 14 wt.% (sample N12Π26-NOV’12) with a mean value of 9±3.3 wt.% and a median value of 9 wt.%.

The mineralogical composition (wt.%) of the 18 samples collected from the center of Thessaloniki, i.e. AUTH location, is given in Table 5.2. Also, the mineral statistics (mean value, standard deviation, median value, maximum and minimum values) are calculated and shown at the end of this table.

Table 5.2. Mineralogical composition (wt.%) and mineral statistics of the examined samples collected for the AUTH location in the center of Thessaloniki.

Year	**Month**	**Day**	**Sample code**	**Q**	**Kf**	**Pl**	**A**	**C**	**Do**	**M**	**Cl**	**Ht**	**Am**
2012	MAY	7-12MAY	M712A	23	**2**	4	1	51	**2**	1	1	1	**14**
2012	MAY	21-29MAY	M2129A	30	4	8	-	37	**15**	1	3	-	**2**
2012	JUNE	1-14 JUNE	J12AA	34	3	4	1	46	**2**	1	1	-	8
2012	NOV	26-11-12	N12A26	26	7	**3**	-	49	3	-	1	-	11
2012	NOV	9-19 NOV	N12A919	27	-	9	2	48	3	1	1	-	9
2013	FEB	12-Feb-13	F13A12	19	4	11	2	45	4	2	2	-	11
2013	FEB	04-Feb-13	F13A4	19	-	**38**	2	**35**	-	2	1	-	3
2013	APRIL	01-Apr-13	A13A1	32	**2**	**3**	-	46	3	-	1	-	13
2013	APRIL	19-26 ARP	A13A1926	**17**	**22**	**3**	1	44	3	1	1	-	8
2013	APRIL	5-12 APR	A13A512	31	4	6	-	44	**2**	1	1	2	9
2013	JAN	10-Jan-13	J13A10	**35**	3	19	1	36	-	1	-	-	5
2013	JAN	14-Jan-13	J13A14	23	-	9	-	45	10	1	1	-	11
2013	JAN	28-Jan-13	J13A28	19	9	7	-	**55**	3	1	-	-	6
2013	JAN	17-21 JAN	J13A1721	23	5	9	2	49	3	1	2	-	6
2013	FEB	01-Feb-13	F13A1	20	-	7	1	55	3	1	2	-	11
2013	MARCH	21-Mar-13	M13A21	28	5	7	-	49	3	1	1	-	6
2013	MARCH	11-Mar-13	M13A11	23	-	13	2	49	**2**	1	-	-	10
2013	MARCH	05-Mar-13	M13A5	18	4	8	1	51	3	1	1	-	13
			n	***18***	***13***	***18***	***11***	***18***	***16***	***16***	***15***	***2***	***18***
			MEAN	25	6	9	1	46	4	1	1	2	9
			SD	5,8	5,3	8,2	0,5	5,7	3,5	0,3	0,6	0,7	3,4
			MEDIAN	23	4	8	1	47	3	1	1	2	9
			MAX	35	22	38	2	55	15	2	3	2	14
			MIN	17	2	3	1	35	2	1	1	1	2

Q: Quartz, Kf: K-feldspar, Pl: Plagioclase, A: Amphibole, probably tremolite, C: Calcite, Do: Dolomite, M: Mica, Cl: Clay minerals, Ht: Hematite, Am: Amorphous phases.

According to Table 5.2, quartz and calcite are the major minerals phases detected in the studied samples, while minor amounts of feldspars (K-rich and plagioclase), amphibole, dolomite, micas, clays and hematite were also present. More specific, quartz was detected in all samples and its amount varied from 17 (sample A13A1926) to 35 wt.% (sample J13A10) with a mean value of 25±5.8 wt.% and a median value of 23 wt.%. Calcite was detected in all samples and its amount varied from 35 (F13A4) to 55 wt.% (J13A28) with a mean value of 46±5.7 wt.% and a median value of 47 wt.%. Dolomite was detected in 16 samples and its amount varied from 2 (samples M712A, J12AA, A13A512 and M13A11) to 15 wt.% (sample M2129A) with a mean value of 4±3.5 wt.% and a median value of 3 wt.%. K-feldspar was detected in 13 samples and its amount varied from 2 (sample M712A and A13A1) to 22 wt.% (sample A13A1926) with a mean value of 6±5.3 wt.% and a median value of 4 wt.%. Plagioclase was detected in all samples and its amount varied from 3 (samples N12A26, A13A1 and A13A1926) to 38 wt.% (sample F13A4) with a mean value of 9±8.2 wt.% and a median value of 8 wt.%. Amphibole was detected in 11 samples and its amount varied between 1 and 2 wt.% in all samples with a mean value of 1±0.5 wt.% and a median value of 1 wt.%. Mica was detected in 16 samples and its amount varied between 1 and 2 wt.% in all samples with a mean value of 1±0.3 wt.% and a median value of 1 wt.%. Clay was minerals detected in 15 samples and their amount is also varied between 1 and 2 wt.% in all samples with a mean value of 1±0.6 wt.% and median value of 1 wt.%. Hematite was detected in 2 samples and its amount varied between 1 and 2 wt.%. Finally, amorphous material was detected in all samples and its amount varied from 2 (sample M2129A) to 14 wt.% (sample M712A) with a mean value of 9±3.4 wt.% and a median value of 9 wt.%.

The mineralogical composition (wt.%) of the 16 samples collected from the west part of Thessaloniki, i.e. PORT location, is given in Table 5.3. Also, the mineral statistics (mean value, standard deviation, median value, maximum and minimum values) are calculated and shown at the end of this table. According to Table 5.3, quartz and calcite are the major minerals phases detected in the studied samples, while minor amounts of feldspars (K-rich and plagioclase), amphibole, dolomite, micas, clays and hematite were also present. More specific, quartz was detected in 15 samples and its amount varied from 12 (sample N12P919) to 42 wt.% (sample M712P) with a mean value of 23±8.5 wt.% and a median value of 21 wt.%. Calcite was detected in all samples and its amount varied from 30 (sample M712P) to 68 wt.% (sample M2129P) with a mean value of 50±8.6 wt.% and a median value of 52 wt.%. Dolomite was detected in 15 samples and its amount varied from 2 (samples M712P, N12P919, M13P11 and A13P1) to 13 wt.% (sample J13P28) with a mean value of 4±2.9 wt.% and a median value of 3 wt.%. K-feldspar was detected in 11 samples and its amount varied from 2 (samples M712P, J13P28, M13P5 and A13P1) to 23 wt.% (sample J13P10) with a mean value of 5±6.1 wt.% and a median value of 3 wt.%. Plagioclase was detected in all samples and its amount varied from 2 (sample J13P28) to 18 wt.% (sample F13P1) with a mean value of 7±3.9 wt.% and a median value of 7 wt.%.

Amphibole was detected in 6 samples and its amount varied from 1 to 6 wt.% (sample M2129P) with a mean value of 2±2.0 wt.% and a median value of 1 wt.%. Mica was detected in 14 samples and its amount is 1 wt.% in all samples, while clay minerals also were detected in 14 samples and their amount is between 1 and 2 wt.% in all samples. Hematite was detected in 2 samples and its amount is between 1 and 3 wt.%. Finally, amorphous material was detected in all samples and its amount varied from 5 (sample F13P1) to 17 wt.% (sample M712P) with a mean value of 11±4.0 wt.% and a median value of 12 wt.%.

Table 5.3. Mineralogical composition (wt.%) and mineral statistics of the examined samples collected for the PORT location in the west part of Thessaloniki.

Year	Month	Day	Sample code	Q	Kf	Pl	A	C	Do	M	Cl	Ht	Am
2012	MAY	7-12MAY	M712P	**42**	**2**	4	-	**30**	**2**	1	1	1	**17**
2012	MAY	21-29MAY	M2129P	-	-	9	6	**68**	6	1	2	-	8
2012	JUNE	1-14 JUNE	J12PA	17	-	9	-	53	6	1	2	-	12
2012	NOV	26-11-12	N12P26	37	-	3	1	46	3	-	1	3	6
2012	NOV	9-19 NOV	N12P919	**12**	5	9	-	59	**2**	1	1	-	11
2013	JAN	10-Jan-13	J13P10	16	**23**	4	-	39	-	1	1	-	16
2013	JAN	14-Jan-13	J13P14	21	4	3	1	50	7	-	1	-	13
2013	JAN	28-Jan-13	J13P28	18	**2**	**2**	1	48	**13**	1	2	-	13
2013	JAN	17-21 JAN	J13P1721	26	-	8	-	56	3	1	-	-	6
2013	FEB	01-Feb-13	F13P1	19	3	**18**	-	50	3	1	1	-	**5**
2013	FEB	12-Feb-13	F13P12	20	5	8	-	53	3	1	1	-	9
2013	MARCH	11-Mar-13	M13P11	21	3	7	1	55	**2**	1	1	-	9
2013	MARCH	05-Mar-13	M13P5	14	**2**	6	-	55	5	1	1	-	16
2013	APRIL	01-Apr-13	A13P1	25	**2**	9	-	46	**2**	1	1	-	14
2013	APRIL	19-26 APR	A13P1926	33	4	7	1	44	4	1	-	-	6
2013	APRIL	5-12 APR	A13P512	24	-	4	-	53	3	1	1	-	14
			n	***15***	***11***	***16***	***6***	***16***	***15***	***14***	***14***	***2***	***16***
			MEAN	23	5	7	2	50	4	1	1	2	11
			SD	8,5	6,1	3,9	2,0	8,6	2,9	-	0,4	1,4	4,0
			MEDIAN	21	3	7	1	52	3	1	1	2	12
			MAX	42	23	18	6	68	13	1	2	3	17
			MIN	12	2	2	1	30	2	1	1	1	5

Q: Quartz, Kf: K-feldspar, Pl: Plagioclase, A: Amphibole, probably tremolite, C: Calcite, Do: Dolomite, M: Mica, Cl: Clay minerals, Ht: Hematite, Am: Amorphous phases.

In Table 5.4 the overall variation of the mineralogical composition (wt.%) of all (48) samples collected from sampling sites, is given. Calcite was detected in all samples and its amount varied between 30 and 68 wt.% with a mean value of 51±8.1 wt.% and a median value of 51 wt.%. Quartz was detected in 47 samples and its amount varied between 2 and 42 wt.% with a mean value of 23±7.2 wt.% and a median value of 22 wt.%. Plagioclase was detected in 47 samples and its amount varied between 2 and 38 wt.% with a mean value of 7±6.1 wt.% and a median value of 7 wt.%. Dolomite was detected in 45 samples and its amount varied between 2 and 15 wt.% with a mean value of 4±2.7 wt.% and a median value of 3 wt.%. Mica was detected in 40 samples and its amount varied between 1 and 2 wt.% with a mean value of 1±0.2 wt.% and a median value of 1 wt.%. Clay minerals were detected in 35 samples and their amount varied between 1 and 3 wt.% with a mean value of 1±0.5 wt.% and a median value of 1 wt.%. K-feldspar was detected in 34 samples and its amount varied between 1 and 23 wt.% with a mean value of 5±5.1 wt.% and a median value of 4 wt.%. Amphibole was detected in 23 samples and its amount varied between 1 and 6 wt.% with a mean value of 2±1.1 wt.% and a median value of 1 wt.%. Hematite was detected in 7 samples and its amount varied between 2 and 17 wt.% with a mean value of 9±3.7 wt.% and a median value of 9 wt.%. Finally, amorphous phase was detected in all samples and its amount varied between 2 and 17 wt.% with a mean value of 9±3.7 wt.% and a median value of 9 wt.%.

Table 5.4. Overall variation in the mineralogical composition (wt.%) of the 48 studied samples from all sampling sites.

Mineral	**Q**	**Kf**	**Pl**	**A**	**C**	**Do**	**M**	**Cl**	**Ht**	**Am**
n	*47*	*34*	*47*	*23*	*48*	*45*	*40*	*35*	*7*	*48*
Mean value	23	5	7	2	51	4	1	1	3	9
SD	7.2	5.1	6.1	1.1	8.1	2.7	0.2	0.5	2.1	3.7
Median value	22	4	7	1	51	3	1	1	3	9
MAX	42	23	38	6	68	15	2	3	6	17
MIN	2	1	2	1	30	2	1	1	1	2

Q: Quartz, Kf: K-feldspar, Pl: Plagioclase, A: Amphibole, probably tremolite, C: Calcite, Do: Dolomite, M: Mica, Cl: Clay minerals, Ht: Hematite, Am: Amorphous phases.

The results of mineralogical analysis of the road dust samples from the district of Thessaloniki have high amounts of amorphous material. According to Kicińska and Bożęcki (2018) amorphisation of the particulate matter usually proves its anthropogenic origin. Dusts rich in mainly quartz, carbonates, and feldspar are usually continental and originate mainly from local sources (Pye 1987). Fibrous amphiboles are present and recent work suggests they are eolian in origin (Buck et al. 2015). Carbonates and chain silicates (micas and clays) can also be transported from Sahara through dust circulation. Hematite and other metallic minerals have mainly anthropogenic contribution and may be linked to the application of metal in the production of alloys commonly used in vehicles (e.g., Fe as a major component of steel and associated rust).

Amato et al. (2014) summarized PM sources apportionment studies conducted in European countries and found that 12–90% of atmospheric particulates originated from non-exhaust sources or road dust. Although natural geomorphological processes affect these dust deposits through time, human disturbance is one of the strongest mechanisms for airborne resuspension of this dust (Goossens and Buck 2009) and therefore human exposure. The amount of dust that is generates and then re-settles on the road surface depends on various factors including traffic speed, vehicle weight, local road conditions and rainfall. In regions with scarce precipitation, such as the Mediterranean countries, road dust resuspension is one of the major sources triggering PM10 exceedances. According to Soukup et al. (2011) quartz, calcite, gypsum, and feldspar minerals are typical for arid climates.

5.3.2. Chemical analysis of examined samples

The chemical composition (wt. %) of the 14 samples collected from the eastern part of Thessaloniki, i.e. KALAMARIA location, is given in Table 5.5. Also, the chemical statistics (mean value, standard deviation, median value, maximum and minimum values) are calculated and shown at the end of this table. According to Table 5.5, Fe_2O_3 (Iron oxide), Al_2O_3 (Aluminum oxide) and MgO (Magnesium oxide) are the major chemical elements detected in the studied samples while minor amount of TiO_2 (Titanium dioxide), CaO (Calcium oxide), K_2O (Potassium oxide), Na_2O (Sodium oxide), P_2O_5 (Phosphorus pentoxide) and SO_3 (Sulphur trioxide) were also present. More specific TiO_2 detected in all samples and its amount varied from 0.07 (sample J13Π28 and A13Π1926) to 0.13 wt. % (sample J13Π10) with a mean value of 0.01 ± 0.02 wt. % and a median value of 0.10 wt. %. Al_2O_3 was detected in all samples and its amount varied from 1.38 (sample F13Π1) to 2.82 wt. % (sample A13Π1) with a mean value 1.75 ± 0.40 wt. % of and a median value of 1.61 wt. %. Fe_2O_3 was detected in all samples and its amount varied from 2.16 (sample N12Π26) to 3.60 wt. % (sample A13Π1926) with a mean value 2.75 ± 0.41 wt. % of and a median value of 2.59 wt. %. CaO was detected in all samples and its amount was >14 wt. %. MgO was detected in all samples and its amount varied from 1.44 (sample J13Π14) to 2.97 wt. % (sample A13Π1) with a mean value 1.83 ± 0.45 wt. % of and a median value of 1.58 wt. %. K_2O was detected in all samples and its amount varied from 0.11 (sample F13Π1) to 0.27 wt. % (sample A13Π1) with a mean value 0.18 ± 0.05 wt. % of and a median value of 0.18 wt. %. Na_2O was detected in all samples and its amount varied from 0.06 (sample M2129Π, J13Π28, F13Π1, M13Π5, A13Π1) to 0.09 wt. % (sample N13Π26) with a mean value 0.07 ± 0.01 wt. % of and a median value of 0.07 wt. %. P_2O_5 was detected in all samples and its amount varied from 0.08 (sample A13Π1) to 0.18 wt. % (sample A13Π1926, A13Π512) with a mean value 0.12 ± 0.03 wt. % of and a median value of 0.11 wt. %. SO_3 was detected in all samples and its amount varied from 0.10 (sample A13Π1) to 0.25 wt. % (sample A13Π1926) with a mean value 0.18 ± 0.04 wt. % of and a median value of 0.17 wt. %.

Table 5.5. Chemical analysis (wt.%) of main elements of the examined samples collected for the KALAMARIA location in the east part of Thessaloniki.

Year	**Month**	**Day**	**Sample code**	**TiO_2**	**Al_2O_3**	**Fe_2O_{3t}**	**CaO**	**MgO**	**K_2O**	**Na_2O**	**P_2O_5**	**SO_3**
2012	May	7-12	M712Π	0.08	1.87	2.46	>14	1.77	0.20	0.08	0.12	0.20
2012	May	21-29	M2129Π	0.12	2.00	2.63	>14	2.17	0.19	0.06	0.10	0.12
2012	June	1-14	J12ΠA	0.10	1.95	2.37	>14	2.16	0.19	0.08	0.09	0.12
2012	Nov	9-19	N12Π919	0.12	1.62	2.54	>14	1.59	0.14	0.08	0.10	0.17
2012	Nov	26	N12Π26	0.08	2.25	2.16	>14	2.44	0.23	0.09	0.09	0.17
2013	Jan	10	J13Π10	0.13	1.55	2.99	>14	1.56	0.13	0.08	0.11	0.22
2013	Jan	14	J13Π14	0.12	1.45	2.57	>14	1.44	0.12	0.07	0.11	0.15
2013	Jan	17-21	J13Π1721	0.10	1.44	2.50	>14	1.51	0.12	0.08	0.10	0.22
2013	Jan	28	J13Π28	0.07	1.44	3.13	>14	1.58	0.17	0.06	0.15	0.20
2013	Feb	01	F13Π1	0.08	1.38	2.49	>14	1.49	0.11	0.06	0.15	0.15
2013	March	05	M13Π5	0.08	1.51	2.97	>14	1.54	0.17	0.06	0.16	0.17
2013	April	01	A13Π1	0.10	2.82	2.62	>14	2.97	0.27	0.06	0.08	0.10
2013	April	5-12	A13Π512	0.10	1.62	3.39	>14	1.54	0.22	0.08	0.18	0.22
2013	April	19-26	A13Π1926	0.07	1.59	3.60	>14	1.79	0.20	0.07	0.18	0.25
			n	*14*	*14*	*14*	-	*14*	*14*	*14*	*14*	*14*
			MEAN	0.10	1.75	2.75	-	1.83	0.18	0.07	0.12	0.18
			SD	0.02	0.40	0.41	-	0.45	0.05	0.01	0.03	0.04
			MEDIAN	0.10	1.61	2.59	-	1.58	0.18	0.07	0.11	0.17
			MAX	0.13	2.82	3.60	-	2.97	0.27	0.09	0.18	0.25
			MIN	0.07	1.38	2.16	>14	1.44	0.11	0.06	0.08	0.10

The chemical composition (wt. %) of the 18 samples collected from in the center of Thessaloniki, i.e. AUTH location, is given in Table 5.6. Also, the chemical statistics (mean value, standard deviation, median value, maximum and minimum values) are calculated and shown at the end of this table. According to Table 5.6, CaO (Calcium oxide), Fe_2O_3 (Iron oxide), Al_2O_3 (Aluminum oxide) and MgO (Magnesium oxide) are the major chemical elements detected in the studied samples while minor amount of TiO_2 (Titanium dioxide), K_2O (Potassium oxide), Na_2O (Sodium oxide), P_2O_5 (Phosphorus pentoxide) and SO_3 (Sulphur trioxide) were also present.

Table 5.6. Chemical analysis (wt.%) of main elements of the examined samples collected for the AUTH location in the center of Thessaloniki.

Year	**Month**	**Day**	**Sample code**	**TiO_2**	**Al_2O_3**	**Fe_2O_{3t}**	**CaO**	**MgO**	**K_2O**	**Na_2O**	**P_2O_5**	**SO_3**
2012	MAY	7-12MAY	M712A	0.08	1.85	3.22	>14	1.58	0.23	0.08	0.17	0.22
2012	MAY	21-29MAY	M2129A	0.12	2.87	5.65	11.50	1.67	0.22	0.11	0.19	0.27
2012	JUNE	1-14 JUNE	J12AA	0.12	1.49	4.46	>14	1.51	0.18	0.08	0.16	0.22
2012	NOV	9-19 NOV	N12A919	0.07	1.62	2.67	>14	1.51	0.17	0.06	0.17	0.17
2012	NOV	26-11-12	N12A26	0.07	1.17	3.23	>14	1.31	0.14	0.09	0.15	0.17
2013	JAN	10-Jan-13	J13A10	0.08	1.64	2.89	>14	1.46	0.13	0.06	0.15	0.20
2013	JAN	14-Jan-13	J13A14	0.12	2.57	3.33	>14	1.38	0.23	0.06	0.17	0.15
2013	JAN	17-21 JAN	J13A1721	0.12	1.72	3.50	>14	1.43	0.13	0.07	0.15	0.20
2013	JAN	28-Jan-13	J13A28	0.12	1.61	3.56	>14	1.36	0.14	0.07	0.14	0.20
2013	FEB	01-Feb-13	F13A1	0.07	1.30	3.33	>14	1.69	0.12	0.05	0.14	0.17
2013	FEB	04-Feb-13	F13A4	0.10	1.53	4.07	>14	1.69	0.19	0.10	0.24	0.25
2013	FEB	12-Feb-13	F13A12	0.08	1.89	3.95	>14	2.14	1.02	0.22	0.39	0.20
2013	MARCH	05-Mar-13	M13A5	0.08	1.40	2.03	>14	1.48	0.13	0.08	0.10	0.20
2013	MARCH	11-Mar-13	M13A11	0.05	1.47	3.13	>14	1.66	0.17	0.06	0.16	0.20
2013	MARCH	21-Mar-13	M13A21	0.10	1.36	2.83	>14	1.44	0.13	0.06	0.14	0.15
2013	APRIL	01-Apr-13	A13A1	0.07	1.40	1.80	>14	1.72	0.12	0.05	0.08	0.10
2013	APRIL	5-12 APR	A13A512	0.08	1.42	3.46	>14	1.48	0.18	0.09	0.16	0.22
2013	APRIL	19-26 ARP	A13A1926	0.08	1.47	4.35	>14	1.66	0.16	0.08	0.15	0.22
			n	*18*	*18*	*18*	*1*	*18*	*18*	*18*	*18*	*18*
			MEAN	0.09	1.66	3.41	-	1.56	0.21	0.08	0.17	0.20
			SD	0.02	0.43	0.89	-	0.19	0.21	0.04	0.06	0.04
			MEDIAN	0.08	1.51	3.33	-	1.51	0.16	0.07	0.16	0.20
			MAX	0.12	2.87	5.65	>14	2.14	1.02	0.22	0.39	0.27
			MIN	0.05	1.17	1.80	11.50	1.31	0.12	0.05	0.08	0.10

More specific TiO_2 was detected in all samples and its amount varied from 0.05 (sample M13A11) to 0.12 wt. % (sample M2129A, J12AA, J13A14, J13A1721, J13A28) with a mean value of 0.09 ± 0.02 wt. % and a median value of 0.08 wt. %. Al_2O_3 was detected in all samples and its amount varied from 1.17 (sample N12A26) to 2.87 wt. % (sample M2129A) with a mean value of 1.66 ± 0.43 wt. % and a median value of 1.51 wt. %. Fe_2O_3 was detected in all samples and its amount varied from 1.80 (sample A13A1) to 5.65 wt. % (sample M2129A) with a mean value of 3.41 ± 0.89 wt. % and a median value of 3.33 wt. %. CaO was detected in all samples and its amount was >14 wt. % except from 11.50 wt. % (sample M2129A) . MgO was detected in all samples and its amount varied from 1.31 (sample N12A26) to 2.14 wt. % (sample F13A12) with a mean value of 1.56 ± 0.19 wt. % and a median value of 1.51 wt. %. K_2O was detected in all samples and its amount varied from 0.12 (sample A13A1) to 1.02 wt. % (sample F13A12) with a mean value of 0.21 ± 0.21 wt. % and a median value of 0.16 wt. %. Na_2O was detected in all samples and its amount varied from 0.05 (sample F13A1, A13A1) to 0.22 wt. % (sample F13A12) with a mean value of 0.08 ± 0.04 wt. % and a median value of 0.07 wt. %. P_2O_5 was detected in all samples and its amount varied from 0.08 (sample A13A1) to 0.39 wt. % (sample F13A12) with a mean value of 0.17 ± 0.06 wt. % and a median value of 0.16 wt. %. SO_3 was detected in all samples and its amount varied from 0.1 (sample A13A1) to 0.27 wt. % (sample M2129A) with a mean value of 0.2 ± 0.04 wt. % and a median value of 0.2 wt. %.

The chemical composition (wt. %) of the 16 samples collected from in the western part of Thessaloniki, i.e. PORT location, is given in Table 5.7. Also, the chemical statistics (mean value, standard deviation, median value, maximum and minimum values) are calculated and shown at the end of this table. According to Table 5.7, Fe_2O_3 (Iron oxide), Al_2O_3 (Aluminum oxide) and MgO (Magnesium oxide) are the major chemical elements detected in the studied samples while minor amount of TiO_2 (Titanium dioxide), K_2O (Potassium oxide), CaO (Calcium oxide), Na_2O (Sodium oxide), P_2O_5 (Phosphorus pentoxide) and SO_3 (Sulphur trioxide) were also present. More specific TiO_2 was detected in all samples and its amount varied from 0.05 (sample N12P26) to 0.12 wt. % (sample J13P28) with a mean value of 0.08 ± 0.01 wt. % and a median value of 0.08 wt. %. Al_2O_3 was detected in all samples and its amount varied from 1.28 (sample F13P1) to 1.89 wt. % (sample M712P) with a mean value of 1.57 ± 0.17 wt. % and a median value of 1.56 wt. %. Fe_2O_3 was detected in all samples and its amount varied from 2.10 (sample A13P1926) to 4.23 wt. % (sample J12PA) with a mean value of 3.30 ± 0.67 wt. % and a median value of 3.53 wt. %. CaO detected in all samples and its amount was >14 wt. %. MgO was detected in all samples and its amount varied from 1.43 (sample J13P28) to 2.07 wt. % (sample M712P) with a mean value of 1.68 ± 0.21 wt. % and a median value of 1.62 wt. %. K_2O was detected in all samples and its amount varied from 0.12

(sample J13P10) to 0.28 wt. % (sample J12PA, A13P1) with a mean value of 0.20 ± 0.05 wt. % and a median value of 0.19 wt. %. Na_2O was detected in all samples and its amount varied from 0.06 (sample J13P10, M13P5, M13P11) to 0.11 wt. % (sample M712P) with a mean value of 0.08 ± 0.01 wt. % and a median value of 0.07 wt. %. P_2O_5 was detected in all samples and its amount varied from 0.12 (sample J13P10, M13P5, A13P1926) to 0.23 wt. % (sample A13P1) with a mean value of 0.16 ± 0.03 wt. % and a median value of 0.16 wt. %. SO_3 was detected in all samples and its amount varied from 0.15 (sample M13P5) to 0.30 wt. % (sample A13P1) with a mean value of 0.22 ± 0.04 wt. % and a median value of 0.22 wt. %.

Table 5.7. Chemical analysis (wt.%) of main elements of the examined samples collected for the PORT location in the west part of Thessaloniki.

Year	**Month**	**Day**	**Sample code**	**TiO_2**	**Al_2O_3**	**Fe_2O_{3t}**	**CaO**	**MgO**	**K_2O**	**Na_2O**	**P_2O_5**	**SO_3**
2012	MAY	7-12MAY	M712P	0.08	1.89	3.79	>14	2.07	0.27	0.11	0.19	0.27
2012	MAY	21-29MAY	M2129P	0.08	1.62	4.05	>14	1.94	0.19	0.08	0.17	0.22
2012	JUNE	1-14 JUNE	J12PA	0.10	1.47	4.23	>14	2.02	0.28	0.09	0.19	0.20
2012	NOV	9-19 NOV	N12P919	0.08	1.51	3.53	>14	1.64	0.19	0.07	0.16	0.25
2012	NOV	26-11-12	N12P26	0.05	1.70	3.60	>14	1.51	0.28	0.09	0.17	0.22
2013	JAN	10-Jan-13	J13P10	0.08	1.32	2.83	>14	1.58	0.12	0.06	0.12	0.17
2013	JAN	14-Jan-13	J13P14	0.07	1.57	3.56	>14	1.69	0.18	0.07	0.16	0.20
2013	JAN	17-21 JAN	J13P1721	0.08	1.38	3.30	>14	1.61	0.19	0.09	0.14	0.25
2013	JAN	28-Jan-13	J13P28	0.12	1.68	3.82	>14	1.43	0.18	0.08	0.16	0.22
2013	FEB	01-Feb-13	F13P1	0.08	1.28	3.07	>14	1.44	0.16	0.07	0.15	0.20
2013	FEB	12-Feb-13	F13P12	0.08	1.79	2.13	>14	1.66	0.17	0.08	0.16	0.25
2013	MARCH	05-Mar-13	M13P5	0.08	1.53	2.20	>14	1.54	0.16	0.06	0.12	0.15
2013	MARCH	11-Mar-13	M13P11	0.08	1.55	3.19	>14	1.81	0.14	0.06	0.16	0.17
2013	APRIL	01-Apr-13	A13P1	0.08	1.61	3.80	>14	1.56	0.28	0.09	0.23	0.30
2013	APRIL	5-12 APR	A13P512	0.08	1.76	3.53	>14	1.89	0.19	0.07	0.17	0.22
2013	APRIL	19-26 APR	A13P1926	0.07	1.49	2.10	>14	1.49	0.17	0.07	0.12	0.17
			n	*16*	*16*	*16*	-	*16*	*16*	*16*	*16*	*16*
			MEAN	0.08	1.57	3.30	-	1.68	0.20	0.08	0.16	0.22
			SD	0.01	0.17	0.67	-	0.21	0.05	0.01	0.03	0.04
			MEDIAN	0.08	1.56	3.53	-	1.62	0.19	0.07	0.16	0.22
			MAX	0.12	1.89	4.23	-	2.07	0.28	0.11	0.23	0.30
			MIN	0.05	1.28	2.10	>14	1.43	0.12	0.06	0.12	0.15

In Table 5.8 the overall variation of the chemical composition (wt. %) of all (48) samples collected from sampling sites, is given. TiO_2 (Titanium dioxide) was detected in all samples and its amount varied between 0.05 and 0.13 wt. % with a mean value of 0.09 ± 0.2 wt.% and a median value of 0.08 wt.%. Al_2O_3 (Aluminum oxide) was detected in all samples and its amount varied between 1.17 and 2.87 wt. % with a mean value of 1.66 ± 0.35 wt.% and a median value of 1.56 wt.%. Fe_2O_3 (Iron oxide) was detected in all samples and its amount varied between 1.80 and 5.65 wt. % with a mean value of 3.18 ± 0.75 wt.% and a median value of 0.08 wt.%. CaO was detected in all samples and its amount was >14 wt. % except from 11.50 wt. % (sample M2129A) . MgO (Magnesium oxide) was detected in all samples and its amount varied between 1.31 and 2.97 wt. % with a mean value of 1.68 ± 0.31 wt.% and a median value of 1.58 wt.%. K_2O (Potassium oxide) was detected in all samples and its amount varied between 0.11 and 1.02 wt. % with a mean value of 0.2 ± 0.13 wt.% and a median value of 0.17 wt.%. Na_2O (Sodium oxide) was detected in all samples and its amount varied between 0.05 and 0.22 wt. % with a mean value of 0.08 ± 0.2 wt.% and a median value of 0.07 wt.%. P_2O_5 (Phosphorus pentoxide) was detected in all samples and its amount varied between 0.08 and 0.39 wt. % with a mean value of 0.15 ± 0.05 wt.% and a median value of 0.15 wt.%. SO_3 (Sulphur trioxide) was detected in all samples and its amount varied between 0.10 and 0.30 wt. % with a mean value of 0.20 ± 0.04 wt.% and a median value of 0.20 wt.%.

Table 5.8. Overall variation of chemical analysis (wt. %) of main elements of all (48) examined samples from all sampling sites

	TiO_2	**Al_2O_3**	**Fe_2O_{3t}**	**CaO**	**MgO**	**K_2O**	**Na_2O**	**P_2O_5**	**SO_3**
n	*48*	*48*	*48*	*1*	*48*	*48*	*48*	*48*	*48*
MEAN	0.09	1.66	3.18	-	1.68	0.20	0.08	0.15	0.20
SD	0.02	0.35	0.75	-	0.31	0.13	0.02	0.05	0.04
MEDIAN	0.08	1.56	3.20		1.58	0.17	0.07	0.15	0.20
MIN	0.05	1.17	1.80	11.50	1.31	0.11	0.05	0.08	0.10
MAX	0.13	2.87	5.65	>14	2.97	1.02	0.22	0.39	0.30

The concentrations (ppm) of trace elements of the 14 samples collected from the eastern part of Thessaloniki, i.e. KALAMARIA location, is given in Table 5.9. Also, the chemical statistics (mean value, standard deviation, median value, maximum and minimum values) are calculated and shown at the end of this table. According to Table 5.9, Mn (Manganese), Cu (Copper), Pb (Lead), Ni (Nickel), Zn (Zinc), Sr (Strontium) and Ba (Barium) are some of the trace elements with major concentrations detected in the studied samples and at minor concentrations Ag (Silver), As (Arsenic), Cd (Cadmium), Co (Cobalt), Cr (Chromium), La (Lanthanum), Mo (Molybdenum), Ni (Nickel), Sb (Antimony), Sc (Scandium), V Vanadium), Y (Yttrium) ,Zr (Zirconium) and below mentionable levels for B (Boron), Be (Beryllium), Bi (Bismuth), Ga (Gallium), Hg (Mercury), Te (Tellurium), Th (Thorium), Tl (Thalium), U (Uranium) and W (Tungsten). More specific Ag was detected in all samples and its amount varied from 0.2 (sample M712Π and N12Π26) to 18.0 ppm (sample M13Π5) with a mean value of 2.8 ± 4.7 ppm and a median value of 1.1 ppm. As was detected in all samples and its amount varied from 6.0 (sample A13Π1) to 72.0 ppm (sample J13Π1721) with a mean value of 29.5 ± 21.3 ppm and a median value of 24.5 ppm. Ba was detected in all samples and its amount varied from 92.0 (sample J13Π1721) to 171.0 ppm (sample A13Π192) with a mean value of 125.8 ± 22.3 ppm and a median value of 123.0 ppm. Cd was detected in 4 samples and its amount varied from 0.5 (sample M13Π5) to 1.0 ppm (sample J13Π28) with a mean value of 0.7 ± 0.2 ppm and a median value of 0.7 ppm. Co was detected in all samples and its amount varied from 5.0 (sample M712Π, J12ΠA, N12Π912, N12Π26, J13Π10, J13Π14, J13Π1721, F13Π1) to 10.0 ppm (sample A13Π1926) with a mean value of 6.0 ± 1.5 ppm and a median value of 5.0 ppm. Cr was detected in all samples and its amount varied from 37.0 (sample N12Π26) to 121.0 ppm (sample A13Π512) with a mean value of 71.1 ± 28.3 ppm and a median value of 58.5 ppm. Cu detected in all samples and its amount varied from 82.0 (sample N12Π26) to 830 ppm (sample A13Π512) with a mean value of 311.8 ± 247.7 ppm and a median value of 178.5 ppm. La was was detected in 11 samples and its amount varied from 10.0 (sample J13Π1721 and A13Π1926) to 13.0 ppm (sample J13Π10 and A13Π512) with a mean value of 11.5 ± 1.0 ppm and a median value of 12.0 ppm. Mn was detected in all samples and its amount varied from 295.0 (sample F13Π1) to 612 ppm (sample A13Π1926) with a mean value of 372.9 ± 84.6 ppm and a median value of 349.5 ppm. Mo was detected in 13 samples and its amount varied from 1.0 (sample J12ΠA and N12Π26) to 6.0 ppm (sample A13Π1926) with a mean value of 2.9 ± 1.6 ppm and a median value of 2.0 ppm. Ni was detected in all samples and its amount varied from 33.0 (sample N12Π26) to 170.0 ppm (sample A13Π1926) with a mean value of 65.1 ± 41.9 ppm and a median value of 46.5 ppm. Pb was detected in all samples and its amount varied from 28.0 (sample N12Π26) to 544.0 ppm (sample A13Π512) with a mean value of 178.8 ± 188.9 ppm and a median value of 79.0 ppm. Sb was detected in all samples and its amount varied from 3.0 (sample A13Π1) to 25.0 ppm (sample A13Π512) with a mean value of 9.8 ± 7.2 ppm and a median value of 6.0 ppm. Sc was detected in all samples and its amount varied from 2.0 (sample M712Π, M2129Π,

J12ΠΑ, N12Π919, N12Π26, J13Π10, J13Π14, J13Π1721, J13Π28, F13Π1, M13Π5, A13Π512, A13Π1926) to 3.0 ppm (sample A13Π1) with a mean value of 2.1 ± 0.3 ppm and a median value of 2.0 ppm. Sr was detected in all samples and its amount varied from 97.0 (sample F13Π1) to 203.0 ppm (sample A13Π1) with a mean value of 128.3 ± 32.0 ppm and a median value of 118.5 ppm.

Table 5.9. Trace elements concentrations (ppm) of the examined samples for the KALAMARIA location in the east part of Thessaloniki.

Year	**Month**	**Day**	**Sample code**	Ag	As	B	Ba	Be	Bi	Cd	Co	Cr	Cu	Ga	Hg	La	Mn	Mo	Ni	Pb	Sb	Sc	Sr	Te	Th	Tl	U	V	W	Y	Zn	Zr
2012	May	7-12	M712Π	0.2	21	<10	114	<0.5	<2	<0,5	5	65	175	<10	<1	11	335	3	47	47	8	2	130	<1	<20	<2	<10	26	<10	6	151	<1
2012	May	21-29	M2129Π	1.3	12	<10	123	<0.5	<2	<0,5	6	57	163	<10	<1	12	350	2	46	50	5	2	158	<1	<20	<2	<10	30	<10	6	111	1
2012	June	1-14	J12ΠA	0.8	7	<10	129	<0.5	<2	<0,5	5	49	140	<10	<1	11	332	1	41	39	5	2	155	<1	<20	<2	<10	26	<10	5	120	1
2012	Nov	9-19	N12Π919	1.0	15	<10	101	<0.5	<2	<0,5	5	51	121	<10	<1	11	314	2	37	53	5	2	120	<1	<20	<2	<10	28	<10	6	108	1
2012	Nov	26	N12Π26	0.2	7	<10	123	<0.5	<2	<0,5	5	37	82	<10	<1	<10	301	1	33	28	3	2	173	<1	<20	<2	<10	25	<10	5	87	1
2013	Jan	10	J13Π10	0.5	56	<10	107	<0.5	<2	<0,5	5	60	182	<10	<1	13	391	2	44	92	5	2	120	<1	<20	<2	<10	35	<10	6	118	1
2013	Jan	14	J13Π14	0.5	56	<10	101	<0.5	<2	<0,5	5	54	141	<10	<1	12	353	2	38	66	6	2	113	<1	<20	<2	<10	31	<10	6	124	1
2013	Jan	17-21	J13Π1721	1.1	72	<10	92	<0.5	<2	<0,5	5	54	230	<10	<1	10	327	2	48	130	6	2	117	<1	<20	<2	<10	28	<10	5	131	<1
2013	Jan	28	J13Π28	2.7	28	<10	147	<0.5	<2	1	8	100	378	<10	<1	<10	490	5	143	175	14	2	99	<1	<20	<2	<10	24	<10	5	304	<1
2013	Feb	01	F13Π1	1.4	18	<10	120	<0.5	<2	<0,5	5	80	632	<10	<1	<10	295	3	65	506	16	2	97	<1	<20	<2	<10	25	<10	5	338	<1
2013	March	05	M13Π5	18.0	33	<10	142	<0.5	<2	0.5	6	106	646	<10	<1	12	349	4	73	452	22	2	104	<1	<20	<2	<10	27	<10	6	295	<1
2013	April	01	A13Π1	0.3	6	<10	147	<0.5	<2	<0,5	7	45	101	<10	<1	12	378	<1	40	31	3	3	203	<1	<20	<2	<10	30	<10	6	108	2
2013	April	5-12	A13Π512	6.2	34	<10	144	<0.5	<2	0.6	7	121	830	<10	<1	13	394	5	87	544	25	2	103	<1	<20	<2	<10	29	<10	6	378	<1
2013	April	19-26	A13Π1926	4.8	48	<10	171	<0.5	<2	0.8	10	117	544	<10	<1	10	612	6	170	290	14	2	104	<1	<20	<2	<10	27	<10	6	334	1
			n	*14*	*14*	-	*14*	-	-	*4*	*14*	*14*	*14*	-	-	*11*	*14*	*14*	*14*	*14*	*14*	*14*	*14*	-	-	-	-	*14*	-	*14*	*14*	*8*
			MEAN	2.8	30	-	126	-	-	0.7	6	71	312	-	-	12	373	3	65	179	10	2	128	-	-	-	-	28	-	6	193	1
			STDEV	4.7	21	-	22	-	-	0.2	2	28	25	-	-	1	85	2	42	189	7	0.3	32	-	-	-	-	3	-	1	108	0.4
			MEDIAN	1.1	25	-	123	-	-	0.7	5	59	179	-	-	12	350	2	47	79	6.0	2.0	119	-	-	-	-	28	-	6	128	1
			MIN	0.2	6	<10	92	<0.5	<2	<0.5	5	37	82	<10	<1	10	295	1	33	28	3	2	97	<1	<20	<2	<10	24	<10	5	87	1
			MAX	18.0	72	<10	171	<0.5	<2	1.0	10	121	830	<10	<1	13	612	6	170	544	25	3	203	<1	<20	<2	<10	35	<10	6	378	2
			Continental crust[1]	0,06	0,2	15	400	3	0,2	0,1	10	100	55	15	0,07	30	900	1,5	20	15	0,2	11	375	0,005	7,2	0,5	2	135	1,5	33	70	165
			Soils[2]	0,13	0,67	42	460	1,34	0,42	0,41	11,3	59,5	38,9	15,2	0,07	27	488	1,1	29	27	0,67	11,7	175	-	9,2	0,5	3	129	1,7	23	70	267
			Top soils of Europe[3]	-	11,6	-	400	2	0,5	0,28	10,4	94,8	17,3	13	0,06	26	524	0,94	37	32	1,04	9,1	130	0,04	9,2	0,8	2,4	68	<5,0	23	68,1	2,1

[1]Mason and Moore (1982), Reimann and de Caritat (1998), [2]Kabata-Pendias and Pendias and Pendias 2011, [3]Means for topsoils of Europe, after FOREGS (2005).

V was detected in all samples and its amount varied from 24.0 (sample J13Π28) to 35.0 ppm (sample J13Π10) with a mean value of 27.9 ± 2.9 ppm and a median value of 27.5 ppm. Y was detected in all samples and its amount varied from 5.0 (sample J12ΠA, N12Π26, J13Π1721, J13Π28, F13Π1) to 6.0 ppm (sample M712Π, M2129Π, N12Π919, J13Π10, J13P14, M13Π5, A13Π1, A13Π512, A13Π1926) with a mean value of 5.6 ± 0.5 ppm and a median value of 6.0 ppm. Zn was detected in all samples and its amount varied from 87.0 (sample N12Π26) to 378.0 ppm (sample A13Π512) with a mean value of 193.4 ± 108.0 ppm and a median value of 127.5 ppm. Zr was detected in 8 samples and its amount varied from 1.0 (sample M2129Π, J12ΠA, N12Π919, N12Π26, J13Π10, J13Π14, A13Π1926) to 2.0 ppm (sample A13Π1) with a mean value of 1.1 ± 0.4 ppm and a median value of 1.0 ppm.

The chemical concentrations (ppm) of the 18 samples collected from the center of the city of Thessaloniki, i.e. AUTH location, is given in Table 5.10. Also, the chemical statistics (mean value, standard deviation, median value, maximum and minimum values) are calculated and shown at the end of this table. According to Table 5.10, Cu (Copper), Mn (Manganese), Zn (Zinc), Pb (Lead), Sr (Strontium), Cr (Chromium), Ba (Barium) and Ni (Nickel), are some of the trace elements with major concentrations detected in the studied samples and at minor concentrations Ag (Silver), As (Arsenic), B (Boron), Bi (Bismuth), Cd (Cadmium), Co (Cobalt), La (Lanthanum), Mo (Molybdenum), Sb (Antimony), Sc (Scandium), Te (Tellurium), V Vanadium), Y (Yttrium) ,Zr (Zirconium) and below mentionable levels for Be (Beryllium), Ga (Gallium), Hg (Mercury), Th (Thorium), Tl (Thalium), U (Uranium) and W (Tungsten). More specific Ag detected in 17 samples and its amount varied from 0.5 (sample M13A5) to 10.5 ppm (sample N12A26) with a mean value of 3.7 ± 2.8 ppm and a median value of 2.7 ppm. As was detected in all samples and its amount varied from 10.0 (sample A13A1) to 56.0 ppm (sample J13A1721) with a mean value of 24.9 ± 12.2 ppm and a median value of 22.0 ppm. B was detected in 5 samples and its amount varied from 10.0 (sample J13A14) to 93.0 ppm (sample F13A12) with a mean value of 41.4 ± 34.7 ppm and a median value of 22.0 ppm. Ba was detected in 18 samples and its amount varied from 83.0 (sample A13A1) to 626.0 ppm (sample F13A4) with a mean value of 197.9 ± 123 ppm and a median value of 168.5 ppm. Bi was detected in 4 samples and its amount varied from 2.0 (sample F13A4) to 18.0 ppm (sample J12A) with a mean value of 12.5 ± 7.3 ppm and a median value of 15.0 ppm. Cd was detected in 9 samples and its amount varied from 0.6 (sample N12A919, N12A226) to 3.8 ppm (sample M712A) with a mean value of 1.3 ± 1.0 ppm and a median value of 0.9 ppm. Co was detected in all samples and its amount varied from 4.0 (sample A13A1) to 14.0 ppm (sample M2129A) with a mean value of 7.8 ±

2.6 ppm and a median value of 7.0 ppm. Cr was detected in all samples and its amount varied from 36.0 (sample A13A1) to 195.0 ppm (sample J12A) with a mean value of 115.3 ± 42.2 ppm and a median value of 119.5 ppm. Cu was detected in all samples and its amount varied from 106.0 (sample A13A1) to 1280.0 ppm (sample F13A4) with a mean value of 557.1 ± 289.4 ppm and a median value of 539.0 ppm. Hg was detected in only 1 sample (M2129A) at 1.0 ppm. La was detected in 8 samples and its amount varied from 11.0 (sample J13A14) to 25.0 ppm (sample M2129A) with a mean value of 14.5 ± 4.5 ppm and a median value of 13.5 ppm. Mn was detected in all samples and its amount varied from 233.0 (sample A13A1) to 1020.0 ppm (sample M2129A) with a mean value of 474.6 ± 219.9 ppm and a median value of 404.0 ppm. Mo detected in all samples and its amount varied from 1.0 (sample A13A1) to 8.0 ppm (sample F13A4) with a mean value of 5.1 ± 1.8 ppm and a median value of 5.0 ppm. Ni was detected in all samples and its amount varied from 30.0 (sample A13A1) to 177.0 ppm (sample M2129A) with a mean value of 100 ± 42.3 ppm and a median value of 90.5 ppm. Pb was detected in all samples and its amount varied from 40.0 (sample A13A1) to 510.0 ppm (sample M13A21) with a mean value of 213.2 ± 122.0 ppm and a median value of 192.0 ppm. Sb was detected in all samples and its amount varied from 5.0 (sample A13A1, M13A5) to 34.0 ppm (sample N12A919) with a mean value of 18.1 ± 7.6 ppm and a median value of 18 ppm. Sc was detected in 17 samples and its amount varied from 1.0 (sample N12A26) to 4.0 ppm (sample J13A14) with a mean value of 2.2 ± 0.6 ppm and a median value of 2.0 ppm. Sr was detected in all samples and its amount varied from 87.0 (sample N12A26) to 213.0 ppm (sample F13A12) with a mean value of 105.4 ± 28.9 ppm and a median value of 97.0 ppm. Te was detected in 7 samples and its amount varied from 2.0 (sample M712A, M2129A, J13A10, J13A14, F13A1, M13A11) to 3.0 ppm (sample F13A12) with a mean value of 2.1 ± 0.4 ppm and a median value of 2.0 ppm. V was detected in all samples and its amount varied from 21.0 (sample A13A1) to 42.0 ppm (sample M2129A) with a mean value of 27.7 ± 5.1 ppm and a median value of 27.0 ppm. Y was detected in all samples and its amount varied from 4.0 (sample N12A26) to 8.0 ppm (sample M2129A) with a mean value of 5.4 ± 0.8 ppm and a median value of 5.0 ppm. Zn was detected in all samples and its amount varied from 94.0 (sample A13A1) to 1360.0 ppm (sample M2129A) with a mean value of 470.2 ± 305.0 ppm and a median value of 384.5 ppm. Zr was detected in 2 samples and its amount varied from 1.0 (sample J12A) to 2.0 ppm (sample M2129A) with a mean value of 1.5 ± 0.7 ppm and a median value of 1.5 ppm.

Table 5.10. Trace elements concentrations (ppm) of the examined samples for the AUTH location in the east part of Thessaloniki.

Year	Month	Day	Sample code	Ag	As	B	Ba	Be	Bi	Cd	Co	Cr	Cu	Ga	Hg	La	Mn	Mo	Ni	Pb	Sb	Sc	Sr	Te	Th	Tl	U	V	W	Y	Zn	Zr
2012	MAY	7-12	M712A	3.4	17	<10	164	<0.5	17	3.8	7	123	431	<10	<1	11	410	4	88	154	21	2	112	2	<20	<2	<10	29	<10	6	371	<1
2012	MAY	21-29	M2129A	7.5	27	21	204	<0.5	13	1.6	14	191	637	<10	1	25	1020	5	177	225	17	3	90	2	<20	<2	<10	42	<10	8	1360	2
2012	JUN	1-14	J12A	4.0	27	<10	175	<0.5	18	1.8	8	195	1020	<10	<1	15	602	7	130	175	28	2	99	<1	<20	<2	<10	33	<10	6	477	1
2012	NOV	9-19	N12A919	2.5	11	<10	182	<0.5	<2	0.6	6	74	307	<10	<1	<10	331	4	64	85	34	2	98	<1	<20	<2	<10	24	<10	5	381	<1
2013	NOV	26	N12A26	10.5	12	22	299	<0.5	<2	0.6	5	127	627	<10	<1	<10	334	7	102	158	21	1	87	<1	<20	<2	<10	22	<10	4	609	<1
2013	JAN	10	J13A10	2.3	42	<10	136	<0.5	<2	<0,5	7	86	407	<10	<1	<10	361	5	75	235	18	2	95	2	<20	<2	<10	26	<10	5	357	<1
2013	JAN	14	J13A14	1.0	14	10	167	<0.5	<2	<0,5	8	101	343	<10	<1	11	374	4	62	127	14	4	87	2	<20	<2	<10	33	<10	6	357	<1
2013	JAN	17-21	J13A1721	1.7	56	<10	133	<0.5	<2	<0,5	8	116	634	<10	<1	13	393	4	84	310	18	3	96	<1	<20	<2	<10	32	<10	6	438	<1
2013	JAN	28	J13A28	2.7	43	<10	170	<0.5	<2	<0,5	7	125	860	<10	<1	12	406	6	82	459	22	2	91	<1	<20	<2	<10	31	<10	6	521	<1
2013	FEB	1	F13A1	4.6	25	<10	233	<0.5	<2	0.9	8	116	369	<10	<1	<10	551	5	138	205	11	2	98	2	<20	<2	<10	24	<10	5	287	<1
2013	FEB	4	F13A4	7.7	20	61	626	<0.5	2	<0,5	7	162	1280	<10	<1	15	402	8	104	284	28	2	114	<1	<20	<2	<10	27	<10	5	1080	<1
2013	FEB	12	F13A12	2.7	20	93	314	<0.5	<2	1.1	12	125	478	<10	<1	<10	988	6	149	120	12	2	213	3	<20	<2	<10	25	<10	5	417	<1
2013	MAR	5	M13A5	0.5	23	<10	85	<0.5	<2	<0,5	5	47	191	<10	<1	<10	260	2	42	94	5	2	112	<1	<20	<2	<10	22	<10	5	128	<1
2013	MAR	11	M13A11	1.8	32	<10	132	<0.5	<2	0.9	10	99	400	<10	<1	<10	504	5	151	199	13	<1	94	2	<20	<2	<10	25	<10	5	359	<1
2013	MAR	21	M13A21	1.2	19	< 10	134	<0.5	< 2	<0,5	6	87	668	< 10	< 1	< 10	333	5	68	510	21	2	98	< 1	< 20	<2	< 10	27	< 10	5	293	< 1
2013	APRIL	1	A13A1	<0.2	10	<10	83	<0.5	<2	<0,5	4	36	106	<10	<1	<10	233	1	30	40	5	2	128	<1	<20	<2	<10	21	<10	5	94	<1
2013	APRIL	5-12	A13A512	2.2	21	<10	181	<0.5	<2	<0,5	7	123	600	<10	<1	14	409	6	93	185	22	2	93	<1	<20	<2	<10	27	<10	5	547	<1
2013	APRIL	19-26	A13A1926	6.8	30	<10	145	<0.5	<2	0.8	11	143	670	<10	<1	<10	632	7	161	273	15	2	92	<1	<20	<2	<10	28	<10	5	388	<1
			n	*17*	*18*	*5*	*18*	-	*4*	*9*	*18*	*18*	*18*	-	-	*8*	*18*	*18*	*18*	*18*	*18*	*17*	*18*	*7*	-	-	-	*18*	-	*18*	*18*	*2*
			MEAN	3.7	25	41	198	<0.5	13	1.3	8	115	557	<10	<1	15	475	5	100	213	18	2	105	2	<20	<2	<10	28	<10	5	470	2
			STDEV	2.8	12	35	123	-	7	1.0	3	42	289	-	-	5	220	2	42	122	8	1	29	0.4	-	-	-	5	-	1	305	1
			MEDIAN	2.7	22	22	169	<0.5	15	0.9	7	120	539	<10	<1	14	404	5	91	192	18	2	97	2	<20	<2	<10	27	<10	5	385	2
			MIN	0.5	10	10	83	<0.5	2	0.6	4	36	106	<10	<1	11	233	1	30	40	5	<1	87	<1	<20	<2	<10	21	<10	4	94	<1
			MAX	10.5	56	93	626	<0.5	18	3.8	14	195	1280	<10	1	25	1020	8	177	510	34	4	213	3	<20	<2	<10	42	<10	8	1360	2
			Continental crust[1]	0,06	0,2	15	400	3	0,2	0,1	10	100	55	15	0,07	30	900	1,5	20	15	0,2	11	375	0,005	7,2	0,5	2	135	1,5	33	70	165
			Soils[2]	0,13	0,67	42	460	1,34	0,42	0,41	11,3	59,5	38,9	15,2	0,07	27	488	1,1	29	27	0,67	11,7	175	-	9,2	0,5	3	129	1,7	23	70	267
			Top soils of Europe[3]	-	11,6	-	400	2	0,5	0,28	10,4	94,8	17,3	13	0,06	26	524	0,9	37	32	1,04	9,1	130	0,04	9,2	0,8	2,4	68	<5,0	23	68,1	2,1

[1] Mason and Moore (1982), Reimann and de Caritat (1998), [2] Kabata-Pendias and Pendias and Pendias 2011, [3] Means for topsoils of Europe, after FOREGS (2005).

The chemical concentrations (ppm) of the 16 samples collected from the western part of the city of Thessaloniki, i.e. PORT location, is given in Table 5.11. Also, the chemical statistics (mean value, standard deviation, median value, maximum and minimum values) are calculated and shown at the end of this table. According to Table 5.11, Mn (Manganese), Cu (Copper), Zn (Zinc), Pb (Lead), Sr (Strontium), Cr (Chromium), Ba (Barium) and Ni (Nickel), are some of the major trace elements concentrations detected in the studied samples and at minor concentrations Ag (Silver), As (Arsenic), B (Boron), Cd (Cadmium), Co (Cobalt), La (Lanthanum), Mo (Molybdenum), Sb (Antimony), Sc (Scandium), Te (Tellurium), V (Vanadium), Y (Yttrium) ,Zr (Zirconium) and below mentionable levels for Be (Beryllium), Bi (Bismuth), Ga (Gallium), Hg (Mercury), Th (Thorium), Tl (Thallium), U (Uranium) and W (Tungsten). More specific Ag was detected in all samples and its amount varied from 0.2 (sample F13P12) to 7.7 ppm (sample A13P1) with a mean value of 2.9 ± 2.3 ppm and a median value of 2.5 ppm. As was detected in all samples and its amount varied from 13.0 (sample N12P26) to 42.0 ppm (sample J13P28) with a mean value of 26.4 ± 8.7 ppm and a median value of 22.5 ppm. B was detected in 6 samples and its amount varied from 10.0 (sample A13P1) to 21.0 ppm (sample J12PA) with a mean value of 14.2 ± 3.9 ppm and a median value of 13.5 ppm. Ba was detected in 16 samples and its amount varied from 95.0 (sample M13P5) to 208.0 ppm (sample A13P512) with a mean value of 150.8 ± 34.6 ppm and a median value of 152.0 ppm. Cd was detected in 12 samples and its amount varied from 0.5 (sample F13P12) to 1.2 ppm (sample M712P) with a mean value of 0.8 ± 0.2 ppm and a median value of 0.8 ppm. Co was detected in all samples and its amount varied from 5.0 (sample F13P12, M13P5, A13P1926) to 13.0 ppm (sample J12PA) with a mean value of 8.3 ± 2.4 ppm and a median value of 8.0 ppm. Cr was detected in all samples and its amount varied from 44.0 (sample F13P12) to 155.0 ppm (sample J12PA) with a mean value of 106.9 ± 34.6 ppm and a median value of 110.5 ppm. Cu was detected in all samples and its amount varied from 134.0 (sample F13P12) to 1180.0 ppm (sample A13P1) with a mean value of 473.6 ± 313.0 ppm and a median value of 405.0 ppm. La was detected in 8 samples and its amount varied from 10.0 (sample N12P919, M13P5) to 17.0 ppm (sample A13P1) with a mean value of 11.8 ± 2.3 ppm and a median value of 11.0 ppm. Mn was detected in all samples and its amount varied from 274.0 (sample A13P1926) to 1350.0 ppm (sample J12PA) with a mean value of 565.2 ± 284.5 ppm and a median value of 527.5 ppm. Mo was detected in all samples and its amount varied from 2.0 (sample F13P12, M13P5, A13P1926) to 7.0 ppm (sample A13P1) with a mean value of 4.8 ± 1.6 ppm and a median value of 5.0 ppm. Ni was detected in all samples and its amount varied from 41.0 (sample F13P12) to 219.0 ppm (sample J12PA) with a mean value of 127.1 ± 56.9 ppm and a median value of 134.0 ppm.

Table 5.11. Trace elements concentrations (ppm) of the examined samples for the PORT location in the east part of Thessaloniki.

Year	**Month**	**Day**	**Sample code**	Ag	As	B	Ba	Be	Bi	Cd	Co	Cr	Cu	Ga	Hg	La	Mn	Mo	Ni	Pb	Sb	Sc	Sr	Te	Th	Tl	U	V	W	Y	Zn	Zr
2012	MAY	7-12	M712P	5.1	20	12	151	<0.5	<2	1.2	11	127	318	<10	<1	11	832	5	192	136	11	2	105	<1	<20	<2	<10	28	<10	6	408	<1
2012	MAY	21-29	M2129P	3.7	23	<10	146	<0.5	<2	1.1	12	146	403	<10	<1	11	1020	6	212	148	11	2	97	2	<20	<2	<10	27	<10	6	365	<1
2012	JUNE	1-14	J12PA	7.2	21	21	176	<0.5	<2	1.1	13	155	454	<10	<1	11	1350	6	219	168	11	2	119	<1	<20	<2	<10	26	<10	6	363	1
2012	NOV	9-19	N12P919	2.7	19	12	160	<0.5	<2	0.8	8	112	408	<10	<1	10	530	6	134	187	14	2	99	1	<20	<2	<10	27	<10	5	322	<1
2012	NOV	26	N12P26	0.8	13	15	168	<0.5	<2	0.8	9	103	365	<10	<1	<10	559	5	115	111	10	2	86	3	<20	<2	<10	25	<10	6	342	1
2013	JAN	10	J13P10	1.2	33	<10	109	<0.5	<2	0.6	8	90	281	<10	<1	<10	489	4	136	141	9	2	91	<1	<20	<2	<10	23	<10	5	243	<1
2013	JAN	14	J13P14	1.7	22	<10	150	<0.5	<2	0.7	9	109	428	<10	<1	<10	536	6	149	196	14	2	99	5	<20	<2	<10	24	<10	5	331	<1
2013	JAN	17-21	J13P1721	3.0	30	<10	179	<0.5	<2	0.6	8	109	475	<10	<1	<10	529	5	134	225	11	2	96	<1	<20	<2	<10	25	<10	5	277	<1
2013	JAN	28	J13P28	2.1	42	15	153	<0.5	<2	0.6	7	131	872	<10	<1	12	412	6	93	306	23	2	91	<1	<20	<2	<10	33	<10	6	468	<1
2013	FEB	1	F13P1	4.2	35	<10	145	<0.5	<2	<0,5	6	116	1130	<10	<1	12	336	5	78	704	21	2	91	<1	<20	<2	<10	26	<10	5	340	<1
2013	FEB	12	F13P12	0.2	17	<10	106	<0.5	<2	<0,5	5	44	134	<10	<1	<10	305	2	41	60	6	2	124	<1	<20	<2	<10	24	<10	5	130	<1
2013	MAR	5	M13P5	0.8	22	<10	95	<0.5	<2	<0,5	5	51	166	<10	<1	10	296	2	43	82	7	2	119	<1	<20	<2	<10	24	<10	5	141	<1
2013	MAR	11	M13P11	2.5	29	<10	173	<0.5	<2	1	9	101	330	<10	<1	<10	526	5	153	178	13	2	106	2	<20	<2	<10	25	<10	6	304	<1
2013	APRIL	1	A13P1	7.7	37	10	199	<0.5	<2	0.5	7	155	1180	<10	<1	17	473	7	114	632	38	2	109	<1	<20	<2	<10	30	<10	6	550	<1
2013	APRIL	5-12	A13P512	2.4	39	<10	208	<0.5	<2	0.8	10	112	407	<10	<1	<10	576	5	175	242	12	2	108	<1	<20	<2	<10	28	<10	6	309	<1
2013	APRIL	19-26	A13P1926	0.3	20	<10	95	<0.5	<2	<0,5	5	50	227	<10	<1	<10	274	2	45	133	7	2	114	6	<20	<2	<10	22	<10	5	161	<1
			n	*16*	*16*	*6*	*16*	-	-	*12*	*16*	*16*	*16*	-	-	*8*	*16*	*16*	*16*	*16*	*16*	*16*	*16*	*6*	-	-	-	*16*	-	*16*	*16*	*2*
			MEAN	2.9	26	14	151	-	-	0.8	8	107	474	-	-	12	565	5	127	228	14	2	103	3	-	-	-	26	-	6	316	1
			STDEV	2.3	9	4	35	-	-	0.2	2	35	313	-	-	2	285	2	57	182	8	0	12	2	-	-	-	3	-	1	112	-
			MEDIAN	2.5	23	14	152	-	-	0.8	8	111	405	-	-	11	528	5	134	173	11	2	102	3	-	-	-	26	-	6	327	1
			MIN	0.2	13	<10	95	<0.5	<2	<0.5	5	44	134	<10	<1	10	274	2	41	60	6	2	86	1	<20	<2	<10	22	<10	5	130	<1
			MAX	7.7	42	21	208	<0.5	<2	1.2	13	155	1180	<10	<1	17	1350	7	219	704	38	2	124	6	<20	<2	<10	33	<10	6	550	1
			Continental crust[1]	0,06	0,2	15	400	3	0,2	0,1	10	100	55	15	0,07	30	900	1,5	20	15	0,2	11	375	0,005	7,2	0,5	2	135	1,5	33	70	165
			Soils[2]	0,13	0,67	42	460	1,34	0,42	0,41	11,3	59,5	38,9	15,2	0,07	27	488	1,1	29	27	0,67	11,7	175	-	9,2	0,5	3	129	1,7	23	70	267
			Top soils of Europe[3]	-	11,6	-	400	2	0,5	0,28	10,4	94,8	17,3	13	0,06	26	524	0,9	37	32	1,04	9,1	130	0,04	9,2	0,8	2,4	68	<5,0	23	68,1	2,1

[1]Mason and Moore (1982), Reimann and de Caritat (1998), [2]Kabata-Pendias and Pendias and Pendias 2011, [3]Means for topsoils of Europe, after FOREGS (2005).

Pb was detected in all samples and its amount varied from 60.0 (sample F13P12) to 704.0 ppm (sample F13P1) with a mean value of 228.1 ± 182.5 ppm and a median value of 173.0 ppm. Sb was detected in all samples and its amount varied from 6.0 (sample F13P12) to 38.0 ppm (sample A13P1) with a mean value of 13.6 ± 7.9 ppm and a median value of 11.0 ppm. Sc was detected in all samples at 2.0 ppm. Sr was detected in all samples and its amount varied from 86.0 (sample N12P26) to 124.0 ppm (sample F13P12) with a mean value of 103.4 ± 11.5 ppm and a median value of 102.0 ppm. Te was detected in 6 samples and its amount varied from 1.0 (sample N12P919) to 6.0 ppm (sample A13P1926) with a mean value of 3.2 ± 1.9 ppm and a median value of 2.5 ppm. V was detected in all samples and its amount varied from 22.0 (sample A13P1926) to 33.0 ppm (sample J13P28) with a mean value of 26.1 ± 2.8 ppm and a median value of 22.5 ppm. Y was detected in all samples and its amount varied from 5.0 (sample N12P919, J13P10, J13P14, J13P1721, F13P1, F13P12, M13P5, A13P1926) to 6.0 ppm (sample M712P,M2129P, J12PA, N12P26, J13P28, M13P11, A13P1, A13P512) with a mean value of 5.5 ± 0.5 ppm and a median value of 5.5 ppm. Zn was detected in all samples and its amount varied from 130.0 (sample F13P12) to 550.0 ppm (sample A13P1) with a mean value of 315.9 ± 112.2 ppm and a median value of 326.5 ppm. Zr was detected in 2 samples at 1.0 ppm

In Table 5.12 the overall variation of trace elements concentration (ppm) from all (48) samples collected from sampling sites is shown, while the box charts given in Figure 5.1 show graphically the statistical variation for the trace elements detected in the studied samples. Ag was detected in 47 samples and its amount varied from 0.2 to 18.0 ppm with a mean value of 3.1±3.3 ppm and a median value of 2.3 ppm. B was detected in 11 samples and its amount varied from 10.0 to 93.0 ppm with a mean value of 26.5±26.3 ppm and a median value of 15.0 ppm. Ba was detected in 48 samples and its amount varied from 83 to 626 ppm with a mean value of 161±83 ppm and a median value of 147 ppm. Co was detected in 48 samples and its amount varied from 4 to 14 ppm with a mean value of 7±2 ppm and a median value of 7 ppm. Cr was detected in 48 samples and its amount varied from 36 to 195 ppm with a mean value of 100±40 ppm and a median value of 105 ppm. Hg was detected in 1 sample with concentration of 1 ppm. La was detected in 27 samples and its amount varied to 25 ppm with a mean value of 13±3 ppm and a median value of 12 ppm. Mn was detected in 48 samples and its amount varied from 233 to 1350 ppm with a mean value of 475±226 ppm and a median value of 398 ppm. Mo was detected in 47 samples and its amount varied from 1 to 8 ppm with a mean value of 4±2 ppm and a median value of 5 ppm.

Table 5.12. Overall variation of concentration (ppm) from all (48) examined trace elements samples.

	Ag	As	B	Ba	Be	Bi	Cd	Co	Cr	Cu	Ga	Hg	La	Mn	Mo	Ni	Pb	Sb	Sc	Sr	Te	Th	Tl	U	V	W	Y	Zn	Zr
n (values)	*47*	*48*	*11*	*48*	-	*4*	*25*	*48*	*48*	*48*	-	*1*	*27*	*48*	*47*	*48*	*48*	*48*	*47*	*48*	*13*	-	-	-	*48*	-	*48*	*48*	*12*
MEAN	3.1	27	27	161	<0.5	13	1.0	7	100	458	<10	-	12	475	4	99	208	14	2	111	3	<20	<2	<10	27	<10	6	338	1
STDEV	3.3	14	26	83	-	7	0.7	2	40	298	-	-	3	226	2	53	162	8	0.4	27	1	-	-	-	4	-	1	232	0.4
MEDIAN	2.3	23	15.0	147	-	15	0.8	7	105	405	-	-	12	398	5	88	172	13	2	104	2	-	-	-	27	-	5	333	1
MIN	0.2	6	10	83	<0.5	2	<0.5	4	36	82	<10	<1	<10	233	1	30	28	3	1	86	<1	<20	<2	<10	21	<10	4	87	<1
MAX	18.0	72	93	626	<0.5	18	3.8	14	195	1280	<10	1	25	1350	8	219	704	38	4	213	6	<20	<2	<10	42	<10	8	1360	2
Continental crust[1]	0.06	0.2	15	400	3	0.2	0.1	10	100	55	15	0.07	30	900	1.5	20	15	0.2	11	375	0.005	7.2	0.5	2	135	1.5	33	70	165
Soils[2]	0.13	0.67	42	460	1.34	0.42	0.41	11.3	59.5	38.9	15.2	0.07	27	488	1.1	29	27	0.67	11.7	175	-	9.2	0.5	3	129	1.7	23	70	267
Top soils of Europe[3]	-	11.6	-	400	2	0.5	0.28	10.4	94.8	17.3	13	0.06	26	524	0.94	37	32	1.04	9.1	130	0.04	9.2	0.82	2.4	68	<5.0	23	68.1	2.1

[1]Mason and Moore (1982), Reimann and de Caritat (1998), [2]Kabata-Pendias and Pendias and Pendias 2011, [3]Means for topsoils of Europe, after FOREGS (2005).

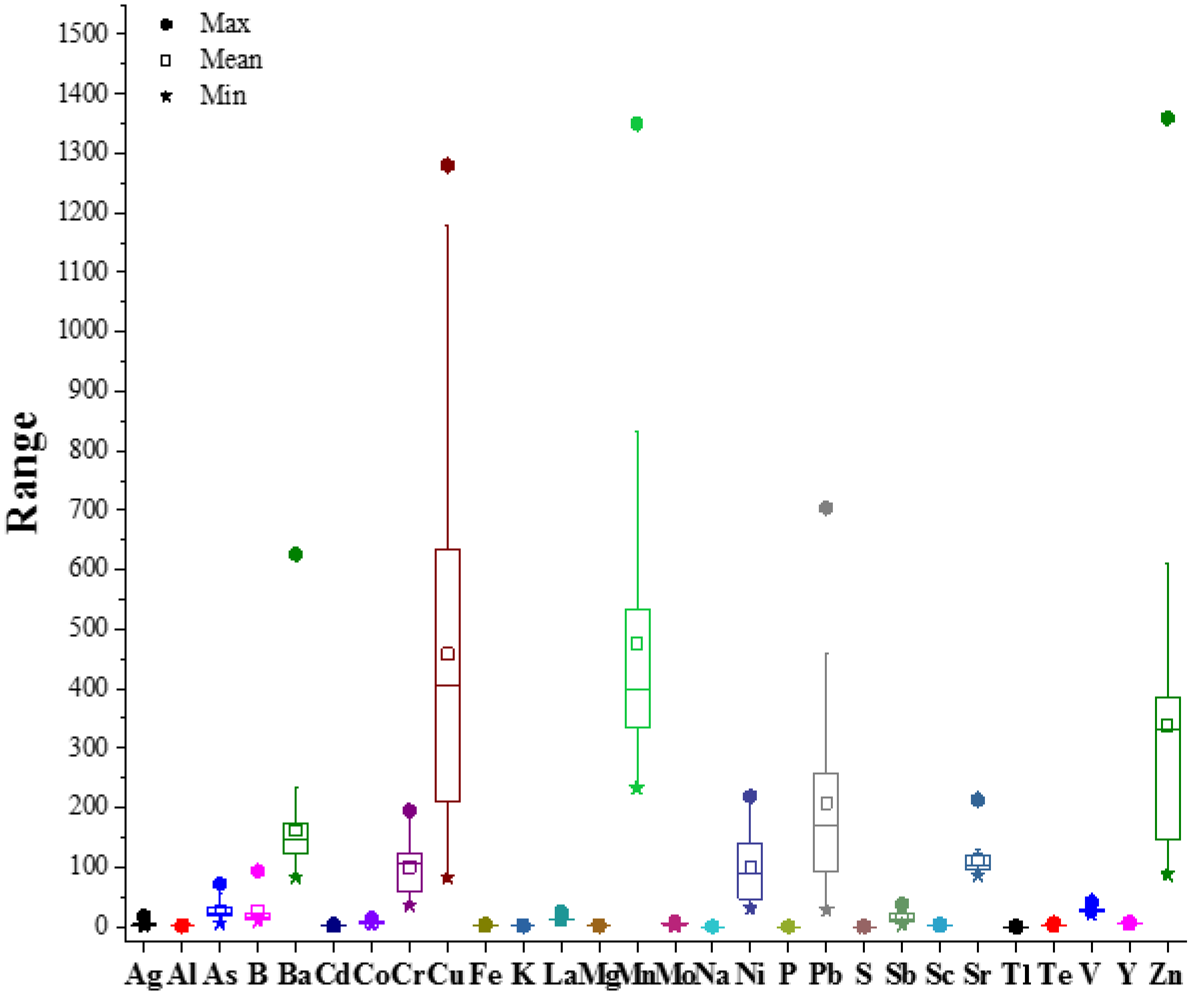

Figure 5.1. Box charts for trace elements detected in the studied samples.

Sc was detected in 47 samples and its amount varied from 1 to 4 ppm with a mean value of 2±0.4 ppm and a median value of 2 ppm. Sr was detected in 48 samples and its amount varied from 86 to 213 ppm with a mean value of 111±27 ppm and a median value of 104 ppm. Te was detected in 13 samples and its amount varied from 1 to 6 ppm with a mean value of 3±1 ppm and a median value of 2 ppm. V was detected in 48 samples and its amount varied from 21 to 42 ppm with a mean value of 27±4 ppm and a median value of 27 ppm. Y was detected in 48 samples and its amount varied from 4 to 8 ppm with a mean value of 6±1 ppm and a median value of 5 ppm. Zr was detected in 12 samples and its amount varied from 1 to 2 ppm with a mean value of 1±0.4 ppm and a median value of 1 ppm. Be, Ga, Cu, Zn, Th, Tl, U and W were measured and found below detection limit.

Hierarchical cluster analysis dendrogram showing common source and/or conditions of transportation and deposition for the trace elements detected in the studied samples is given in Figure 5.2. As shown in this figure trace elements are clustered into six groups with significant differences in contamination sources. Moreover, Ag and Ba, Cr, Fe, Mo, Zn and S constitute the first cluster. Cu, Sb and Pd and Co, Mn and Ni constitute the second and third cluster, respectively. K, Na and P and Al, V and As constitute the fourth and fifth cluster, respectively, while Mg and Sr constitute the last (sixth) cluster. There will be an extensive discussion on the origin and danger of the detected trace elements, especially for the heavy metals.

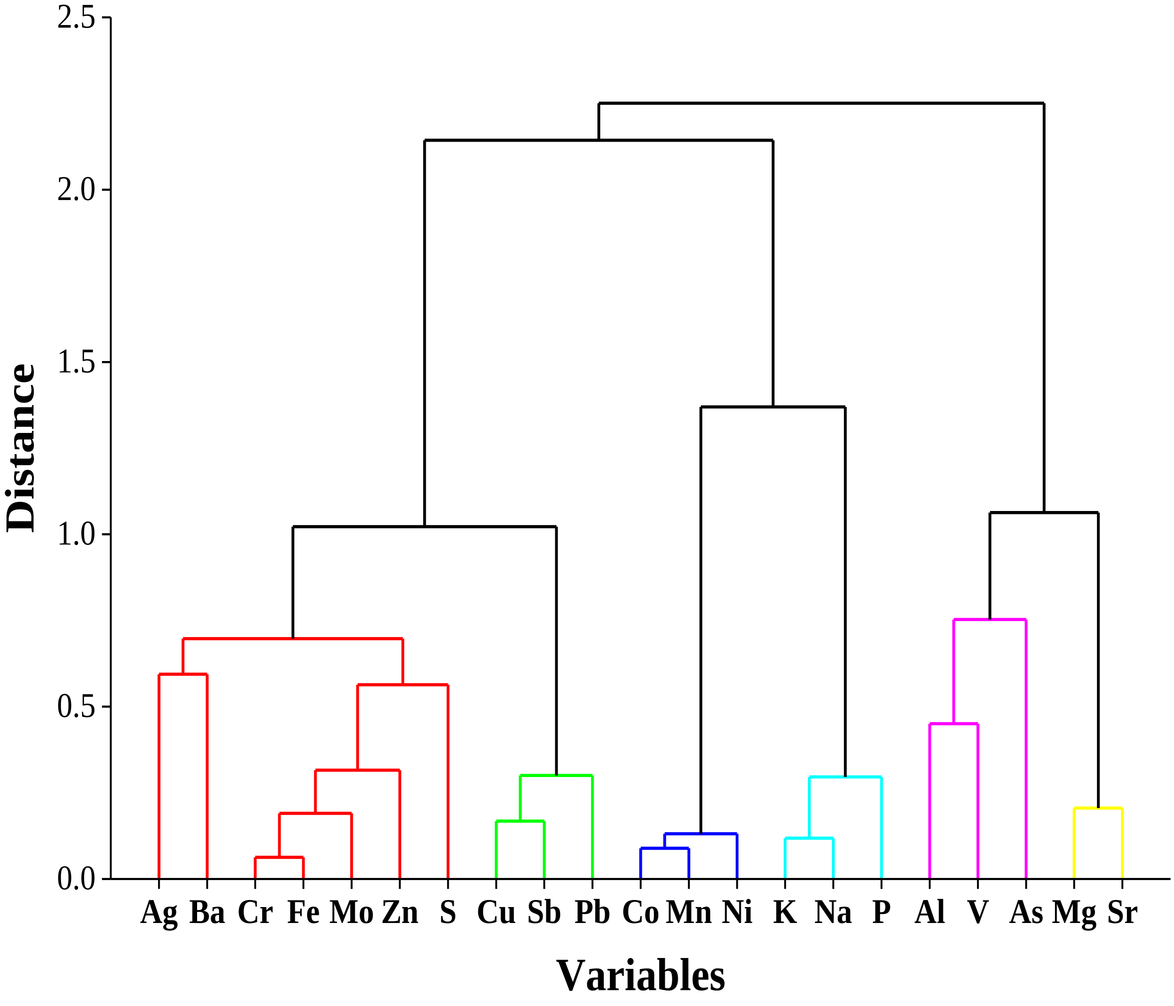

Figure 5.2. Hierarchical cluster analysis dendrogram for the trace elements detected in the studied samples.

5.4. Detected heavy metals

It is clear from samples statistics (Table 5.12 and Figure 5.1) concerning trace elements concentration (ppm) that for heavy metals As, Bi, Cd, Cr, Cu, Hg, Mn, Ni, Pb, Sb and Zn a more extensive discussion must be done according to international bibliography, European Chemicals Agency and Agency for Toxic Substances & Disease Registry.

Arsenic (As)

Arsenic (As) was detected in 48 samples and its amount varied from 6.0 to 72.0 ppm with a mean value of 27±14 ppm. Arsenic median value of 23 ppm shows increased levels, compared to continental crust levels of 0.20 ppm as noted by Mason and Moore (1982) and Reimann and de Caritat (1998), soil levels of 0.67 as noted by Kabata-Pendias (2011), and finally top soil levels of 11.6 ppm as noted for the mean top soil of Europe, after FOREGS (2005). According to Misaelides et al. (1993) the mean As concentration for the rural area near Thessaloniki, Greece for the period 1989-1990 was 2.7 ppm.

According to European Chemicals Agency (ECHA-echa.europa.eu) the hazard classification and labeling for arsenic (As) is set to that of dangerous toxic substance if swallowed or inhaled also its very toxic to aquatic life with long lasting effects. The average content of As in the Earth’s crust is estimated as 1.8 mg/kg. Generally, recovered from sludge and flue dust during smelting of Cu, Zn, Pb, Au, and Ag ores, arsenics global production was estimated at 53.5 kt in 2008 (USDI 2009). Initially As was used in pesticides manufacturing but due to its toxicity it was reduced to 50%, though it is still dominating the pesticides market (Matschullat 2000). Forms of As from irrigation waters, industrial wastes, and pesticides may need decades to get converted into non-phytotoxic forms in soils. Other uses of As are in wood preservation, photoelectric devices, glassware, and Pb-acid batteries and in improving corrosion resistance and tensile strength of Cu alloys. Arsenic elevated content level in coal is of great environmental concern and shows extreme variability ranging from 0.5–80 ppm and averages 60.0 ppm in fly ash. Arsenic emissions in the 15 EU countries were estimated in 2000 at 176.6 t, and in 2005 at 83.1 t. (Kabata - Pendias, 2011). According to Chilvers and Peterson (1987) 60% of the atmospheric global inputs of As are derived from natural sources. Significant anthropogenic sources of As are related to industrial activities (metal processing, chemical works based on S and P minerals, coal combustion, and geothermal power plants) and to the use of arsenical sprays, particularly in orchards (Kabata-Pendias 2011). Arsenic can be emitted to the environment from volcanic eruption. Anthropogenic sources of arsenic include nonferrous metal smelting, coal, oil and wood combustion and municipal waste incineration. Power plants release arsenic to the atmosphere through their emissions while arsenic in the particulate phase is the predominant form of arsenic in the troposphere according to Matschullat (2000). Air samples of smelter or coal-fired power plant origin consist of large amounts of arsenic in both vapor and particulate form (Pacyna 1987, ATSDR 2007).

Bismuth (Bi)

Bismuth (Bi) was detected in 4 samples and its amount varied from 2.0 to 18.0 ppm with a mean value of 13±7 ppm. Bismuth median value of 15 ppm shows increased levels, compared to continental crust levels of 0.20 ppm as noted by Mason and Moore (1982) and Reimann and de Caritat (1998), soil levels of 0.42 ppm as noted by Kabata-Pendias (2011), and finally top soil levels of 0.50 ppm as noted for mean top soil of Europe, after FOREGS (2005).

According to European Chemicals Agency (ECHA- echa.europa.eu) there is no hazard classification for Bismuth. Probably due to the great insolubility of bismuth salts that prevent their absorption they also have physical qualities decumulus and protective of skin and mucus membranes. It is though flammable in powder form and can react with acid fumes and emit toxic fumes (Lewis 2007). Bi is considered a rare metal with mean occurrence in Earth’s crust approx. 0.2 ppm and is usually found in veins associated with metals such as Ag, Co, Pb, Zn. Bismuth is extensively used in low-melting alloys, fuses, sprinklers, glass and ceramics production as well as a catalyst in rubber (tyre) production. There are also uses of Bismuth in metallurgical industries and in a variety of electronic devices. Bismuth (Bi) is used in several food-processing equipment and in pellets as a nontoxic replacement for Lead (Pb). It is also used in dentistry and medicine and in pharmaceutical and cosmetic production, due to its versatile properties.

Cadmium (Cd)

Cadmium (Cd) was detected in 25 samples and its amount varied from 0.5 to 3.8 ppm with a mean value of 1.0 ± 0.7 ppm. Cadmium median value of 0.8 ppm shows increased levels, compared to continental crust levels of 0.10 ppm as noted by Mason and Moore (1982) and Reimann and de Caritat (1998), soil levels of 0.41 ppm as noted by Kabata-Pendias (2011), and finally top soil levels of 0.28 ppm as noted for the mean top soil of Europe, after FOREGS (2005).

According to European Chemicals Agency (ECHA- echa.europa.eu) and Agency for Toxic Substances & Disease Registry (ATSDR 2012), the hazard classification for Cadmium is that of a very dangerous and toxic substance, fatal if inhaled, very toxic to aquatic life with long lasting effects and responsible for causing damage to organs after prolonged or repeated exposure, capable of causing genetic defects and cancer. Also, it is suspected of damaging fertility and it is very flammable if exposed to air. Cadmium occurs in the earth's crust at concentrations ranging from 0.1 to 0.5 ppm and is associated with Zn, Pb and Cu ores. Surface soil concentrations are dependent on various factors as atmospheric deposition and fertilizers. Volcanic eruptions, forest fires, sea salt aerosols and other natural phenomena occurrences contribute to natural emissions of cadmium to the environment. Cadmium is a toxic metal used in nickel-cadmium batteries, pigments, coatings and plantings, stabilizers for plastics and photovoltaic devices. 80% of cadmium production is associated with zinc production and the remaining 20% is associated with lead and copper byproduct production (Morrow 2001). Cadmium can be released to the atmosphere via fossil fuel combustion, metal production activities and waste incineration. According to Shevchenko et al. (2003) cadmium can travel long distances in the atmosphere and then deposit onto surface soil and water related in increased cadmium concentrations even in remote locations. According to European Chemicals Agency (ECHA- echa.europa.eu) cadmium can be released to environment by industrial use.

Chromium (Cr)

Chromium (Cr) was detected in 48 samples and its amount varied from 36 to 195 ppm with a mean value of 100±40 ppm. Chromium median value of 105 ppm shows increased levels, compared to continental crust levels of 100 ppm as noted by Mason and Moore (1982) and Reimann and de Caritat (1998), soil levels of 59.5 ppm as noted by Kabata-Pendias (2011), and finally top soil levels of 94.8 ppm as noted for the mean top soil of Europe, after FOREGS (2005).

According to Agency for Toxic Substances & Disease Registry (ATSDR 2012) chromium compounds, especially chromium (VI), can be extremely toxic (Kazakis et al. 2015, 2016). Exposure to chromium occurs mainly by ingestion via gastrointestinal tract, inhalation via lungs, ocular and skin contact. When inhaled chromium compounds, especially Cr (VI), irritate directly the respiratory tract resulting in airway obstruction and lung, nasal and even cancer with prolonged exposure causing adverse health effects. It can be noted that inhalation of chromium containing dust can be considered directly responsible for causing asthma, chronic bronchitis, chronic pharyngitis and rhinitis, polyps in the upper respiratory tract and tracheobronchitis. Also, skin irritations and symptoms of dizziness are some of its toxic effects. Chromium is a natural occurring element in earth's crust averages to 100 ppm. Chromium is released to the environment from natural and anthropogenic sources (industrial emissions). Chromium was initially used as pigment due to its yellowish color. The main industrial uses of chromium are in chemical, refractory and metallurgical industries mainly used for stainless steel production and chromate plating. In the chemical industry, in pigments, metal finishing, and wood preservatives. Dyestuffs and leather tanning wastes discharged directly into waste streams, either as liquids or solids are some of the major contributors of chromium pollution and there is a great contribution from sewage treatment plants from industrial and residential sources. Additional uses are applied in manufacturing green tints for paints, varnishes, glazes, and inks. Moreover, it is used in various phases of paper manufacture (Kabata-Pendias 2011, ATSDR 2012). It can be noted that chromium can be released in the air from the burning of natural gas, oil or coal industries (Kazakis et al. 2017, 2018).

Copper (Cu)

Cu was detected in 48 samples and its amount varied from 82 to 1280 ppm with a mean value of 458±298 ppm. Copper median value of 405 ppm shows increased levels, compared to continental crust levels of 55 ppm as noted by Mason and Moore (1982) and Reimann and de Caritat (1998), soil levels of 38.9 ppm as noted by Kabata-Pendias (2011), and finally top soil levels of 17.3 ppm as noted for the mean top soil of Europe, after FOREGS (2005).

According to European Chemicals Agency (ECHA- echa.europa.eu) the hazard classification for copper (Cu) is that of a very dangerous toxic substance, toxic to aquatic life with long lasting effects, though essential for good health increased level of exposure can be harmful. Long term exposure to copper dust acts as respiratory tract irritant, toxic if inhaled and harmful if swallowed it may also cause severe mouth, nose and eyes irritation. Additionally, effects of headaches, dizziness, nausea and diarrhea may arise. At high intake levels copper can cause liver and kidney damage or even demise. Copper is a reddish metal occurring naturally in rock, soil, water, sediment and at low air level as well. It occurs naturally in all plants and animals. At low inhalable levels it's essential for all known organisms including humans and animals while at higher levels toxic effects occur. The term copper refers not only to copper metal but to copper compounds in environment. Having the ability of easily molded shape, metallic copper is utilized in electric wiring, water pipes, coins and other metal products. Also, copper compounds are used in agriculture for plant diseases treatment or water treatment and as wood, leather and fabrics preservatives. Environment can be affected from copper releases deriving from copper mining and from factories that utilize or create copper metal or copper compounds. Furthermore, copper may affect environment through waste dumps, domestic water waste, fossil fuel combustion and wastes, wood products, phosphate fertilizer production and from natural sources such as volcanoes eruption, re-suspended dust via strong wind currents, forest fires, native soils, decaying vegetation and sea sprays. Copper is carried through particles emitted from ore and smelter processing plants and deposited back to surface through gravity. Copper particles can also be carried in air on wind gusts as metallurgical dust. Most copper compounds found in air are strongly attached to dust, dirt or imbedded minerals. Airborne copper is associated with particulates obtained from suspended soils, combustion sources, copper containing materials manufacturing or processing materials. Indoor copper releases are mainly caused from combustion processes for domestic heating (Kabata-Pendias 2011, ATSDR 2004).

Nickel (Ni)

Ni was detected in 48 samples and its amount varied from 30 to 219 ppm with a mean value of 99±53 ppm. Nickel median value of 88 ppm shows increased levels, compared to continental crust levels of 20 ppm as noted by Mason and Moore (1982) and Reimann and de Caritat (1998), soil levels of 29.0 ppm as noted by Kabata-Pendias (2011), and finally top soil levels of 37.0 ppm as noted for the mean top soil of Europe, after FOREGS (2005).

According to European Chemicals Agency (ECHA-echa.europa.eu) the hazard classification for nickel is that of a very dangerous and toxic substance capable of causing severe damage to organs through prolonged exposure, toxic to aquatic life with long lasting effects, capable of causing genetic effects, allergic skin reactions and allergic asthma, breathing disorders and finally may cause cancer. Nickel is a natural occurring element in the earth’s crust and in its pure form it’s a silver-white hard metal which has desirable properties when combined with other metals to form alloys. It can be found in all soils and it can be emitted by volcanic eruption. Iron, copper, chromium and zinc are some of the metals that nickel alloys can be combined. In industry these alloys are utilized for the creation of heat exchangers, valves, jewelry and coins. Nickel is also used for making stainless steel while nickel compounds are used for making nickel platings, batteries and color ceramics and also as catalyst increasing the rate of chemical reactions. Nickel is released in the atmosphere by industries during the process of nickel mining, making nickel alloys or nickel compounds. Also, nickel can be released in the atmosphere by oil and coal burning power plants and trash incinerators. It can be noted that when nickel which originates from coal-oil power plants leaves the stack to the atmosphere it attaches to small particles of dust that may travel via favoring conditions and finally settle to ground level. It takes many days for nickel to be removed from the air since it is attached to very small dust particles (Kabata-Pendias 2011, ATSDR 2005).

Lead (Pb)

Pb was detected in 48 samples and its amount varied from 28 to 704 ppm with a mean value of 208±162 ppm. Lead median value of 172 ppm shows increased levels, compared to continental crust levels of 15 ppm as noted by Mason and Moore (1982) and Reimann and de Caritat (1998), soil levels of 27 ppm as noted by Kabata-Pendias (2011), and finally top soil levels of 32.0 ppm as noted in Means for top soils of Europe, after FOREGS (2005).

According to European Chemicals Agency (ECHA-echa.europa.eu) the hazard classification level for lead is that of a dangerous and toxic substance that causes damage to internal organs through prolonged or repeated exposure, may damage fertility, it’s very toxic to aquatic life with long lasting effects, may harm breast-feeding of infants and is a possible carcinogenic. Lead is an element that its deposits are widely distributed throughout the world. Major source of lead in the environment has been anthropogenic emissions to the atmosphere from leaded gasoline combustion (banned in 1993). Additional anthropogenic sources of lead include mining and smelting of ore, manufacturing of Pb-containing products and pesticides as well as combustion of coal, oil and waste incineration power plants. Particulate matter contaminated with lead (Pb) can be transported through air via favoring meteorological weather conditions (Kabata-Pendias 2011, ATSDR 2019).

Antimony (Sb)

Antimony (Sb) was detected in 48 samples and its amount varied from 3 to 38 ppm with a mean value of 14±8 ppm. Antimony median value of 13 ppm shows increased levels, compared to continental crust levels of 0.20 ppm as noted by Mason and Moore (1982) and Reimann and de Caritat (1998), soil levels of 0.67 ppm as noted by Kabata-Pendias (2011), and finally top soil levels of 1.04 ppm as noted for the mean top soil of Europe, after FOREGS (2005).

According to European Chemicals Agency (ECHA-echa.europa.eu) and Agency for Toxic Substances & Disease Registry (ATSDR 2019), the hazard classification for antimony (Sb) is that of a toxic substance which may damage reproductive fertility, may cause harm to infant breastfeeding, prolonged or repeated exposure may cause damage to internal organs, it is harmful to aquatic life with long-term effects and finally it is suspected for causing cancer. Distributed throughout the body with the lungs showing the highest concentration following gastrointestinal tract, red blood cells, liver, kidney, bone, spleen and thyroid. Antimony is naturally present in the earth’s crust ranging from 0.2 to 0.3 ppm. It can be transported from anthropogenic sources and from natural weathering. Natural and anthropogenic sources are resulting to antimony releases to the atmosphere. Antimony enters the environment by the production of antimony metal, alloys, antimony oxide, during mining and processing of antimony containing ores and combinations of antimony with other substances (Grund et al. 2012). Small amounts of antimony can be released to environment by coal burning power plants and incinerators (Belzile et al. 2011) also emissions from combustion fuels, lead, zinc and copper production industries nonferrous production, steel production, municipal waste and sewage sludge (Pacyna and Pacyna 2001). Antimony can be inhaled from particulate matter containing it in air according to Bentley and Chasteen (2002) furthermore antimony emission sources from brake abrasion dust from vehicles and waste fly ash were monitored according to Lijima et al. (2009) as well as from brake tires, street surfaces and vehicle exhausts (WHO 2013).

Zinc (Zn)

Zinc (Zn) was detected in 48 samples and its amount varied from 87 to 1360 ppm with a mean value of 338±232 ppm. Zinc median value of 333 ppm shows increased levels, compared to continental crust levels of 70 ppm as noted by Mason and Moore (1982) and Reimann and de Caritat (1998), soil levels of 70 ppm as noted by Kabata-Pendias (2011), and finally top soil levels of 68.1 ppm as noted for the mean top soil of Europe, after FOREGS (2005).

According to European Chemicals Agency (ECHA-echa.europa.eu) the hazard classification level for lead is that of a dangerous and toxic substance, very toxic to aquatic life with long lasting effects, it is explosive in powder form and may burst into flames if stored in dump places. Zinc is one of the most common element in earth’s crust and has bluish-white shiny metal form. Metallic zinc has many uses in industry, it can prevent rust and corrosion of other metals with its coating process also known as galvanization. It is used to create dry cell batteries and when combined with other elements such as chlorine and oxygen it forms zinc compounds which are widely used in drug industry as ingredients of vitamin supplements. Another industrial use of zinc compounds is in the creation of white paints, ceramics and other products from zinc sulfide and zinc oxide. Zinc oxide is also used in rubber production while zinc acetate, chloride and sulfate are used in manufacturing, dyeing fabrics and wood preservation additives. Natural emissions of zinc in the air are mainly caused due to wildborne soil particles, volcanic eruption emissions and forest fires. Released mainly from anthropogenic sources zinc in the atmosphere can be at increased levels in the form of dust and fumes from activities such as mining, steel production, zinc purification methods, lead and cadmium ores, coal and wastes burning. In air zinc is present mostly as fine dust particles while rain and snow aid in its removal.

The increased concentrations of the heavy metals we analyzed earlier necessitate the use of further investigation in order to identify possible emitting sources that intensify their augmented levels. For that reason, the use of atmospheric particle dispersion models is vital in order to track down backward and forward in time the sources that contribute to our results (Kabata-Pendias 2011, ATSDR 2005)

CHAPTER 6: CASE STUDY 4

6.1. Introduction

In chapter 6 the application of the high resolution FLEXPART-WRF system for a source-receptor approach of atmospheric particle dispersion of re-suspended dust in the city of Thessaloniki 2012-2013, is presented. In this chapter we examine the impact of air pollutants in the atmosphere of Thessaloniki regional unit. Morphological, mineralogical and chemical analysis was implemented to falling dust collected samples, as mentioned in the previous chapter, from three sampling areas, East (Kalamaria District), Central (Aristotle University), and West near Thessaloniki’s Seaport. The chemical analysis of the analyzed dust samples from the sampling locations during 2012-2013 indicated increased levels of toxic metals which favored by the meteorological conditions, resulted in augmented air pollution levels. In order to identify possible emitting sources and to verify at what content external parameters augmented the pollution levels of our examined dust samples we implemented Flexpart-WRF.

The lagradgian dispersion model Flexpart capable of forward and backward trajectory particle simulations and long-range and mesoscale dispersion calculation of air pollutants from point sources (stohl et al. 2005, 2010), with high resolution data feedback from the non-hydrostatic mesoscale numerical meteorological model WRF with the advanced research dynamic solver AWR (Skamarock et al. 2008) with analysis data from the ECMWF (European Centre for Medium-Range Weather Forecasts) was implemented to selected dates that indicated increased heavy metals concentration such as As, Zn, Mn, Co, Cr, Cu, Ba, Br, Hg, Mn, Ni, Pb, Sb, Ti, in order to provide the meteorological input data to the atmospheric dispersion model Flexpart-WRF applied at high resolution (600 m) for the region of Thessaloniki aiming to identify the origin of the re-suspended dust particles on the air quality of the city of Thessaloniki. The WRF setup efficiency was verified according to Karacostas et al. (2018) and Pytharoulis et al. (2014). Meteorological conditions favored the re-suspension and transfer of the air pollutants deposition to the locations that indicated increased toxic metal activity. This can be seen by the visualization of the outputs of Flexpart-WRF model showing the plume course for selected days of intensively high concentrations.

6.2.Methodology

For WRF a one-way interactive model domains covering a part of Greece-Europe-Asia, northern Greece and the wider area of Thessaloniki city Greece (Macedonia) at horizontal grid-spacing of 5.4 km x 5.4 km (d1), 1.8 km x 1.8 km (d2) and 0.6 x 0.6 km (d3) (Fig. 6.1) have been used, utilizing the staggered Arakawa C grid with 30 time step, Ferrier microphysics for all domains and cumulus scheme of Betts-Miller-Janjic for the d01.

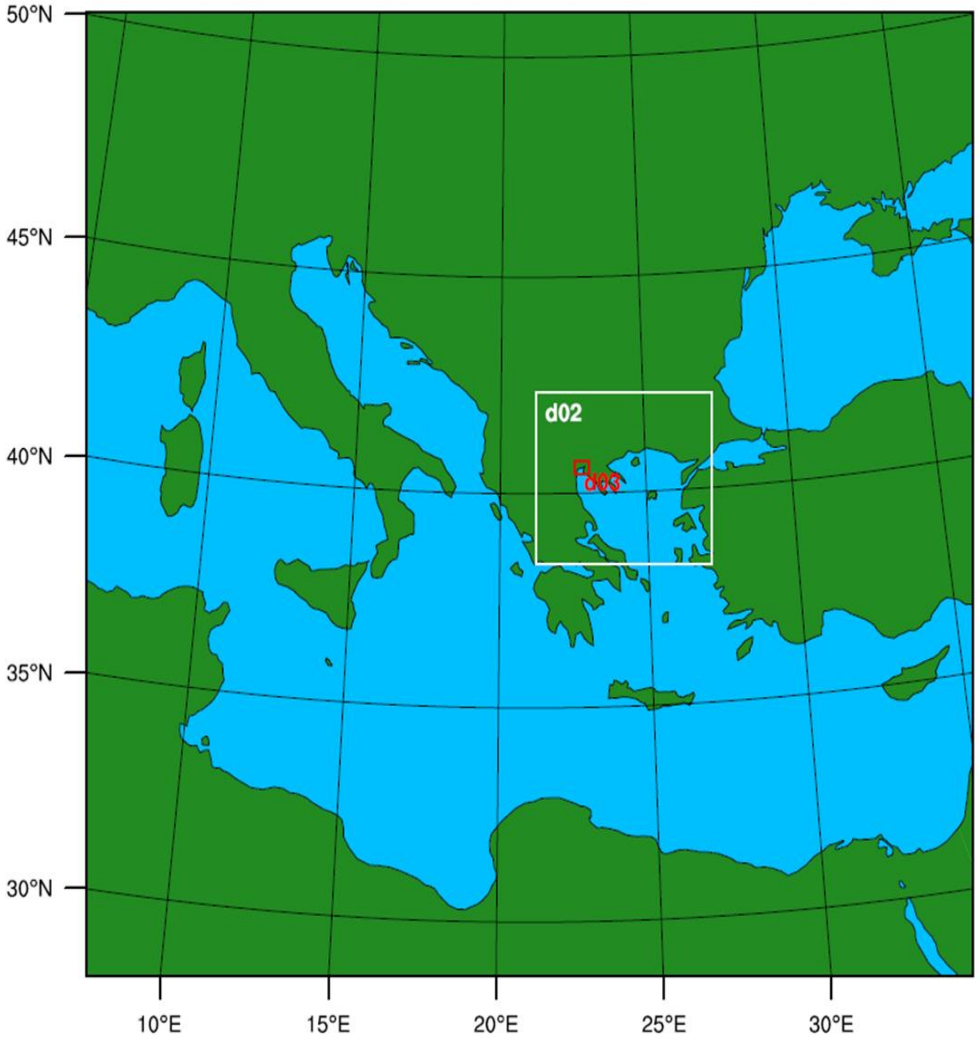

Figure 6.1. WRF nested domains –WRF Domain Wizard at horizontal grid-spacing of 5.4 km x 5.4 km (d1), 1.8 km x 1.8 km (d2) and 0.6 x 0.6 km (d3).

As initial and lateral boundary conditions for the coarse domain, ECMWF 6-hourly analyses were used to increase the resolution focusing on the local topography. The analyses were available on a 0.125° x 0.125° regular grid. The necessary fields were retrieved at and near the surface and on the pressure levels of 1000, 950, 925, 900, 850, 800, 700, 600, 500, 400, 300, 250, 200, 150, 100, 70, 50, 30, 20, 10 mb. WRF run for the specific days mentioned below that we had augmented levels of heavy metals after the chemical, mineralogical and morphological analysis of our dust samples. Output was set every 180 min for d1 and 60 min for d2 and d3 respectively.

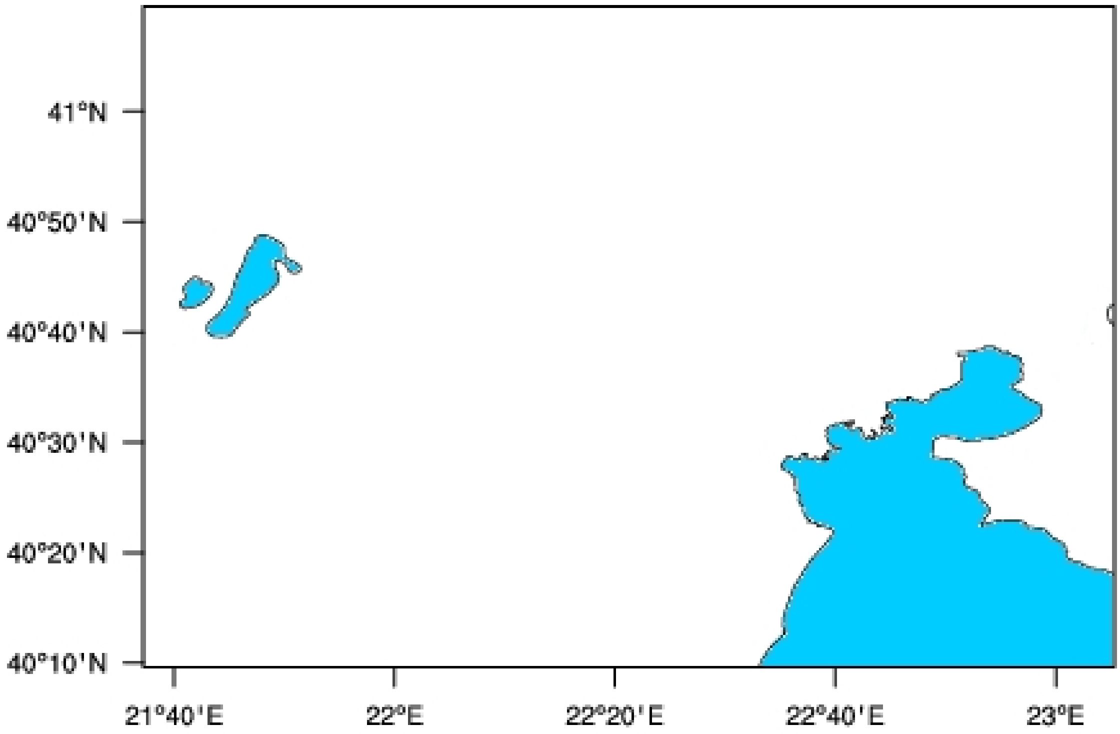

Figure 6.2. WRF d3 with horizontal grid-spacing of 0.6 x 0.6 km.

The d3 WRF data output with 0.6 km high resolution (Fig. 6.2) is utilized as input for Flexpart-WRF for the selected periods of the examined analyzed dust samples that showed increased heavy metals concentration. Flexpart-WRF according to Brioude et al. (2013), was set up to run backwards and the particles were released in the selected sampling location areas where we had increased heavy metals concentrations. Also, to verify more accurately the chemical analyzed dust sample findings Flexpart-WRF also run forward for the possible emitting sites located westerly in the industrial zone of the city of Thessaloniki and northerly from the city in specific industrial areas at pressure levels from 0-500 m and at 8 vertical levels starting from 1 km with 3h output and 180 min sampling rate while the model output where given a 12h initiation time allowing adequate time for the model spin-up.

6.3. Flexpart-WRF visualization output results

Sampling locations are named, AUTH - Aristotle University of Thessaloniki, located in the city center of Thessaloniki, PORT - multi-storey parking lot located westerly near the commercial port of the city, KALAM – multi-storey apartments building located easterly in Kalamaria district.The selected days that also showed increased concentration levels of toxic metals were chosen from January and February 2013. The weathering condition (rain and wind speed) for this months are given in Figures 6.3 and 6.4.

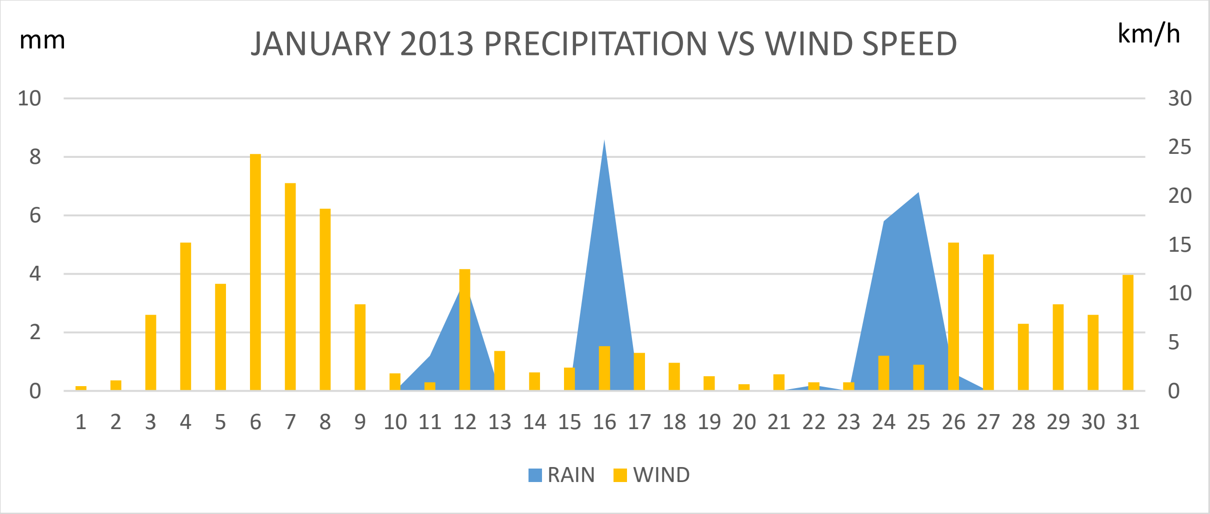

Figure 6.3. Precipitation versus wind speed during selected sampling month of January 2013.

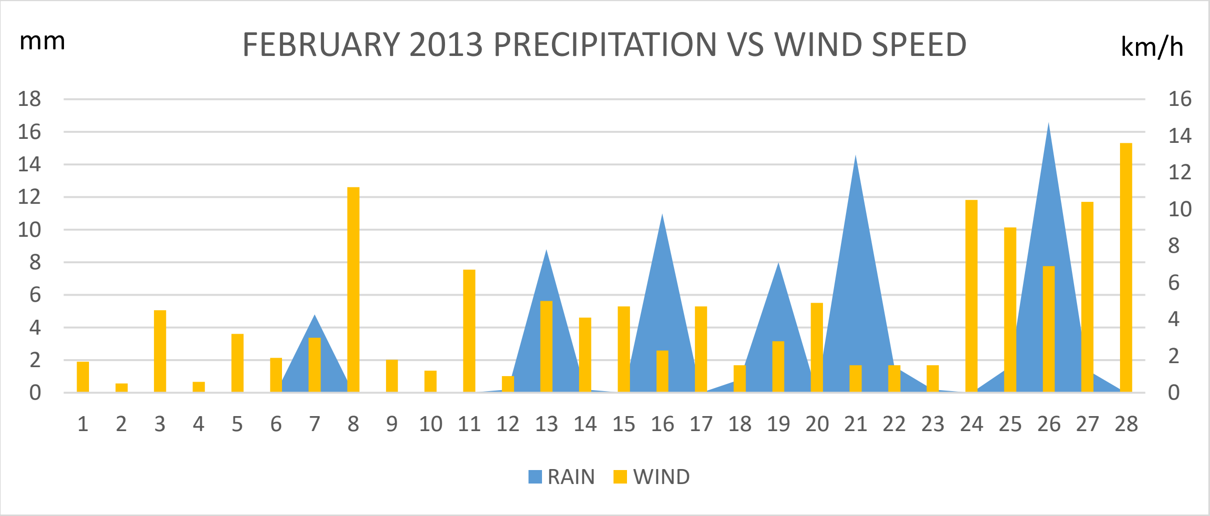

Figure 6.4. Precipitation versus wind speed during selected sampling month of February 2013.

Flexpart-WRF run backwards and forward for the following cases (Table 6.1): Regarding January from 9th to 11th January with 10th being the day of interest (with high concentrations of As), from 13th to 15th January with 14th being the day of interest (with high concentrations of As), from 31st January to 2nd February with 1st February being the day of interest (with high concentrations of Zn and Mn), from 3rd to 5th February with 4th February being the day of interest (with high concentrations of Zn) and finally from 11th to 13th February with 12th February being the day of interest (with high concentrations of Mn). Regarding the selected dates the toxic metals findings were more than those mentioned in brackets as seen in previous chapter fig. toxic metals for selected dates)

Table 6.1. Selected sample dates of identified heavy metals in 2013.

Month	Days	Pollutant target on the day of interest
January	9 to 11	High concentration of As on January 10
January	13 to 15	High concentration of As on January 14
January -February	31 to 2	High concentration of Zn and Mn on February 1
February	3 to 5	High concentration of Zn on February 4
February	11 to 13	High concentration of Mn on February 12

6.4. Synoptic conditions sampling date 10th January 2013

For the sampling day of 10th January 2013 and more specifically one day earlier 9th January from our day of interest in 9th January average wind speed was 8.9 km/h and wind directions NW with maximum wind speed of 27.4 km/h (02:00am).

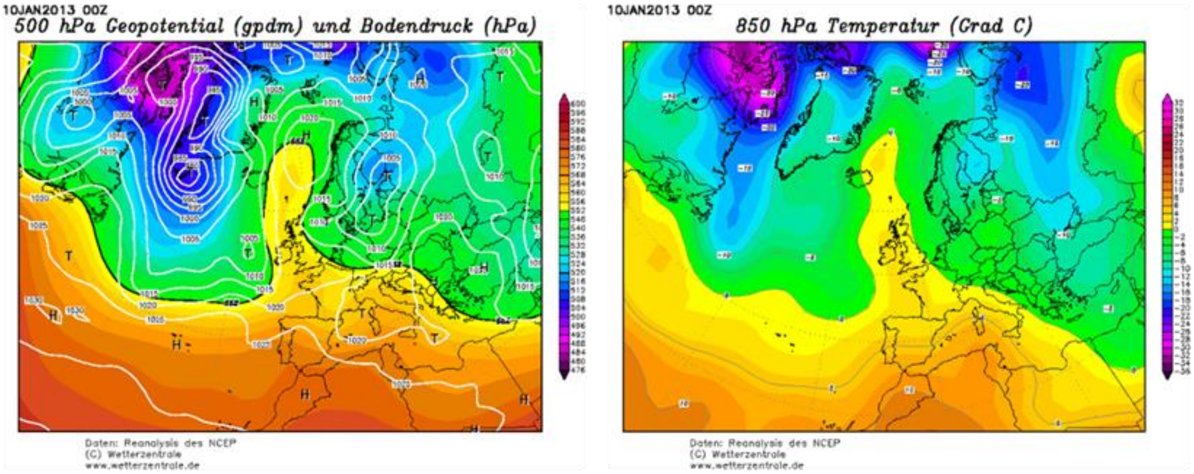

Figure 6.5. The synoptic conditions of the 10th January 2013, as they are depicted through the weather charts of 500 hPa (highlighting the geopotential heights and the surface isobars) and 850 hPa (highlighting the geopotential heights and the temperature gradients).

The synoptic conditions of the 10th January 2013 are indicated in Figure 6.5, where the weather charts at the 500 hPa (highlighting the geopotential heights and the surface isobars) and 850 hPa (highlighting the geopotential heights and the temperature gradients) are depicted. According to the classification method proposed by Karacostas (2003) and Karacostas et al. (2018), this is a North-West flow (NW). A long wave ridge is located over the major area of Great Britain, with a short-wave ridge to be formed over Croatia and a long wave trough to be over eastern Mediterranean. This configuration resulted in a northwest flow over the area of interest.

6.4.1 Flexpart-WRF visualization analysis run 9th to 11th January 2013

For 10th January 2013 where our samples were analyzed and according to the aforementioned synoptic conditions, the prevailing wind conditions indicated daily wind speed average of 1.8 km/h and wind direction WNW with maximum wind speed of 14.5 km/h (00:00am). These conditions assisted the transportation of the pollutants plume from the industrial area located west and at a north part in the city suburbs and affected all three sampling sites mostly west (Port) central (Auth) and finally to the east (Kalamaria). This can be noted in the backward visualization of the model depicted below for 3 hourly time step output, where we can notice the direction of the plume changing from time-step of +09 to +21 (Figs 6.6-6.8) as well as in the forward model visualization originating westerly and northerly from the possible identified emitting locations indicating the intensity of the phenomenon affecting our sampling sites (Figs 6.9-6.10) as noted from time-steps of +03 to +21 (more intensive dispersion).

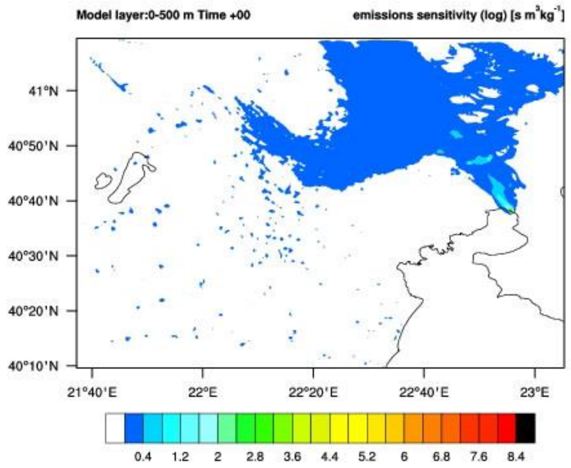

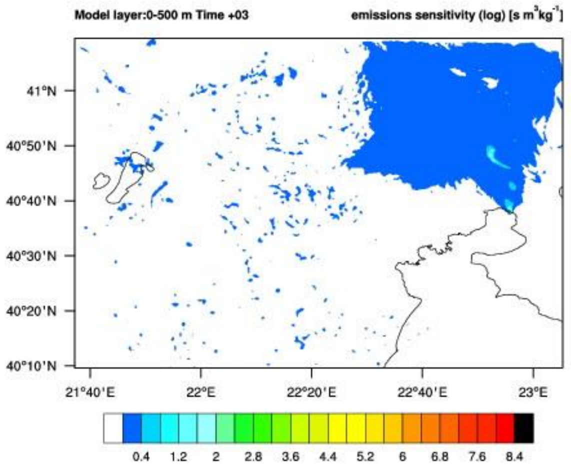

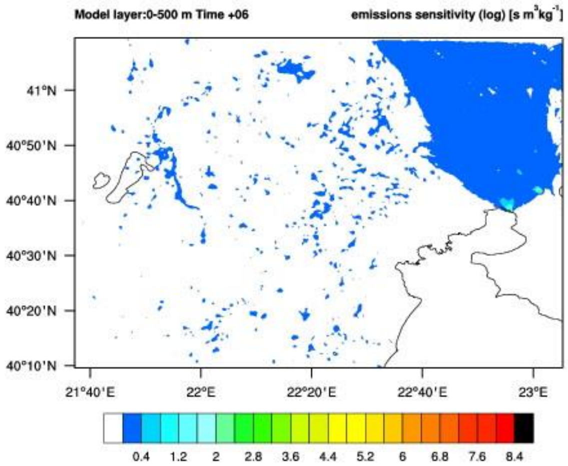
Model layer:0-500 m Time +06
emissions sensitivity (log) [s m^{3}kg^{-1}]
41°N
40°50'N
40°40'N
40°30'N
40°20'N
40°10'N
21°40'E
22°E
22°20'E
22°40'E
23°E
0.4
1.2
2
2.8
3.6
4.4
5.2
6
6.8
7.6
8.4

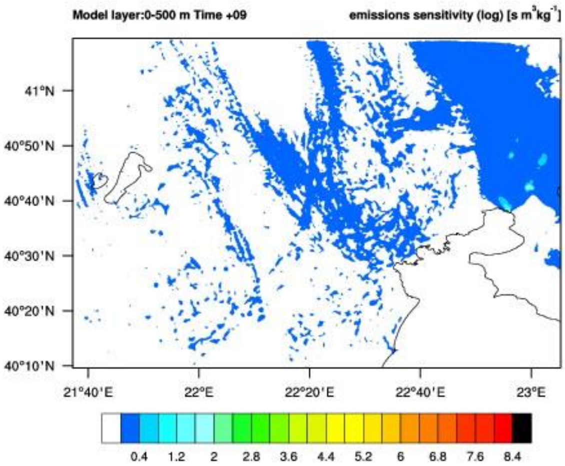
Model layer:0-500 m Time +09
emissions sensitivity (log) [s m^{3}kg^{-1}]
41°N
40°50'N
40°40'N
40°30'N
40°20'N
40°10'N
21°40'E
22°E
22°20'E
22°40'E
23°E
0.4
1.2
2
2.8
3.6
4.4
5.2
6
6.8
7.6
8.4

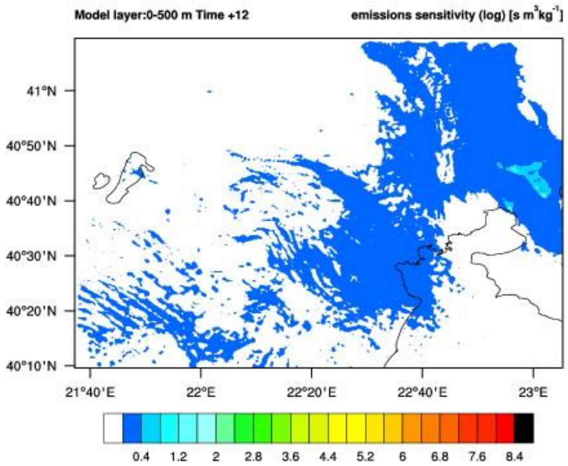
Model layer:0-500 m Time +12
emissions sensitivity (log) [s m^{3}kg^{-1}]
41°N
40°50'N
40°40'N
40°30'N
40°20'N
40°10'N
21°40'E
22°E
22°20'E
22°40'E
23°E
0.4
1.2
2
2.8
3.6
4.4
5.2
6
6.8
7.6
8.4

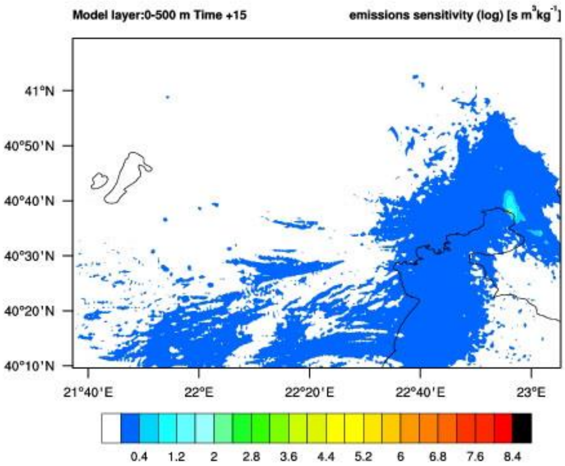
Model layer:0-500 m Time +15
emissions sensitivity (log) [s m^{3}kg^{-1}]
41°N
40°50'N
40°40'N
40°30'N
40°20'N
40°10'N
21°40'E
22°E
22°20'E
22°40'E
23°E
0.4
1.2
2
2.8
3.6
4.4
5.2
6
6.8
7.6
8.4

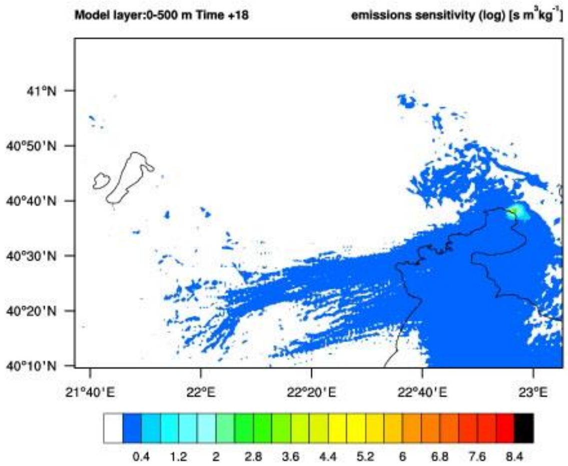
Model layer:0-500 m Time +18
emissions sensitivity (log) [s m^{3}kg^{-1}]
41°N
40°50'N
40°40'N
40°30'N
40°20'N
40°10'N
21°40'E
22°E
22°20'E
22°40'E
23°E
0.4
1.2
2
2.8
3.6
4.4
5.2
6
6.8
7.6
8.4

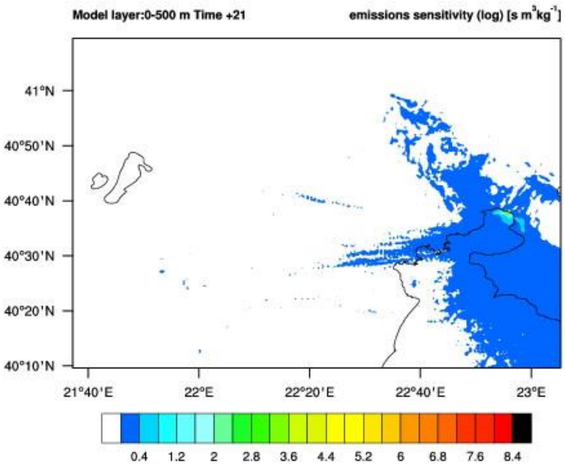
Model layer:0-500 m Time +21
emissions sensitivity (log) [s m^{3}kg^{-1}]
41°N
40°50'N
40°40'N
40°30'N
40°20'N
40°10'N
21°40'E
22°E
22°20'E
22°40'E
23°E
0.4
1.2
2
2.8
3.6
4.4
5.2
6
6.8
7.6
8.4

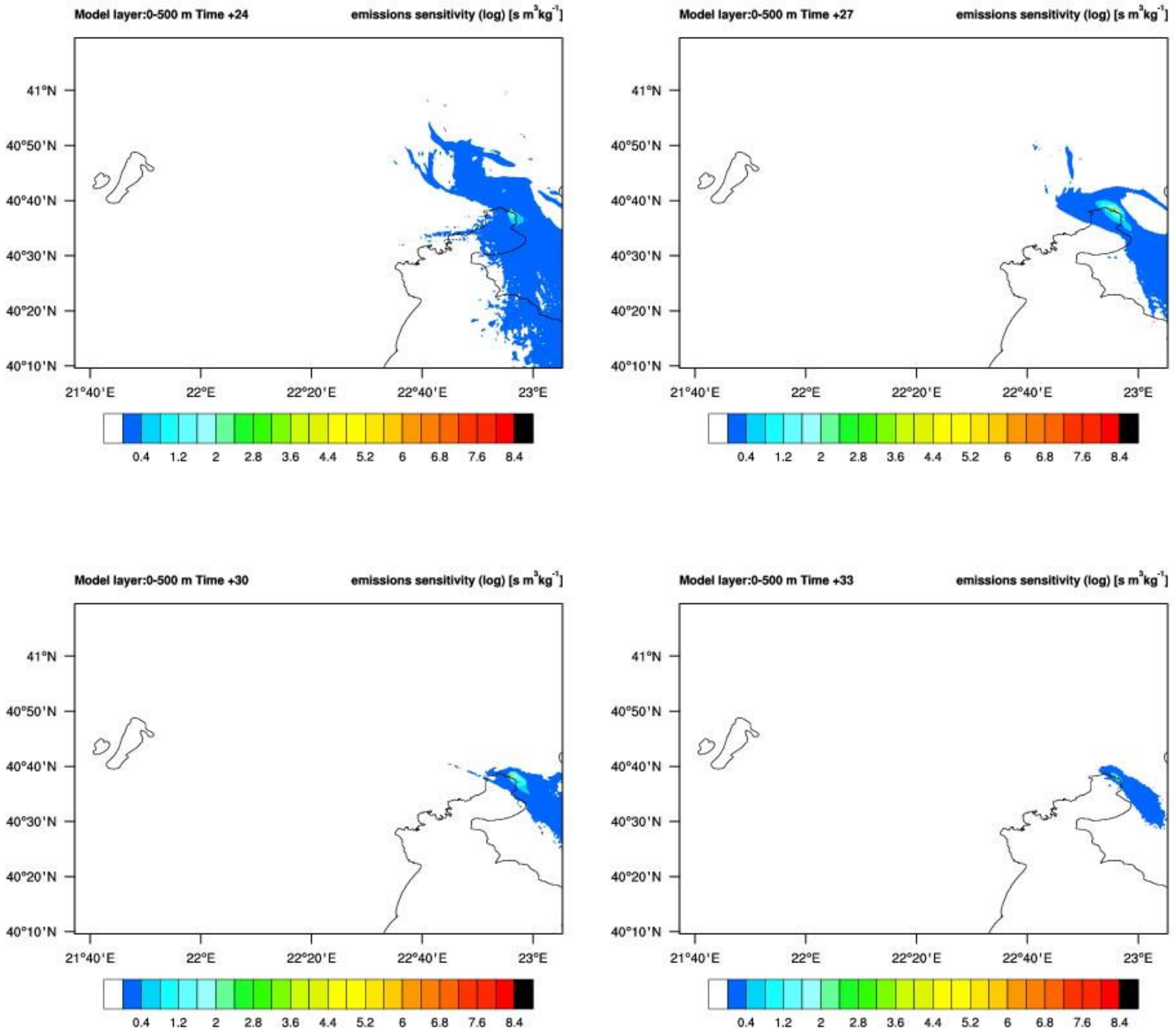

Figure 6.6. 9 to 11 January visualization of 3h output time-step based on Flexpart-WRF backward simulation from the sampling site PORT located west (Twelve storey Parking building near commercial Port of Thessaloniki) initiation time 12:00 UTC.

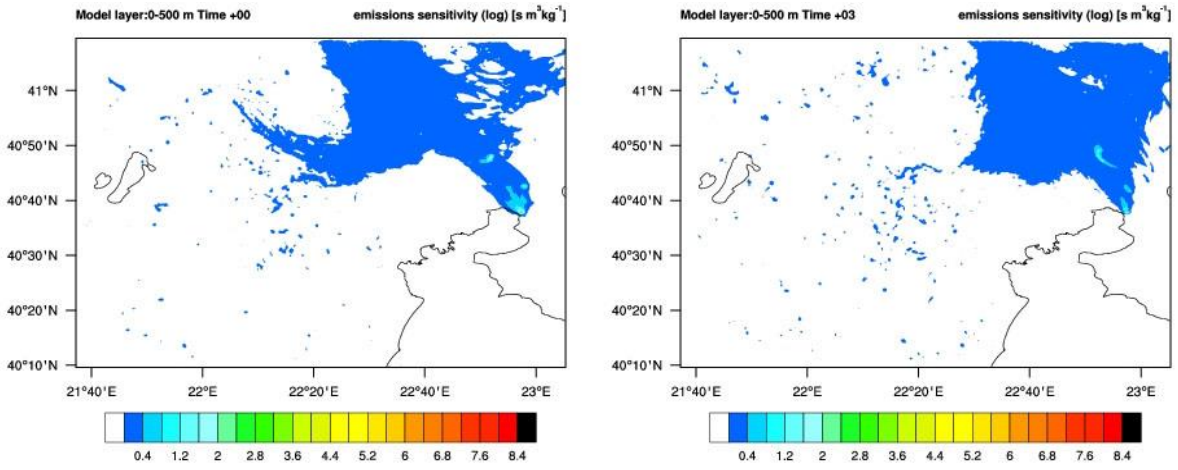

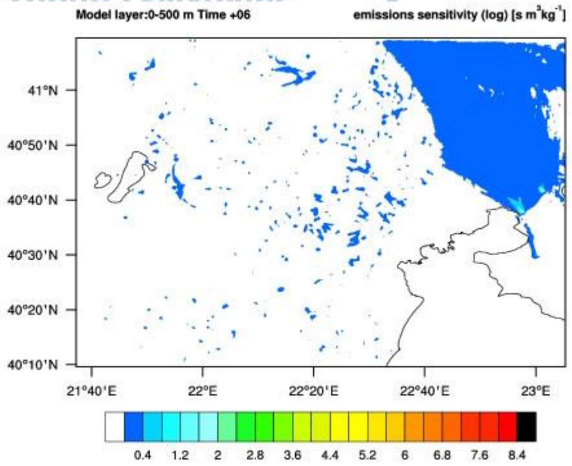
Model layer:0-500 m Time +06
emissions sensitivity (log) [s m^{3}kg^{-1}]
41°N
40°50'N
40°40'N
40°30'N
40°20'N
40°10'N
21°40'E
22°E
22°20'E
22°40'E
23°E
0.4 1.2 2 2.8 3.6 4.4 5.2 6 6.8 7.6 8.4

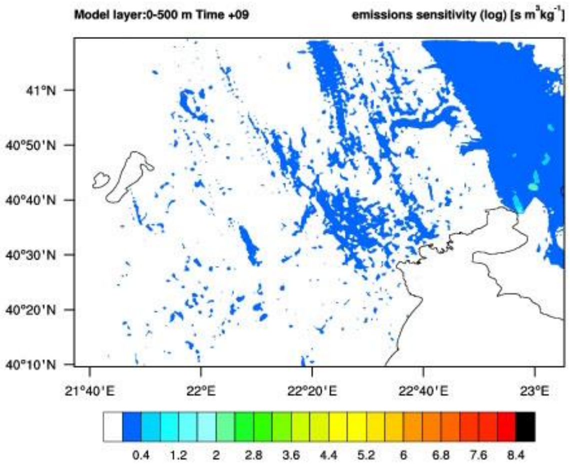
Model layer:0-500 m Time +09
emissions sensitivity (log) [s m^{3}kg^{-1}]
41°N
40°50'N
40°40'N
40°30'N
40°20'N
40°10'N
21°40'E
22°E
22°20'E
22°40'E
23°E
0.4 1.2 2 2.8 3.6 4.4 5.2 6 6.8 7.6 8.4

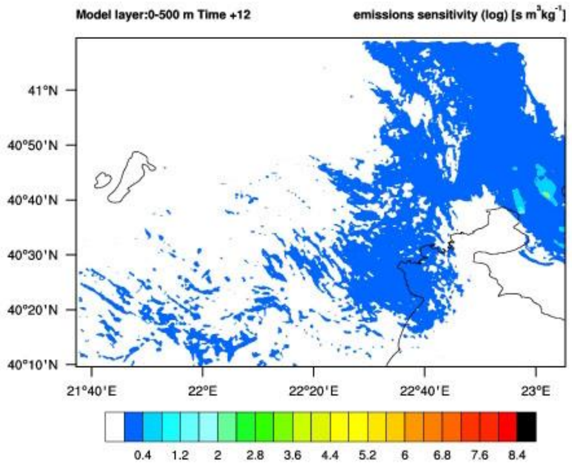
Model layer:0-500 m Time +12
emissions sensitivity (log) [s m^{3}kg^{-1}]
41°N
40°50'N
40°40'N
40°30'N
40°20'N
40°10'N
21°40'E
22°E
22°20'E
22°40'E
23°E
0.4 1.2 2 2.8 3.6 4.4 5.2 6 6.8 7.6 8.4

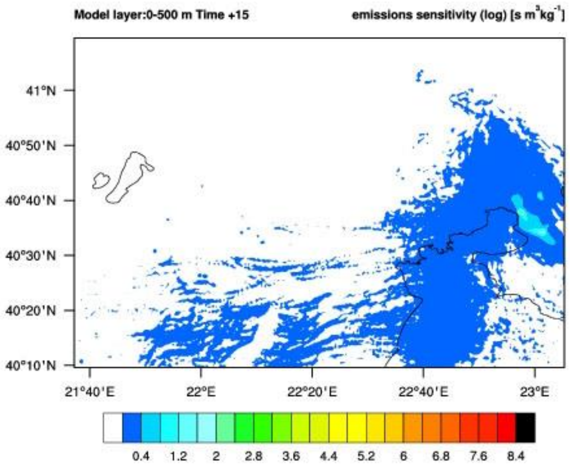
Model layer:0-500 m Time +15
emissions sensitivity (log) [s m^{3}kg^{-1}]
41°N
40°50'N
40°40'N
40°30'N
40°20'N
40°10'N
21°40'E
22°E
22°20'E
22°40'E
23°E
0.4 1.2 2 2.8 3.6 4.4 5.2 6 6.8 7.6 8.4

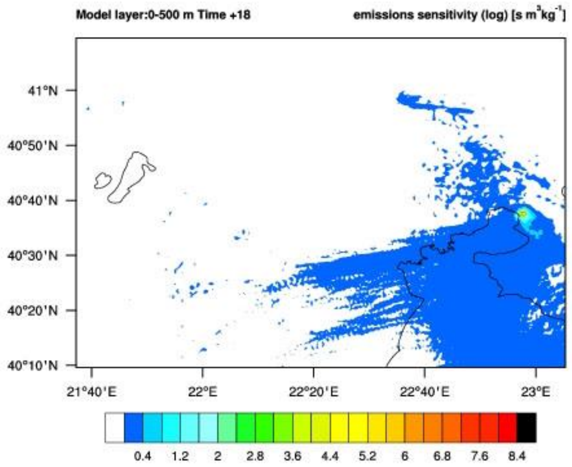
Model layer:0-500 m Time +18
emissions sensitivity (log) [s m^{3}kg^{-1}]
41°N
40°50'N
40°40'N
40°30'N
40°20'N
40°10'N
21°40'E
22°E
22°20'E
22°40'E
23°E
0.4 1.2 2 2.8 3.6 4.4 5.2 6 6.8 7.6 8.4

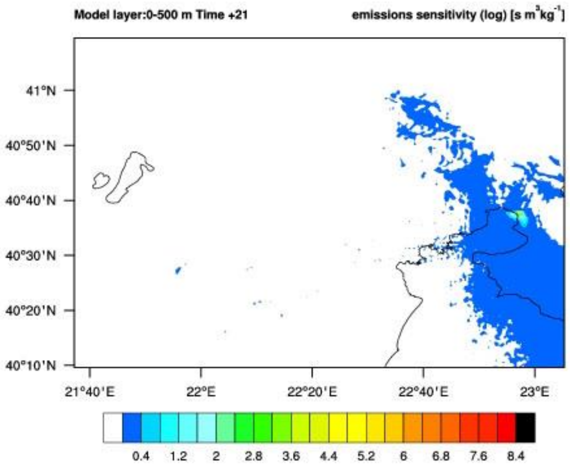
Model layer:0-500 m Time +21
emissions sensitivity (log) [s m^{3}kg^{-1}]
41°N
40°50'N
40°40'N
40°30'N
40°20'N
40°10'N
21°40'E
22°E
22°20'E
22°40'E
23°E
0.4 1.2 2 2.8 3.6 4.4 5.2 6 6.8 7.6 8.4

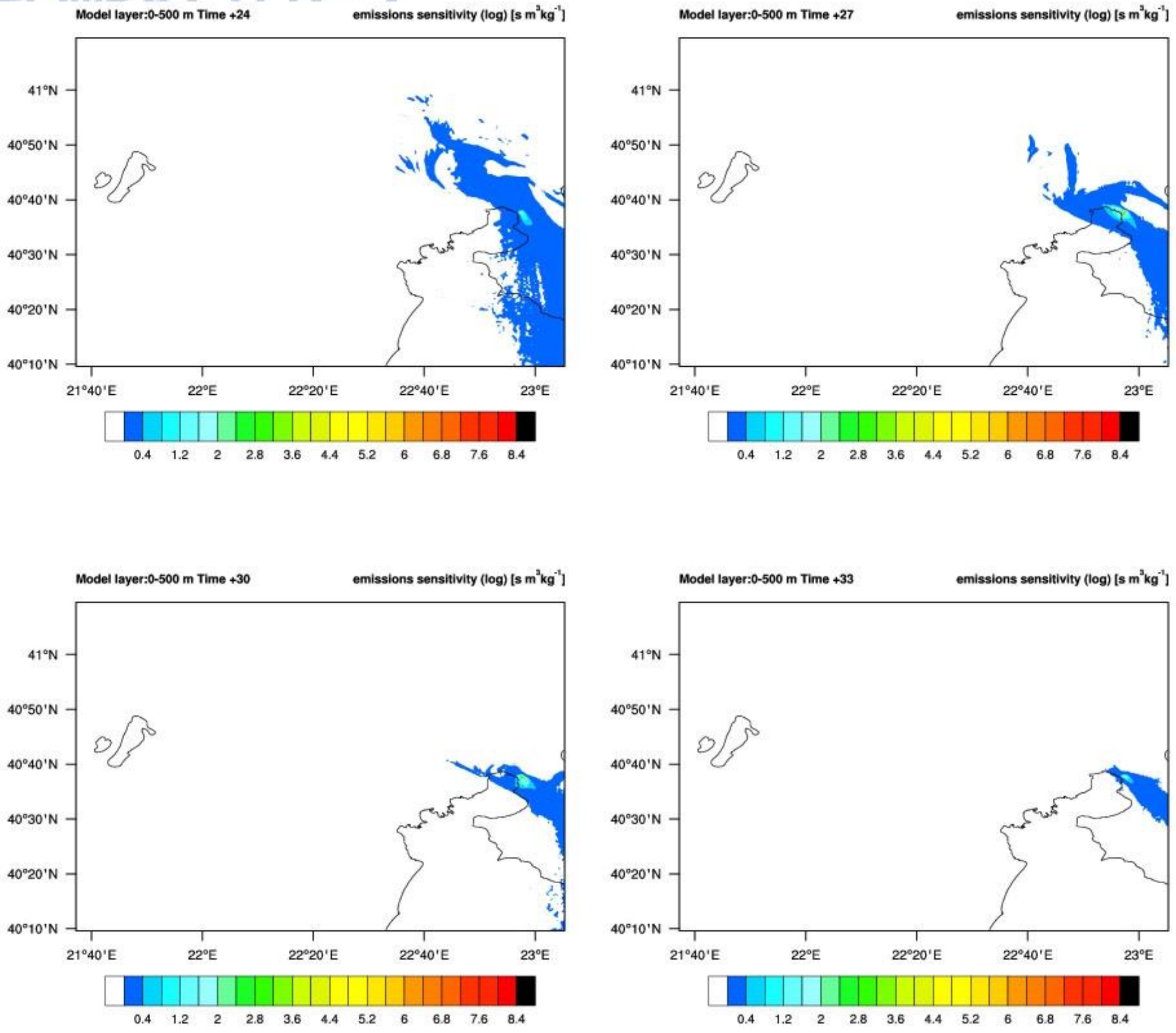

Figure 6.7. 9 to 11 January visualization of 3h output time-step based on Flexpart-WRF backward simulation from the sampling site AUTH located in city center (Aristotle University of Thessaloniki) initiation time 12:00 UTC.

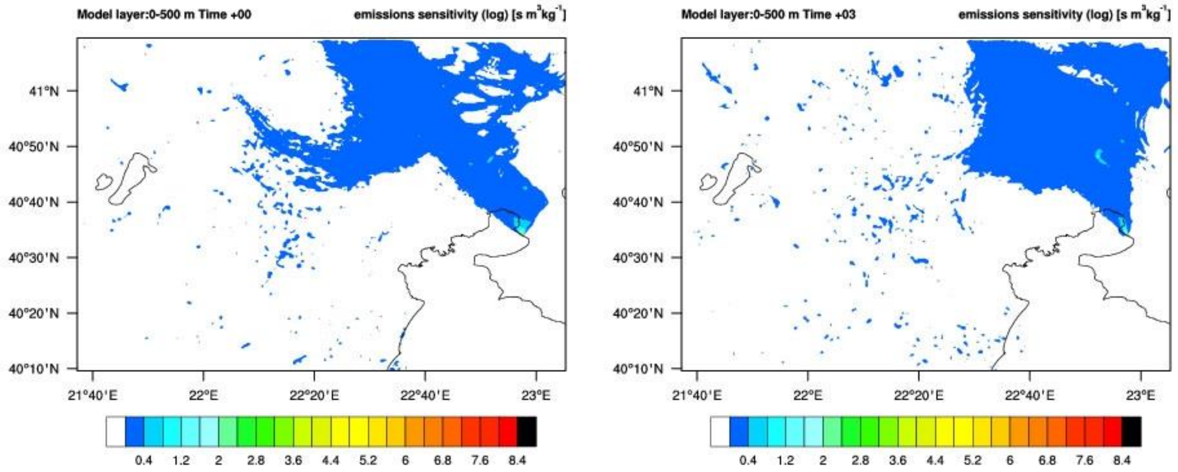

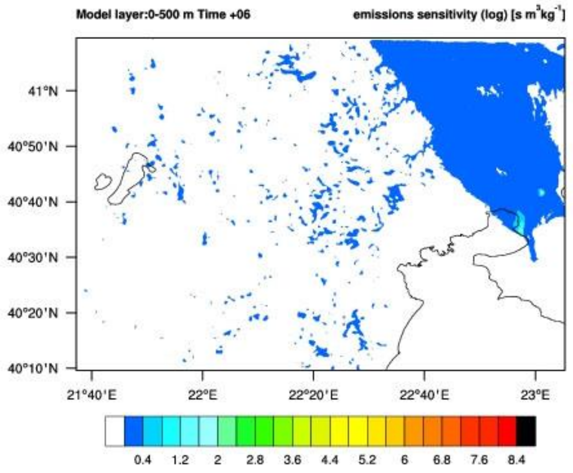
Model layer:0-500 m Time +06
emissions sensitivity (log) [s m³kg⁻¹]
41°N
40°50'N
40°40'N
40°30'N
40°20'N
40°10'N
21°40'E
22°E
22°20'E
22°40'E
23°E
0.4 1.2 2 2.8 3.6 4.4 5.2 6 6.8 7.6 8.4

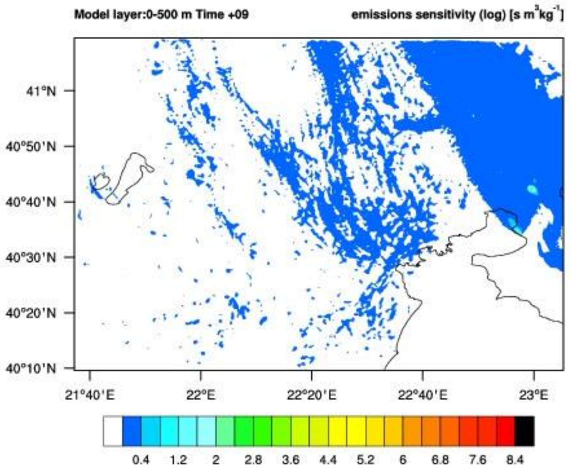
Model layer:0-500 m Time +09
emissions sensitivity (log) [s m³kg⁻¹]
41°N
40°50'N
40°40'N
40°30'N
40°20'N
40°10'N
21°40'E
22°E
22°20'E
22°40'E
23°E
0.4 1.2 2 2.8 3.6 4.4 5.2 6 6.8 7.6 8.4

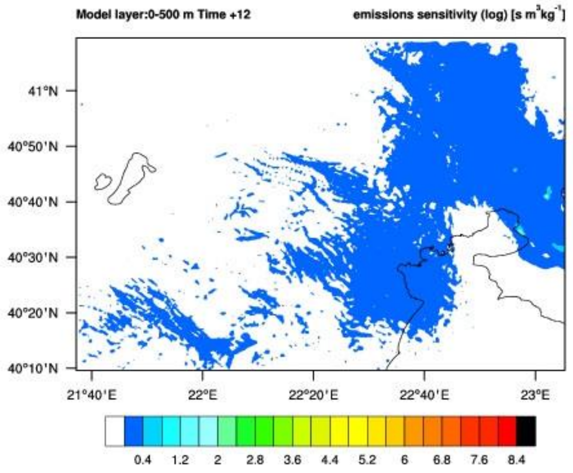
Model layer:0-500 m Time +12
emissions sensitivity (log) [s m³kg⁻¹]
41°N
40°50'N
40°40'N
40°30'N
40°20'N
40°10'N
21°40'E
22°E
22°20'E
22°40'E
23°E
0.4 1.2 2 2.8 3.6 4.4 5.2 6 6.8 7.6 8.4

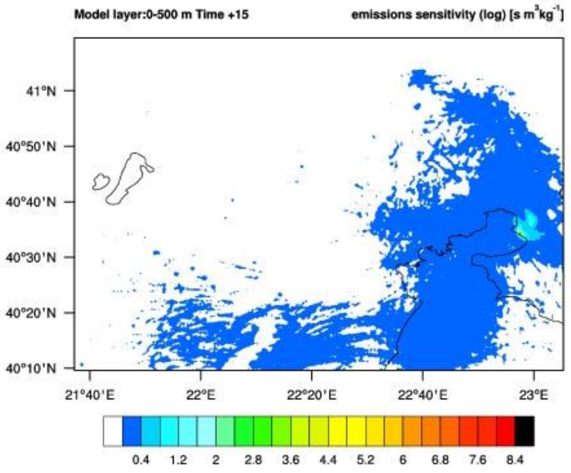
Model layer:0-500 m Time +15
emissions sensitivity (log) [s m³kg⁻¹]
41°N
40°50'N
40°40'N
40°30'N
40°20'N
40°10'N
21°40'E
22°E
22°20'E
22°40'E
23°E
0.4 1.2 2 2.8 3.6 4.4 5.2 6 6.8 7.6 8.4

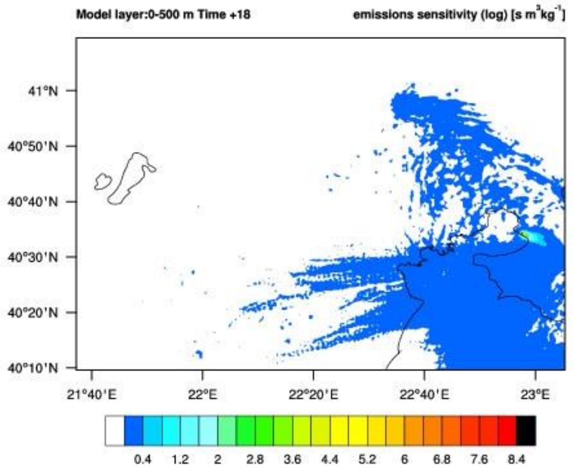
Model layer:0-500 m Time +18
emissions sensitivity (log) [s m³kg⁻¹]
41°N
40°50'N
40°40'N
40°30'N
40°20'N
40°10'N
21°40'E
22°E
22°20'E
22°40'E
23°E
0.4 1.2 2 2.8 3.6 4.4 5.2 6 6.8 7.6 8.4

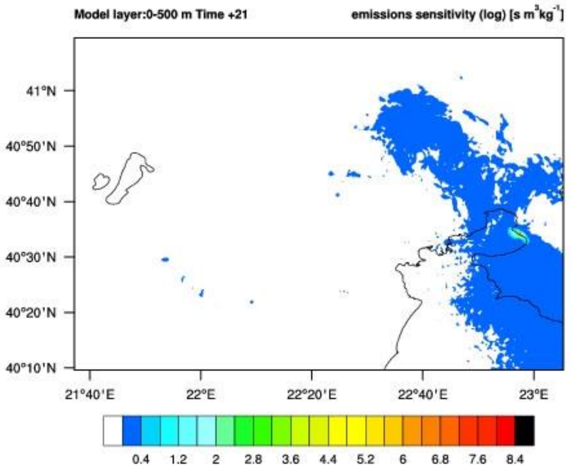
Model layer:0-500 m Time +21
emissions sensitivity (log) [s m³kg⁻¹]
41°N
40°50'N
40°40'N
40°30'N
40°20'N
40°10'N
21°40'E
22°E
22°20'E
22°40'E
23°E
0.4 1.2 2 2.8 3.6 4.4 5.2 6 6.8 7.6 8.4

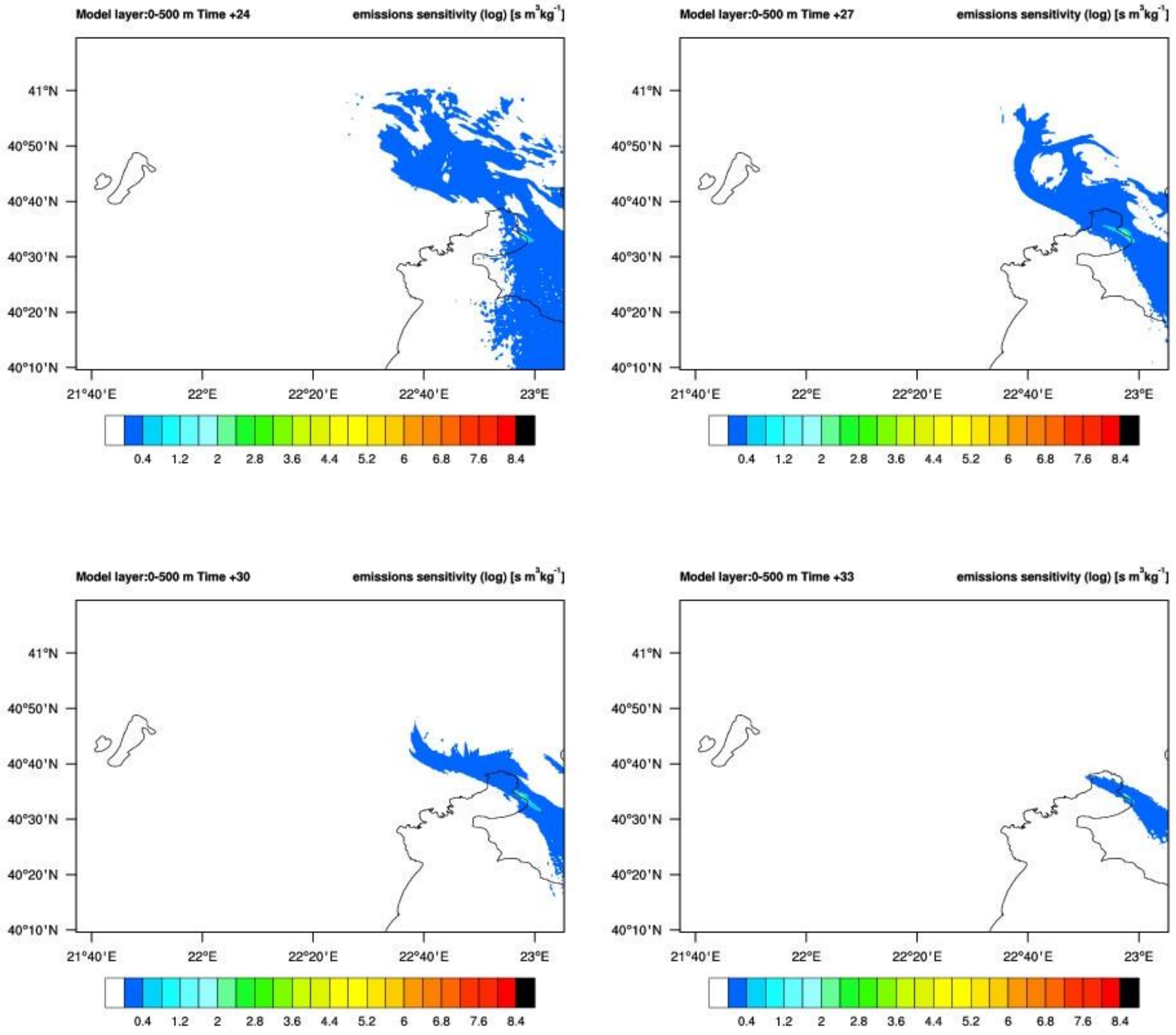

Figure 6.8. 9 to 11 January visualization of 3h output time-step based on Flexpart-WRF backward simulation from the sampling site KALAMARIA located South-East (Multi-storey building in Kalamaria region) initiation time 12:00 UTC.

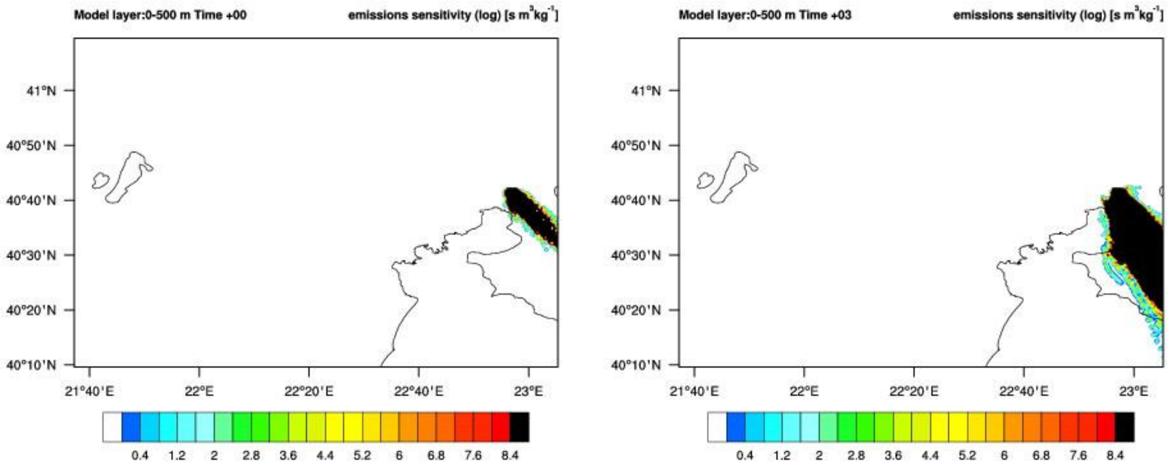

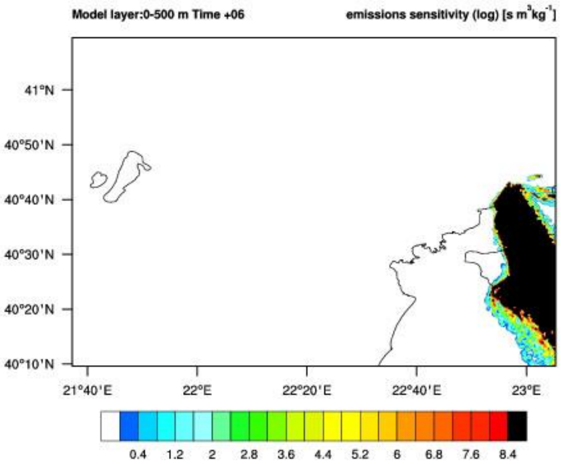
Model layer:0-500 m Time +06
emissions sensitivity (log) [s m^{3}kg^{-1}]
41°N
40°50'N
40°40'N
40°30'N
40°20'N
40°10'N
21°40'E
22°E
22°20'E
22°40'E
23°E
0.4
1.2
2
2.8
3.6
4.4
5.2
6
6.8
7.6
8.4

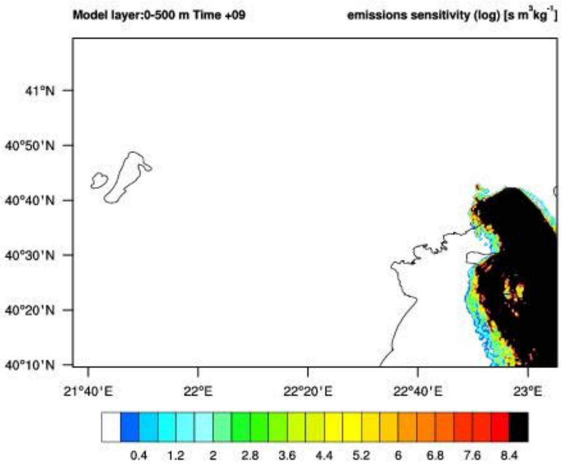
Model layer:0-500 m Time +09
emissions sensitivity (log) [s m^{3}kg^{-1}]
41°N
40°50'N
40°40'N
40°30'N
40°20'N
40°10'N
21°40'E
22°E
22°20'E
22°40'E
23°E
0.4
1.2
2
2.8
3.6
4.4
5.2
6
6.8
7.6
8.4

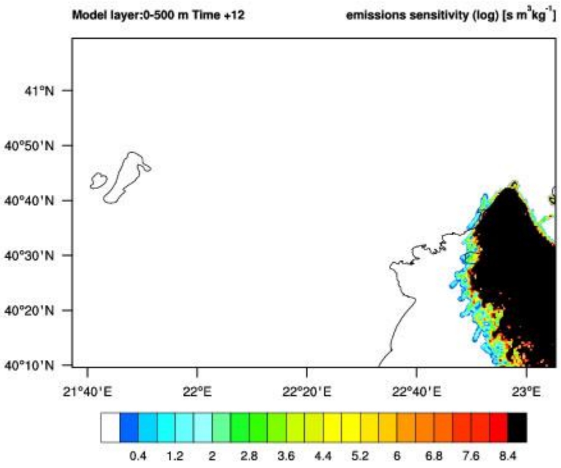
Model layer:0-500 m Time +12
emissions sensitivity (log) [s m^{3}kg^{-1}]
41°N
40°50'N
40°40'N
40°30'N
40°20'N
40°10'N
21°40'E
22°E
22°20'E
22°40'E
23°E
0.4
1.2
2
2.8
3.6
4.4
5.2
6
6.8
7.6
8.4

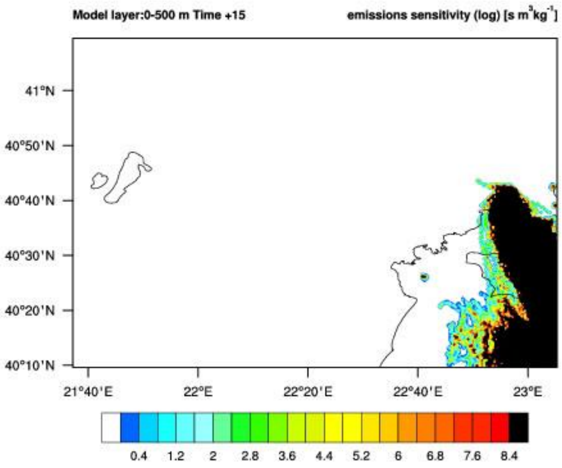
Model layer:0-500 m Time +15
emissions sensitivity (log) [s m^{3}kg^{-1}]
41°N
40°50'N
40°40'N
40°30'N
40°20'N
40°10'N
21°40'E
22°E
22°20'E
22°40'E
23°E
0.4
1.2
2
2.8
3.6
4.4
5.2
6
6.8
7.6
8.4

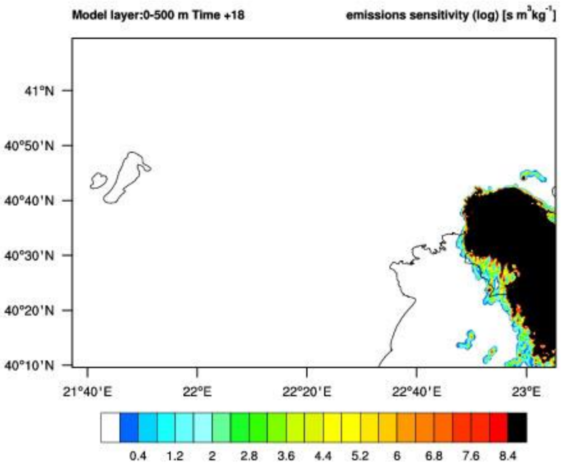
Model layer:0-500 m Time +18
emissions sensitivity (log) [s m^{3}kg^{-1}]
41°N
40°50'N
40°40'N
40°30'N
40°20'N
40°10'N
21°40'E
22°E
22°20'E
22°40'E
23°E
0.4
1.2
2
2.8
3.6
4.4
5.2
6
6.8
7.6
8.4

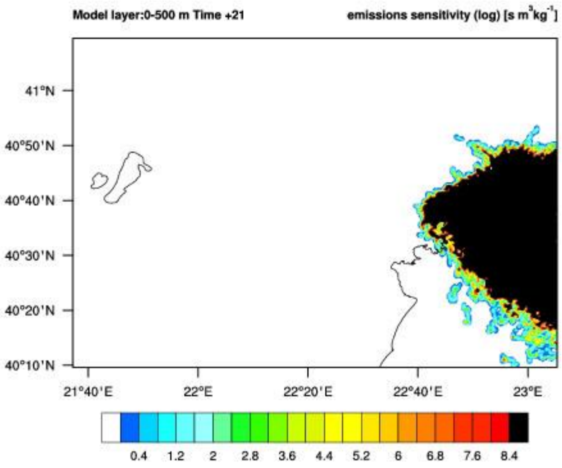
Model layer:0-500 m Time +21
emissions sensitivity (log) [s m^{3}kg^{-1}]
41°N
40°50'N
40°40'N
40°30'N
40°20'N
40°10'N
21°40'E
22°E
22°20'E
22°40'E
23°E
0.4
1.2
2
2.8
3.6
4.4
5.2
6
6.8
7.6
8.4

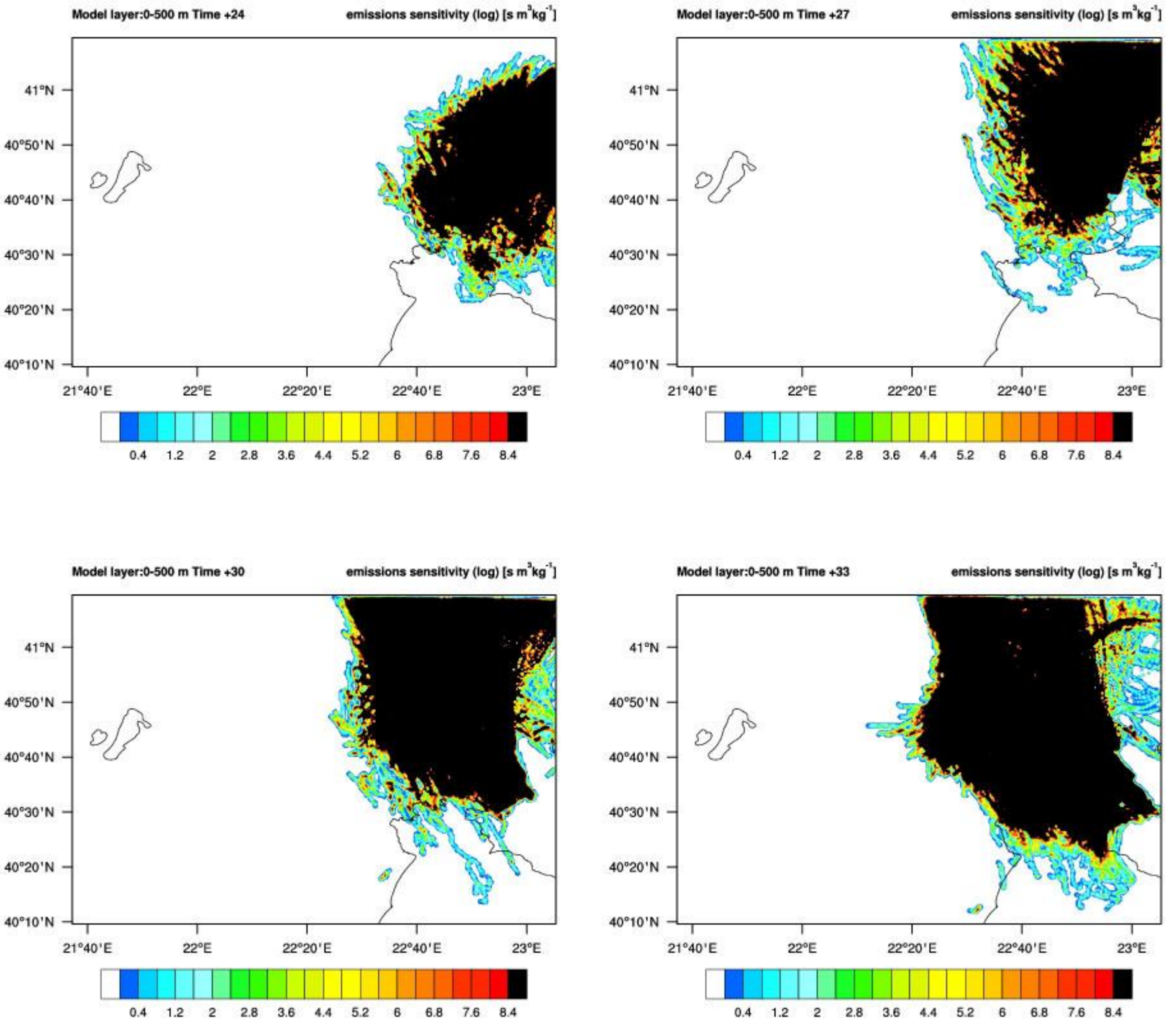

Figure 6.9. 9 to 11 January visualization of 3h output time-step based on Flexpart-WRF forward simulation from emitting site located North in city suburbs initiation time 12:00 UTC.

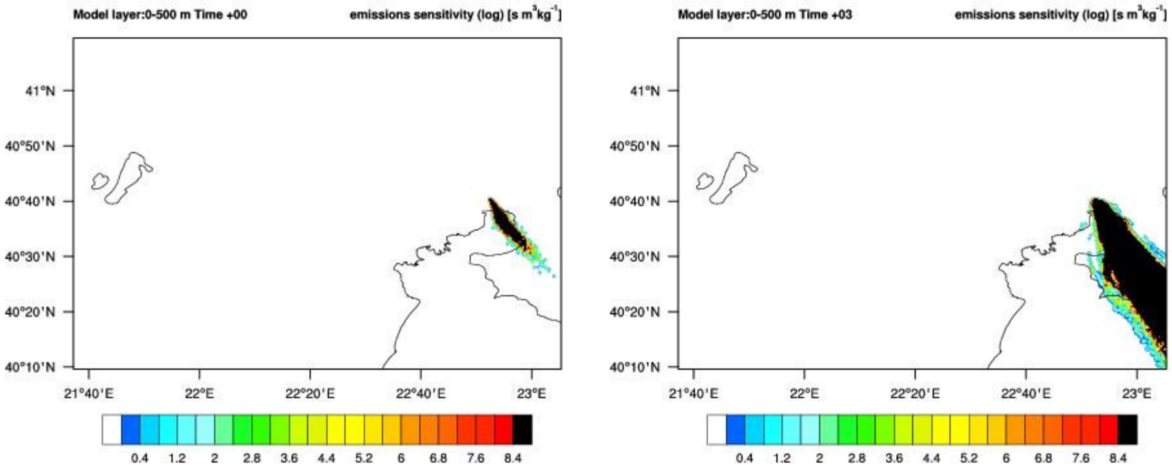

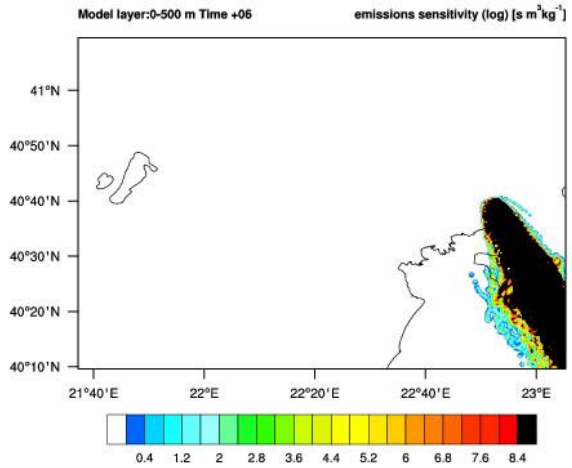
Model layer:0-500 m Time +06
emissions sensitivity (log) [s m^{3}kg^{-1}]
41°N
40°50'N
40°40'N
40°30'N
40°20'N
40°10'N
21°40'E
22°E
22°20'E
22°40'E
23°E
0.4 1.2 2 2.8 3.6 4.4 5.2 6 6.8 7.6 8.4

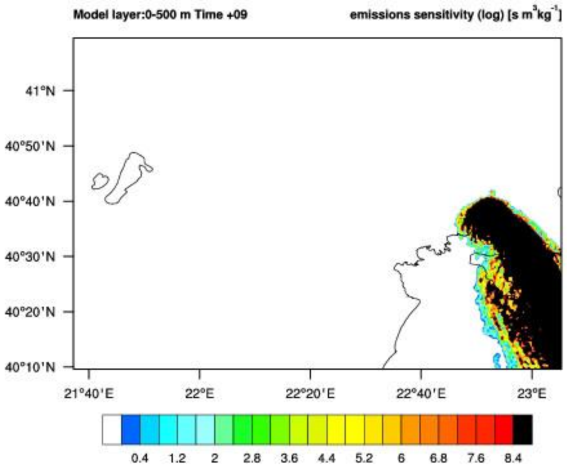
Model layer:0-500 m Time +09
emissions sensitivity (log) [s m^{3}kg^{-1}]
41°N
40°50'N
40°40'N
40°30'N
40°20'N
40°10'N
21°40'E
22°E
22°20'E
22°40'E
23°E
0.4 1.2 2 2.8 3.6 4.4 5.2 6 6.8 7.6 8.4

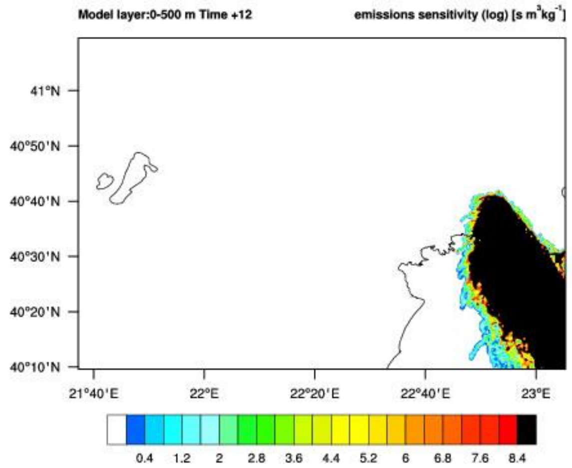
Model layer:0-500 m Time +12
emissions sensitivity (log) [s m^{3}kg^{-1}]
41°N
40°50'N
40°40'N
40°30'N
40°20'N
40°10'N
21°40'E
22°E
22°20'E
22°40'E
23°E
0.4 1.2 2 2.8 3.6 4.4 5.2 6 6.8 7.6 8.4

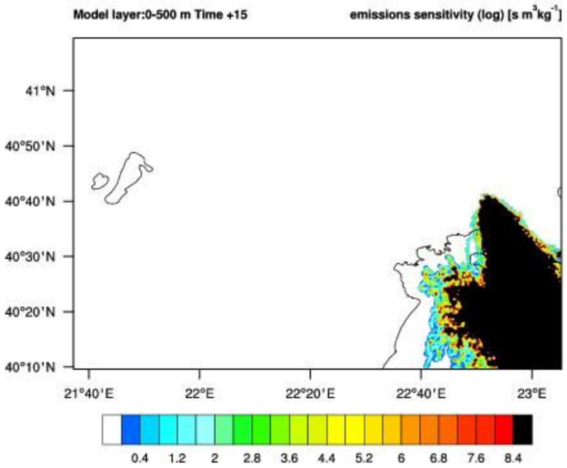
Model layer:0-500 m Time +15
emissions sensitivity (log) [s m^{3}kg^{-1}]
41°N
40°50'N
40°40'N
40°30'N
40°20'N
40°10'N
21°40'E
22°E
22°20'E
22°40'E
23°E
0.4 1.2 2 2.8 3.6 4.4 5.2 6 6.8 7.6 8.4

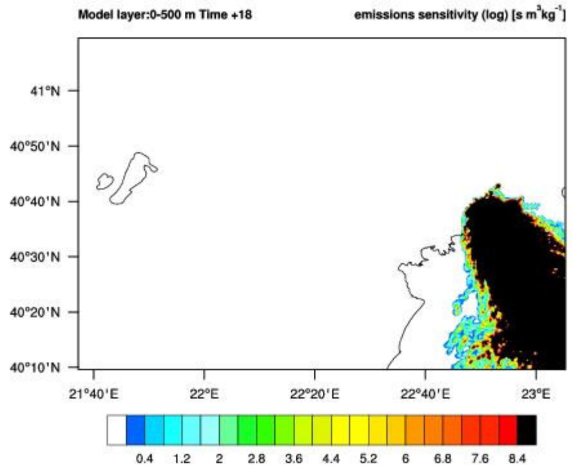
Model layer:0-500 m Time +18
emissions sensitivity (log) [s m^{3}kg^{-1}]
41°N
40°50'N
40°40'N
40°30'N
40°20'N
40°10'N
21°40'E
22°E
22°20'E
22°40'E
23°E
0.4 1.2 2 2.8 3.6 4.4 5.2 6 6.8 7.6 8.4

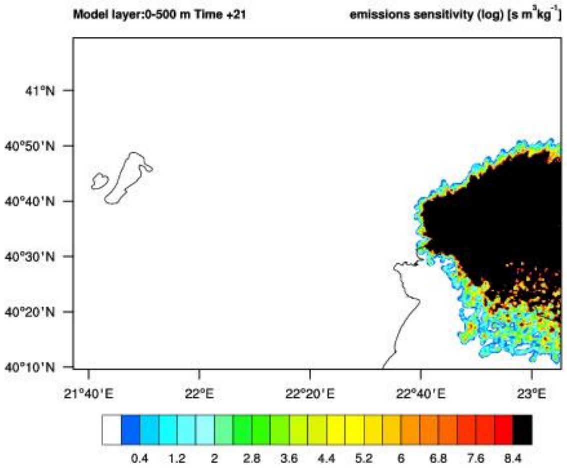
Model layer:0-500 m Time +21
emissions sensitivity (log) [s m^{3}kg^{-1}]
41°N
40°50'N
40°40'N
40°30'N
40°20'N
40°10'N
21°40'E
22°E
22°20'E
22°40'E
23°E
0.4 1.2 2 2.8 3.6 4.4 5.2 6 6.8 7.6 8.4

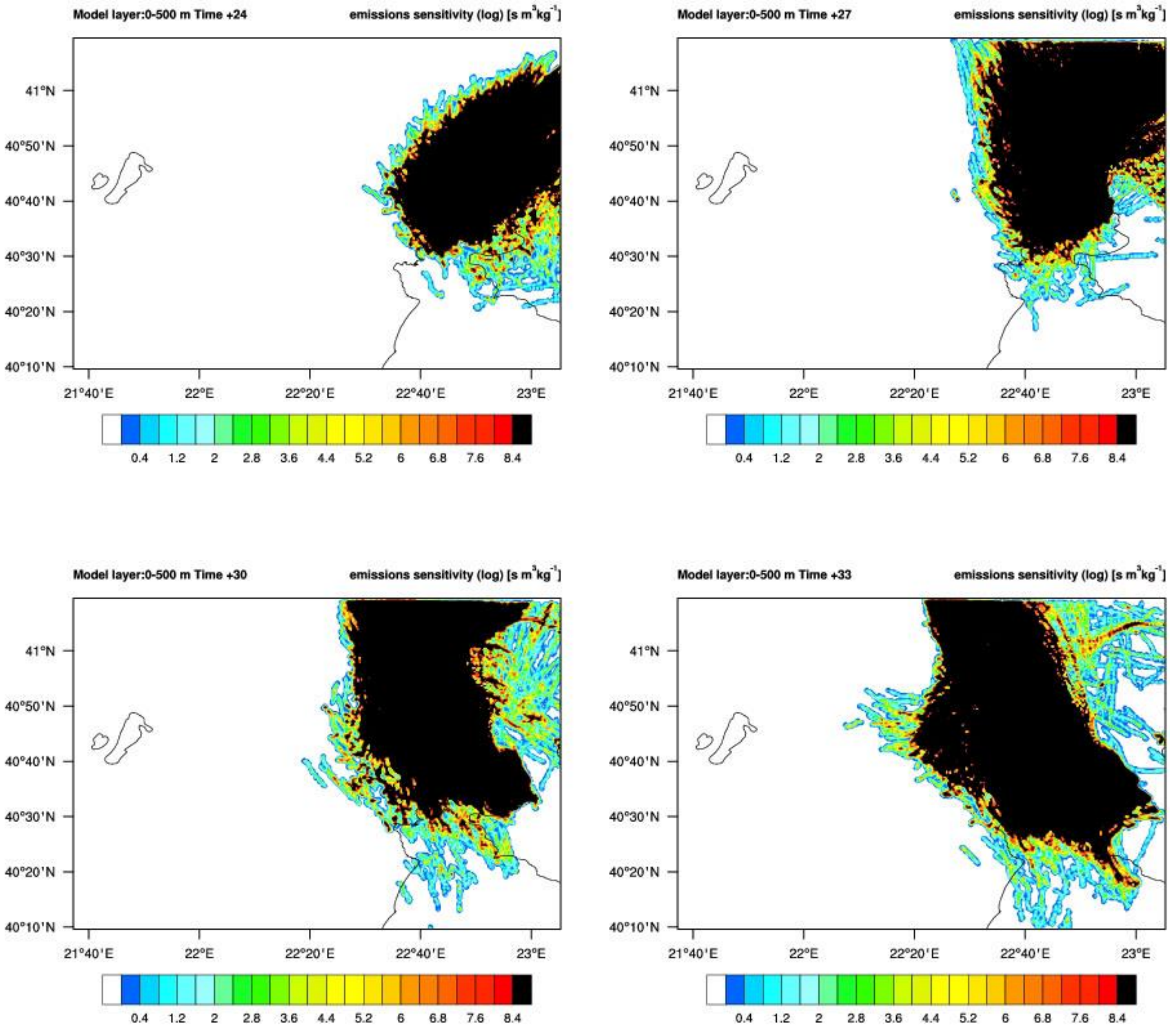

Figure 6.10. 9 to 11 visualization of 3h output time-step based on Flexpart-WRF forward simulation from emitting site located West in the industrial area of the city initiation time 12:00 UTC.

6.5. Synoptic conditions sampling date 14th January 2013

For the sampling day of 14th January 2013 and more specifically one day earlier from our day of interest in 13th the average wind speed was 4.1 km/h and westerly wind directions W with maximum wind speed of 29 km/h (01:50 am).

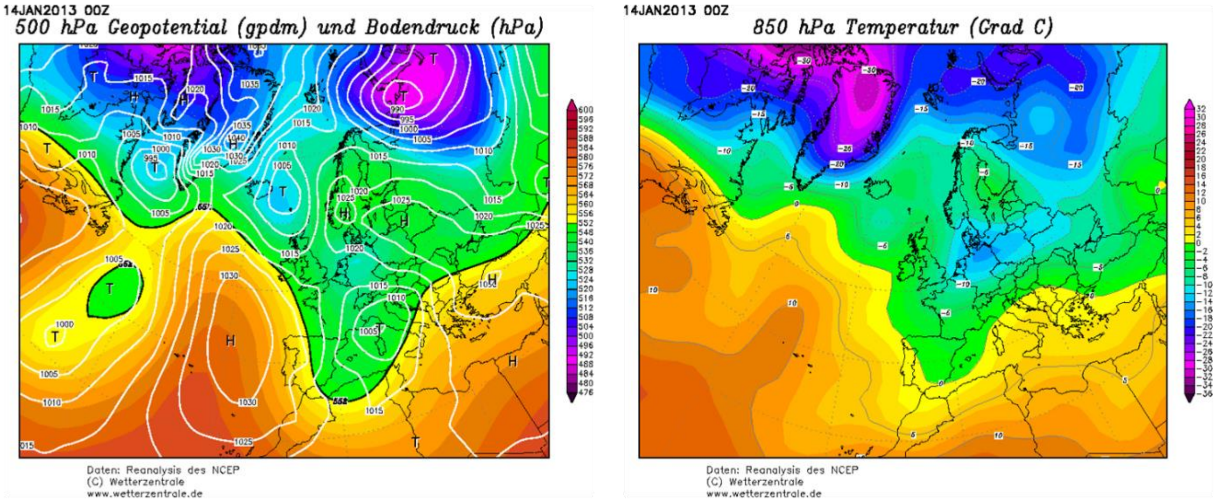

Figure 6.11. The synoptic conditions of the 14th January 2013, as they are depicted through the weather charts of 500 hPa (highlighting the geopotential heights and the surface isobars) and 850 hPa (highlighting the geopotential heights and the temperature gradients).

The synoptic conditions of the 14th January 2013 are indicated in Figure 6.11, where the weather charts at the 500 hPa (highlighting the geopotential heights and the surface isobars) and 850 hPa (highlighting the geopotential heights and the temperature gradients) are depicted. According to the classification method proposed by Karacostas (2003) and Karacostas et al., (2018), this is a South-West flow (SW). This synoptic type is characterized by the presence of a long wave trough situated over central and mostly western Mediterranean that is to the west of the area of interest (Figure 6.11). Accordingly, a short-wave ridge is present in the Balkan area, resulting to a prevailing southwest flow over the area of interest. The orientation of the trough axis tilts airflow from south-easterly to north-westerly directions. At the surface, a low-pressure system is observed at the area of the gulf of Geneva and a n anticyclone over the Black Sea. The chart of 850 hPa indicates also a short-wave ridge over the examined area, dominating the south-westerly airmass circulation.

6.5.1 Flexpart-WRF visualization analysis run 13th to 15th January 2013

For 14th January 2013 where our samples were analyzed and according to the aforementioned synoptic conditions, the prevailing wind conditions showed daily wind speed average of 1.9 km/h and south west wind direction SW with maximum wind speed of 17.7 km/h (05:40a.m.) with western winds mostly assisting the dispersion of the dust particles pollutants to our sampling sites as it can be noted in the backward visualizations starting from time-step +03 till to +21(more intensively) with a slight turn of the plume at +15 (Figs 6.12-6.14) and with contribution initially from northern emitting areas as seen in forward simulations of time-step +00 and western emitting areas as seen in the rest time-steps of our visualizations originating from the possible identified emitting locations indicating the intensity of the phenomenon (Figs 6.15-6.16).

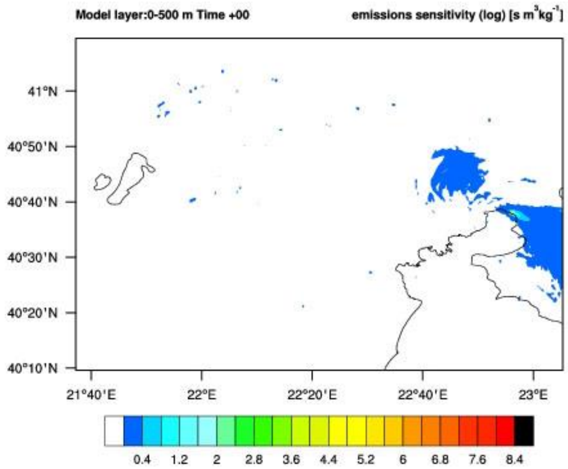

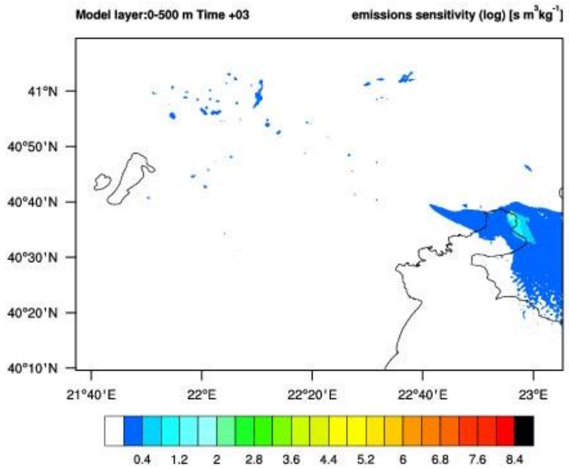

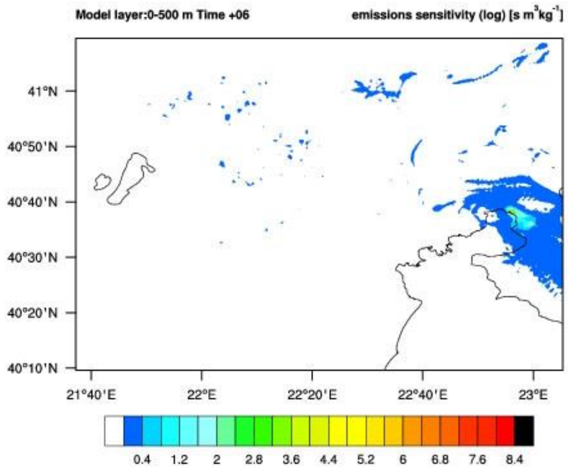

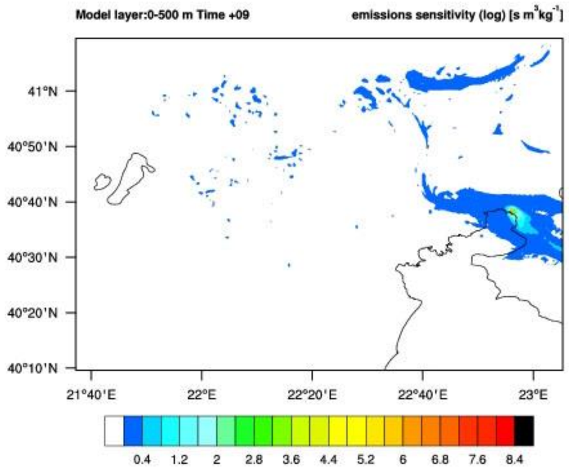

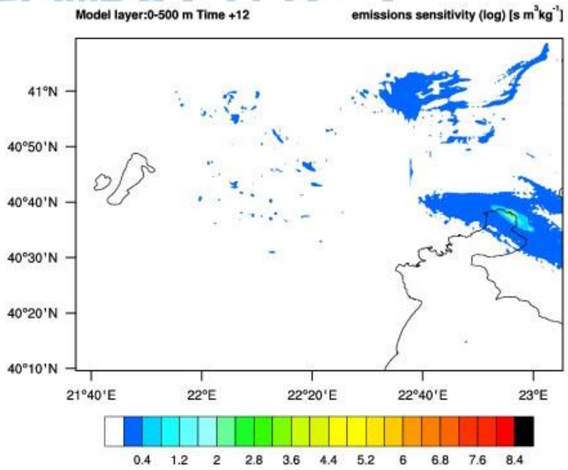
Model layer:0-500 m Time +12
emissions sensitivity (log) [s m^3kg^{-1}]
41°N
40°50'N
40°40'N
40°30'N
40°20'N
40°10'N
21°40'E
22°E
22°20'E
22°40'E
23°E
0.4
1.2
2
2.8
3.6
4.4
5.2
6
6.8
7.6
8.4

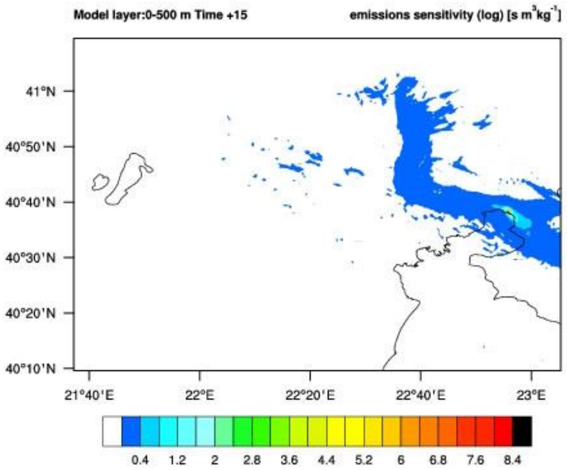
Model layer:0-500 m Time +15
emissions sensitivity (log) [s m^3kg^{-1}]
41°N
40°50'N
40°40'N
40°30'N
40°20'N
40°10'N
21°40'E
22°E
22°20'E
22°40'E
23°E
0.4
1.2
2
2.8
3.6
4.4
5.2
6
6.8
7.6
8.4

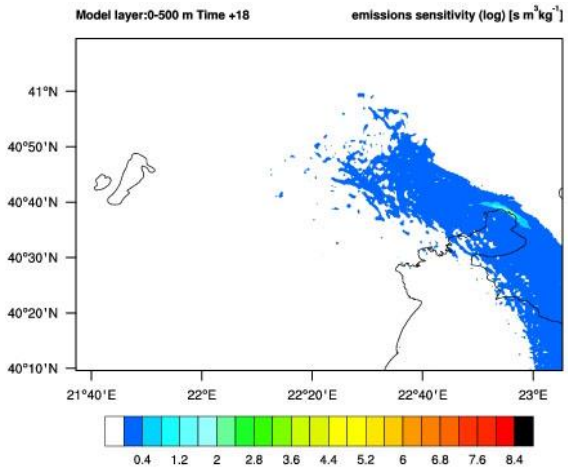
Model layer:0-500 m Time +18
emissions sensitivity (log) [s m^3kg^{-1}]
41°N
40°50'N
40°40'N
40°30'N
40°20'N
40°10'N
21°40'E
22°E
22°20'E
22°40'E
23°E
0.4
1.2
2
2.8
3.6
4.4
5.2
6
6.8
7.6
8.4

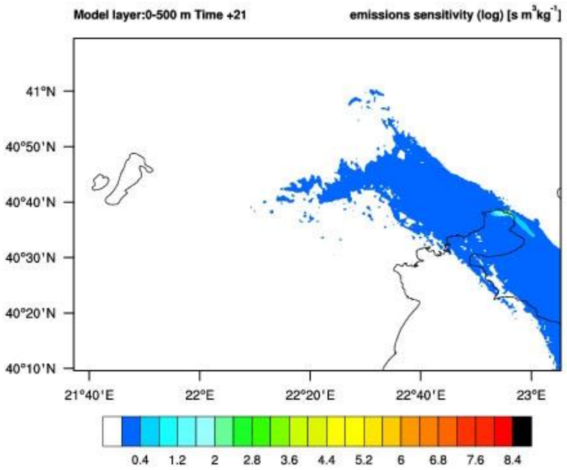
Model layer:0-500 m Time +21
emissions sensitivity (log) [s m^3kg^{-1}]
41°N
40°50'N
40°40'N
40°30'N
40°20'N
40°10'N
21°40'E
22°E
22°20'E
22°40'E
23°E
0.4
1.2
2
2.8
3.6
4.4
5.2
6
6.8
7.6
8.4

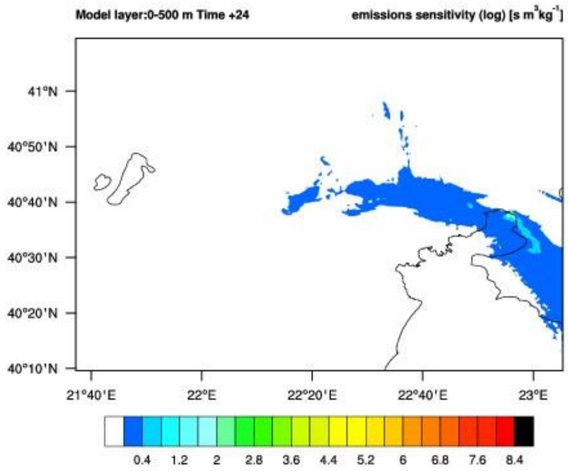
Model layer:0-500 m Time +24
emissions sensitivity (log) [s m^3kg^{-1}]
41°N
40°50'N
40°40'N
40°30'N
40°20'N
40°10'N
21°40'E
22°E
22°20'E
22°40'E
23°E
0.4
1.2
2
2.8
3.6
4.4
5.2
6
6.8
7.6
8.4

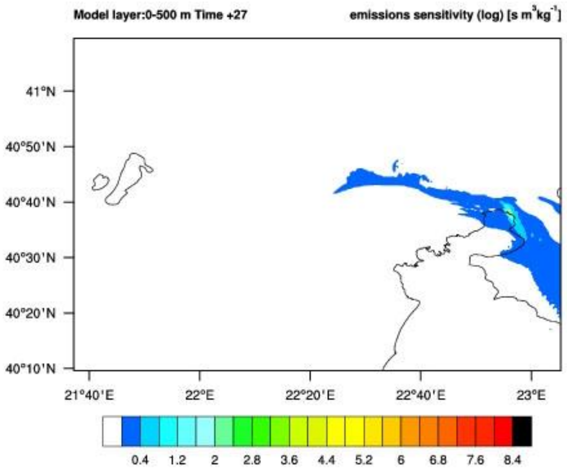
Model layer:0-500 m Time +27
emissions sensitivity (log) [s m^3kg^{-1}]
41°N
40°50'N
40°40'N
40°30'N
40°20'N
40°10'N
21°40'E
22°E
22°20'E
22°40'E
23°E
0.4
1.2
2
2.8
3.6
4.4
5.2
6
6.8
7.6
8.4

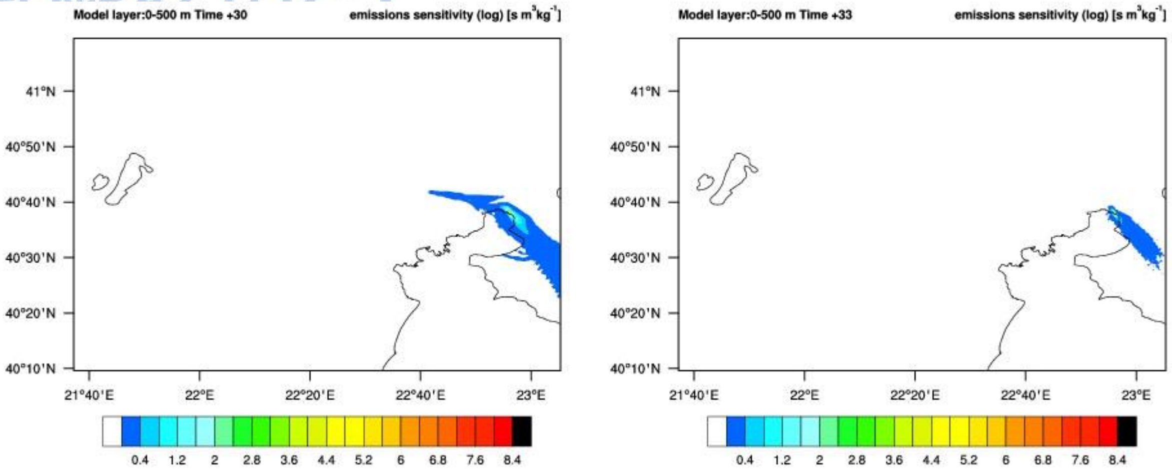

Figure 6.12. 13 to 15 January visualization of 3h output time-step based on Flexpart-WRF backward simulation from the sampling site PORT located west (Twelve storey Parking building near commercial Port of Thessaloniki) initiation time 12:00 UTC.

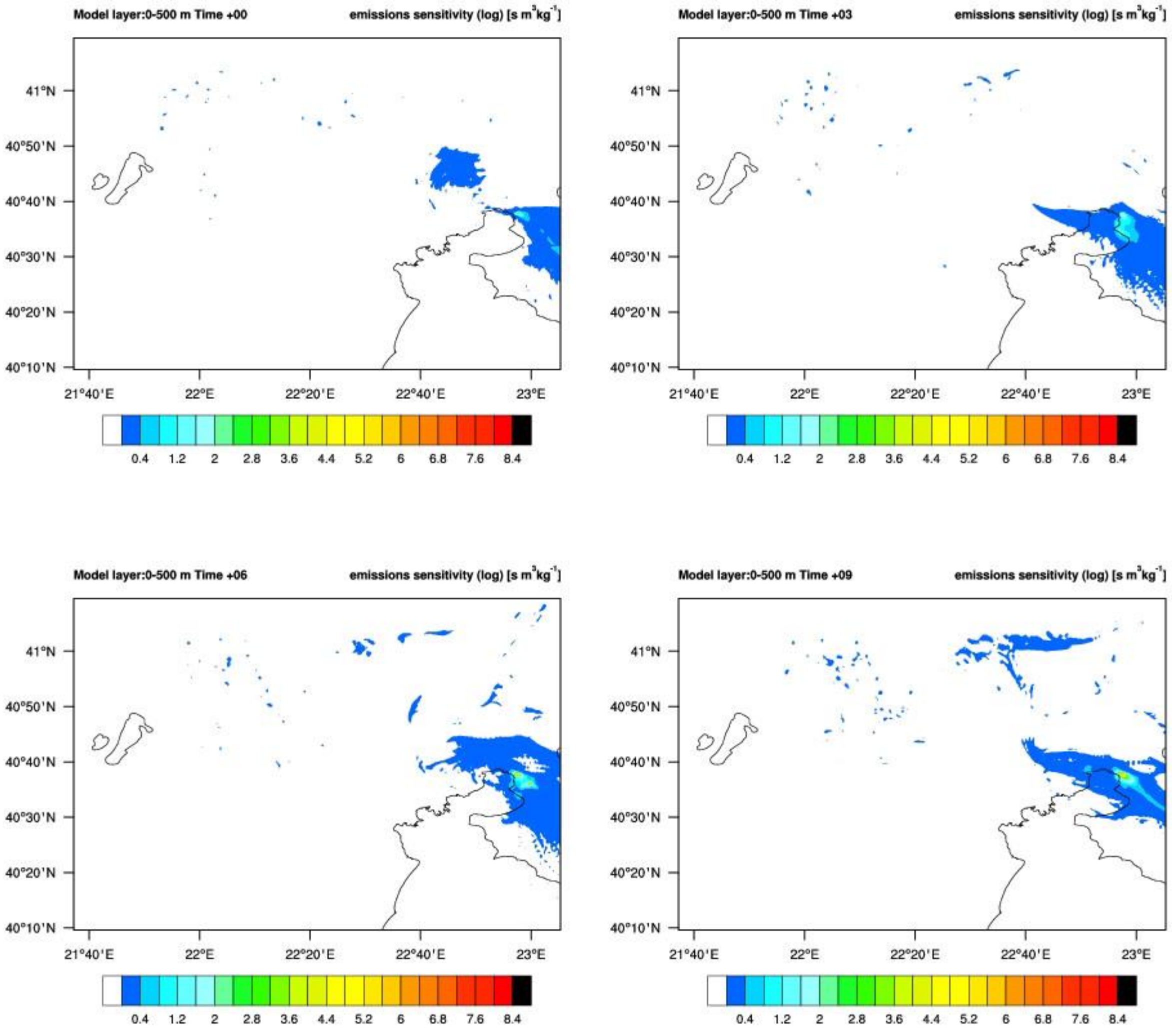

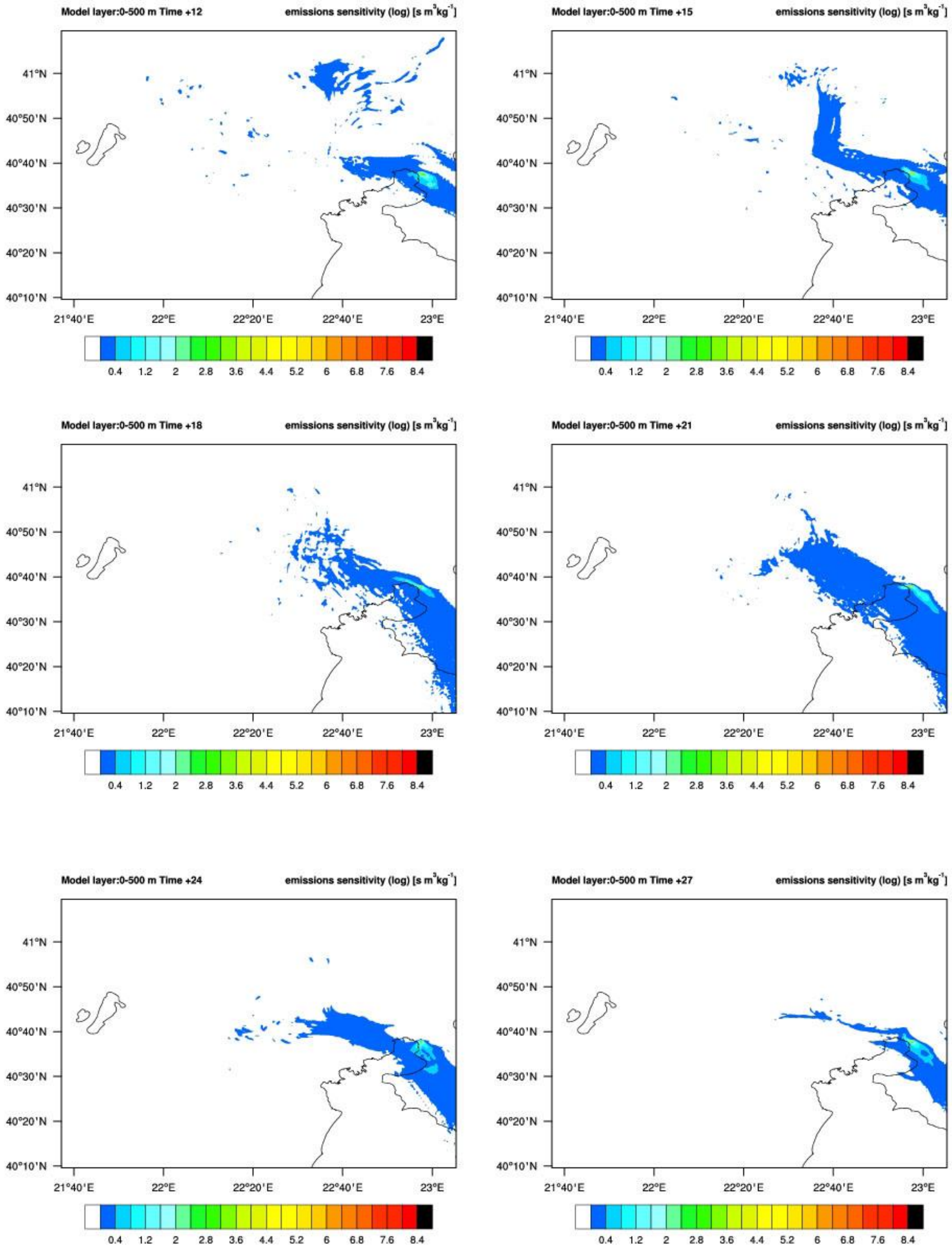
Model layer:0-500 m Time +12
emissions sensitivity (log) [s m^{3}kg^{-1}]
Model layer:0-500 m Time +15
emissions sensitivity (log) [s m^{3}kg^{-1}]
Model layer:0-500 m Time +18
emissions sensitivity (log) [s m^{3}kg^{-1}]
Model layer:0-500 m Time +21
emissions sensitivity (log) [s m^{3}kg^{-1}]
Model layer:0-500 m Time +24
emissions sensitivity (log) [s m^{3}kg^{-1}]
Model layer:0-500 m Time +27
emissions sensitivity (log) [s m^{3}kg^{-1}]
41°N
40°50'N
40°40'N
40°30'N
40°20'N
40°10'N
21°40'E
22°E
22°20'E
22°40'E
23°E
0.4
1.2
2
2.8
3.6
4.4
5.2
6
6.8
7.6
8.4

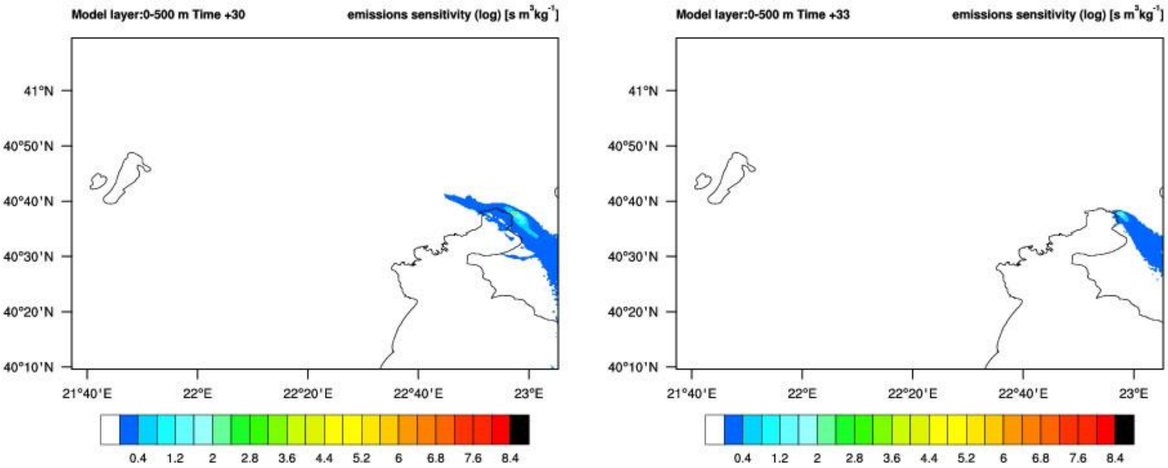

Figure 6.13. 13 to 15 visualization of 3h output time-step based on Flexpart-WRF backward simulation from the sampling site AUTH located in city center (Aristotle University of Thessaloniki) initiation time 12:00 UTC.

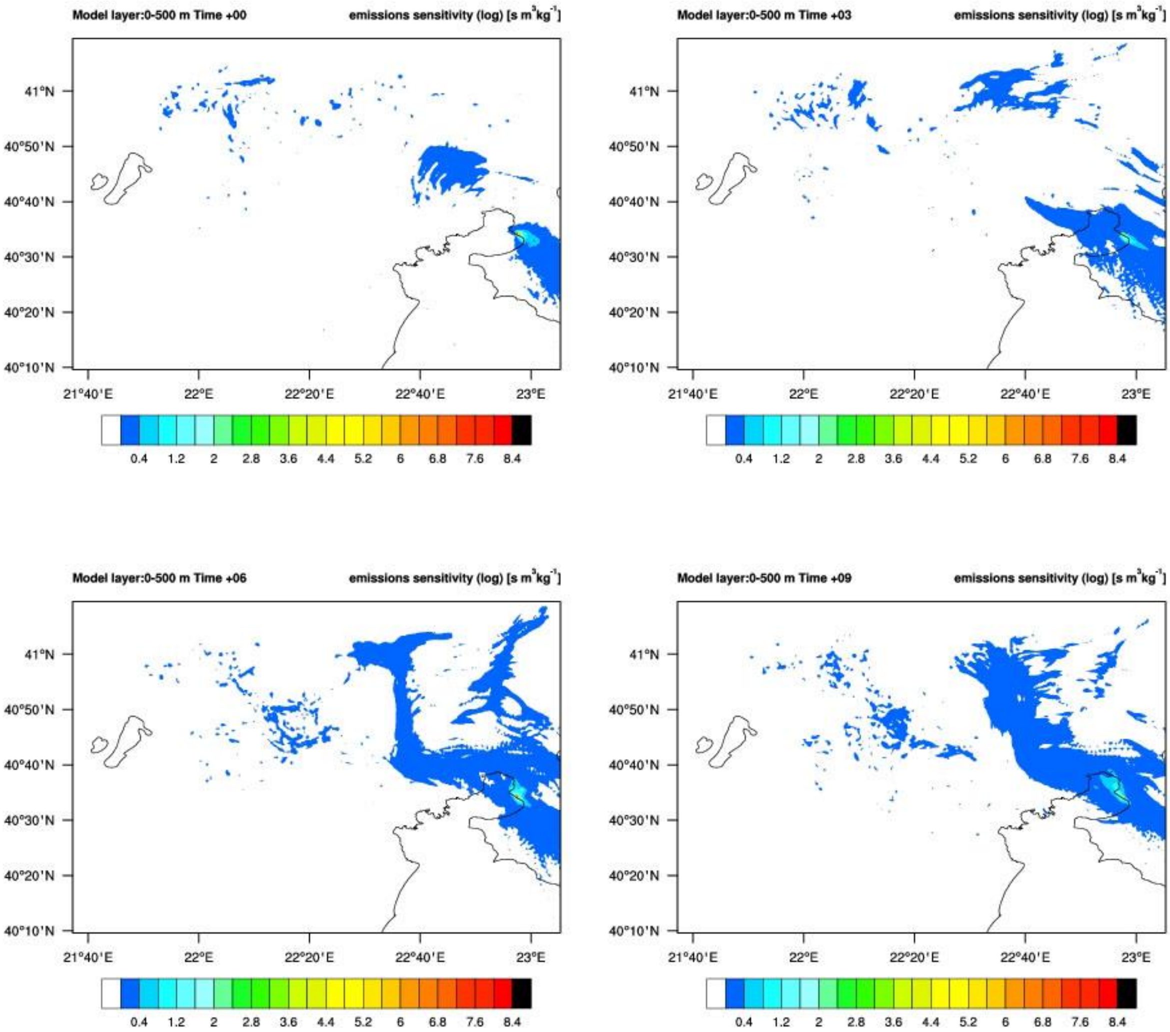

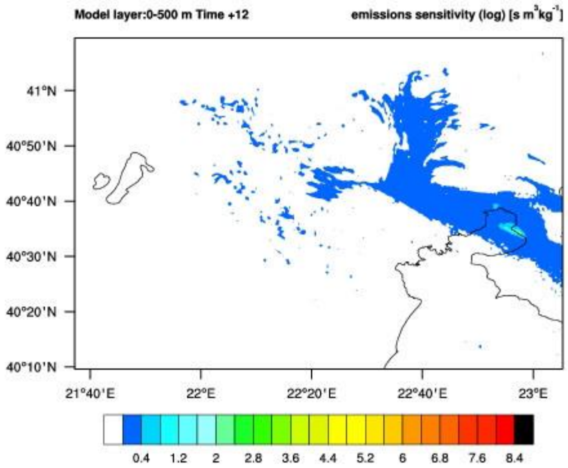
Model layer:0-500 m Time +12
emissions sensitivity (log) [s m³kg⁻¹]
41°N
40°50'N
40°40'N
40°30'N
40°20'N
40°10'N
21°40'E
22°E
22°20'E
22°40'E
23°E
0.4 1.2 2 2.8 3.6 4.4 5.2 6 6.8 7.6 8.4

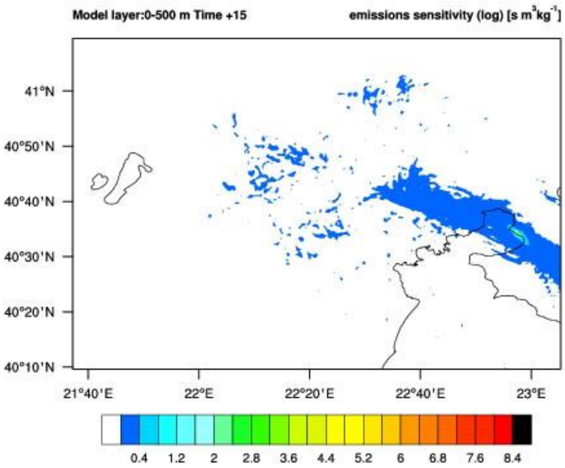
Model layer:0-500 m Time +15
emissions sensitivity (log) [s m³kg⁻¹]
41°N
40°50'N
40°40'N
40°30'N
40°20'N
40°10'N
21°40'E
22°E
22°20'E
22°40'E
23°E
0.4 1.2 2 2.8 3.6 4.4 5.2 6 6.8 7.6 8.4

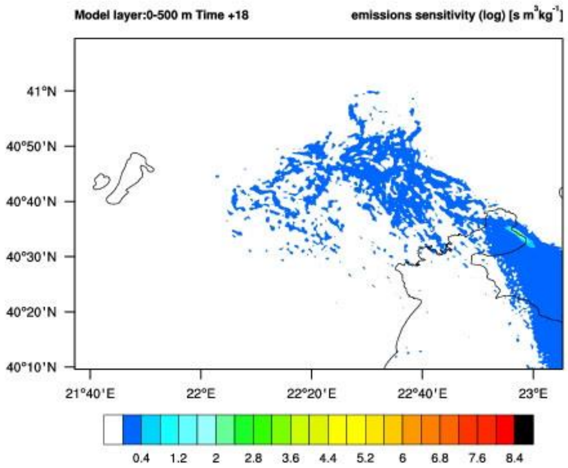
Model layer:0-500 m Time +18
emissions sensitivity (log) [s m³kg⁻¹]
41°N
40°50'N
40°40'N
40°30'N
40°20'N
40°10'N
21°40'E
22°E
22°20'E
22°40'E
23°E
0.4 1.2 2 2.8 3.6 4.4 5.2 6 6.8 7.6 8.4

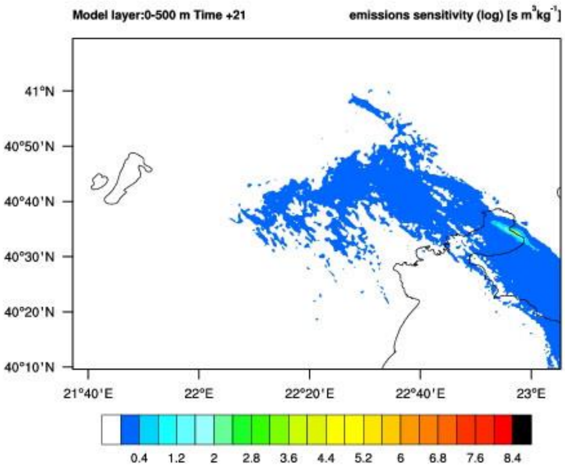
Model layer:0-500 m Time +21
emissions sensitivity (log) [s m³kg⁻¹]
41°N
40°50'N
40°40'N
40°30'N
40°20'N
40°10'N
21°40'E
22°E
22°20'E
22°40'E
23°E
0.4 1.2 2 2.8 3.6 4.4 5.2 6 6.8 7.6 8.4

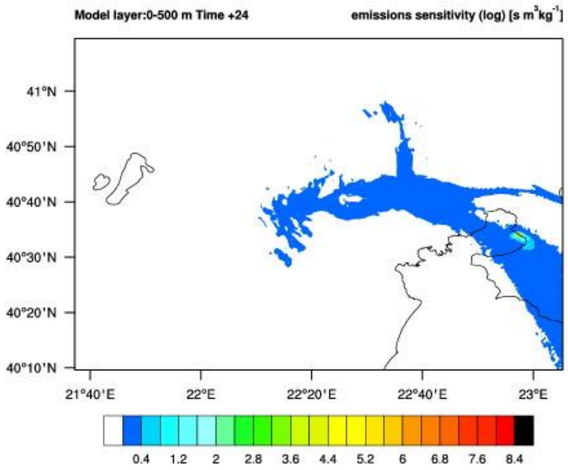
Model layer:0-500 m Time +24
emissions sensitivity (log) [s m³kg⁻¹]
41°N
40°50'N
40°40'N
40°30'N
40°20'N
40°10'N
21°40'E
22°E
22°20'E
22°40'E
23°E
0.4 1.2 2 2.8 3.6 4.4 5.2 6 6.8 7.6 8.4

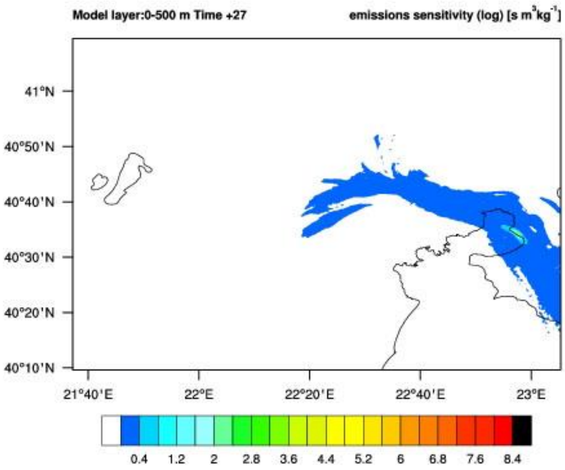
Model layer:0-500 m Time +27
emissions sensitivity (log) [s m³kg⁻¹]
41°N
40°50'N
40°40'N
40°30'N
40°20'N
40°10'N
21°40'E
22°E
22°20'E
22°40'E
23°E
0.4 1.2 2 2.8 3.6 4.4 5.2 6 6.8 7.6 8.4

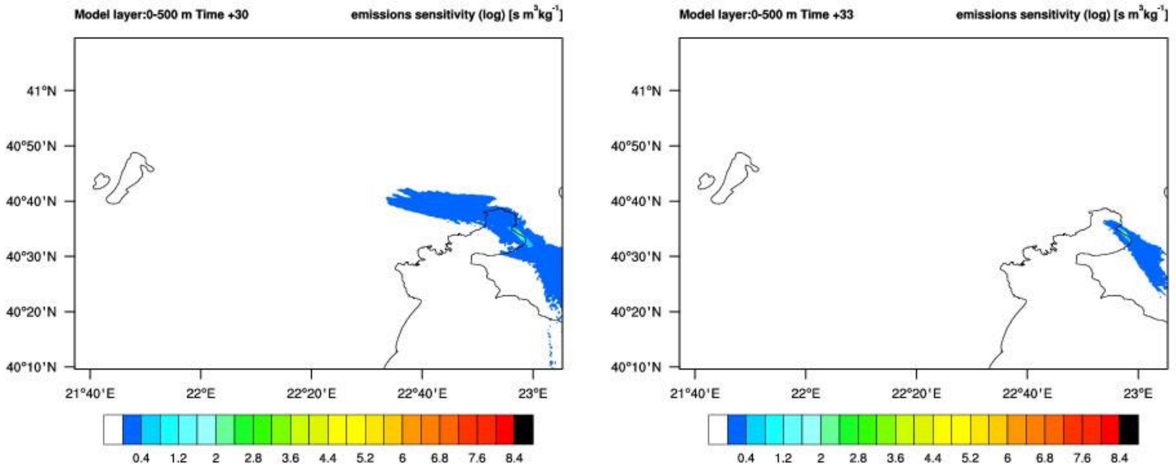

Figure 6.14. 13 to 15 January visualization of 3h output time-step based on Flexpart-WRF backward simulation from the sampling site KALAMARIA located South-East (Multi-storey building in Kalamaria region) initiation time 12:00 UTC.

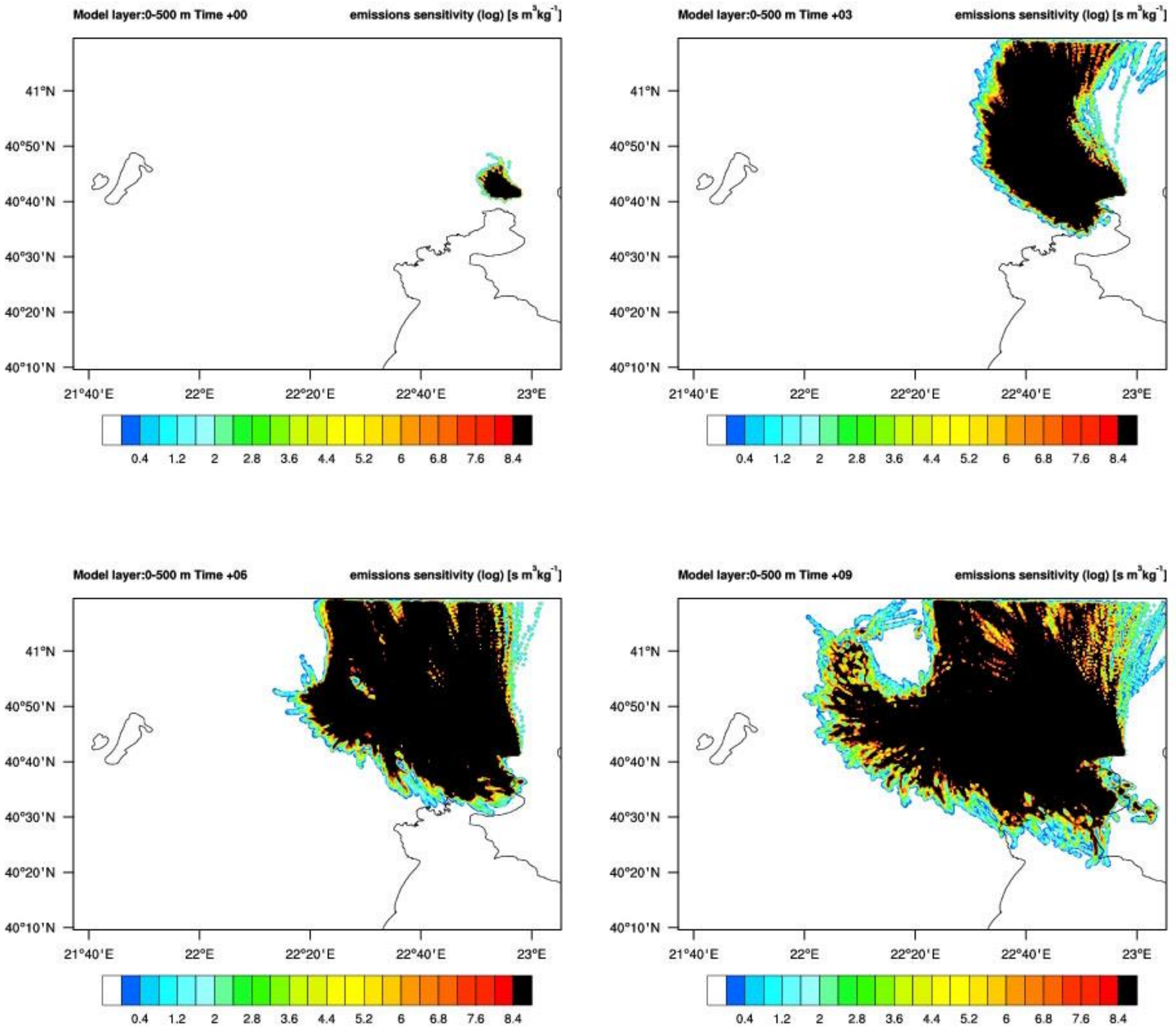

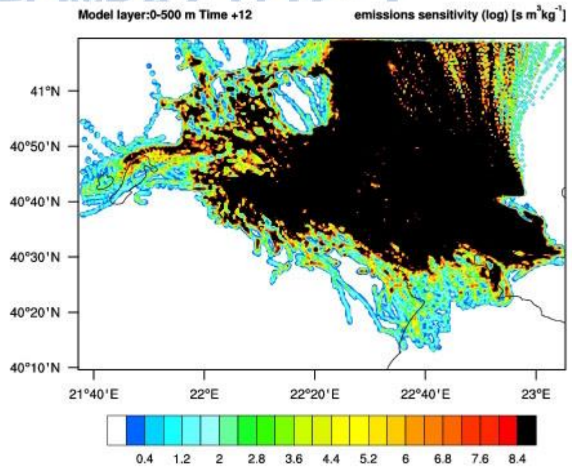
Model layer:0-500 m Time +12
emissions sensitivity (log) [s m^{3}kg^{-1}]
41°N
40°50'N
40°40'N
40°30'N
40°20'N
40°10'N
21°40'E
22°E
22°20'E
22°40'E
23°E
0.4 1.2 2 2.8 3.6 4.4 5.2 6 6.8 7.6 8.4

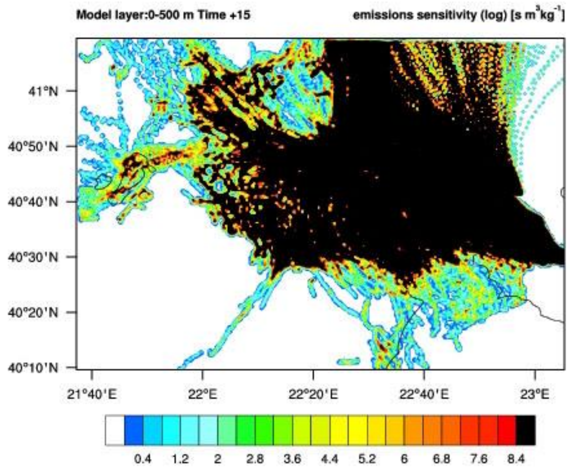
Model layer:0-500 m Time +15
emissions sensitivity (log) [s m^{3}kg^{-1}]
41°N
40°50'N
40°40'N
40°30'N
40°20'N
40°10'N
21°40'E
22°E
22°20'E
22°40'E
23°E
0.4 1.2 2 2.8 3.6 4.4 5.2 6 6.8 7.6 8.4

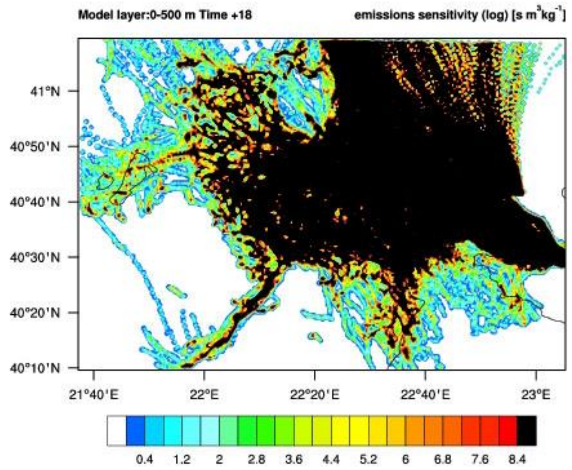
Model layer:0-500 m Time +18
emissions sensitivity (log) [s m^{3}kg^{-1}]
41°N
40°50'N
40°40'N
40°30'N
40°20'N
40°10'N
21°40'E
22°E
22°20'E
22°40'E
23°E
0.4 1.2 2 2.8 3.6 4.4 5.2 6 6.8 7.6 8.4

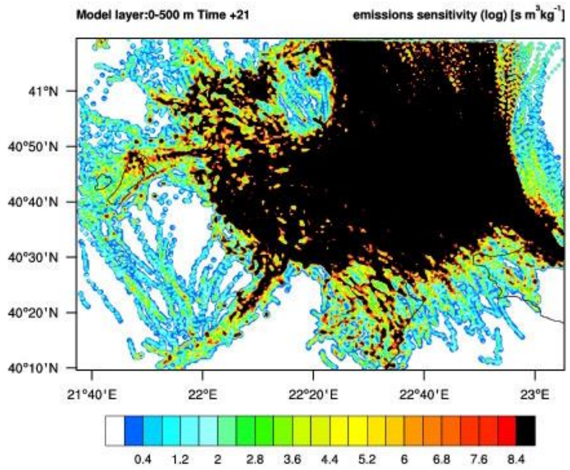
Model layer:0-500 m Time +21
emissions sensitivity (log) [s m^{3}kg^{-1}]
41°N
40°50'N
40°40'N
40°30'N
40°20'N
40°10'N
21°40'E
22°E
22°20'E
22°40'E
23°E
0.4 1.2 2 2.8 3.6 4.4 5.2 6 6.8 7.6 8.4

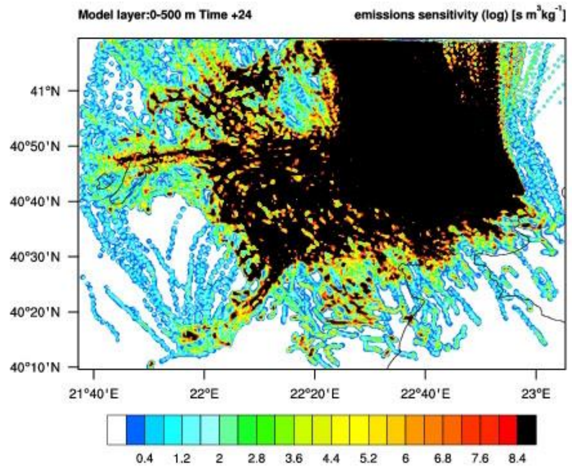
Model layer:0-500 m Time +24
emissions sensitivity (log) [s m^{3}kg^{-1}]
41°N
40°50'N
40°40'N
40°30'N
40°20'N
40°10'N
21°40'E
22°E
22°20'E
22°40'E
23°E
0.4 1.2 2 2.8 3.6 4.4 5.2 6 6.8 7.6 8.4

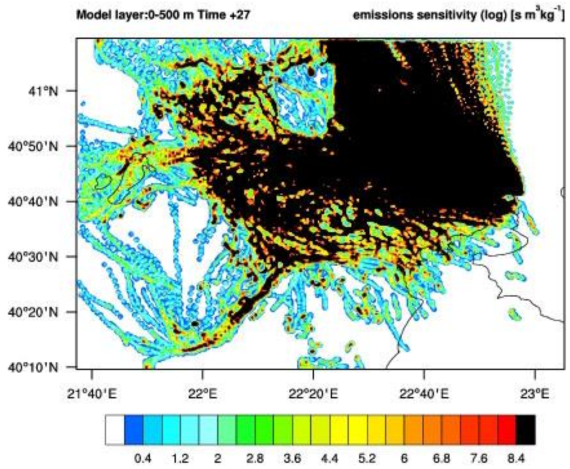
Model layer:0-500 m Time +27
emissions sensitivity (log) [s m^{3}kg^{-1}]
41°N
40°50'N
40°40'N
40°30'N
40°20'N
40°10'N
21°40'E
22°E
22°20'E
22°40'E
23°E
0.4 1.2 2 2.8 3.6 4.4 5.2 6 6.8 7.6 8.4

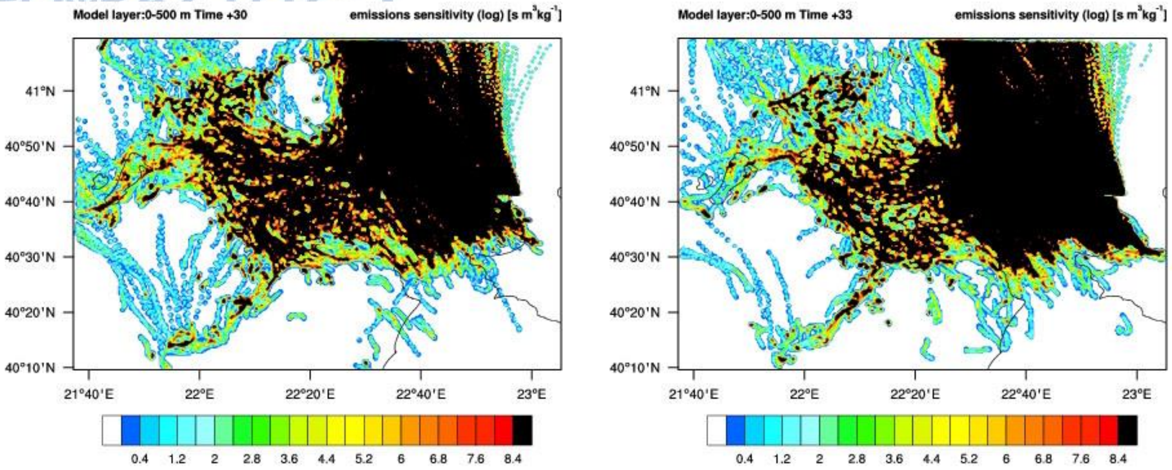

Figure 6.15. 13 to 15 January visualization of 3h output time-step based on Flexpart-WRF forward simulation from emitting site located North in city suburbs initiation time 12:00 UTC.

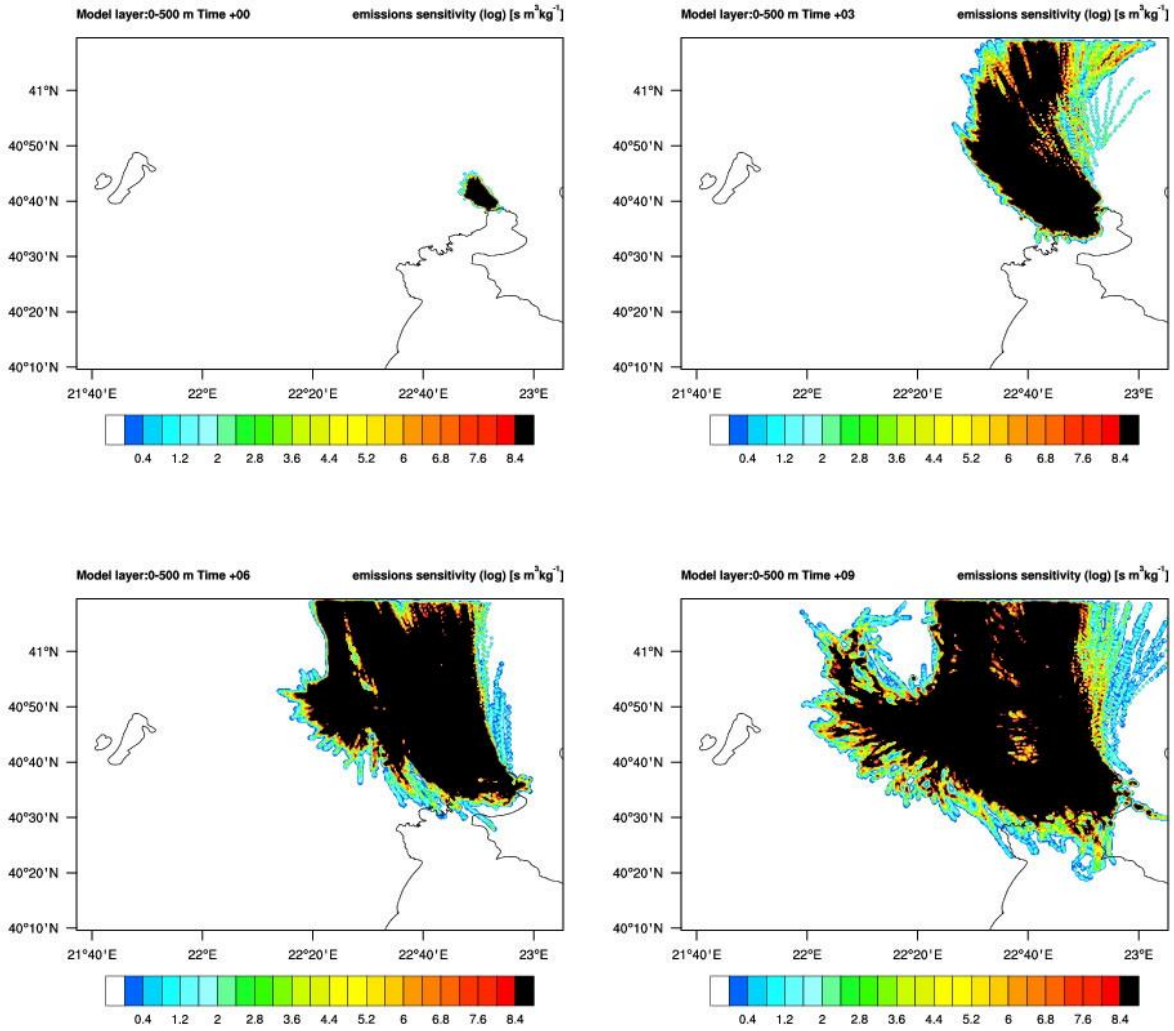

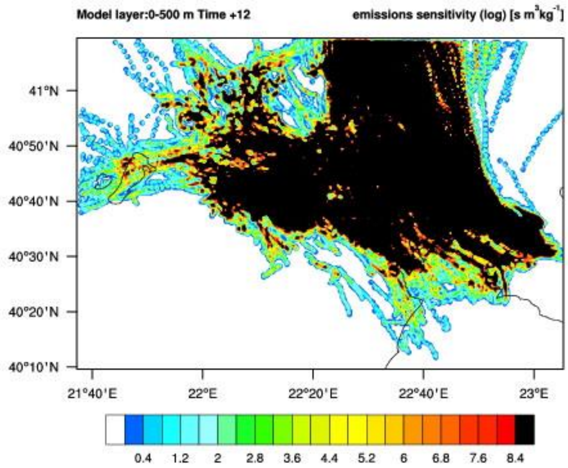
Model layer:0-500 m Time +12
emissions sensitivity (log) [s m^{3}kg^{-1}]
41°N
40°50'N
40°40'N
40°30'N
40°20'N
40°10'N
21°40'E
22°E
22°20'E
22°40'E
23°E
0.4
1.2
2
2.8
3.6
4.4
5.2
6
6.8
7.6
8.4

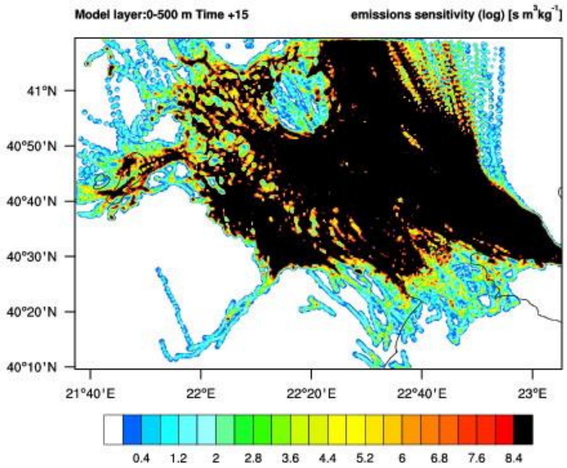
Model layer:0-500 m Time +15
emissions sensitivity (log) [s m^{3}kg^{-1}]
41°N
40°50'N
40°40'N
40°30'N
40°20'N
40°10'N
21°40'E
22°E
22°20'E
22°40'E
23°E
0.4
1.2
2
2.8
3.6
4.4
5.2
6
6.8
7.6
8.4

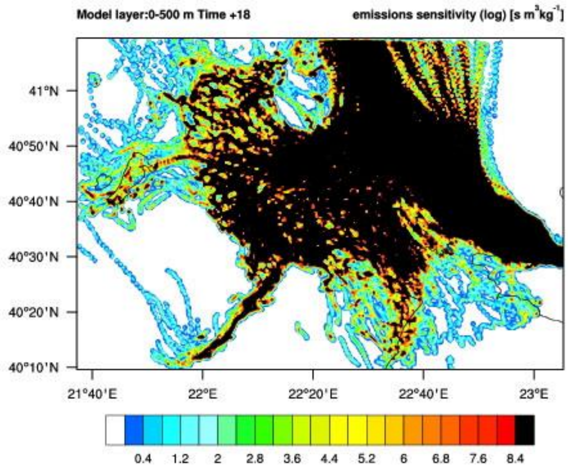
Model layer:0-500 m Time +18
emissions sensitivity (log) [s m^{3}kg^{-1}]
41°N
40°50'N
40°40'N
40°30'N
40°20'N
40°10'N
21°40'E
22°E
22°20'E
22°40'E
23°E
0.4
1.2
2
2.8
3.6
4.4
5.2
6
6.8
7.6
8.4

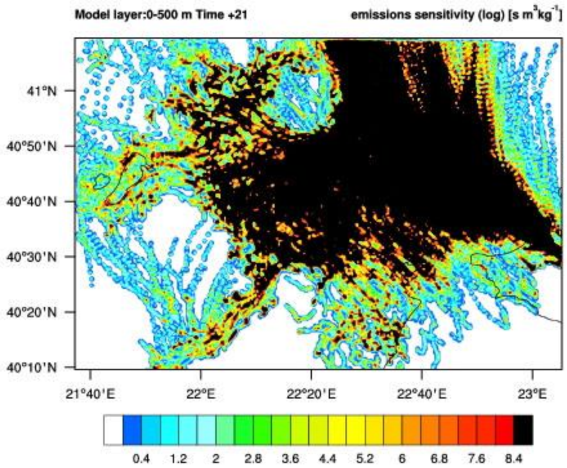
Model layer:0-500 m Time +21
emissions sensitivity (log) [s m^{3}kg^{-1}]
41°N
40°50'N
40°40'N
40°30'N
40°20'N
40°10'N
21°40'E
22°E
22°20'E
22°40'E
23°E
0.4
1.2
2
2.8
3.6
4.4
5.2
6
6.8
7.6
8.4

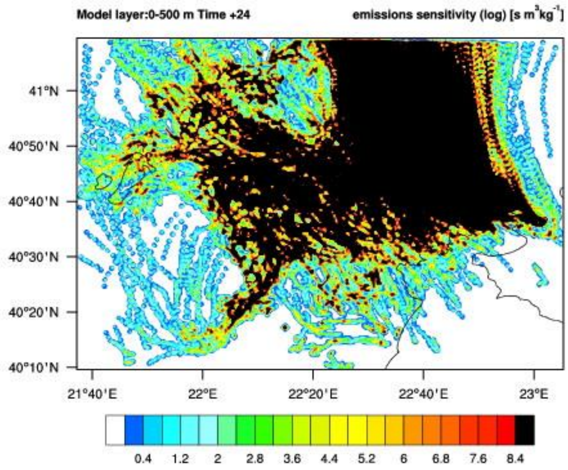
Model layer:0-500 m Time +24
emissions sensitivity (log) [s m^{3}kg^{-1}]
41°N
40°50'N
40°40'N
40°30'N
40°20'N
40°10'N
21°40'E
22°E
22°20'E
22°40'E
23°E
0.4
1.2
2
2.8
3.6
4.4
5.2
6
6.8
7.6
8.4

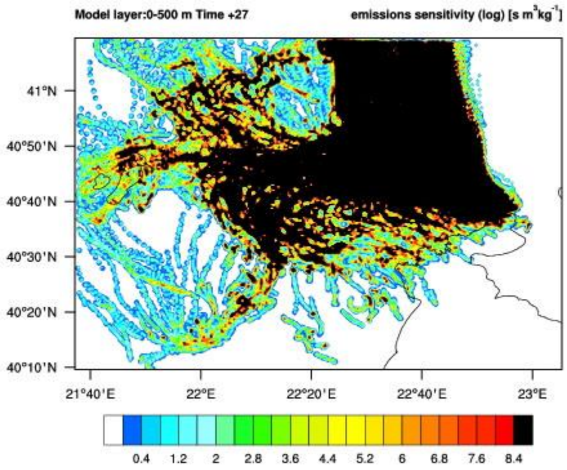
Model layer:0-500 m Time +27
emissions sensitivity (log) [s m^{3}kg^{-1}]
41°N
40°50'N
40°40'N
40°30'N
40°20'N
40°10'N
21°40'E
22°E
22°20'E
22°40'E
23°E
0.4
1.2
2
2.8
3.6
4.4
5.2
6
6.8
7.6
8.4

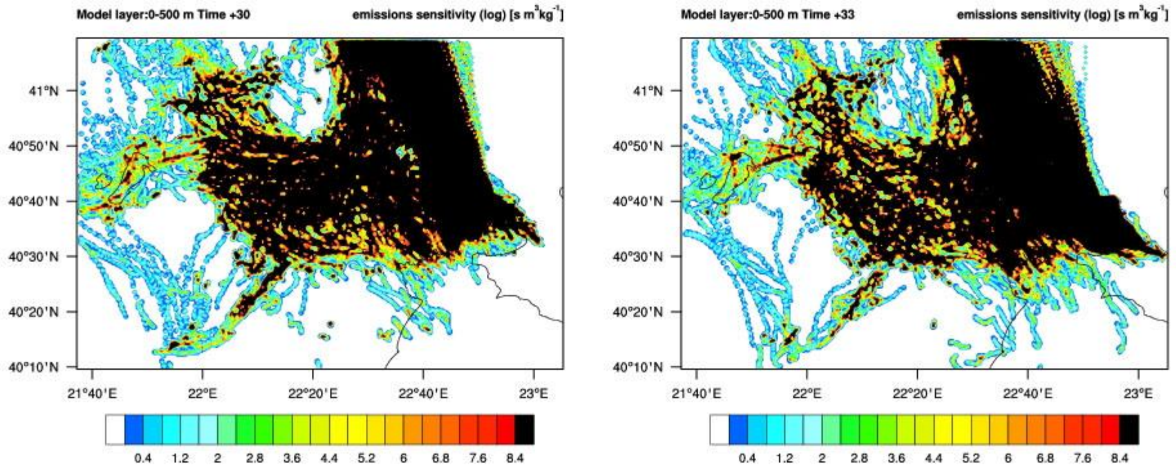

Figure 6.16. 13 to 15 January visualization of 3h output time-step based on Flexpart-WRF forward simulation from emitting site located West in the industrial area of the city initiation time 12:00 UTC.

6.6. Synoptic conditions sampling date 1st February 2013

For samples from 1st February 2013 and more specifically one day earlier from our day of interest in 31st January the average wind speed was 11.9 km/h with maximum wind speed of 64.4 km/h (16:20 pm) and wind directions NW.

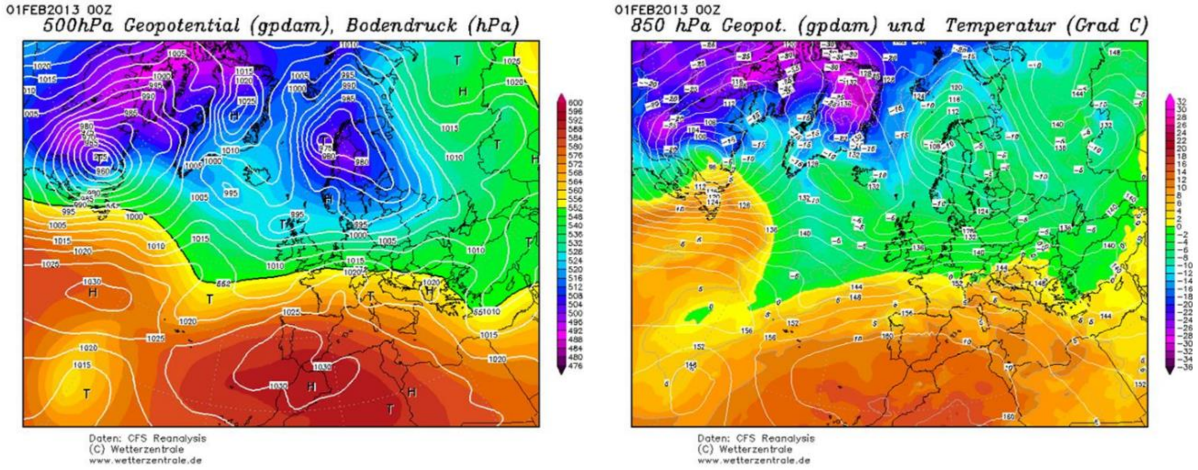

Figure 6.17. The synoptic conditions of the 14th January 2013, as they are depicted through the weather charts of 500 hPa (highlighting the geopotential heights and the surface isobars) and 850 hPa (highlighting the geopotential heights and the temperature gradients).

The synoptic conditions of the 1st February 2013 are indicated in Figure 6.17, where the weather charts at the 500 hPa (highlighting the geopotential heights and the surface isobars) and 850 hPa (highlighting the geopotential heights and the temperature gradients) are depicted. According to the classification method proposed by Karacostas (2003) and Karacostas et al. (2018), this is mostly a Zonal flow (ZON), coupled with some local characteristics of north-west orientation (NW), particularly over the examined area. This synoptic type is characterized by the weak pressure gradient much west of the area of interest, resulting to light and variable westerly winds. However, over the area of interest north-westerly winds are prevailing. At the surface, a very extensive anticyclone is dominating the central and western Mediterranean. Similar atmospheric conditions are indicated at the 850 hPa chart.

6.6.1 Flexpart-WRF visualization analysis run 31st January to 1st February 2013

For 1st February 2013 where our samples were analyzed and according to the aforementioned synoptic conditions, the prevailing wind conditions showed daily wind speed average of 1.7 km/h and with maximum wind speed of 25.7 km/h (02:30 am) with wind direction WSW dominating the dispersion phenomenon from the industrial area (Figs 6.18-6.20) even though initially, at the first time-steps the plume for our backward simulations appears at the opposite direction it then swifts and circles the area from time-step +06 to +15 and intensifies towards our sampling sites as seen in time-step +21 and onwards. Regarding northern and western emitting areas of our forward simulations there seems to be a more direct and intense emitting source affecting our sampling areas as seen from time-step +06 to +12 affecting initially the western and center locations and the eastern sampling location sites (Figs 6.21-6.22) and then spreading further affecting a wider area of Thessaloniki region as seen in time-step +15 and onwards.

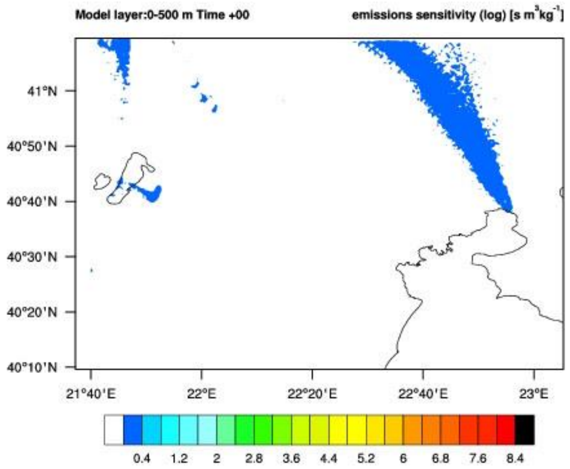

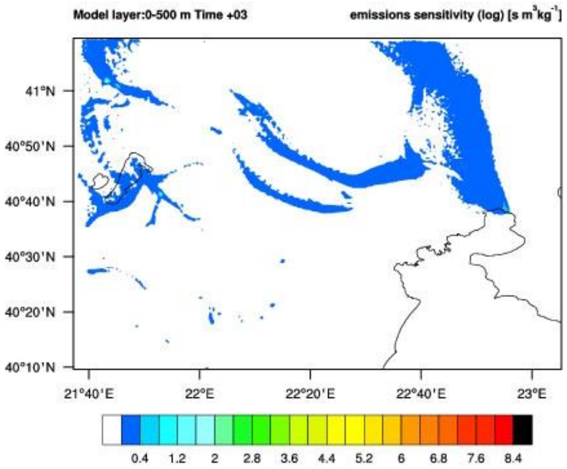

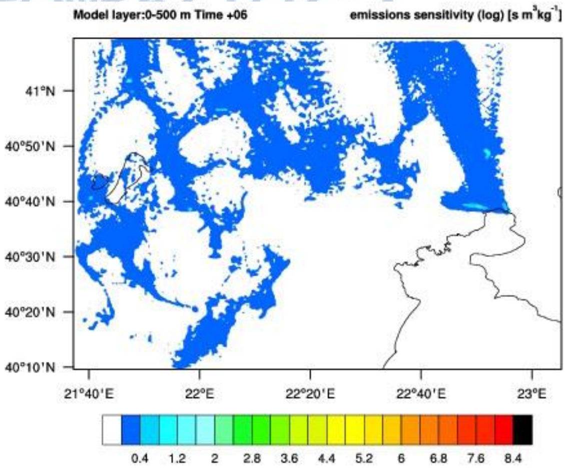
Model layer:0-500 m Time +06
emissions sensitivity (log) [$s\ m^3kg^{-1}$]
41°N
40°50'N
40°40'N
40°30'N
40°20'N
40°10'N
21°40'E
22°E
22°20'E
22°40'E
23°E
0.4 1.2 2 2.8 3.6 4.4 5.2 6 6.8 7.6 8.4

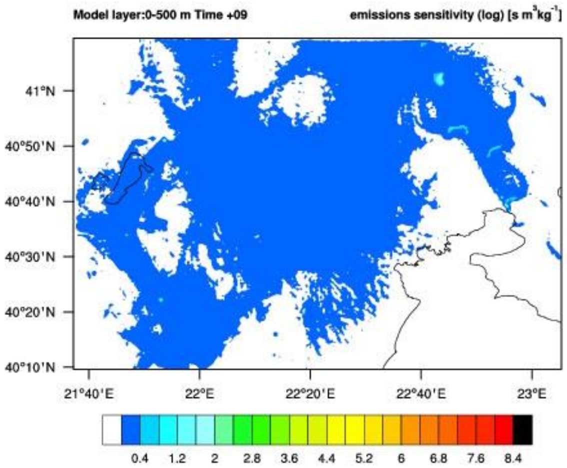
Model layer:0-500 m Time +09
emissions sensitivity (log) [$s\ m^3kg^{-1}$]
41°N
40°50'N
40°40'N
40°30'N
40°20'N
40°10'N
21°40'E
22°E
22°20'E
22°40'E
23°E
0.4 1.2 2 2.8 3.6 4.4 5.2 6 6.8 7.6 8.4

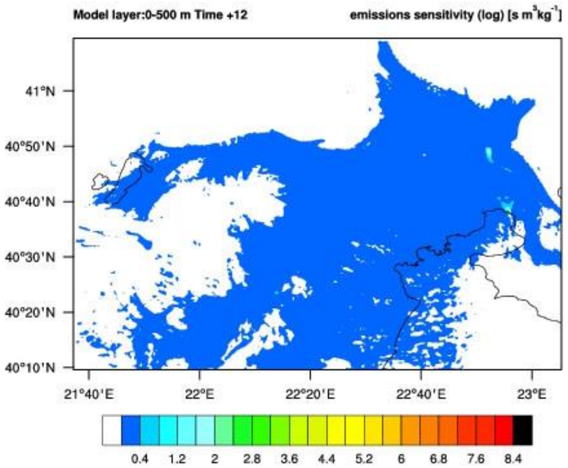
Model layer:0-500 m Time +12
emissions sensitivity (log) [$s\ m^3kg^{-1}$]
41°N
40°50'N
40°40'N
40°30'N
40°20'N
40°10'N
21°40'E
22°E
22°20'E
22°40'E
23°E
0.4 1.2 2 2.8 3.6 4.4 5.2 6 6.8 7.6 8.4

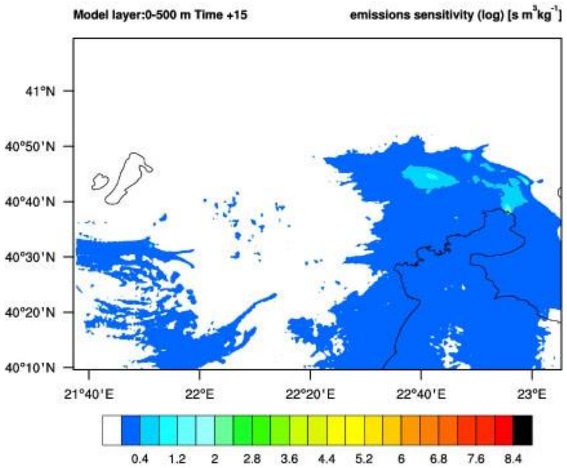
Model layer:0-500 m Time +15
emissions sensitivity (log) [$s\ m^3kg^{-1}$]
41°N
40°50'N
40°40'N
40°30'N
40°20'N
40°10'N
21°40'E
22°E
22°20'E
22°40'E
23°E
0.4 1.2 2 2.8 3.6 4.4 5.2 6 6.8 7.6 8.4

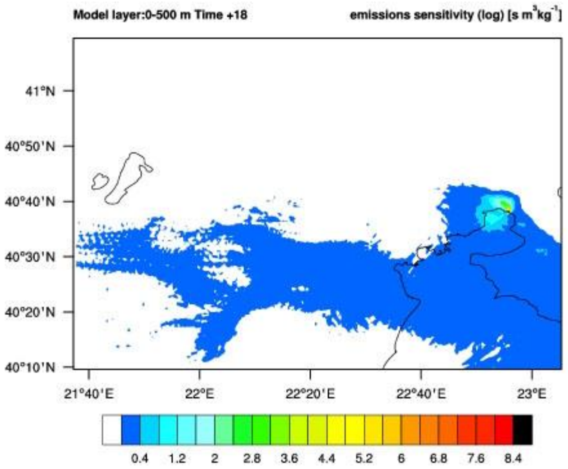
Model layer:0-500 m Time +18
emissions sensitivity (log) [$s\ m^3kg^{-1}$]
41°N
40°50'N
40°40'N
40°30'N
40°20'N
40°10'N
21°40'E
22°E
22°20'E
22°40'E
23°E
0.4 1.2 2 2.8 3.6 4.4 5.2 6 6.8 7.6 8.4

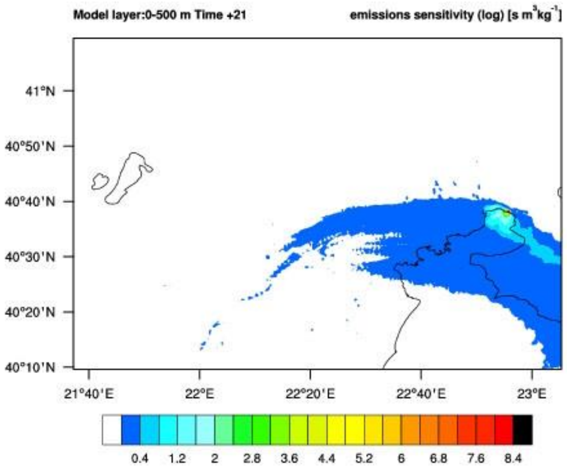
Model layer:0-500 m Time +21
emissions sensitivity (log) [$s\ m^3kg^{-1}$]
41°N
40°50'N
40°40'N
40°30'N
40°20'N
40°10'N
21°40'E
22°E
22°20'E
22°40'E
23°E
0.4 1.2 2 2.8 3.6 4.4 5.2 6 6.8 7.6 8.4

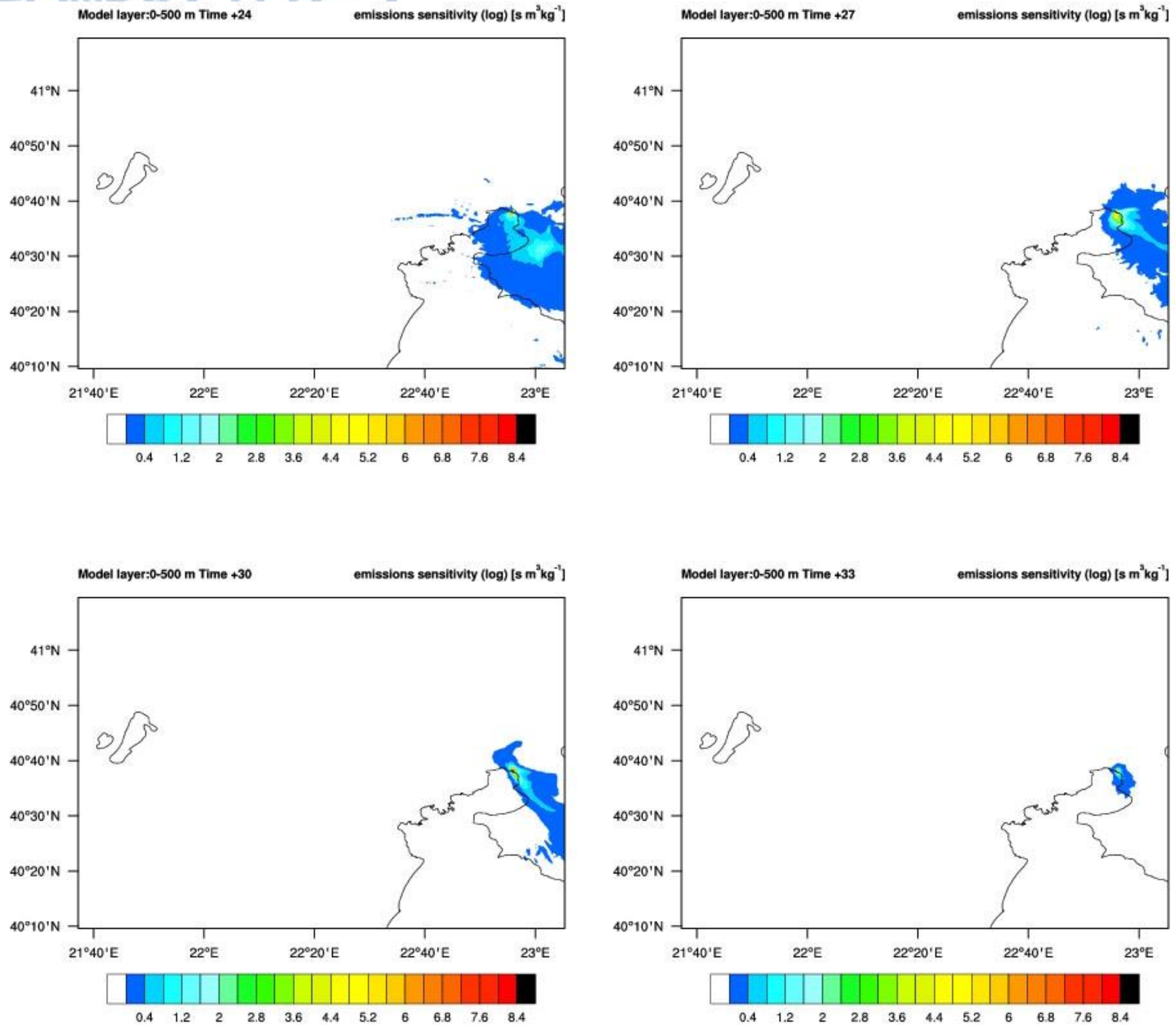

Figure 6.18. 31 January to 2 February visualization of 3h output time-step based on Flexpart-WRF backward simulation from the sampling site PORT located west (Twelve storey Parking building near commercial Port of Thessaloniki) initiation time 12:00 UTC.

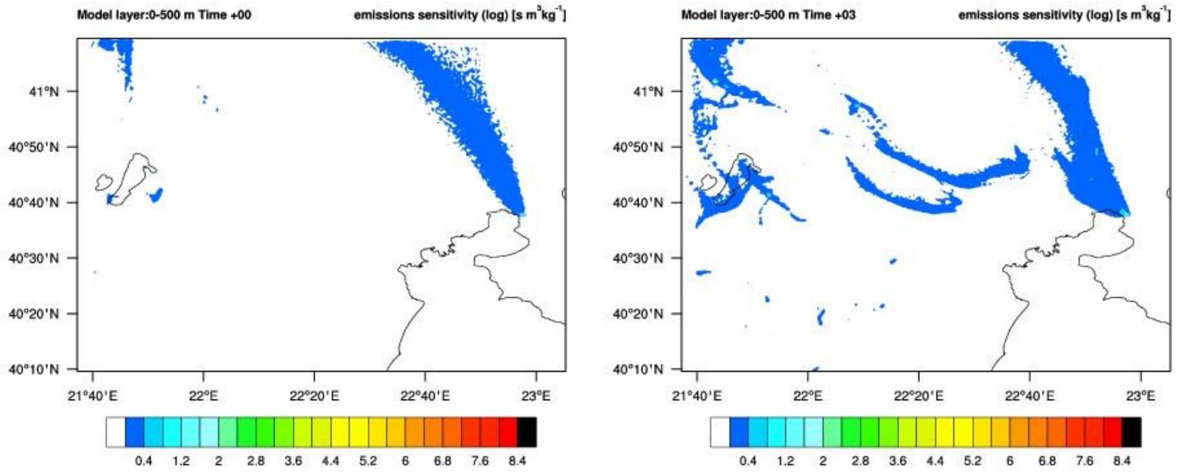

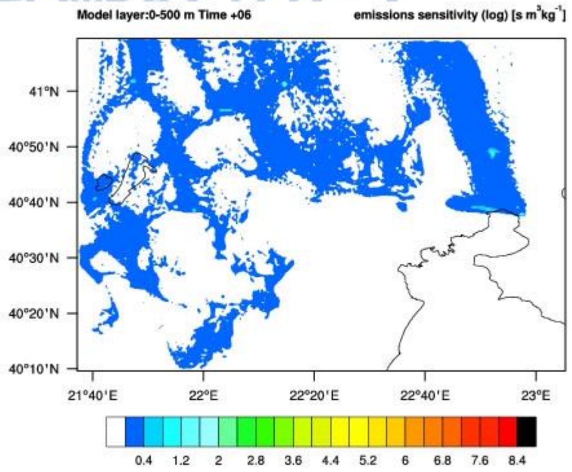

Model layer:0-500 m Time +06 emissions sensitivity (log) [s m^{3}kg^{-1}]

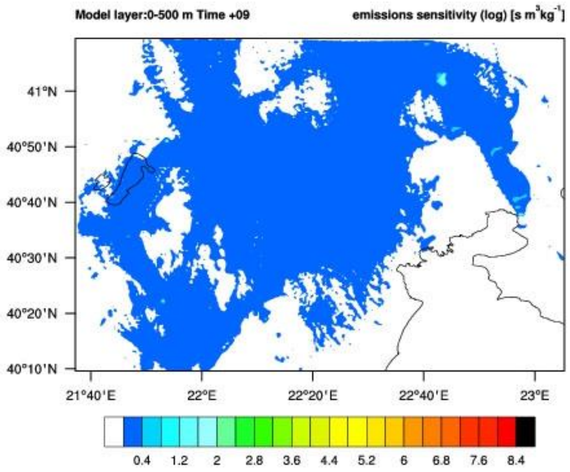

Model layer:0-500 m Time +09 emissions sensitivity (log) [s m^{3}kg^{-1}]

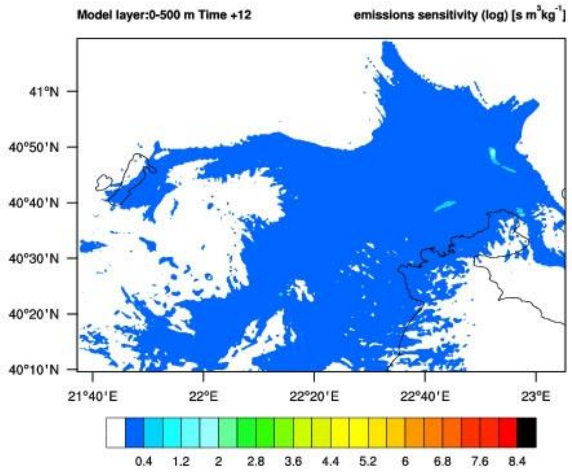

Model layer:0-500 m Time +12 emissions sensitivity (log) [s m^{3}kg^{-1}]

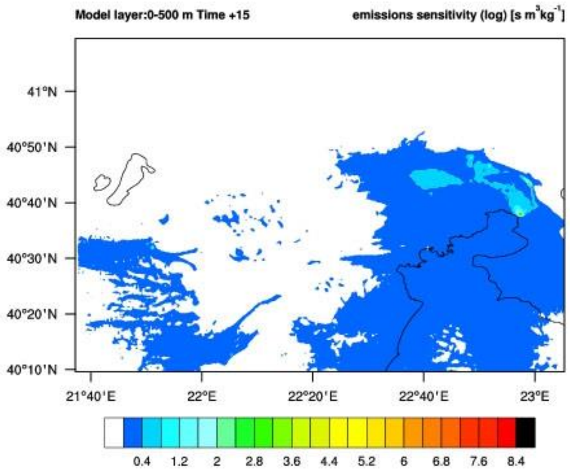

Model layer:0-500 m Time +15 emissions sensitivity (log) [s m^{3}kg^{-1}]

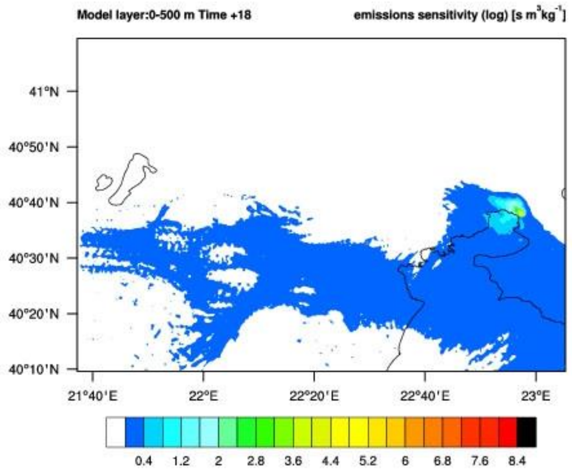

Model layer:0-500 m Time +18 emissions sensitivity (log) [s m^{3}kg^{-1}]

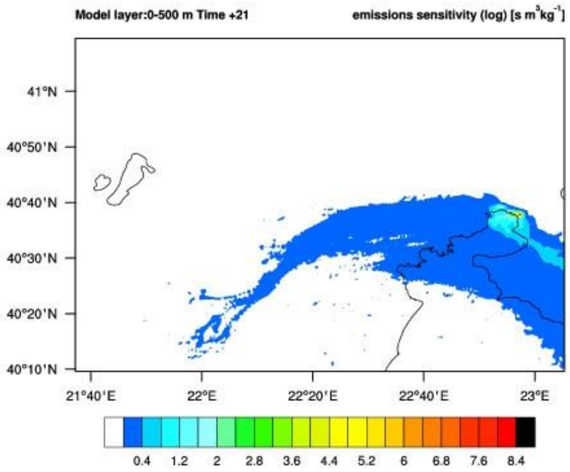

Model layer:0-500 m Time +21 emissions sensitivity (log) [s m^{3}kg^{-1}]

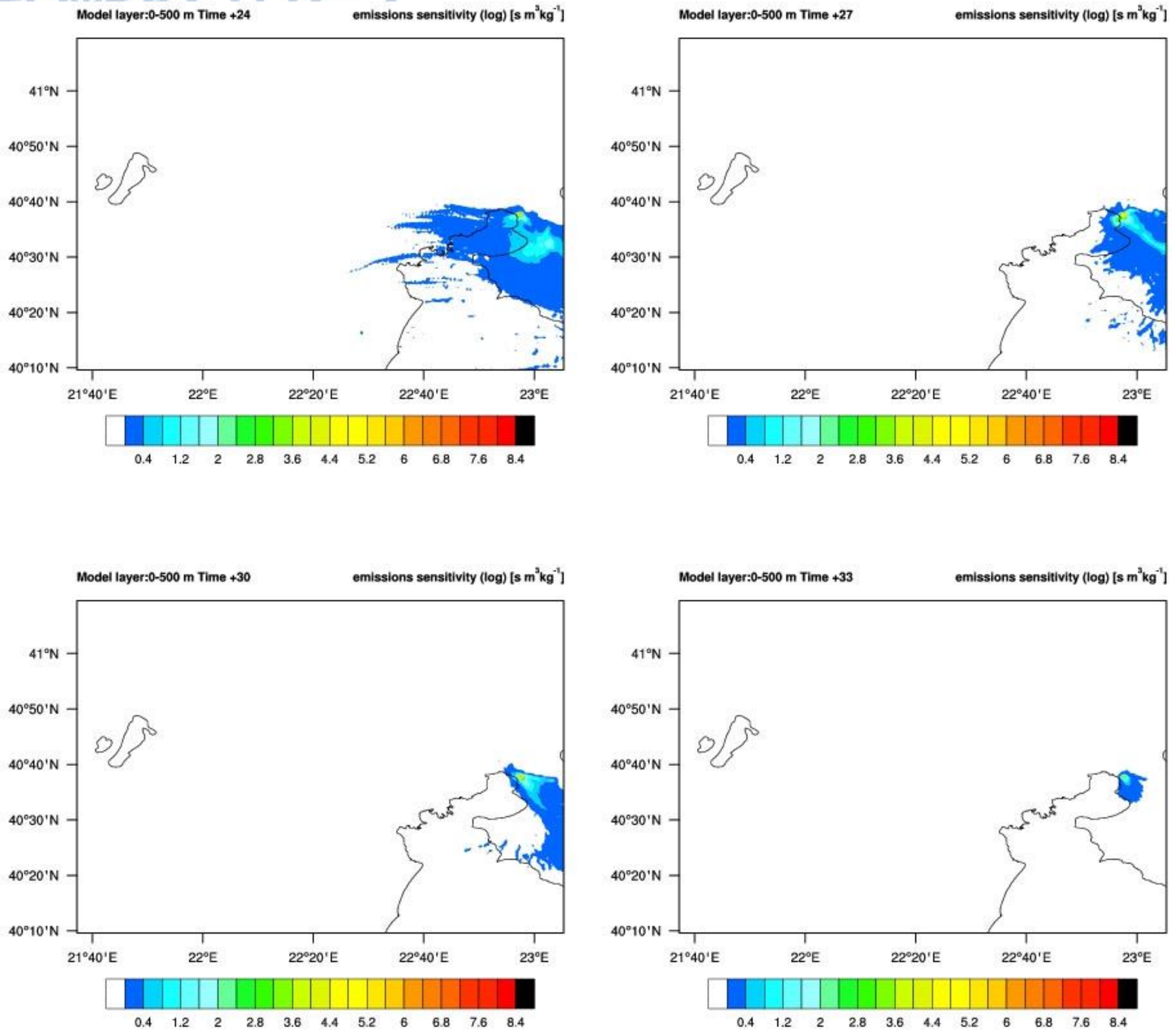

Figure 6.19. 31 January to 2 February visualization of 3h output time-step based on Flexpart-WRF backward simulation from the sampling site AUTH located in city center (Aristotle University of Thessaloniki) initiation time 12:00 UTC.

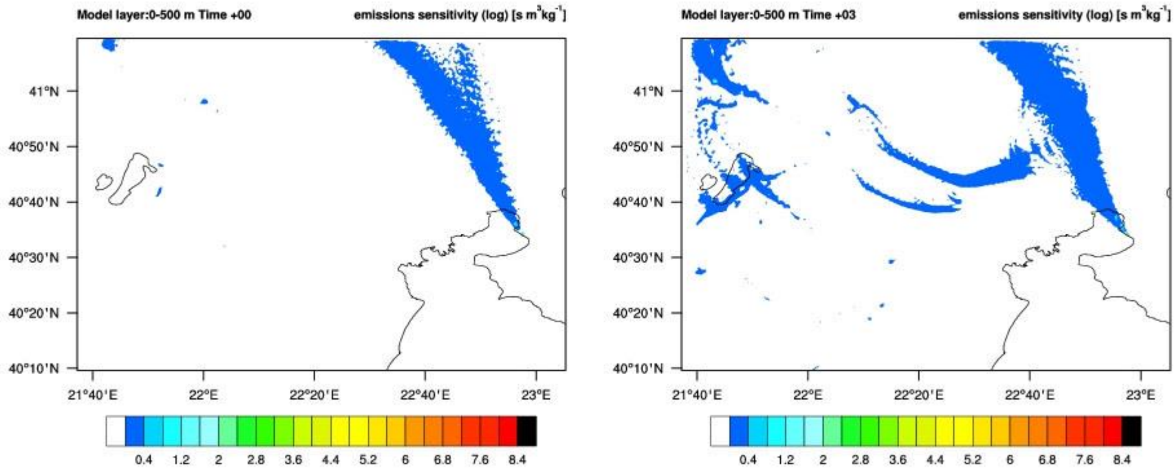

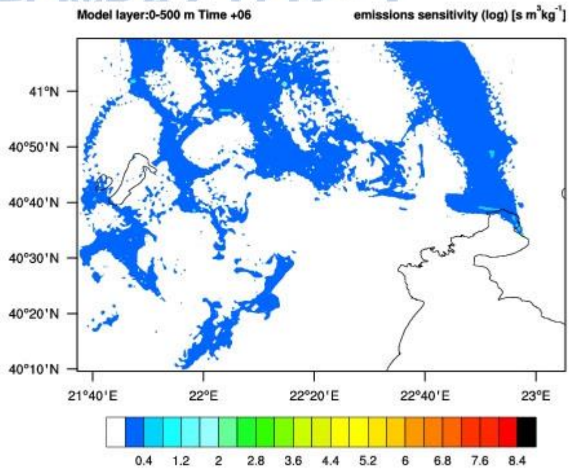
Model layer:0-500 m Time +06
emissions sensitivity (log) [s m^{3}kg^{-1}]
41°N
40°50'N
40°40'N
40°30'N
40°20'N
40°10'N
21°40'E
22°E
22°20'E
22°40'E
23°E
0.4 1.2 2 2.8 3.6 4.4 5.2 6 6.8 7.6 8.4

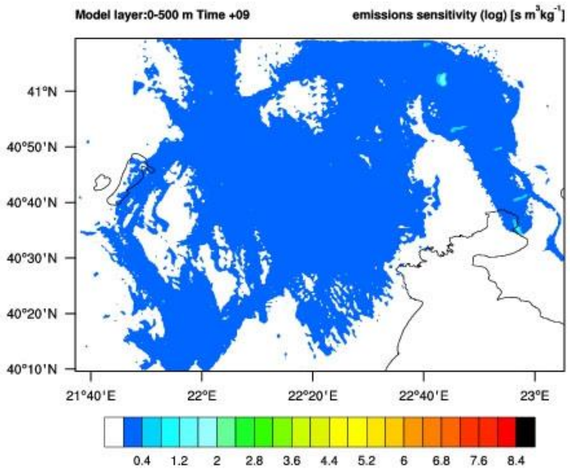
Model layer:0-500 m Time +09
emissions sensitivity (log) [s m^{3}kg^{-1}]
41°N
40°50'N
40°40'N
40°30'N
40°20'N
40°10'N
21°40'E
22°E
22°20'E
22°40'E
23°E
0.4 1.2 2 2.8 3.6 4.4 5.2 6 6.8 7.6 8.4

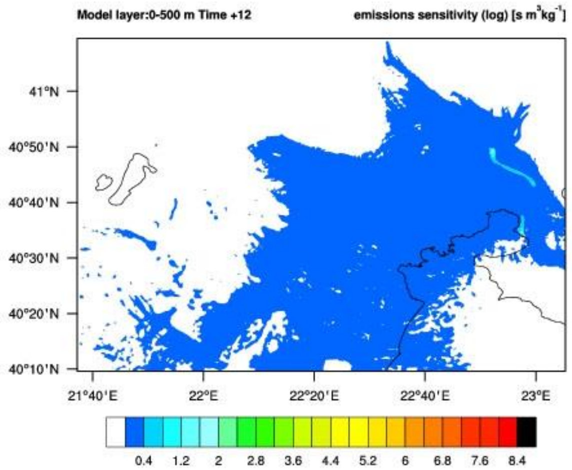
Model layer:0-500 m Time +12
emissions sensitivity (log) [s m^{3}kg^{-1}]
41°N
40°50'N
40°40'N
40°30'N
40°20'N
40°10'N
21°40'E
22°E
22°20'E
22°40'E
23°E
0.4 1.2 2 2.8 3.6 4.4 5.2 6 6.8 7.6 8.4

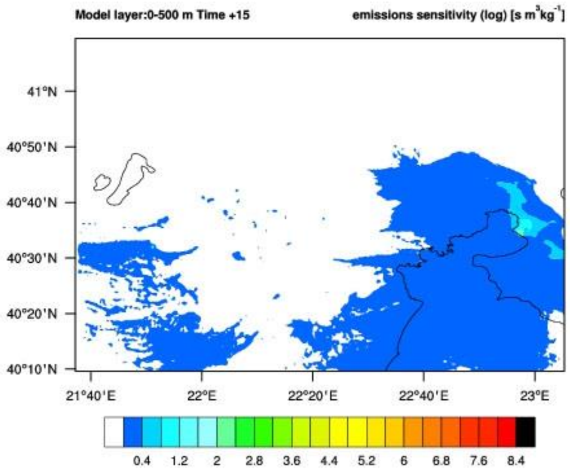
Model layer:0-500 m Time +15
emissions sensitivity (log) [s m^{3}kg^{-1}]
41°N
40°50'N
40°40'N
40°30'N
40°20'N
40°10'N
21°40'E
22°E
22°20'E
22°40'E
23°E
0.4 1.2 2 2.8 3.6 4.4 5.2 6 6.8 7.6 8.4

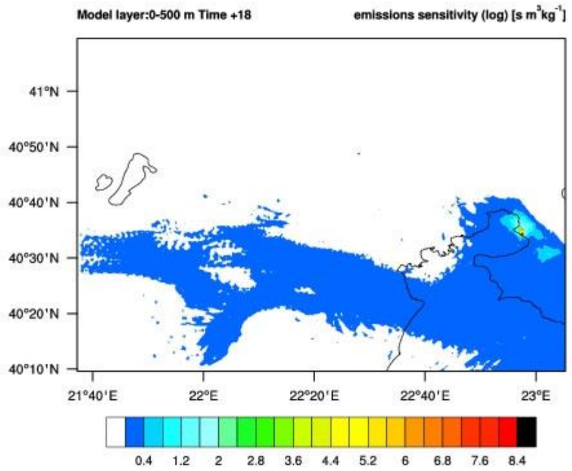
Model layer:0-500 m Time +18
emissions sensitivity (log) [s m^{3}kg^{-1}]
41°N
40°50'N
40°40'N
40°30'N
40°20'N
40°10'N
21°40'E
22°E
22°20'E
22°40'E
23°E
0.4 1.2 2 2.8 3.6 4.4 5.2 6 6.8 7.6 8.4

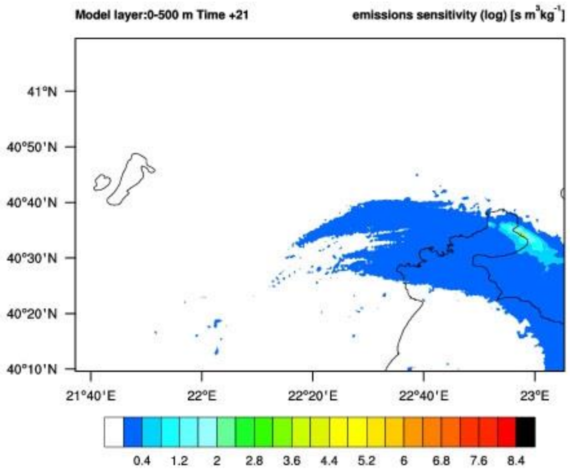
Model layer:0-500 m Time +21
emissions sensitivity (log) [s m^{3}kg^{-1}]
41°N
40°50'N
40°40'N
40°30'N
40°20'N
40°10'N
21°40'E
22°E
22°20'E
22°40'E
23°E
0.4 1.2 2 2.8 3.6 4.4 5.2 6 6.8 7.6 8.4

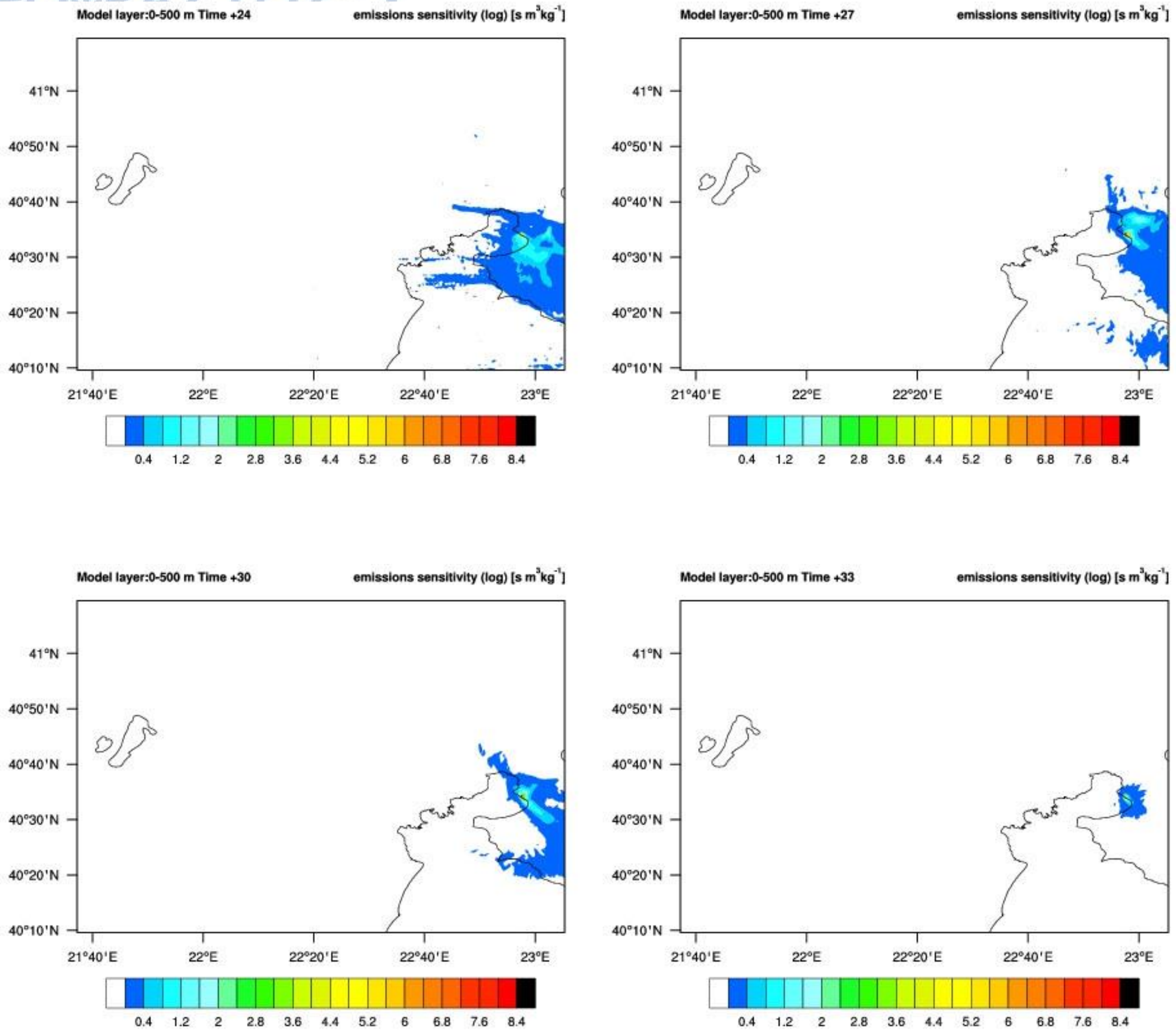

Figure 6.20. 31 January to 2 February visualization of 3h output time-step based on Flexpart-WRF backward simulation from the sampling site KALAMARIA located South-East (Multi-storey building in Kalamaria region) initiation time 12:00 UTC.

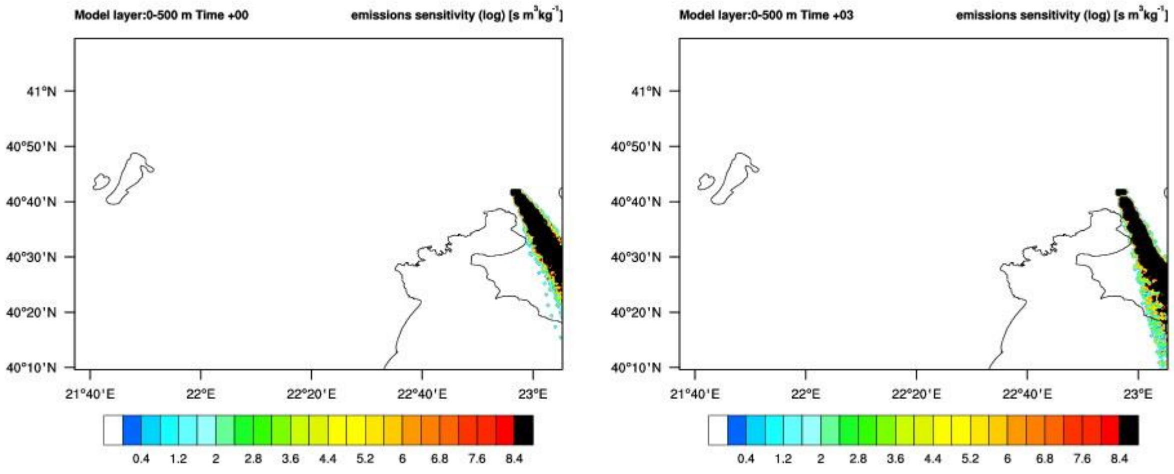

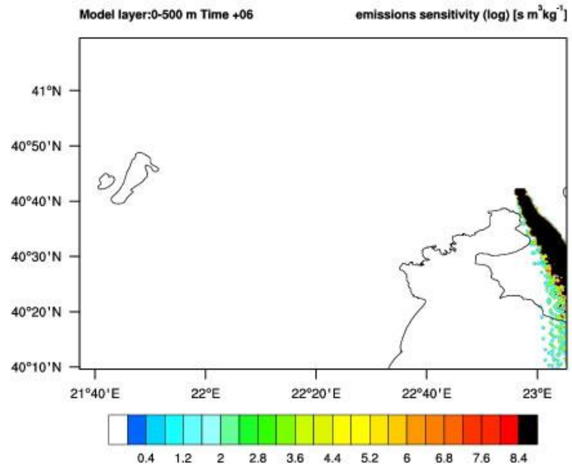
Model layer:0-500 m Time +06
emissions sensitivity (log) [s m^{3}kg^{-1}]
41°N
40°50'N
40°40'N
40°30'N
40°20'N
40°10'N
21°40'E
22°E
22°20'E
22°40'E
23°E
0.4 1.2 2 2.8 3.6 4.4 5.2 6 6.8 7.6 8.4

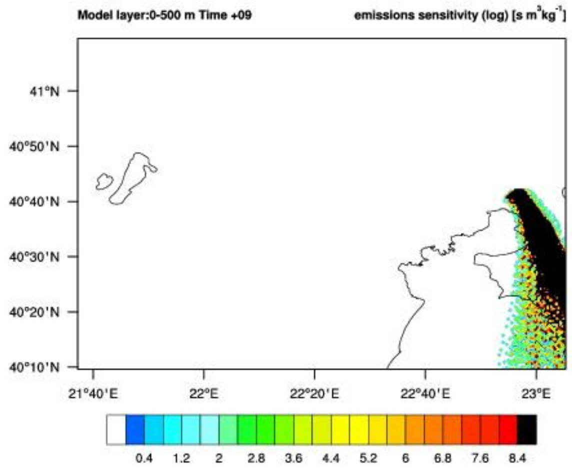
Model layer:0-500 m Time +09
emissions sensitivity (log) [s m^{3}kg^{-1}]
41°N
40°50'N
40°40'N
40°30'N
40°20'N
40°10'N
21°40'E
22°E
22°20'E
22°40'E
23°E
0.4 1.2 2 2.8 3.6 4.4 5.2 6 6.8 7.6 8.4

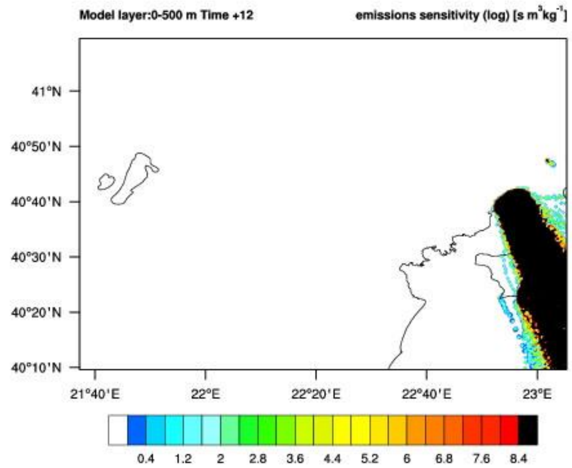
Model layer:0-500 m Time +12
emissions sensitivity (log) [s m^{3}kg^{-1}]
41°N
40°50'N
40°40'N
40°30'N
40°20'N
40°10'N
21°40'E
22°E
22°20'E
22°40'E
23°E
0.4 1.2 2 2.8 3.6 4.4 5.2 6 6.8 7.6 8.4

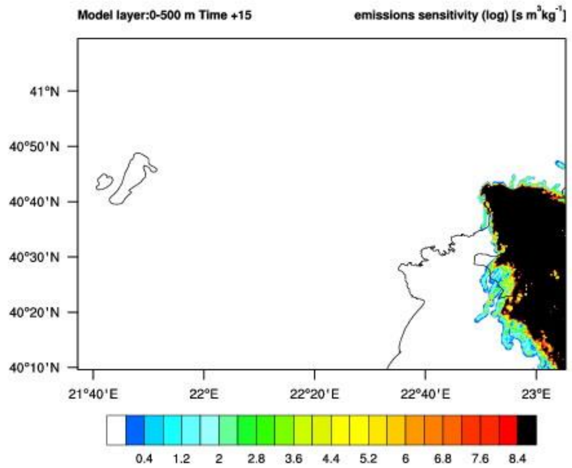
Model layer:0-500 m Time +15
emissions sensitivity (log) [s m^{3}kg^{-1}]
41°N
40°50'N
40°40'N
40°30'N
40°20'N
40°10'N
21°40'E
22°E
22°20'E
22°40'E
23°E
0.4 1.2 2 2.8 3.6 4.4 5.2 6 6.8 7.6 8.4

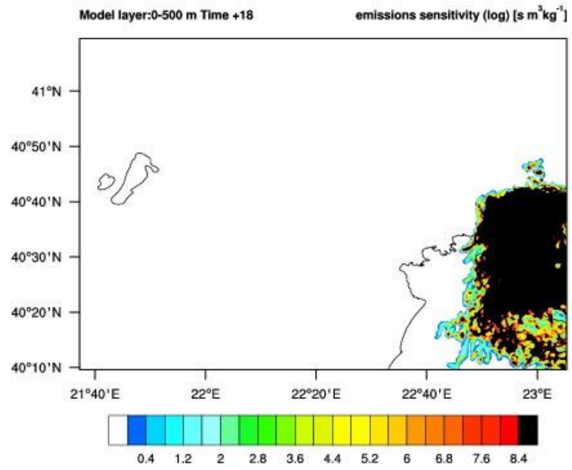
Model layer:0-500 m Time +18
emissions sensitivity (log) [s m^{3}kg^{-1}]
41°N
40°50'N
40°40'N
40°30'N
40°20'N
40°10'N
21°40'E
22°E
22°20'E
22°40'E
23°E
0.4 1.2 2 2.8 3.6 4.4 5.2 6 6.8 7.6 8.4

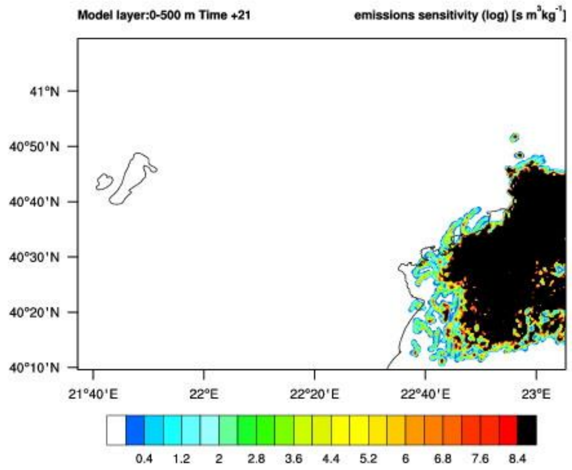
Model layer:0-500 m Time +21
emissions sensitivity (log) [s m^{3}kg^{-1}]
41°N
40°50'N
40°40'N
40°30'N
40°20'N
40°10'N
21°40'E
22°E
22°20'E
22°40'E
23°E
0.4 1.2 2 2.8 3.6 4.4 5.2 6 6.8 7.6 8.4

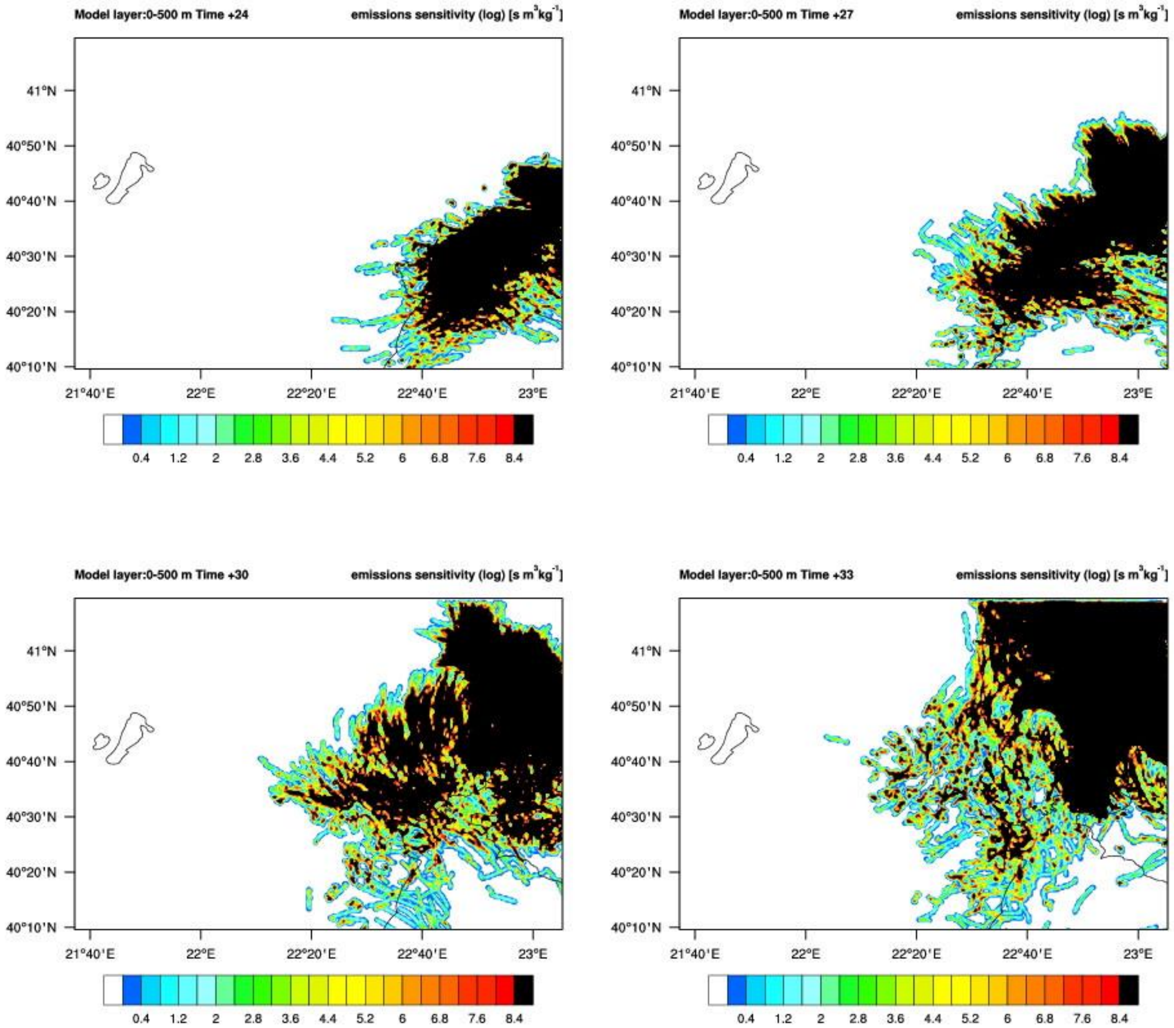

Figure 6.21. 31 January to 2 February visualization of 3h output time-step based on Flexpart-WRF forward simulation from emitting site located North in city suburbs initiation time 12:00 UTC.

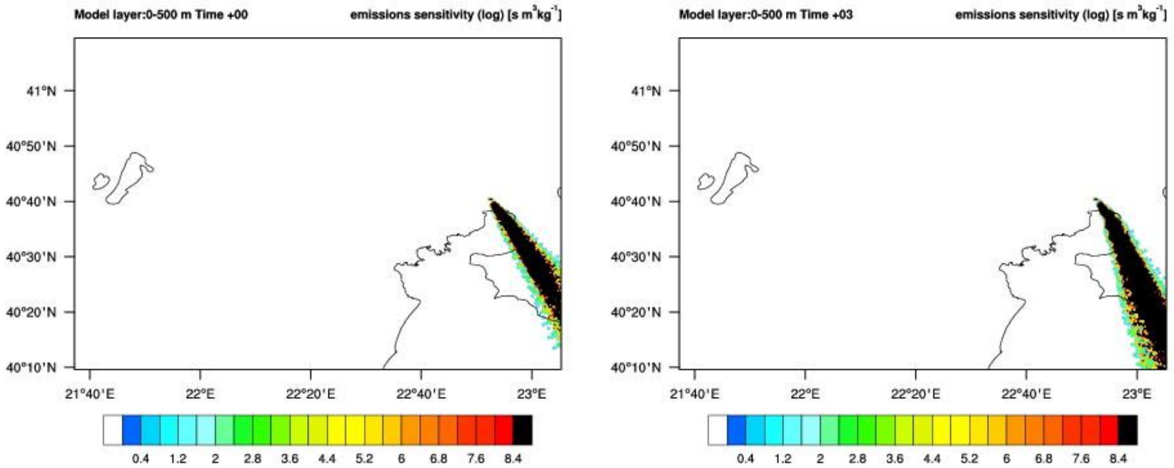

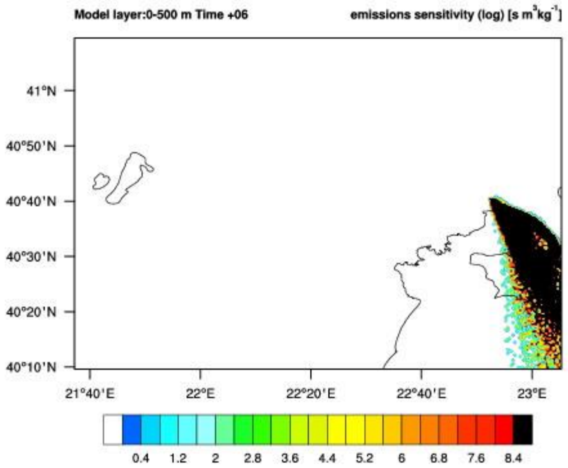
Model layer:0-500 m Time +06
emissions sensitivity (log) [s m^{3}kg^{-1}]
41°N
40°50'N
40°40'N
40°30'N
40°20'N
40°10'N
21°40'E
22°E
22°20'E
22°40'E
23°E
0.4
1.2
2
2.8
3.6
4.4
5.2
6
6.8
7.6
8.4

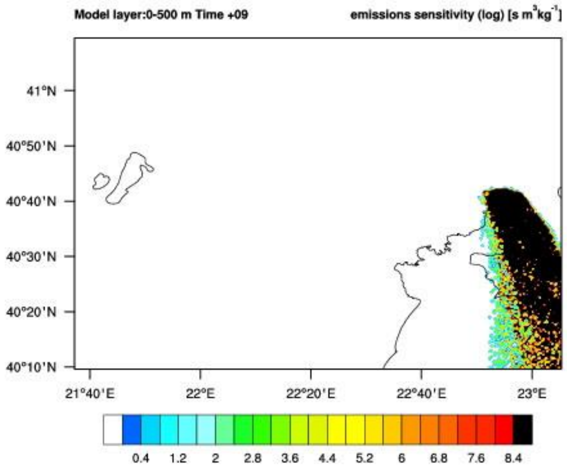
Model layer:0-500 m Time +09
emissions sensitivity (log) [s m^{3}kg^{-1}]
41°N
40°50'N
40°40'N
40°30'N
40°20'N
40°10'N
21°40'E
22°E
22°20'E
22°40'E
23°E
0.4
1.2
2
2.8
3.6
4.4
5.2
6
6.8
7.6
8.4

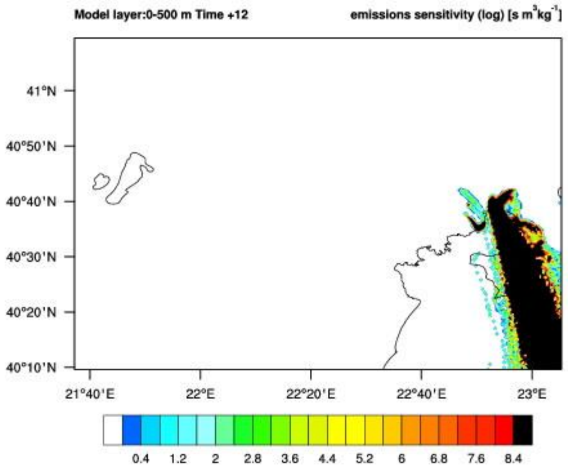
Model layer:0-500 m Time +12
emissions sensitivity (log) [s m^{3}kg^{-1}]
41°N
40°50'N
40°40'N
40°30'N
40°20'N
40°10'N
21°40'E
22°E
22°20'E
22°40'E
23°E
0.4
1.2
2
2.8
3.6
4.4
5.2
6
6.8
7.6
8.4

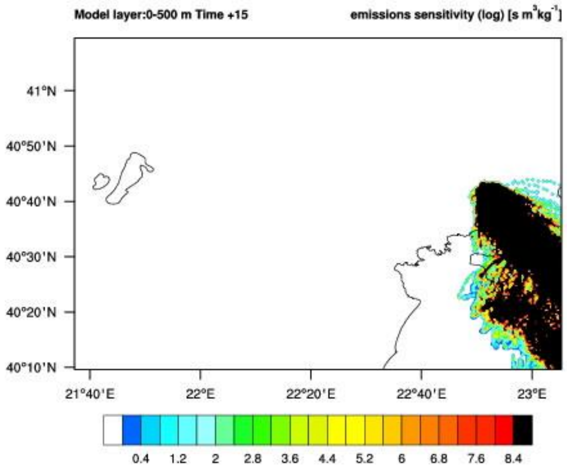
Model layer:0-500 m Time +15
emissions sensitivity (log) [s m^{3}kg^{-1}]
41°N
40°50'N
40°40'N
40°30'N
40°20'N
40°10'N
21°40'E
22°E
22°20'E
22°40'E
23°E
0.4
1.2
2
2.8
3.6
4.4
5.2
6
6.8
7.6
8.4

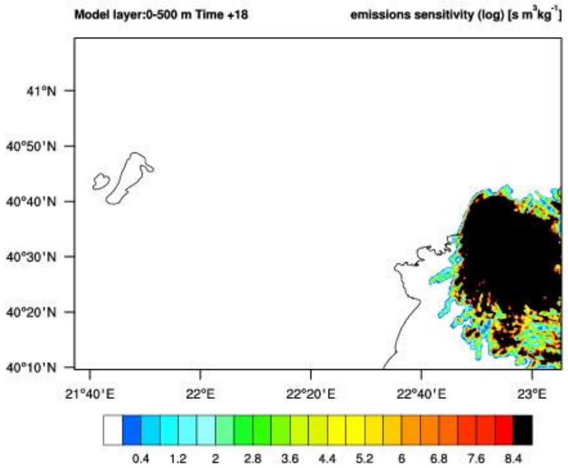
Model layer:0-500 m Time +18
emissions sensitivity (log) [s m^{3}kg^{-1}]
41°N
40°50'N
40°40'N
40°30'N
40°20'N
40°10'N
21°40'E
22°E
22°20'E
22°40'E
23°E
0.4
1.2
2
2.8
3.6
4.4
5.2
6
6.8
7.6
8.4

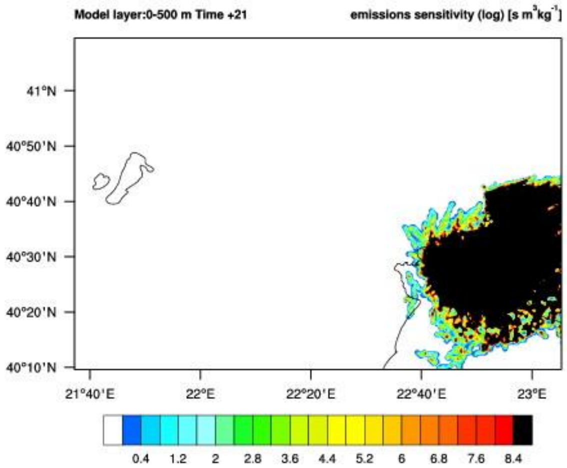
Model layer:0-500 m Time +21
emissions sensitivity (log) [s m^{3}kg^{-1}]
41°N
40°50'N
40°40'N
40°30'N
40°20'N
40°10'N
21°40'E
22°E
22°20'E
22°40'E
23°E
0.4
1.2
2
2.8
3.6
4.4
5.2
6
6.8
7.6
8.4

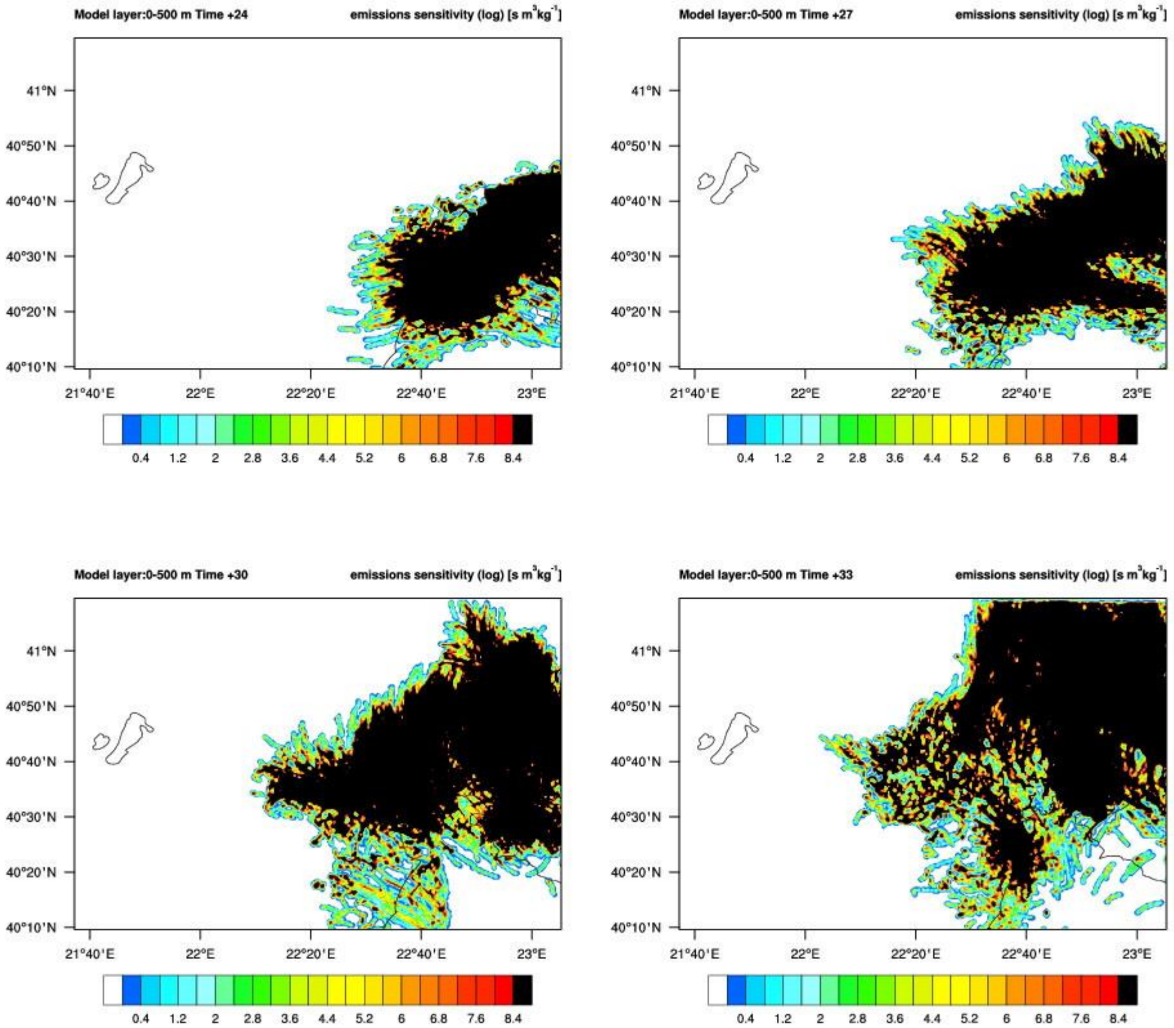

Figure 6.22. 31 January to 2 February visualization of 3h output time-step based on Flexpart-WRF forward simulation from emitting site located West in the industrial area of the city initiation time 12:00 UTC.

6.7. Synoptic conditions sampling date 4th February 2013

For samples from 4th February 2013 and more specifically one day earlier from our day of interest in 3rd February the average wind speed was 4.5 km/h with maximum wind speed of 30.6 km/h (12:10 pm) and wind directions ESE.

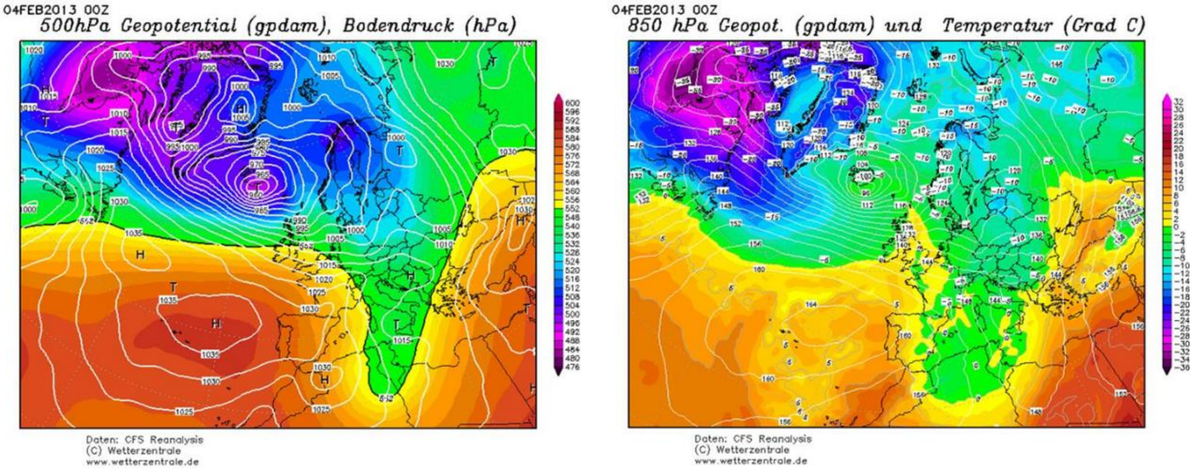

Figure 6.23. The synoptic conditions of the 4th February 2013, as they are depicted through the weather charts of 500 hPa (highlighting the geopotential heights and the surface isobars) and 850 hPa (highlighting the geopotential heights and the temperature gradients).

The synoptic conditions of the 4th February 2013 are indicated in Figure 6.23, where the weather charts at the 500 hPa (highlighting the geopotential heights and the surface isobars) and 850 hPa (highlighting the geopotential heights and the temperature gradients) are depicted. According to the classification method proposed by Karacostas (2003) and Karacostas et al. (2018), this is a South-West flow (SW) with some more emphasis to southerly winds. This synoptic type is characterized by the presence of a very intense, cold air, long wave trough situated over central Mediterranean, being extended from central Europe all the way to the northern Africa (Figure 6.23). Accordingly, a strong, long wave ridge, with warm air mass is extended over eastern Mediterranean all the way, through Turkey, to eastern Europe and western Asia, resulting to a prevailing southwest flow over the area of interest, with emphasis to more southerly component. This system seems to be very well organized, because similar synoptic conditions are encountered and at the 850 hPa chart.

6.7.1 Flexpart-WRF visualization analysis run 3rd to 5th February 2013

For 4th February 2013 where our samples were analyzed and according to the aforementioned synoptic conditions, the prevailing wind conditions showed daily wind speed average of 0.6km/h and with maximum wind speed of 9.7km/h (02:30a.m.) with wind direction WSW this can be seen from the visualization of our backward simulations even though one day earlier wind direction was ESE the plume eventually turned affecting the location of our sampling sites as noted from time-steps +09 to +15 showing a dispersion phenomenon from the industrial area (Figs 6.24-6.26) as well as the northern and western emitting area in our forward runs (Figs 6.27-6.28) where initially seem to be heading south there is a swift change directed WSW towards all the sampling location sites as seen from time-steps +06 to +24.

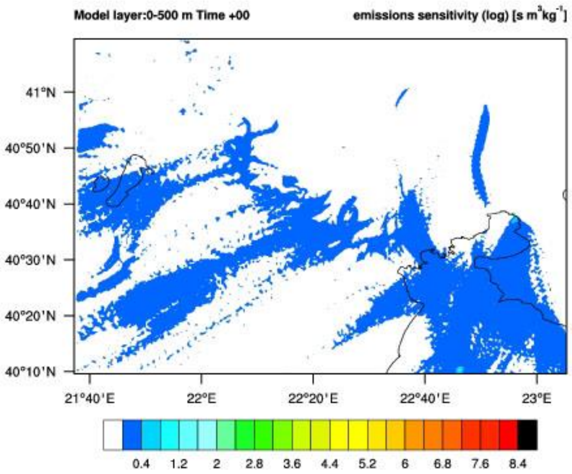

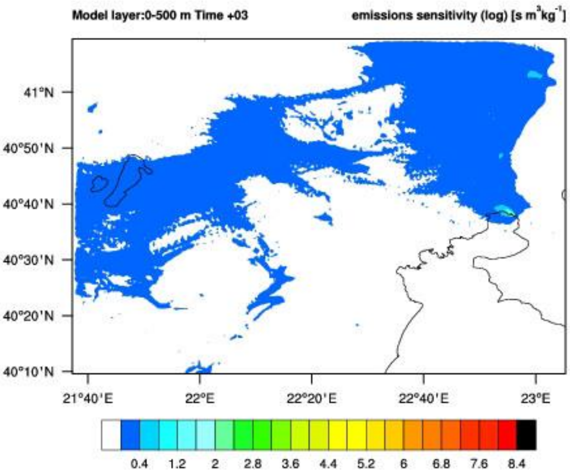

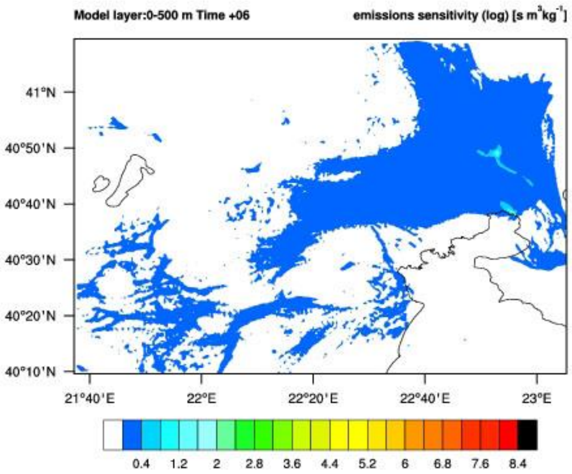

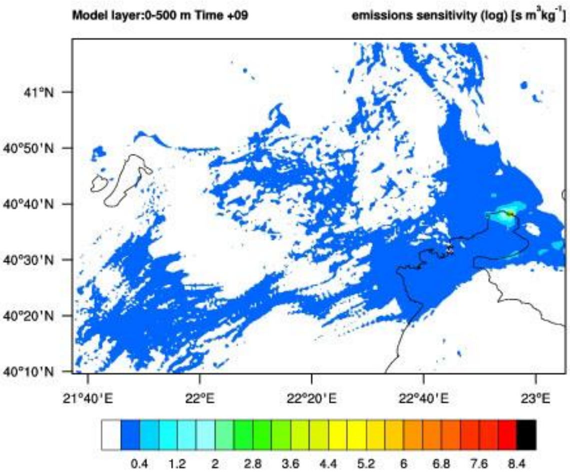

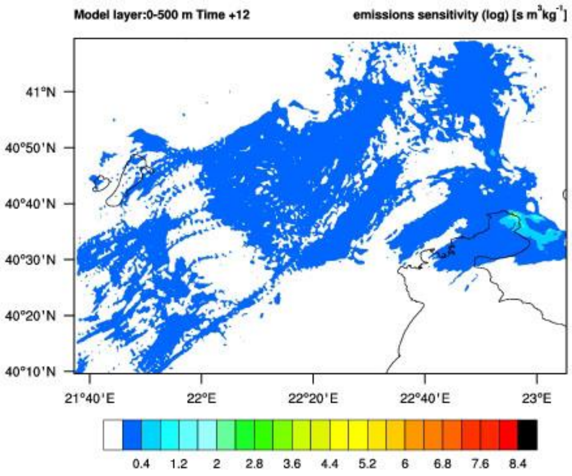
Model layer:0-500 m Time +12
emissions sensitivity (log) [s m³kg⁻¹]
41°N
40°50'N
40°40'N
40°30'N
40°20'N
40°10'N
21°40'E
22°E
22°20'E
22°40'E
23°E
0.4 1.2 2 2.8 3.6 4.4 5.2 6 6.8 7.6 8.4

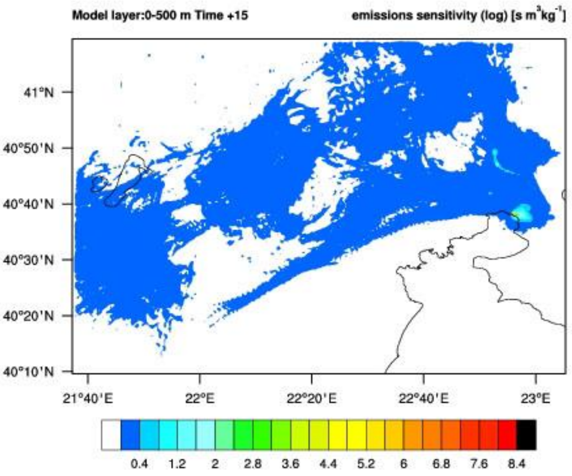
Model layer:0-500 m Time +15
emissions sensitivity (log) [s m³kg⁻¹]
41°N
40°50'N
40°40'N
40°30'N
40°20'N
40°10'N
21°40'E
22°E
22°20'E
22°40'E
23°E
0.4 1.2 2 2.8 3.6 4.4 5.2 6 6.8 7.6 8.4

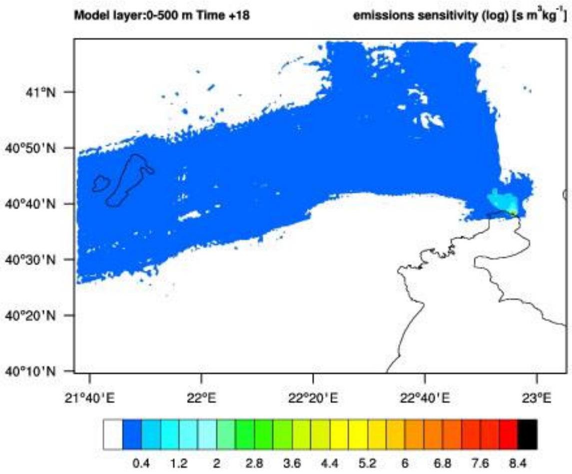
Model layer:0-500 m Time +18
emissions sensitivity (log) [s m³kg⁻¹]
41°N
40°50'N
40°40'N
40°30'N
40°20'N
40°10'N
21°40'E
22°E
22°20'E
22°40'E
23°E
0.4 1.2 2 2.8 3.6 4.4 5.2 6 6.8 7.6 8.4

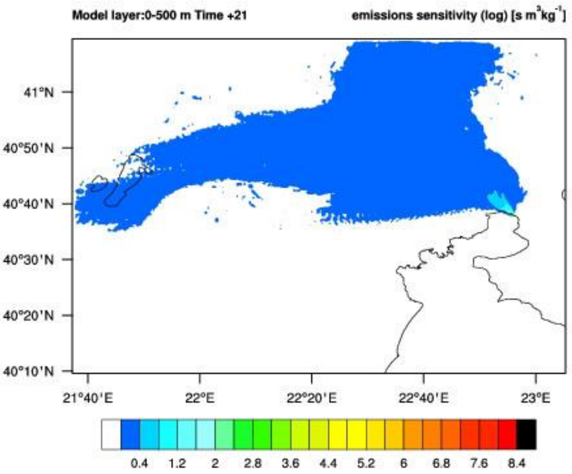
Model layer:0-500 m Time +21
emissions sensitivity (log) [s m³kg⁻¹]
41°N
40°50'N
40°40'N
40°30'N
40°20'N
40°10'N
21°40'E
22°E
22°20'E
22°40'E
23°E
0.4 1.2 2 2.8 3.6 4.4 5.2 6 6.8 7.6 8.4

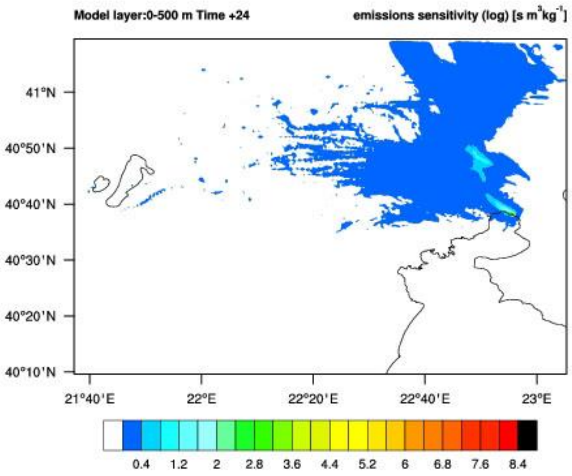
Model layer:0-500 m Time +24
emissions sensitivity (log) [s m³kg⁻¹]
41°N
40°50'N
40°40'N
40°30'N
40°20'N
40°10'N
21°40'E
22°E
22°20'E
22°40'E
23°E
0.4 1.2 2 2.8 3.6 4.4 5.2 6 6.8 7.6 8.4

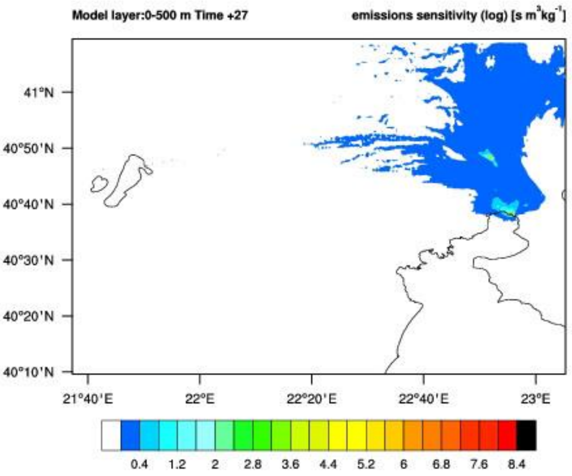
Model layer:0-500 m Time +27
emissions sensitivity (log) [s m³kg⁻¹]
41°N
40°50'N
40°40'N
40°30'N
40°20'N
40°10'N
21°40'E
22°E
22°20'E
22°40'E
23°E
0.4 1.2 2 2.8 3.6 4.4 5.2 6 6.8 7.6 8.4

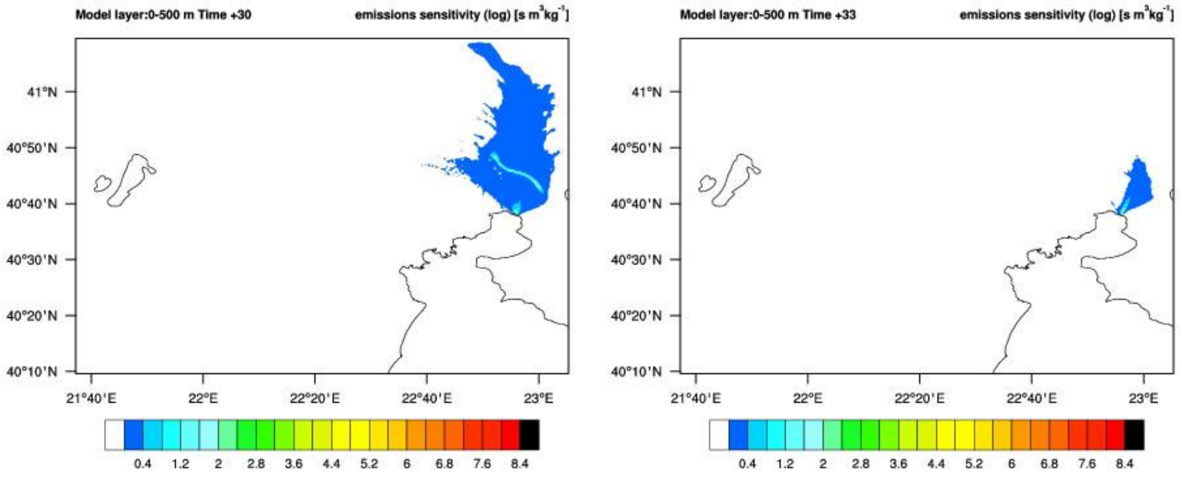

Figure 6.24. 3 to 5 February visualization of 3h output time-step based on Flexpart-WRF backward simulation from the sampling site PORT located west (Twelve storey Parking building near commercial Port of Thessaloniki) initiation time 12:00 UTC.

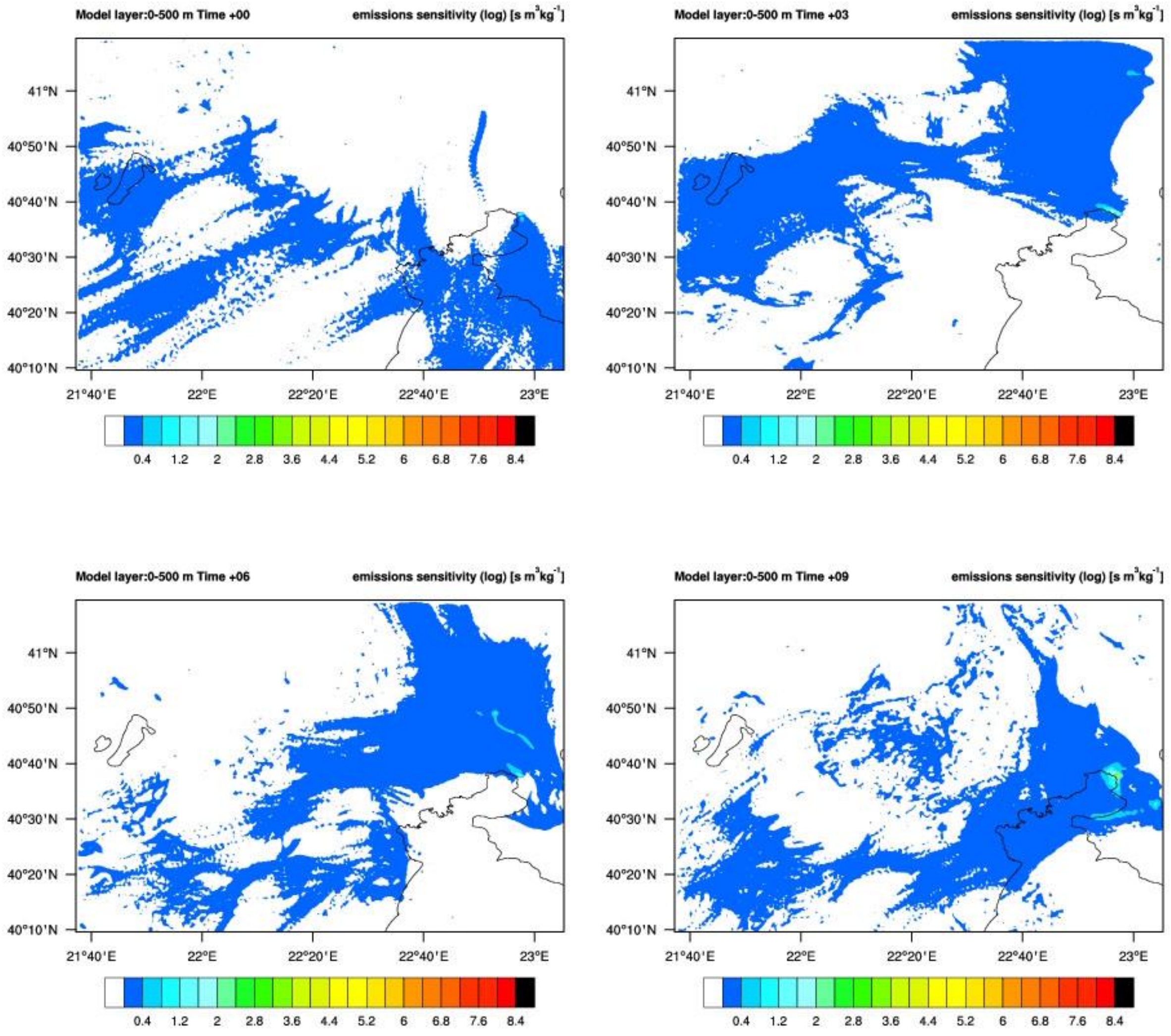

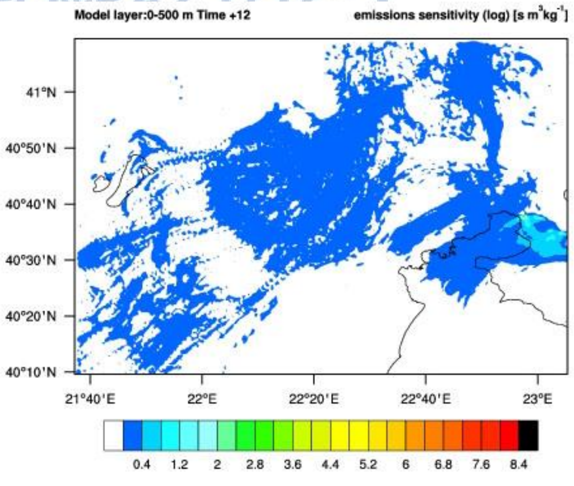
Model layer:0-500 m Time +12
emissions sensitivity (log) [s m^{3}kg^{-1}]
41°N
40°50'N
40°40'N
40°30'N
40°20'N
40°10'N
21°40'E
22°E
22°20'E
22°40'E
23°E
0.4 1.2 2 2.8 3.6 4.4 5.2 6 6.8 7.6 8.4

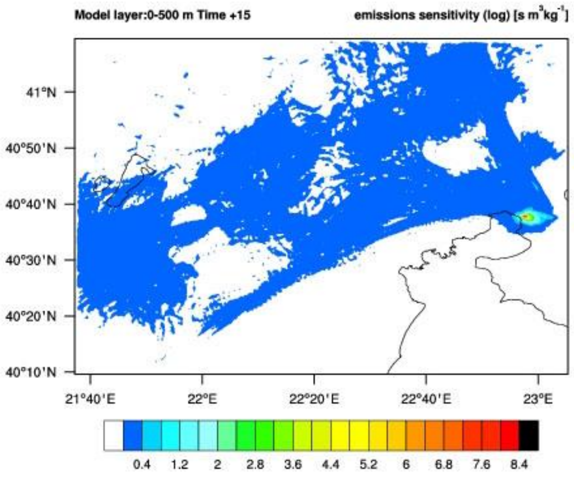
Model layer:0-500 m Time +15
emissions sensitivity (log) [s m^{3}kg^{-1}]
41°N
40°50'N
40°40'N
40°30'N
40°20'N
40°10'N
21°40'E
22°E
22°20'E
22°40'E
23°E
0.4 1.2 2 2.8 3.6 4.4 5.2 6 6.8 7.6 8.4

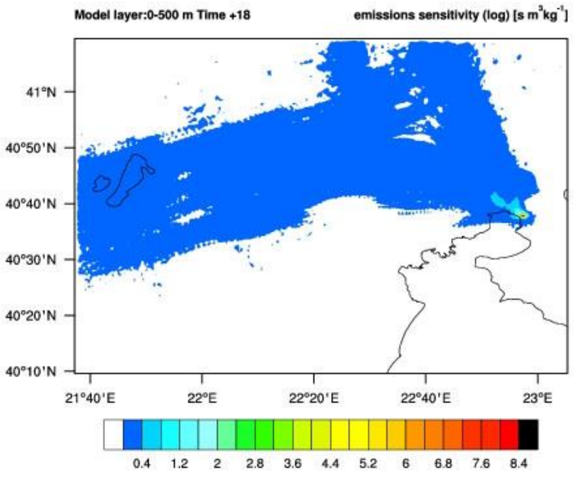
Model layer:0-500 m Time +18
emissions sensitivity (log) [s m^{3}kg^{-1}]
41°N
40°50'N
40°40'N
40°30'N
40°20'N
40°10'N
21°40'E
22°E
22°20'E
22°40'E
23°E
0.4 1.2 2 2.8 3.6 4.4 5.2 6 6.8 7.6 8.4

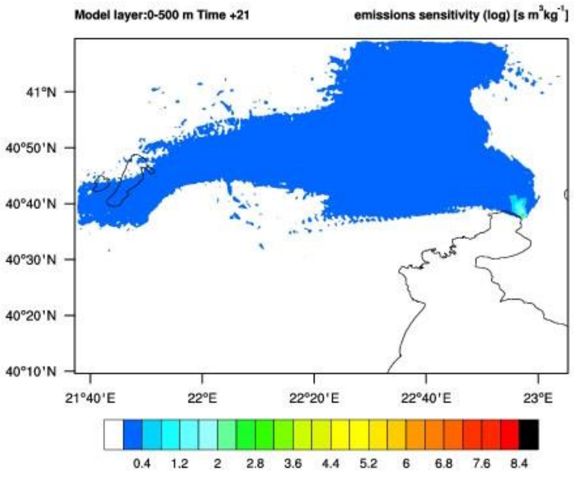
Model layer:0-500 m Time +21
emissions sensitivity (log) [s m^{3}kg^{-1}]
41°N
40°50'N
40°40'N
40°30'N
40°20'N
40°10'N
21°40'E
22°E
22°20'E
22°40'E
23°E
0.4 1.2 2 2.8 3.6 4.4 5.2 6 6.8 7.6 8.4

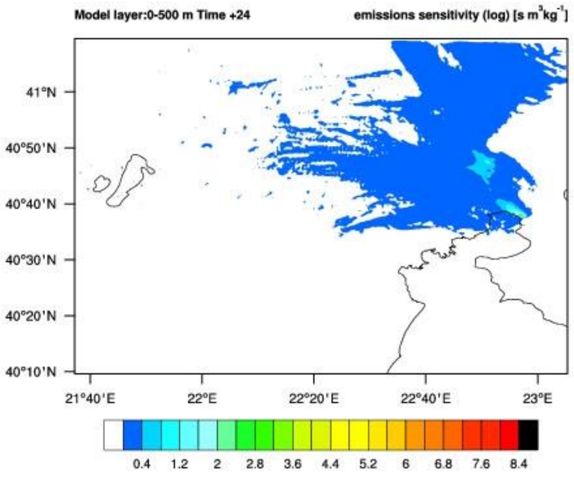
Model layer:0-500 m Time +24
emissions sensitivity (log) [s m^{3}kg^{-1}]
41°N
40°50'N
40°40'N
40°30'N
40°20'N
40°10'N
21°40'E
22°E
22°20'E
22°40'E
23°E
0.4 1.2 2 2.8 3.6 4.4 5.2 6 6.8 7.6 8.4

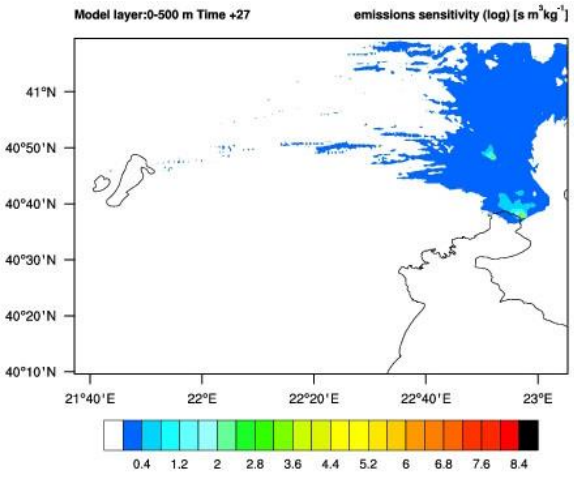
Model layer:0-500 m Time +27
emissions sensitivity (log) [s m^{3}kg^{-1}]
41°N
40°50'N
40°40'N
40°30'N
40°20'N
40°10'N
21°40'E
22°E
22°20'E
22°40'E
23°E
0.4 1.2 2 2.8 3.6 4.4 5.2 6 6.8 7.6 8.4

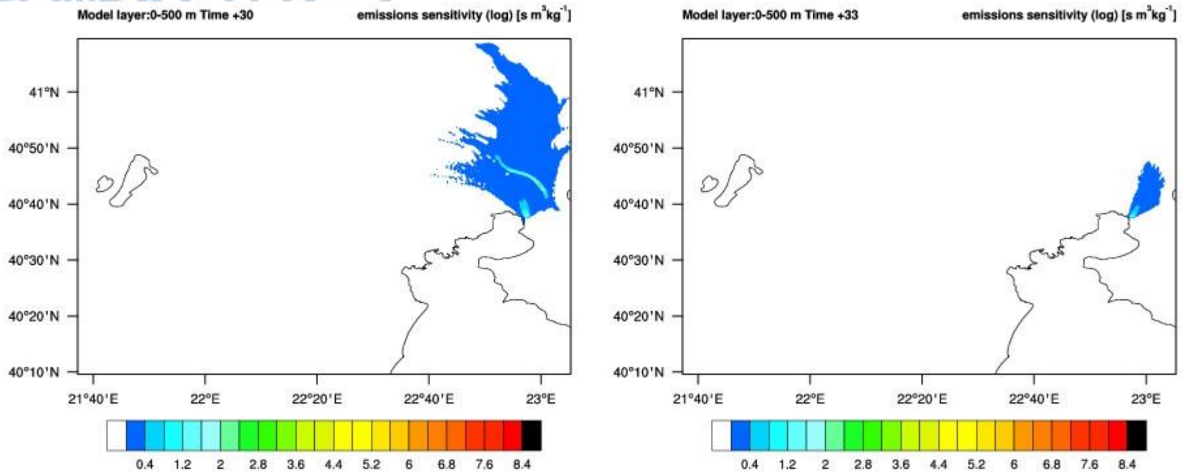

Figure 6.25. 3 to 5 February Flexpart-WRF visualization of 3h output time-step based on Flexpart-WRF backward simulation from the sampling site AUTH located in city center (Aristotle University of Thessaloniki) initiation time 12:00 UTC.

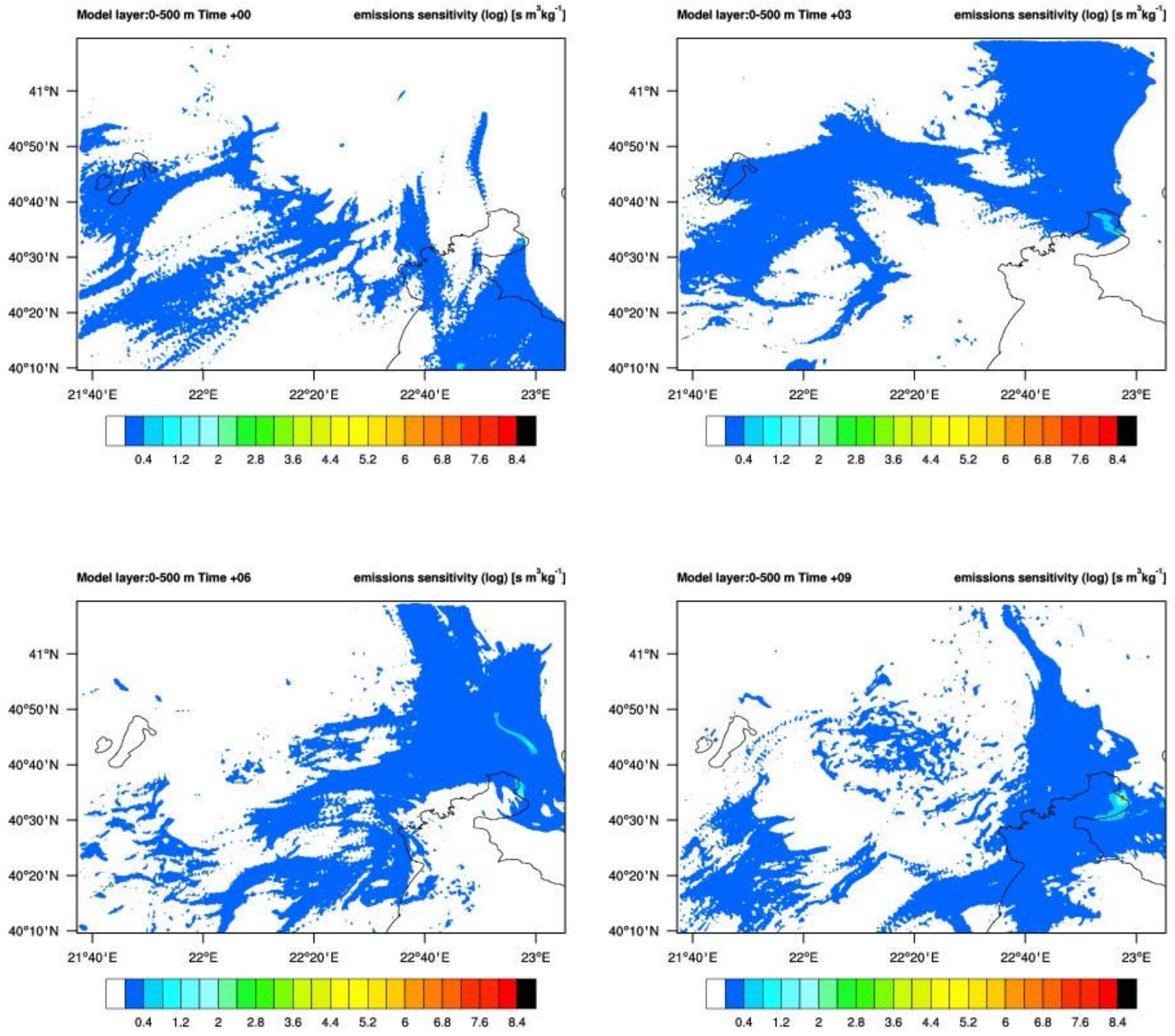

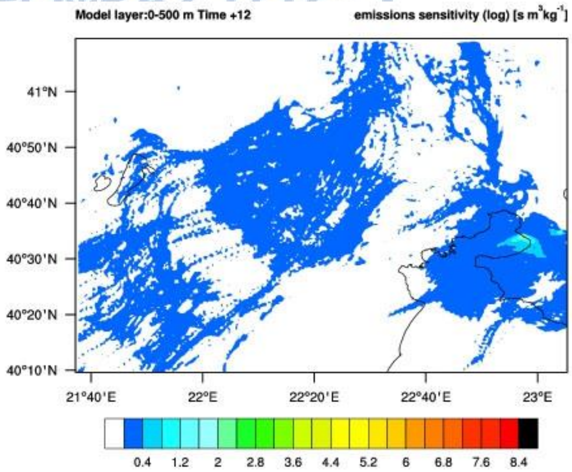
Model layer:0-500 m Time +12
emissions sensitivity (log) [s m^3kg^-1]
41°N
40°50'N
40°40'N
40°30'N
40°20'N
40°10'N
21°40'E
22°E
22°20'E
22°40'E
23°E
0.4
1.2
2
2.8
3.6
4.4
5.2
6
6.8
7.6
8.4

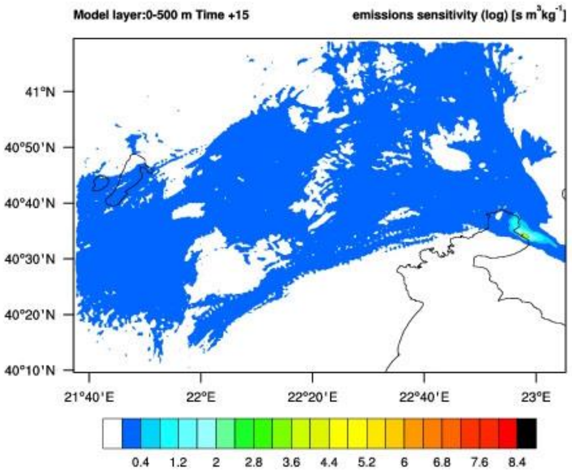
Model layer:0-500 m Time +15
emissions sensitivity (log) [s m^3kg^-1]
41°N
40°50'N
40°40'N
40°30'N
40°20'N
40°10'N
21°40'E
22°E
22°20'E
22°40'E
23°E
0.4
1.2
2
2.8
3.6
4.4
5.2
6
6.8
7.6
8.4

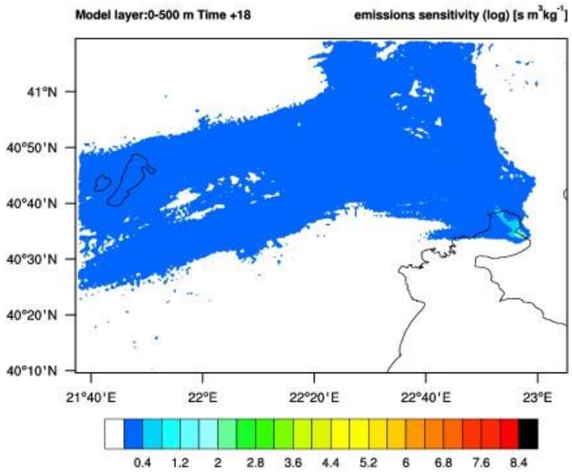
Model layer:0-500 m Time +18
emissions sensitivity (log) [s m^3kg^-1]
41°N
40°50'N
40°40'N
40°30'N
40°20'N
40°10'N
21°40'E
22°E
22°20'E
22°40'E
23°E
0.4
1.2
2
2.8
3.6
4.4
5.2
6
6.8
7.6
8.4

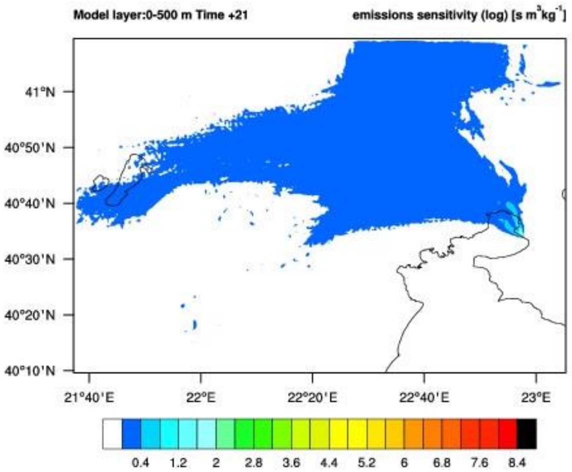
Model layer:0-500 m Time +21
emissions sensitivity (log) [s m^3kg^-1]
41°N
40°50'N
40°40'N
40°30'N
40°20'N
40°10'N
21°40'E
22°E
22°20'E
22°40'E
23°E
0.4
1.2
2
2.8
3.6
4.4
5.2
6
6.8
7.6
8.4

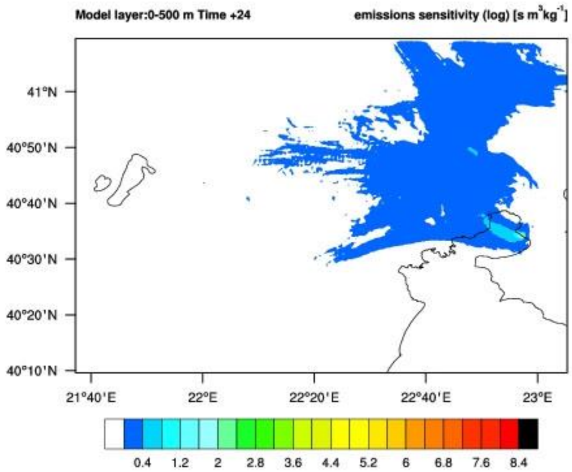
Model layer:0-500 m Time +24
emissions sensitivity (log) [s m^3kg^-1]
41°N
40°50'N
40°40'N
40°30'N
40°20'N
40°10'N
21°40'E
22°E
22°20'E
22°40'E
23°E
0.4
1.2
2
2.8
3.6
4.4
5.2
6
6.8
7.6
8.4

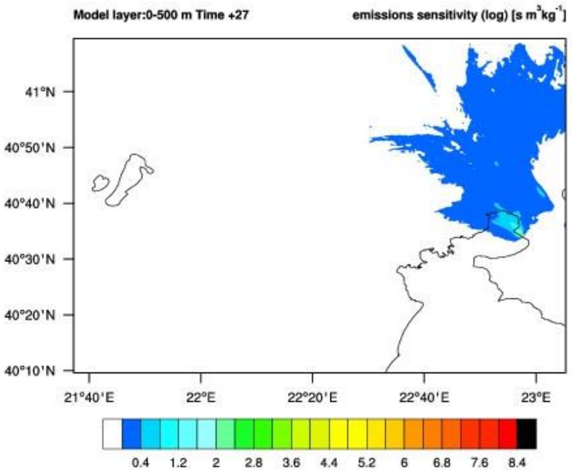
Model layer:0-500 m Time +27
emissions sensitivity (log) [s m^3kg^-1]
41°N
40°50'N
40°40'N
40°30'N
40°20'N
40°10'N
21°40'E
22°E
22°20'E
22°40'E
23°E
0.4
1.2
2
2.8
3.6
4.4
5.2
6
6.8
7.6
8.4

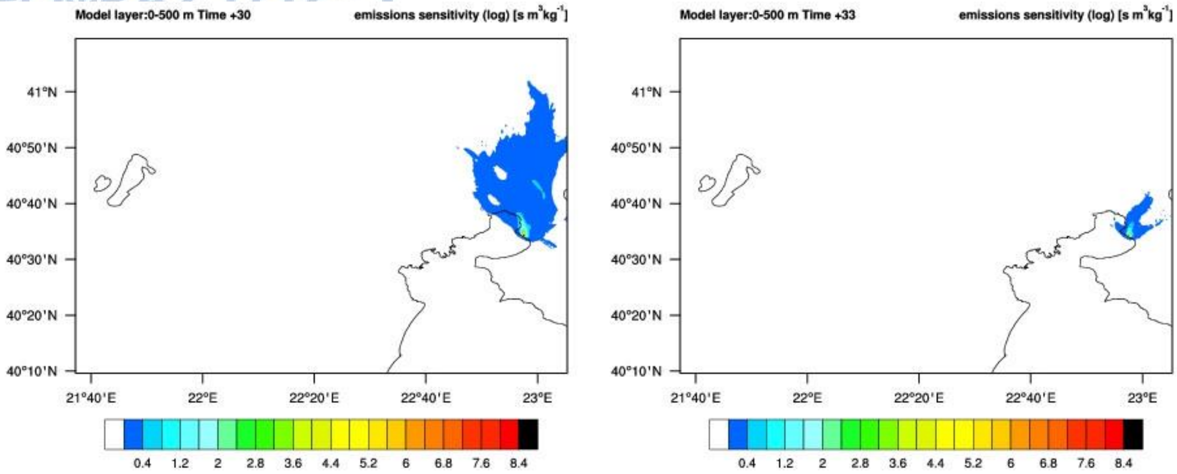

Figure 6.26. 3 to 5 February visualization of 3h output time-step based on Flexpart-WRF backward simulation from the sampling site KALAMARIA located South-East (Multi-storey building in Kalamaria region) initiation time 12:00 UTC.

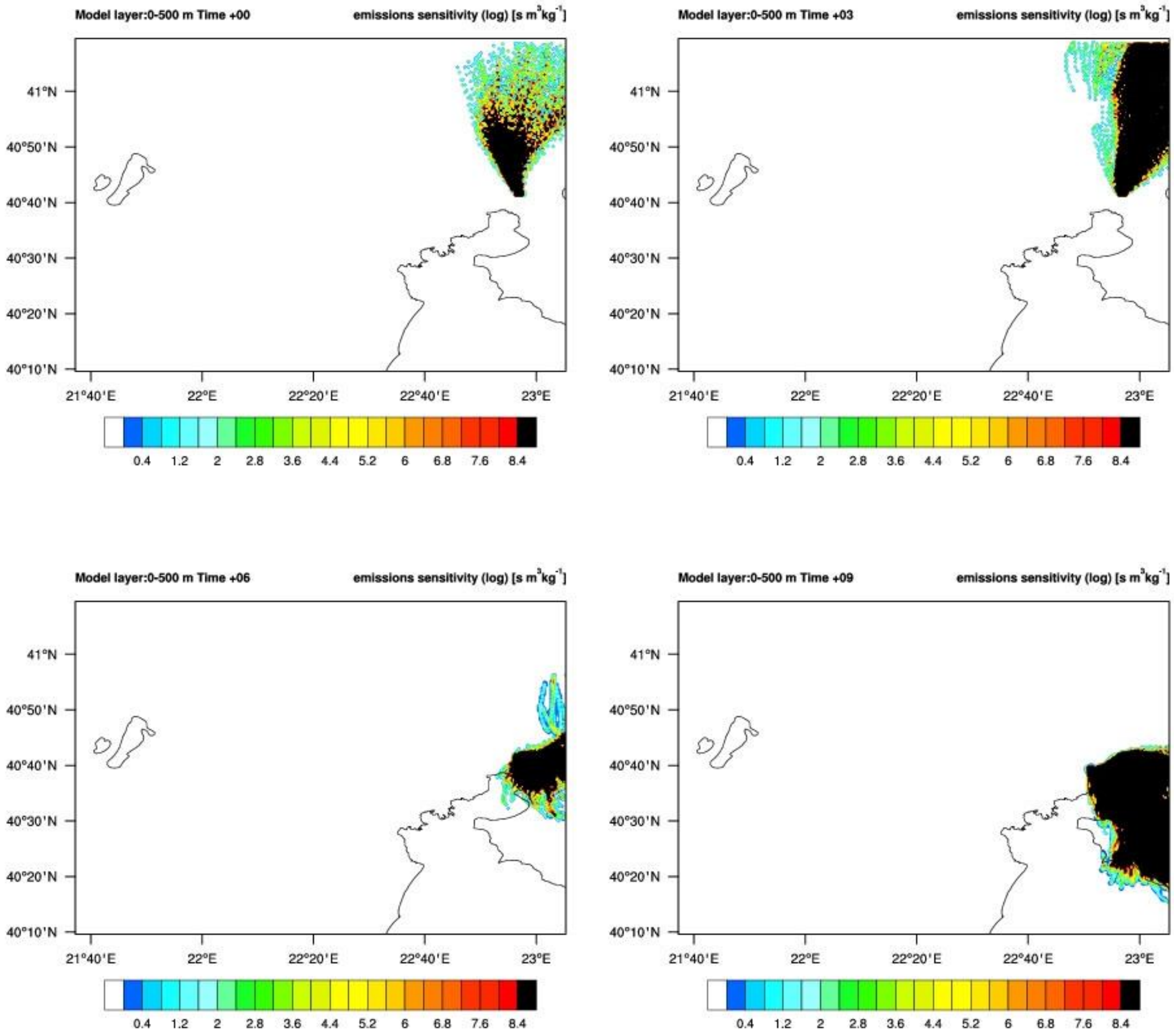

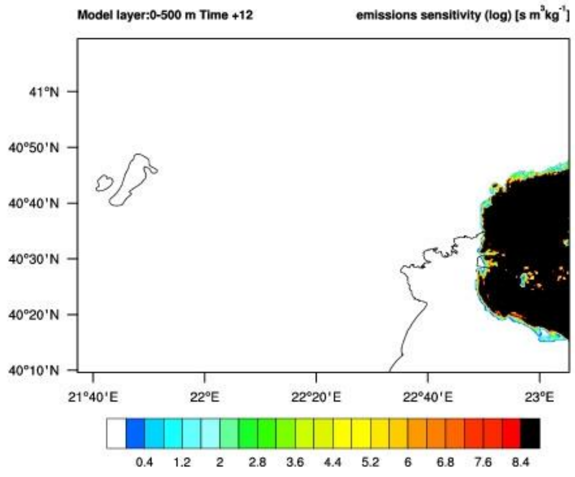
Model layer:0-500 m Time +12
emissions sensitivity (log) [s m^{3}kg^{-1}]
41°N
40°50'N
40°40'N
40°30'N
40°20'N
40°10'N
21°40'E
22°E
22°20'E
22°40'E
23°E
0.4 1.2 2 2.8 3.6 4.4 5.2 6 6.8 7.6 8.4

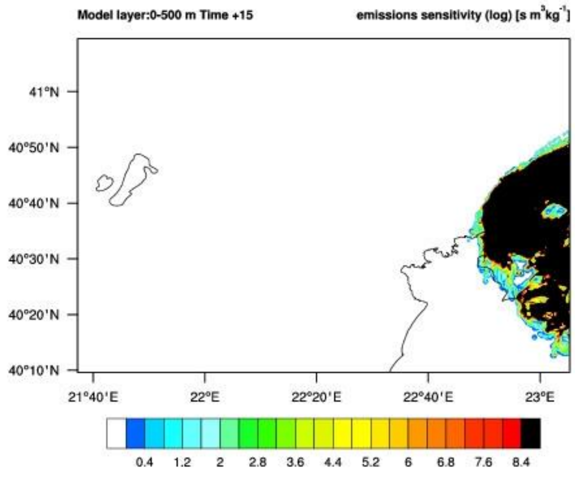
Model layer:0-500 m Time +15
emissions sensitivity (log) [s m^{3}kg^{-1}]
41°N
40°50'N
40°40'N
40°30'N
40°20'N
40°10'N
21°40'E
22°E
22°20'E
22°40'E
23°E
0.4 1.2 2 2.8 3.6 4.4 5.2 6 6.8 7.6 8.4

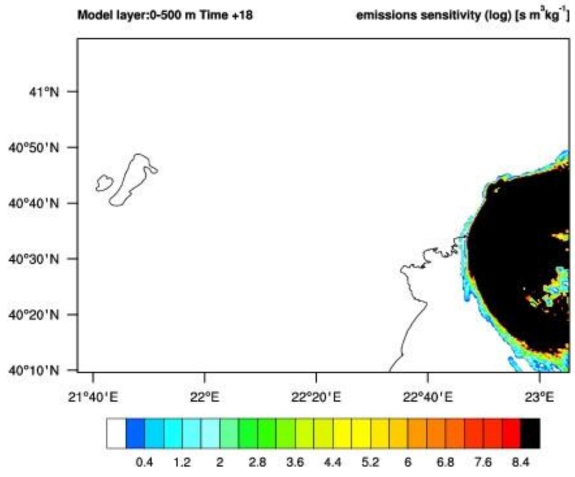
Model layer:0-500 m Time +18
emissions sensitivity (log) [s m^{3}kg^{-1}]
41°N
40°50'N
40°40'N
40°30'N
40°20'N
40°10'N
21°40'E
22°E
22°20'E
22°40'E
23°E
0.4 1.2 2 2.8 3.6 4.4 5.2 6 6.8 7.6 8.4

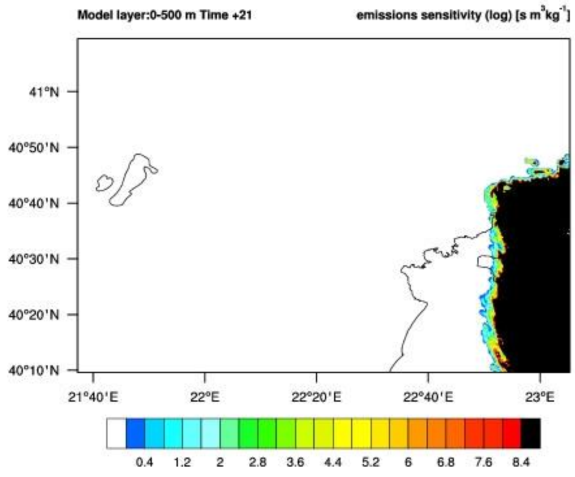
Model layer:0-500 m Time +21
emissions sensitivity (log) [s m^{3}kg^{-1}]
41°N
40°50'N
40°40'N
40°30'N
40°20'N
40°10'N
21°40'E
22°E
22°20'E
22°40'E
23°E
0.4 1.2 2 2.8 3.6 4.4 5.2 6 6.8 7.6 8.4

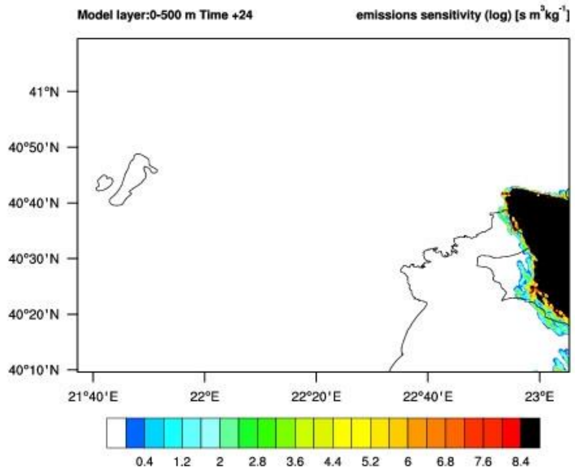
Model layer:0-500 m Time +24
emissions sensitivity (log) [s m^{3}kg^{-1}]
41°N
40°50'N
40°40'N
40°30'N
40°20'N
40°10'N
21°40'E
22°E
22°20'E
22°40'E
23°E
0.4 1.2 2 2.8 3.6 4.4 5.2 6 6.8 7.6 8.4

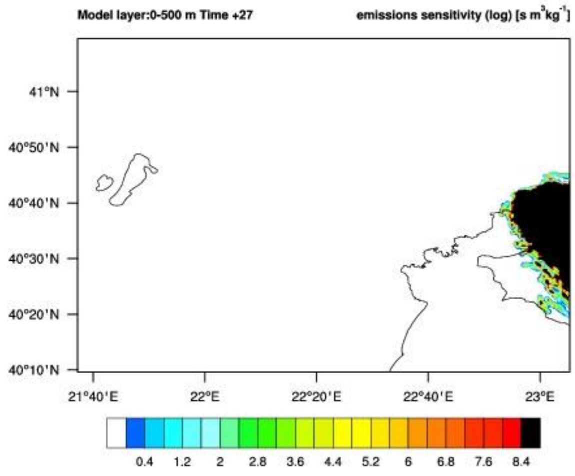
Model layer:0-500 m Time +27
emissions sensitivity (log) [s m^{3}kg^{-1}]
41°N
40°50'N
40°40'N
40°30'N
40°20'N
40°10'N
21°40'E
22°E
22°20'E
22°40'E
23°E
0.4 1.2 2 2.8 3.6 4.4 5.2 6 6.8 7.6 8.4

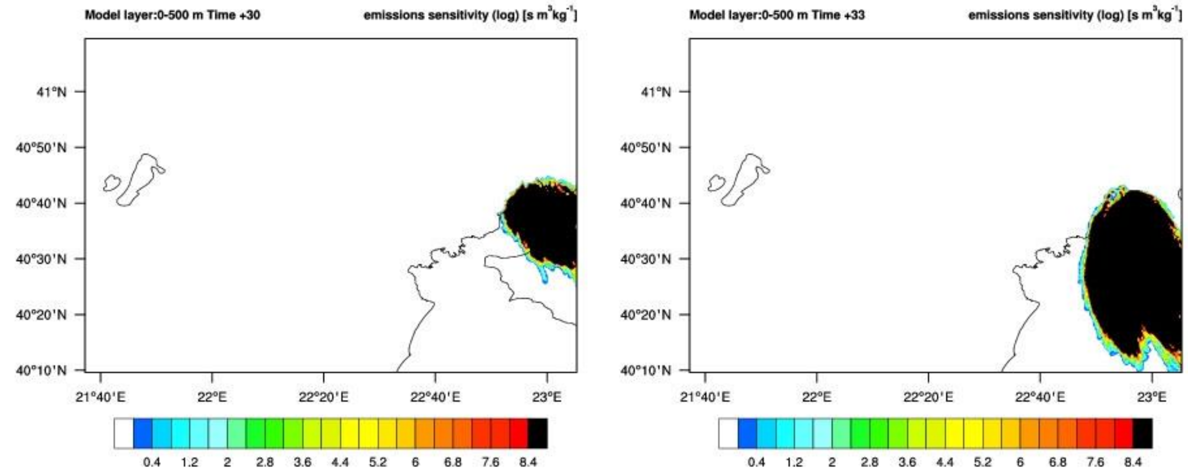

Figure 6.27. 3 to 5 February visualization of 3h output time-step based on Flexpart-WRF forward simulation from emitting site located North in city suburbs initiation time 12:00 UTC.

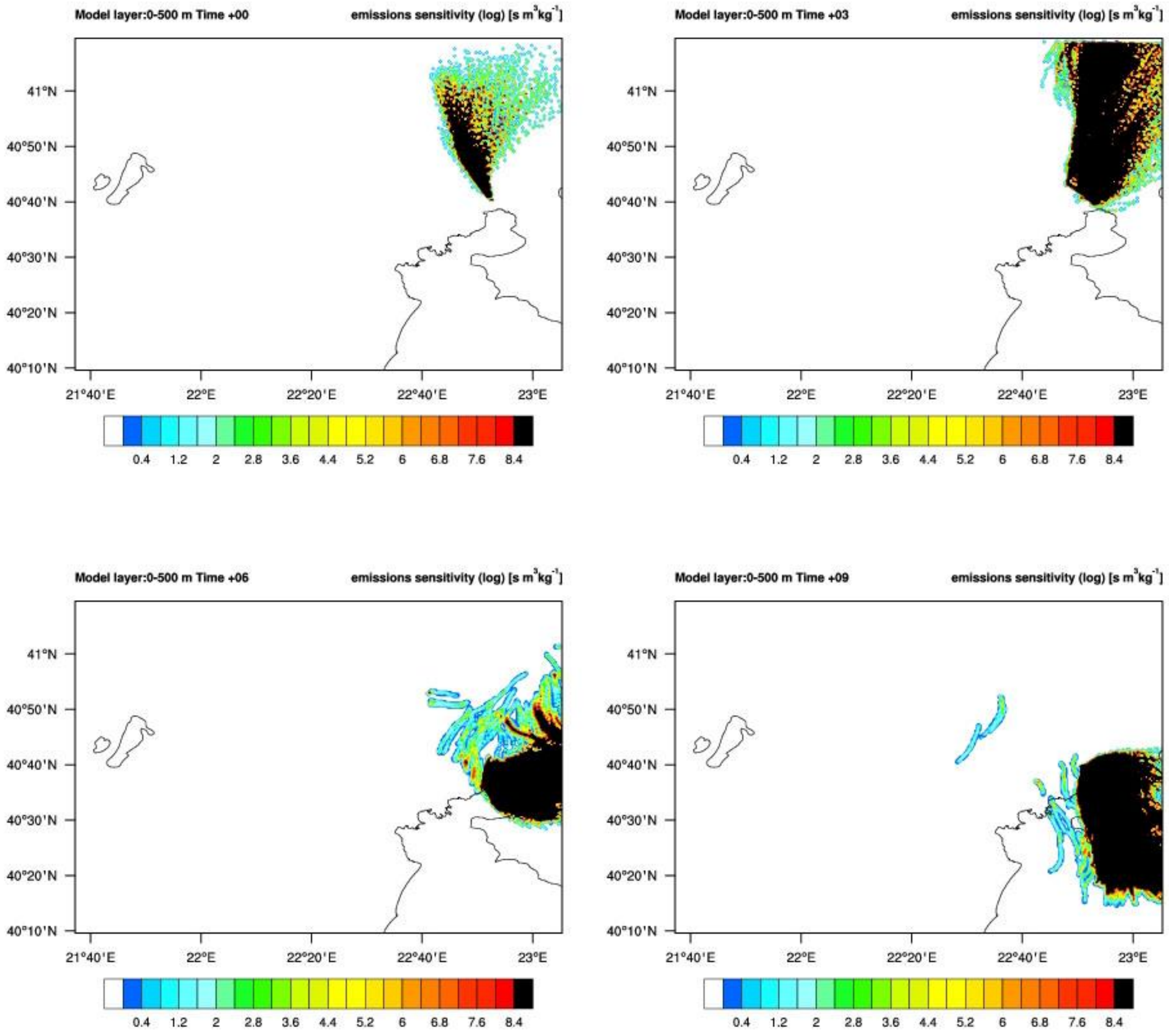

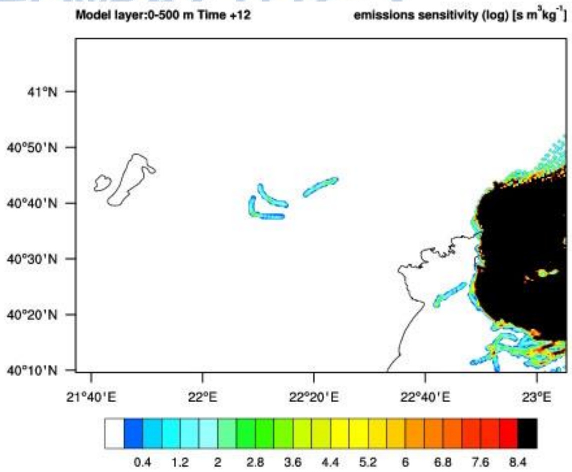

Model layer:0-500 m Time +12 emissions sensitivity (log) [s m^{3}kg^{-1}]

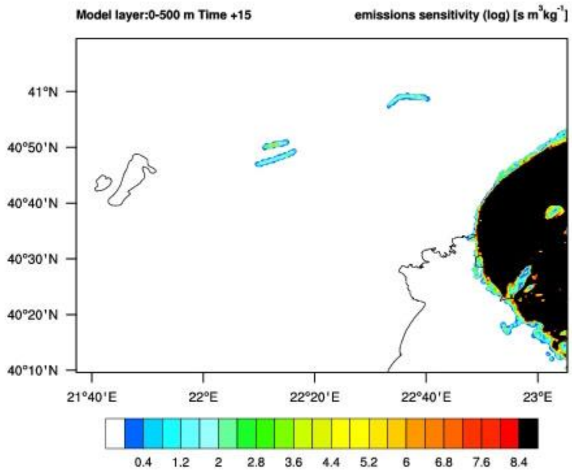

Model layer:0-500 m Time +15 emissions sensitivity (log) [s m^{3}kg^{-1}]

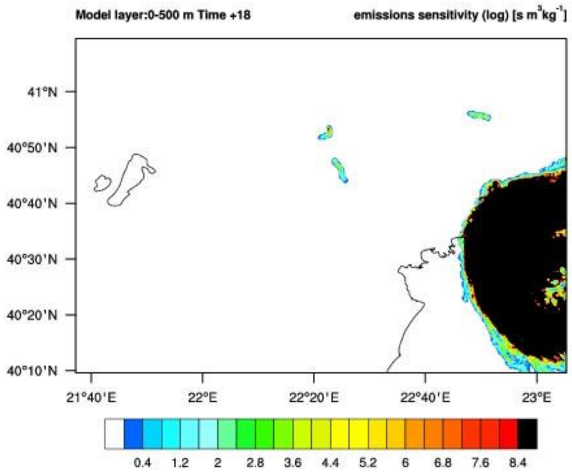

Model layer:0-500 m Time +18 emissions sensitivity (log) [s m^{3}kg^{-1}]

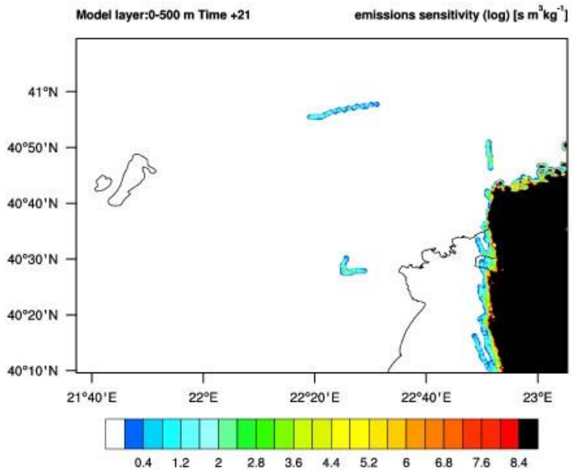

Model layer:0-500 m Time +21 emissions sensitivity (log) [s m^{3}kg^{-1}]

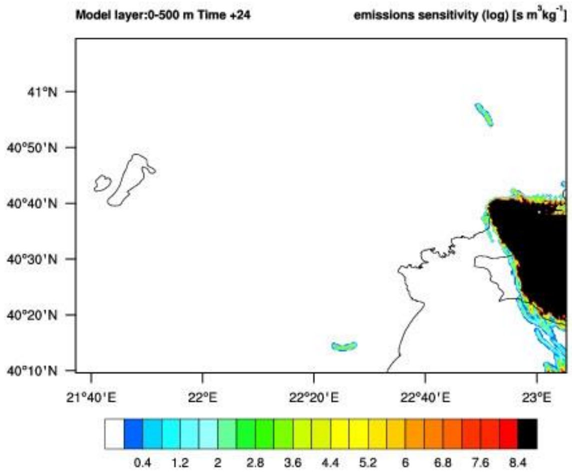

Model layer:0-500 m Time +24 emissions sensitivity (log) [s m^{3}kg^{-1}]

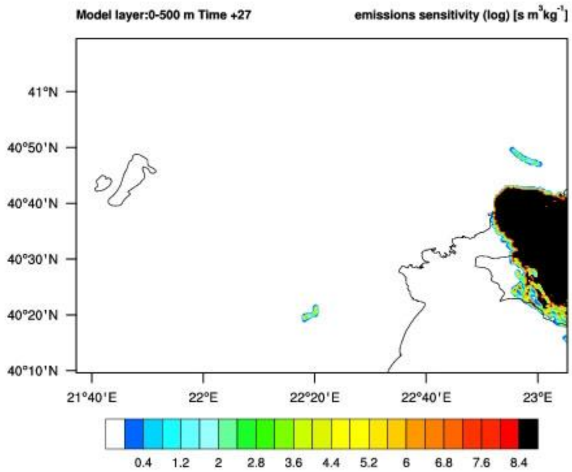

Model layer:0-500 m Time +27 emissions sensitivity (log) [s m^{3}kg^{-1}]

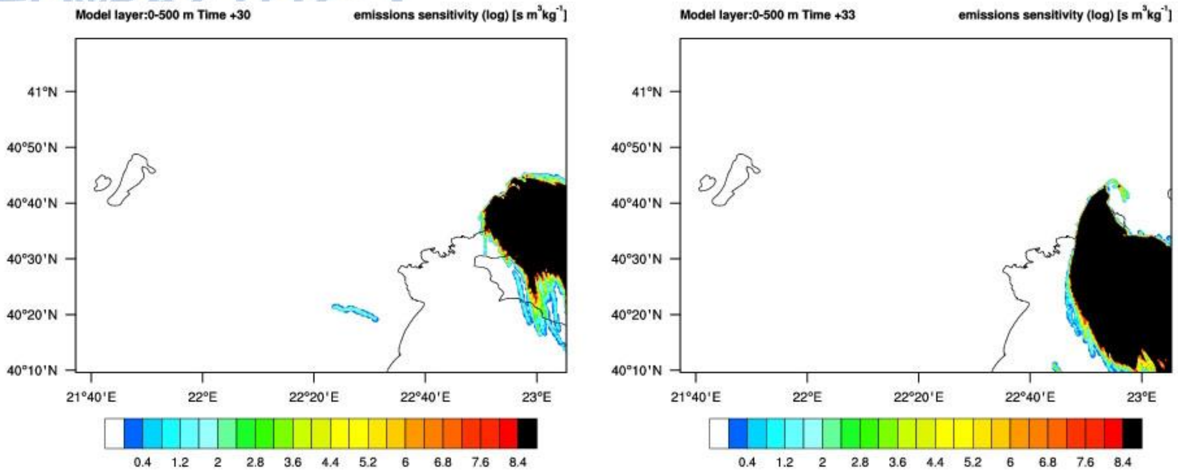

Figure 6.28. 3 to 5 February visualization of 3h output time-step based on Flexpart-WRF forward simulation from emitting site located West in the industrial area of the city initiation time 12:00 UTC.

6.8. Synoptic conditions sampling date 12th February 2013

For samples from 12th February 2013 and more specifically one day earlier from our day of interest in 11th February the average wind speed was 6.7 km/h with maximum wind speed of 24.1 km/h (10:10 am) and wind directions NW.

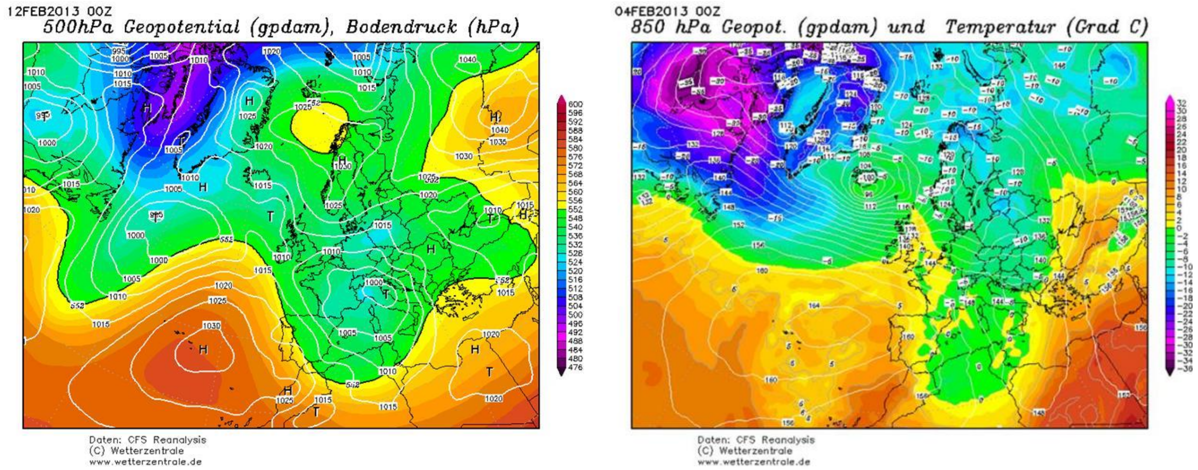

Daten: CFS Reanalysis
(C) Wetterzentrale
www.wetterzentrale.de

Daten: CFS Reanalysis
(C) Wetterzentrale
www.wetterzentrale.de

Figure 6.29. The synoptic conditions of the 12th February 2013, as they are depicted through the weather charts of 500 hPa (highlighting the geopotential heights and the surface isobars) and 850 hPa (highlighting the geopotential heights and the temperature gradients).

The synoptic conditions of the 12th February 2013 are indicated in Figure 6.29, where the weather charts at the 500 hPa (highlighting the geopotential heights and the surface isobars) and 850 hPa (highlighting the geopotential heights and the temperature gradients) are depicted. According to the classification method proposed by Karacostas (2003) and Karacostas et al. (2018), this is a reverse, mirror image, Omega circulation (OME). This synoptic type is characterized by the presence of a very intense, long wave and broad long wave trough, being situated over all Europe. This trough is bounded from both sides by intense anticyclones, covering the north-east Atlantic and the northern Black Sea area (Figure 6.29). Similar synoptic conditions are identified at the 850 hPa chart, because the whole system is very well organized. Due to the aforementioned configuration, some south-west winds are expected aloft, while a most southerly component over the lower levels.

6.8.1 Flexpart-WRF visualization analysis run 11th to 13th February 2013

For 12th February 2013 where our samples were analyzed and according to the aforementioned synoptic conditions, the prevailing wind conditions showed daily wind speed average of 0.9km/h and with maximum wind speed of 9.7km/h (03:10a.m.) with westerly wind direction W showing the dispersion from western industrial area and northern emitting sites locations this can be noted intensively for our forward simulations from time-steps +06 to +21 affecting the whole area of our sampling sites (Figs 6.30-6.32) while for our forward simulations (Figs 6.33-6.34)for time-step from +00 to +09 and then turning the plume on the other side and again resending it to the initial area for time-step of +18 to +21 before shifting it again towards opposite direction, reflecting the effect on our sampling site locations.

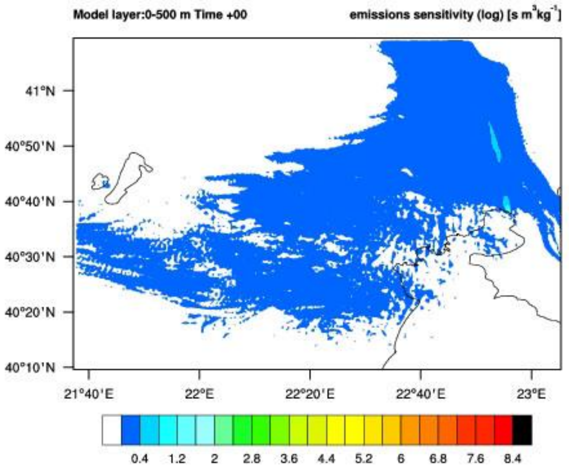

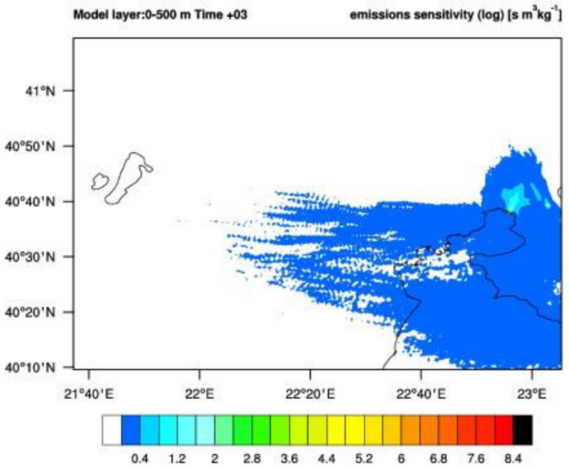

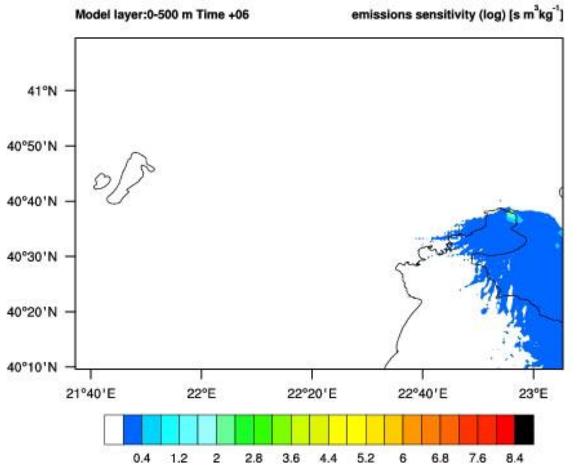
Model layer:0-500 m Time +06
emissions sensitivity (log) $[s\ m^3 kg^{-1}]$
41°N
40°50'N
40°40'N
40°30'N
40°20'N
40°10'N
21°40'E
22°E
22°20'E
22°40'E
23°E
0.4
1.2
2
2.8
3.6
4.4
5.2
6
6.8
7.6
8.4

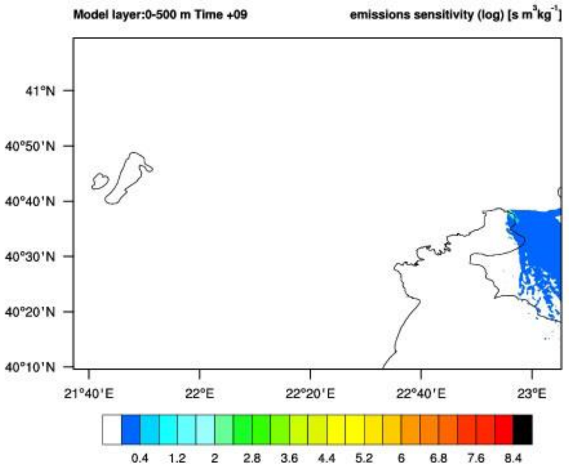
Model layer:0-500 m Time +09
emissions sensitivity (log) $[s\ m^3 kg^{-1}]$
41°N
40°50'N
40°40'N
40°30'N
40°20'N
40°10'N
21°40'E
22°E
22°20'E
22°40'E
23°E
0.4
1.2
2
2.8
3.6
4.4
5.2
6
6.8
7.6
8.4

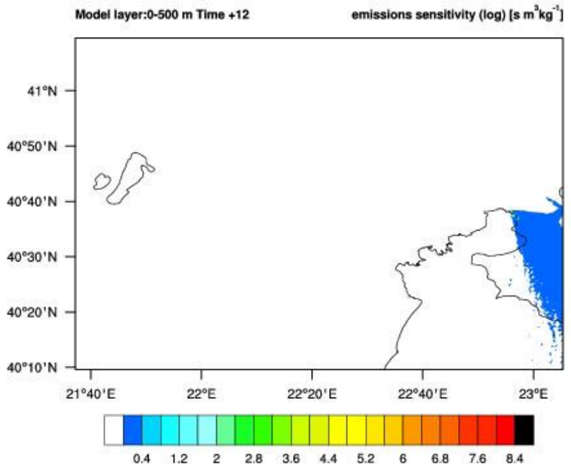
Model layer:0-500 m Time +12
emissions sensitivity (log) $[s\ m^3 kg^{-1}]$
41°N
40°50'N
40°40'N
40°30'N
40°20'N
40°10'N
21°40'E
22°E
22°20'E
22°40'E
23°E
0.4
1.2
2
2.8
3.6
4.4
5.2
6
6.8
7.6
8.4

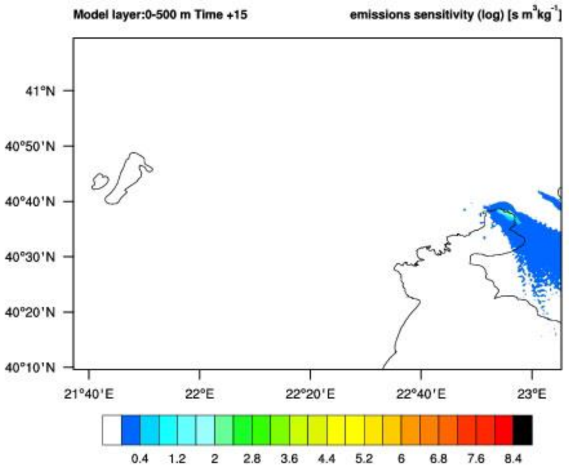
Model layer:0-500 m Time +15
emissions sensitivity (log) $[s\ m^3 kg^{-1}]$
41°N
40°50'N
40°40'N
40°30'N
40°20'N
40°10'N
21°40'E
22°E
22°20'E
22°40'E
23°E
0.4
1.2
2
2.8
3.6
4.4
5.2
6
6.8
7.6
8.4

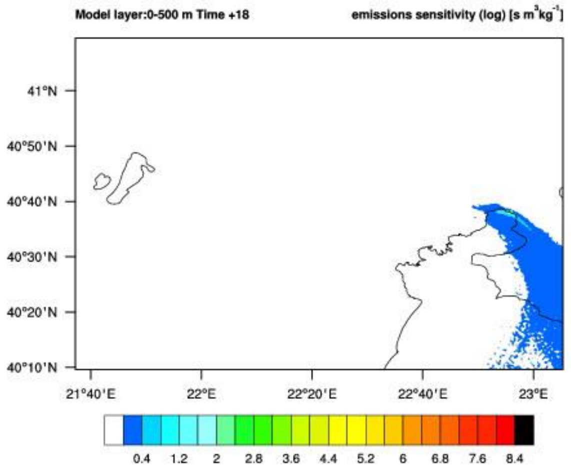
Model layer:0-500 m Time +18
emissions sensitivity (log) $[s\ m^3 kg^{-1}]$
41°N
40°50'N
40°40'N
40°30'N
40°20'N
40°10'N
21°40'E
22°E
22°20'E
22°40'E
23°E
0.4
1.2
2
2.8
3.6
4.4
5.2
6
6.8
7.6
8.4

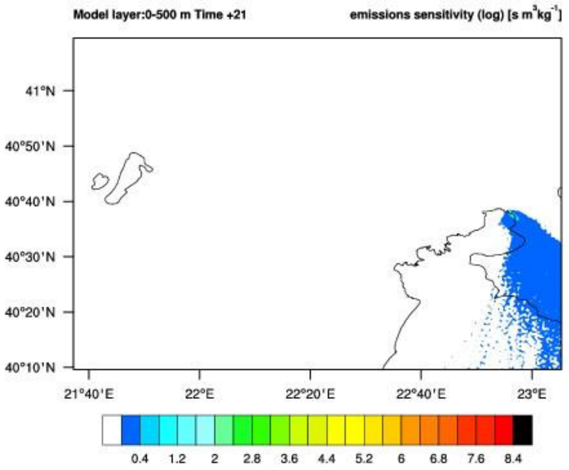
Model layer:0-500 m Time +21
emissions sensitivity (log) $[s\ m^3 kg^{-1}]$
41°N
40°50'N
40°40'N
40°30'N
40°20'N
40°10'N
21°40'E
22°E
22°20'E
22°40'E
23°E
0.4
1.2
2
2.8
3.6
4.4
5.2
6
6.8
7.6
8.4

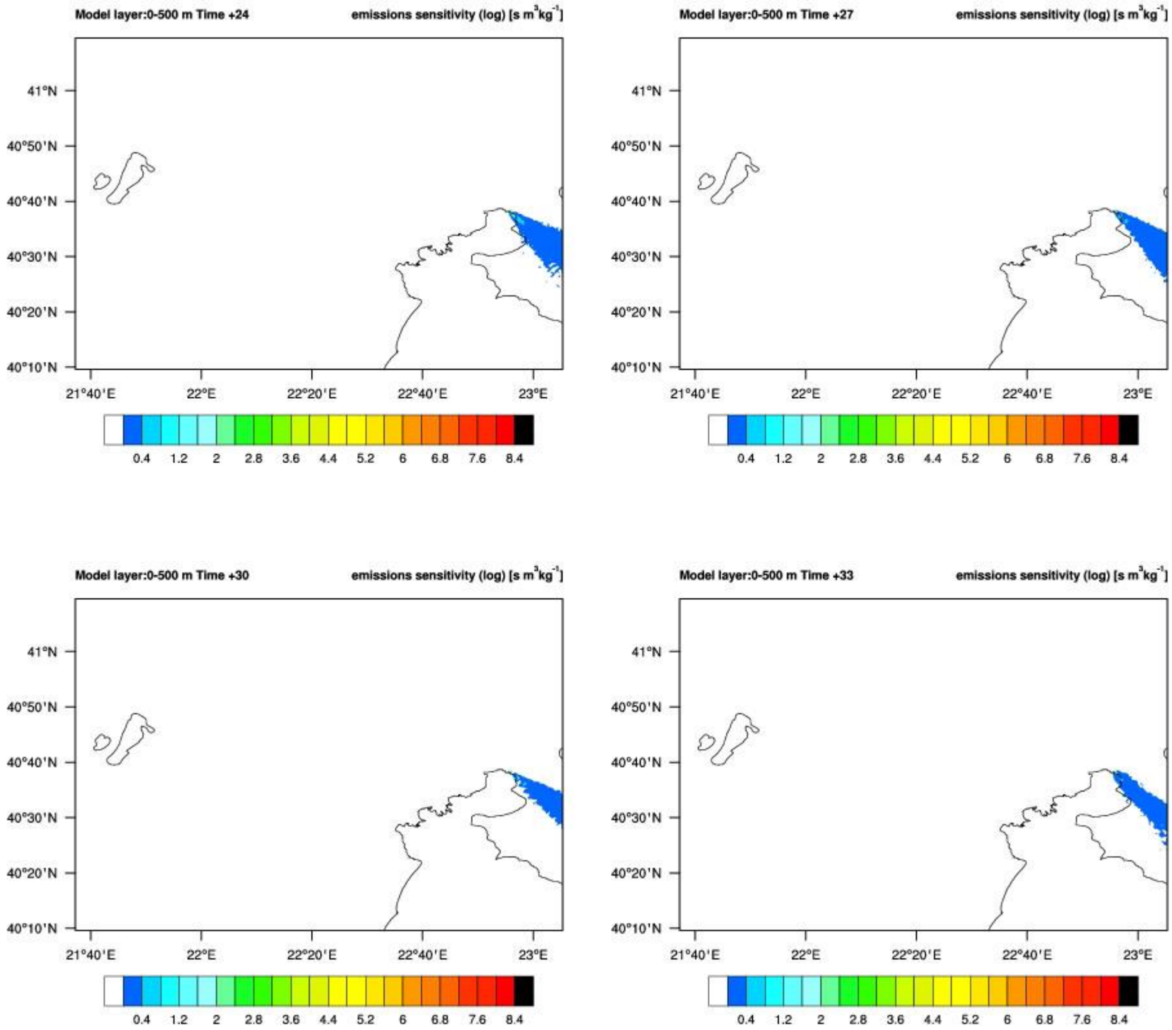

Figure 6.30. 11 to 13 February visualization of 3h output time-step based on Flexpart-WRF backward simulation from the sampling site PORT located west (Twelve storey Parking building near commercial Port of Thessaloniki) initiation time 12:00 UTC.

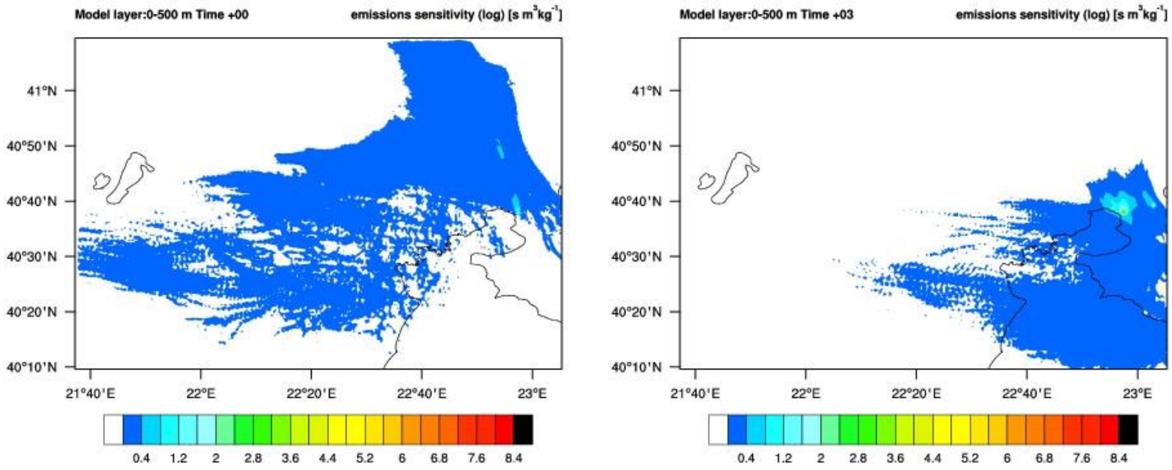

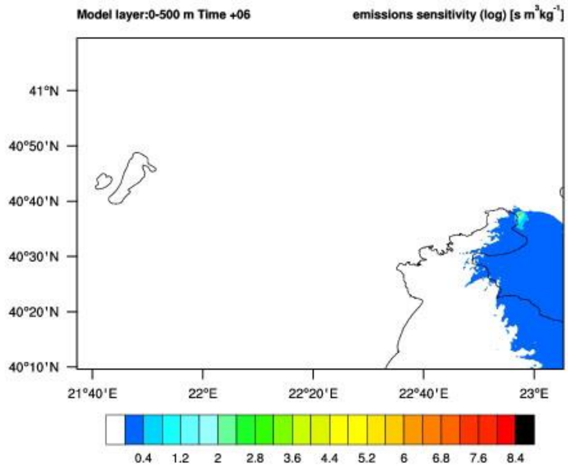
Model layer:0-500 m Time +06
emissions sensitivity (log) [s m³kg⁻¹]
41°N
40°50'N
40°40'N
40°30'N
40°20'N
40°10'N
21°40'E
22°E
22°20'E
22°40'E
23°E
0.4
1.2
2
2.8
3.6
4.4
5.2
6
6.8
7.6
8.4

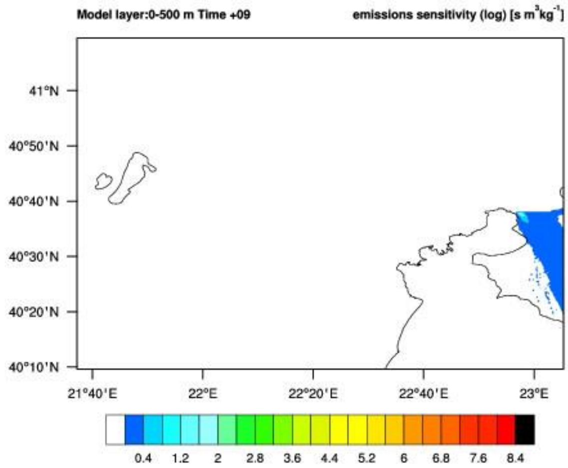
Model layer:0-500 m Time +09
emissions sensitivity (log) [s m³kg⁻¹]
41°N
40°50'N
40°40'N
40°30'N
40°20'N
40°10'N
21°40'E
22°E
22°20'E
22°40'E
23°E
0.4
1.2
2
2.8
3.6
4.4
5.2
6
6.8
7.6
8.4

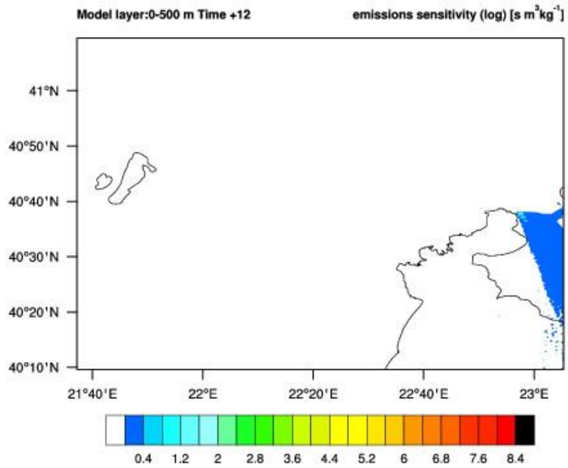
Model layer:0-500 m Time +12
emissions sensitivity (log) [s m³kg⁻¹]
41°N
40°50'N
40°40'N
40°30'N
40°20'N
40°10'N
21°40'E
22°E
22°20'E
22°40'E
23°E
0.4
1.2
2
2.8
3.6
4.4
5.2
6
6.8
7.6
8.4

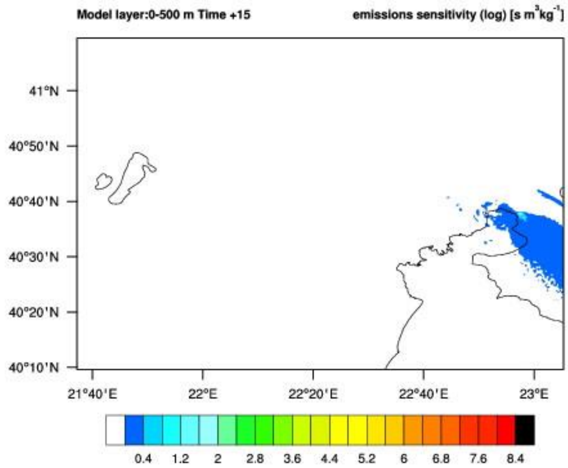
Model layer:0-500 m Time +15
emissions sensitivity (log) [s m³kg⁻¹]
41°N
40°50'N
40°40'N
40°30'N
40°20'N
40°10'N
21°40'E
22°E
22°20'E
22°40'E
23°E
0.4
1.2
2
2.8
3.6
4.4
5.2
6
6.8
7.6
8.4

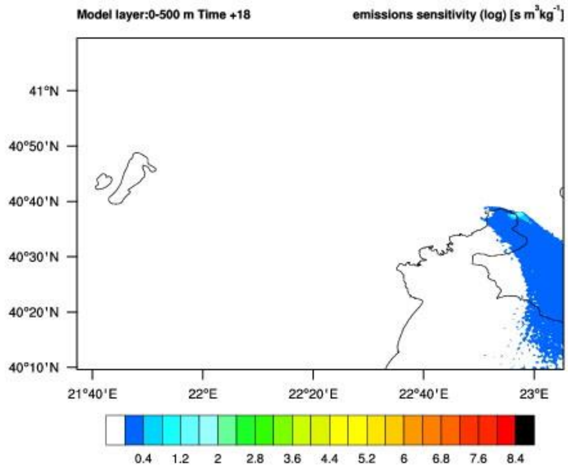
Model layer:0-500 m Time +18
emissions sensitivity (log) [s m³kg⁻¹]
41°N
40°50'N
40°40'N
40°30'N
40°20'N
40°10'N
21°40'E
22°E
22°20'E
22°40'E
23°E
0.4
1.2
2
2.8
3.6
4.4
5.2
6
6.8
7.6
8.4

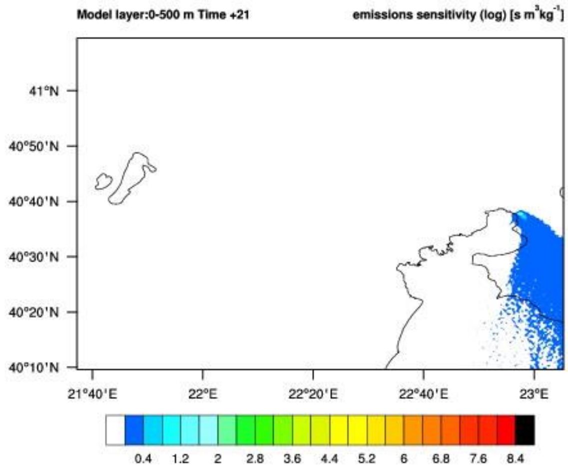
Model layer:0-500 m Time +21
emissions sensitivity (log) [s m³kg⁻¹]
41°N
40°50'N
40°40'N
40°30'N
40°20'N
40°10'N
21°40'E
22°E
22°20'E
22°40'E
23°E
0.4
1.2
2
2.8
3.6
4.4
5.2
6
6.8
7.6
8.4

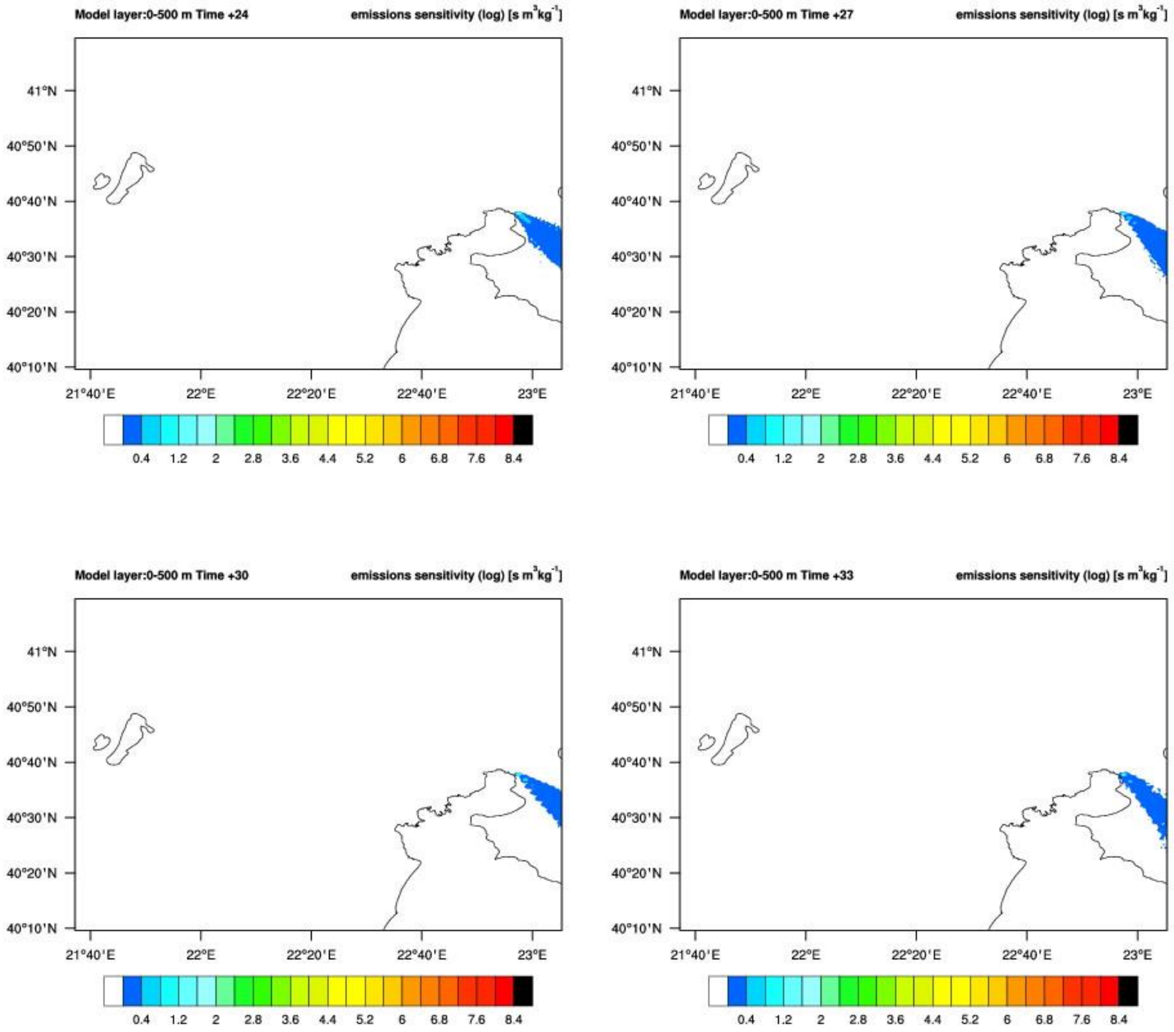

Figure 6.31. 11 to 13 February visualization of 3h output time-step based on Flexpart-WRF backward simulation from the sampling site AUTH located in city center (Aristotle University of Thessaloniki) initiation time 12:00 UTC.

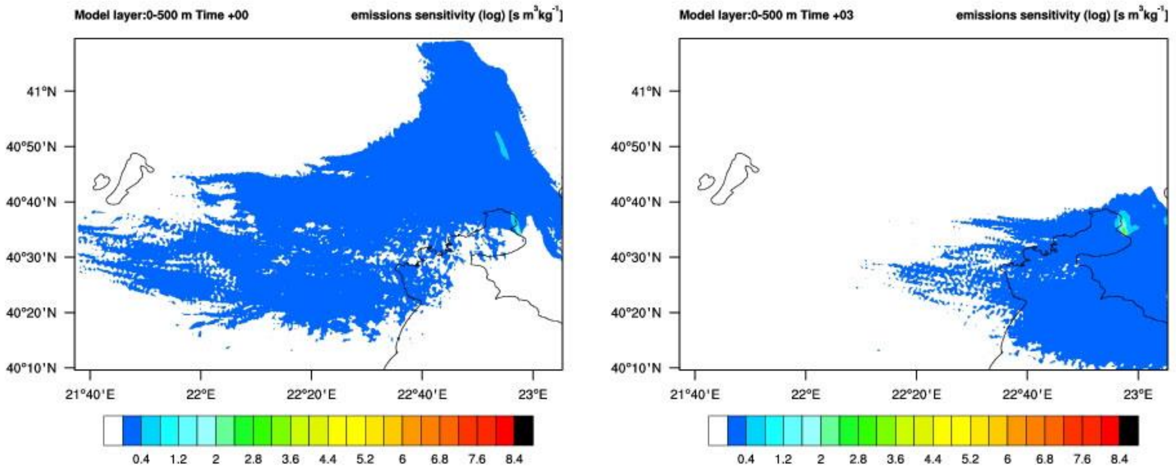

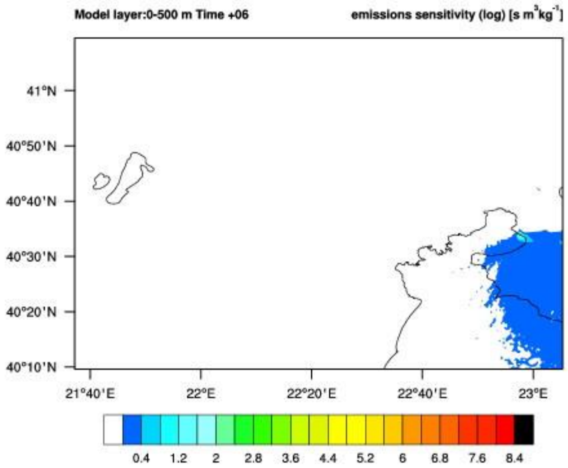
Model layer:0-500 m Time +06
emissions sensitivity (log) [s m^{3}kg^{-1}]
41°N
40°50'N
40°40'N
40°30'N
40°20'N
40°10'N
21°40'E
22°E
22°20'E
22°40'E
23°E
0.4 1.2 2 2.8 3.6 4.4 5.2 6 6.8 7.6 8.4

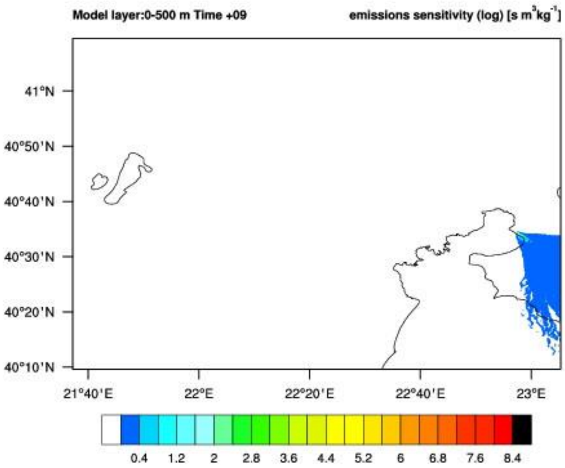
Model layer:0-500 m Time +09
emissions sensitivity (log) [s m^{3}kg^{-1}]
41°N
40°50'N
40°40'N
40°30'N
40°20'N
40°10'N
21°40'E
22°E
22°20'E
22°40'E
23°E
0.4 1.2 2 2.8 3.6 4.4 5.2 6 6.8 7.6 8.4

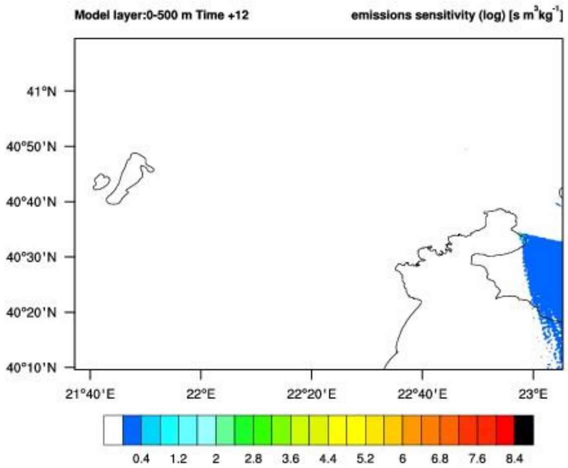
Model layer:0-500 m Time +12
emissions sensitivity (log) [s m^{3}kg^{-1}]
41°N
40°50'N
40°40'N
40°30'N
40°20'N
40°10'N
21°40'E
22°E
22°20'E
22°40'E
23°E
0.4 1.2 2 2.8 3.6 4.4 5.2 6 6.8 7.6 8.4

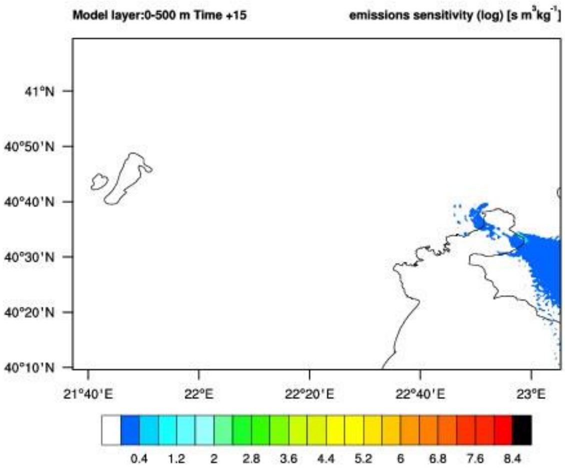
Model layer:0-500 m Time +15
emissions sensitivity (log) [s m^{3}kg^{-1}]
41°N
40°50'N
40°40'N
40°30'N
40°20'N
40°10'N
21°40'E
22°E
22°20'E
22°40'E
23°E
0.4 1.2 2 2.8 3.6 4.4 5.2 6 6.8 7.6 8.4

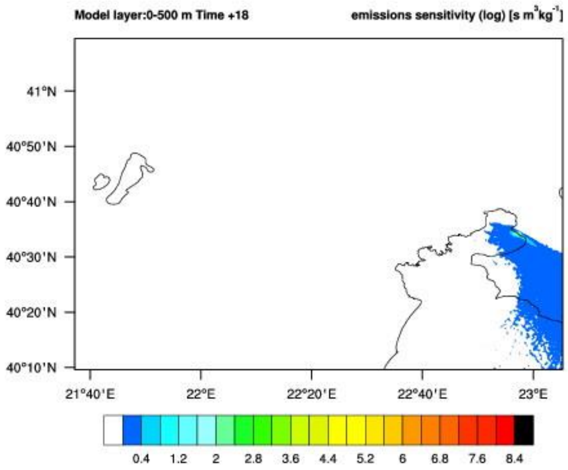
Model layer:0-500 m Time +18
emissions sensitivity (log) [s m^{3}kg^{-1}]
41°N
40°50'N
40°40'N
40°30'N
40°20'N
40°10'N
21°40'E
22°E
22°20'E
22°40'E
23°E
0.4 1.2 2 2.8 3.6 4.4 5.2 6 6.8 7.6 8.4

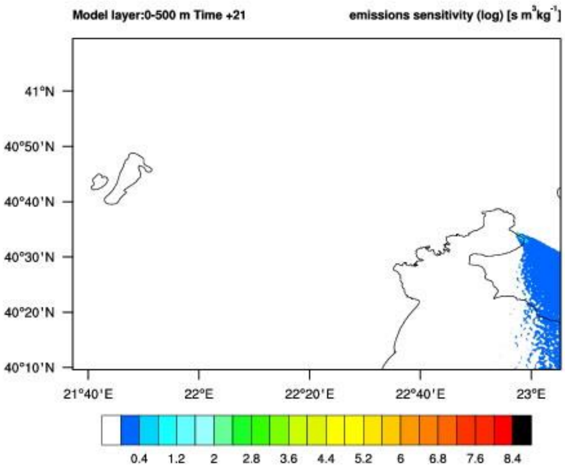
Model layer:0-500 m Time +21
emissions sensitivity (log) [s m^{3}kg^{-1}]
41°N
40°50'N
40°40'N
40°30'N
40°20'N
40°10'N
21°40'E
22°E
22°20'E
22°40'E
23°E
0.4 1.2 2 2.8 3.6 4.4 5.2 6 6.8 7.6 8.4

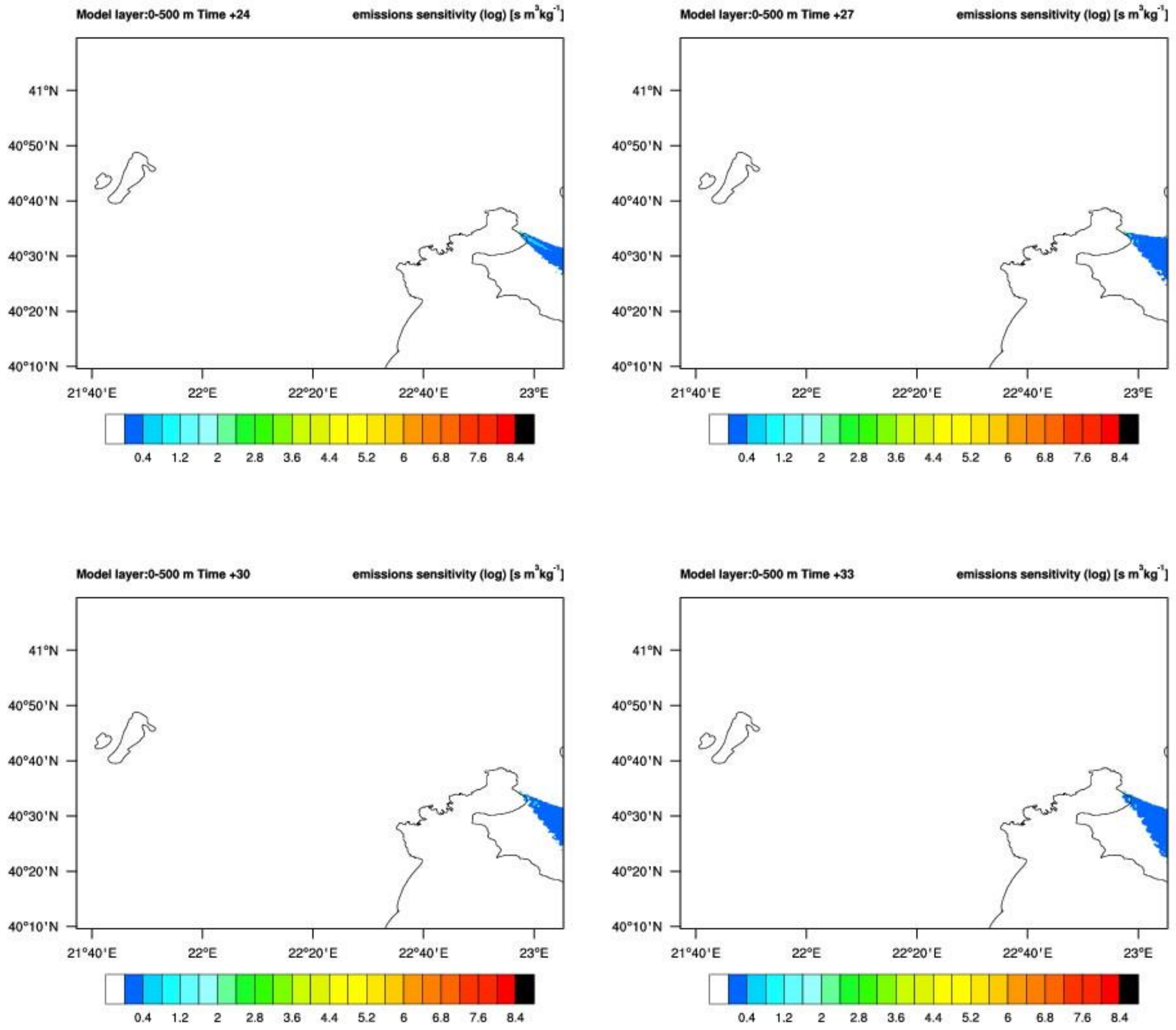

Figure 6.32. 11 to 13 February visualization of 3h output time-step based on Flexpart-WRF backward simulation from the sampling site KALAMARIA located South-East (Multi-storey building in Kalamaria region) initiation time 12:00 UTC.

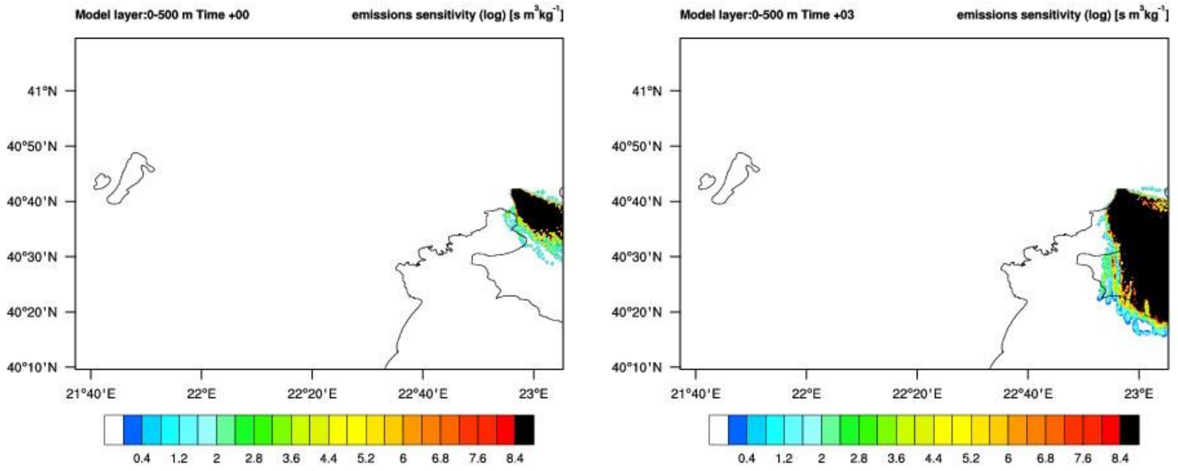

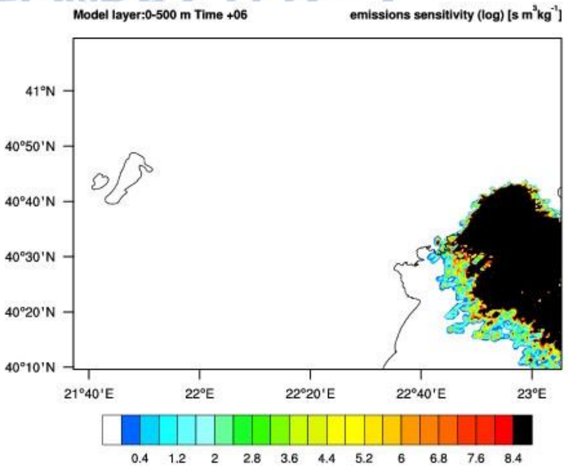
Model layer:0-500 m Time +06
emissions sensitivity (log) [s m^{3}kg^{-1}]
41°N
40°50'N
40°40'N
40°30'N
40°20'N
40°10'N
21°40'E
22°E
22°20'E
22°40'E
23°E
0.4 1.2 2 2.8 3.6 4.4 5.2 6 6.8 7.6 8.4

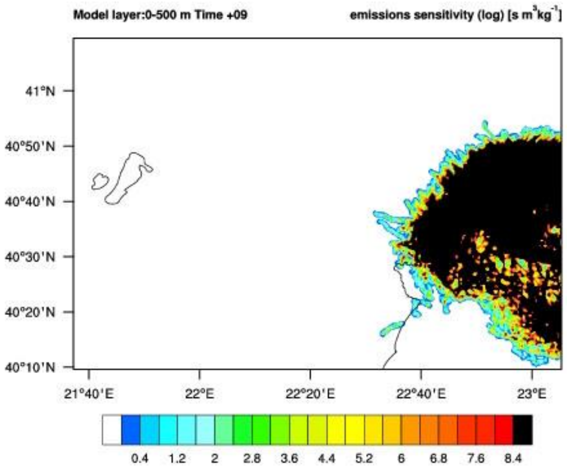
Model layer:0-500 m Time +09
emissions sensitivity (log) [s m^{3}kg^{-1}]
41°N
40°50'N
40°40'N
40°30'N
40°20'N
40°10'N
21°40'E
22°E
22°20'E
22°40'E
23°E
0.4 1.2 2 2.8 3.6 4.4 5.2 6 6.8 7.6 8.4

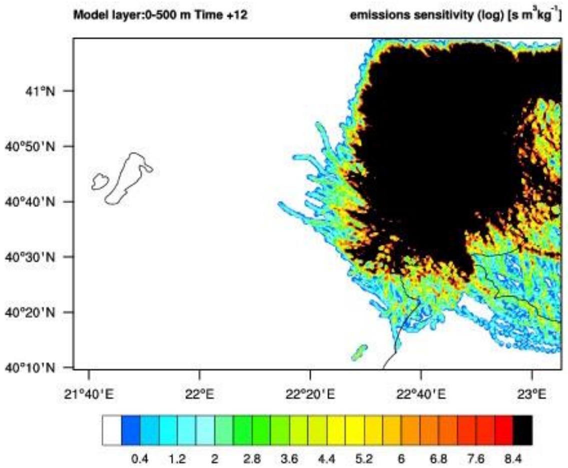
Model layer:0-500 m Time +12
emissions sensitivity (log) [s m^{3}kg^{-1}]
41°N
40°50'N
40°40'N
40°30'N
40°20'N
40°10'N
21°40'E
22°E
22°20'E
22°40'E
23°E
0.4 1.2 2 2.8 3.6 4.4 5.2 6 6.8 7.6 8.4

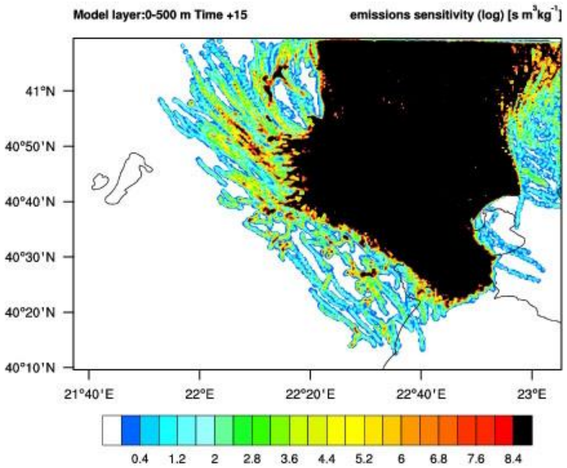
Model layer:0-500 m Time +15
emissions sensitivity (log) [s m^{3}kg^{-1}]
41°N
40°50'N
40°40'N
40°30'N
40°20'N
40°10'N
21°40'E
22°E
22°20'E
22°40'E
23°E
0.4 1.2 2 2.8 3.6 4.4 5.2 6 6.8 7.6 8.4

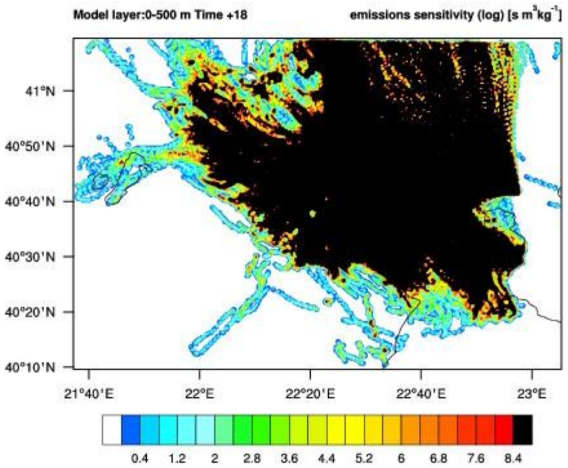
Model layer:0-500 m Time +18
emissions sensitivity (log) [s m^{3}kg^{-1}]
41°N
40°50'N
40°40'N
40°30'N
40°20'N
40°10'N
21°40'E
22°E
22°20'E
22°40'E
23°E
0.4 1.2 2 2.8 3.6 4.4 5.2 6 6.8 7.6 8.4

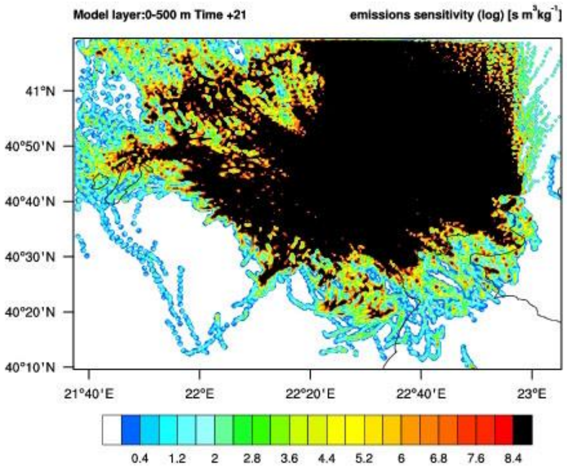
Model layer:0-500 m Time +21
emissions sensitivity (log) [s m^{3}kg^{-1}]
41°N
40°50'N
40°40'N
40°30'N
40°20'N
40°10'N
21°40'E
22°E
22°20'E
22°40'E
23°E
0.4 1.2 2 2.8 3.6 4.4 5.2 6 6.8 7.6 8.4

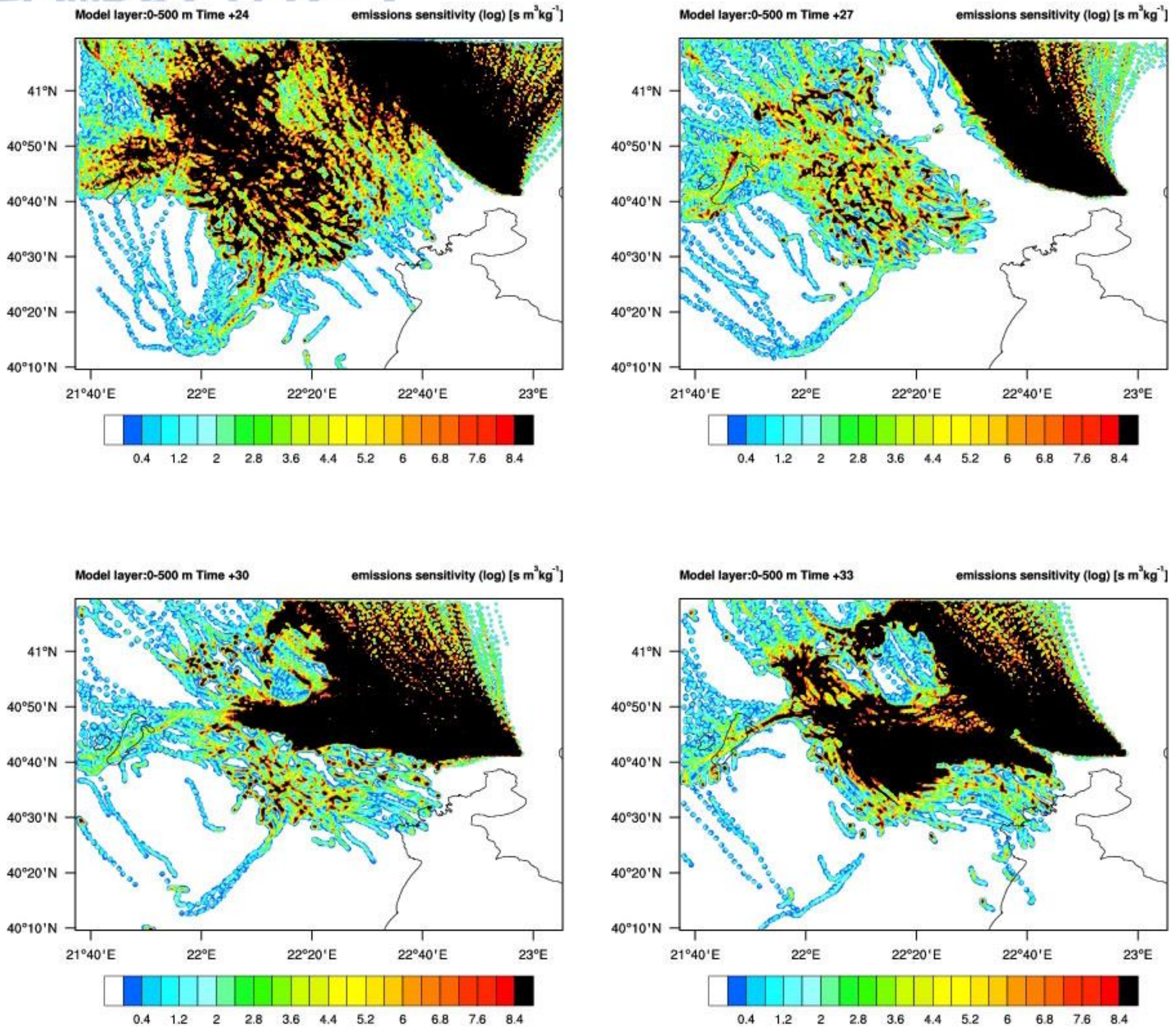

Figure 6.33. 11 to 13 February visualization of 3h output time-step based on Flexpart-WRF forward simulation from emitting site located North in city suburbs initiation time 12:00 UTC.

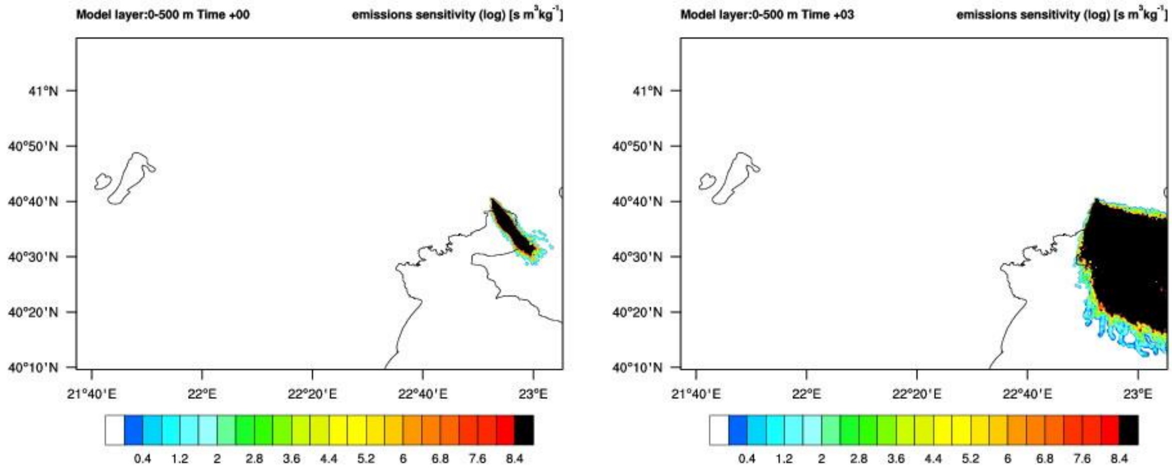

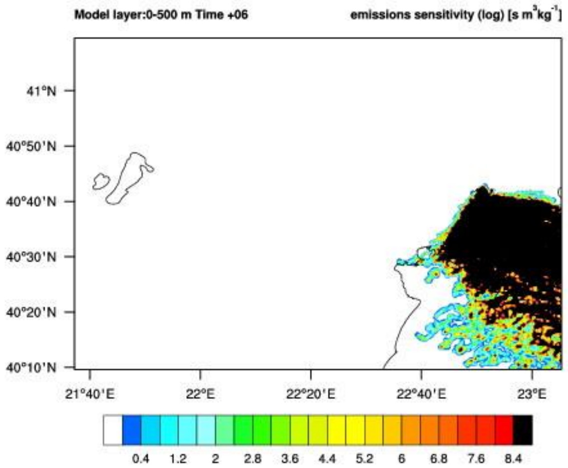
Model layer:0-500 m Time +06
emissions sensitivity (log) [s m³kg⁻¹]
41°N
40°50'N
40°40'N
40°30'N
40°20'N
40°10'N
21°40'E
22°E
22°20'E
22°40'E
23°E
0.4 1.2 2 2.8 3.6 4.4 5.2 6 6.8 7.6 8.4

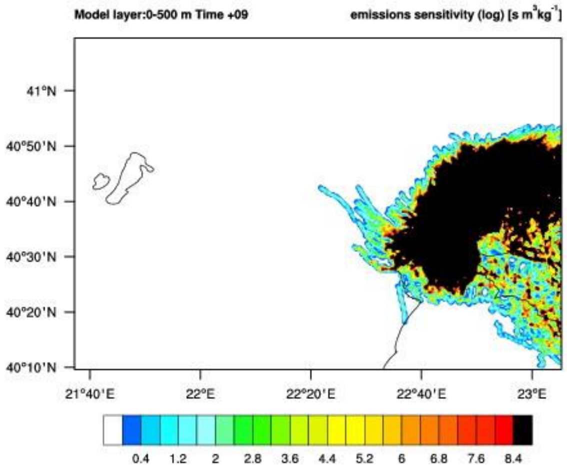
Model layer:0-500 m Time +09
emissions sensitivity (log) [s m³kg⁻¹]
41°N
40°50'N
40°40'N
40°30'N
40°20'N
40°10'N
21°40'E
22°E
22°20'E
22°40'E
23°E
0.4 1.2 2 2.8 3.6 4.4 5.2 6 6.8 7.6 8.4

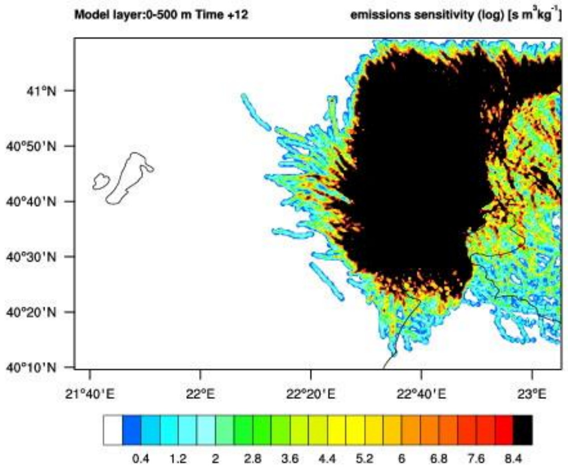
Model layer:0-500 m Time +12
emissions sensitivity (log) [s m³kg⁻¹]
41°N
40°50'N
40°40'N
40°30'N
40°20'N
40°10'N
21°40'E
22°E
22°20'E
22°40'E
23°E
0.4 1.2 2 2.8 3.6 4.4 5.2 6 6.8 7.6 8.4

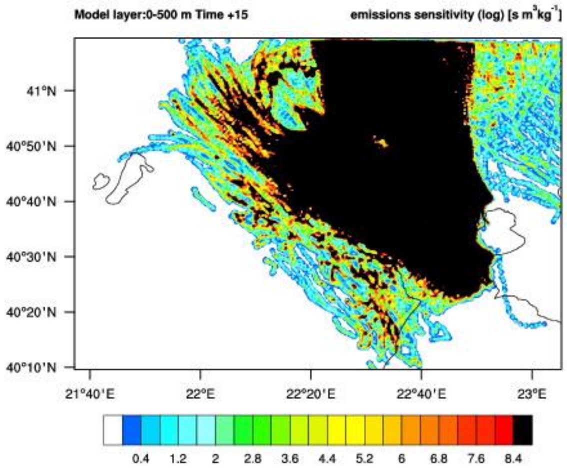
Model layer:0-500 m Time +15
emissions sensitivity (log) [s m³kg⁻¹]
41°N
40°50'N
40°40'N
40°30'N
40°20'N
40°10'N
21°40'E
22°E
22°20'E
22°40'E
23°E
0.4 1.2 2 2.8 3.6 4.4 5.2 6 6.8 7.6 8.4

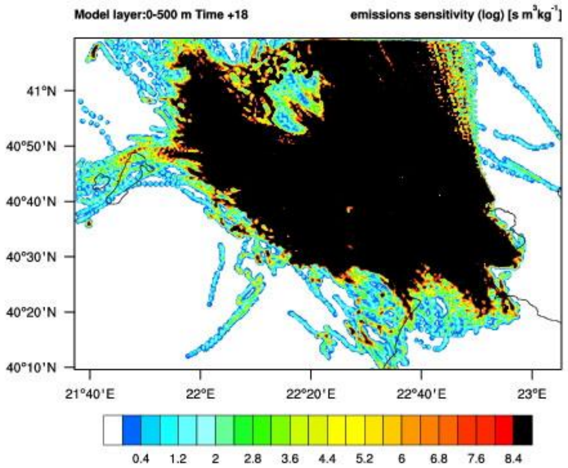
Model layer:0-500 m Time +18
emissions sensitivity (log) [s m³kg⁻¹]
41°N
40°50'N
40°40'N
40°30'N
40°20'N
40°10'N
21°40'E
22°E
22°20'E
22°40'E
23°E
0.4 1.2 2 2.8 3.6 4.4 5.2 6 6.8 7.6 8.4

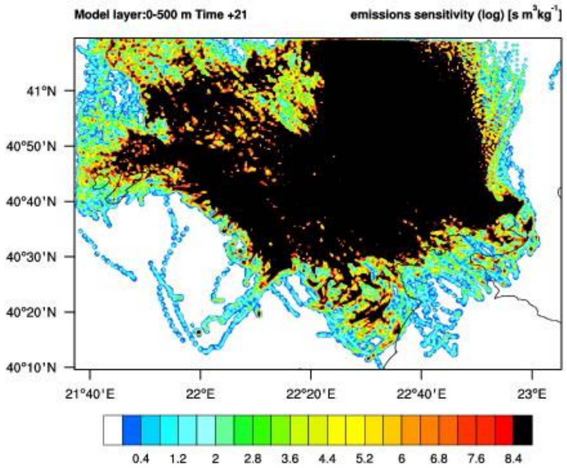
Model layer:0-500 m Time +21
emissions sensitivity (log) [s m³kg⁻¹]
41°N
40°50'N
40°40'N
40°30'N
40°20'N
40°10'N
21°40'E
22°E
22°20'E
22°40'E
23°E
0.4 1.2 2 2.8 3.6 4.4 5.2 6 6.8 7.6 8.4

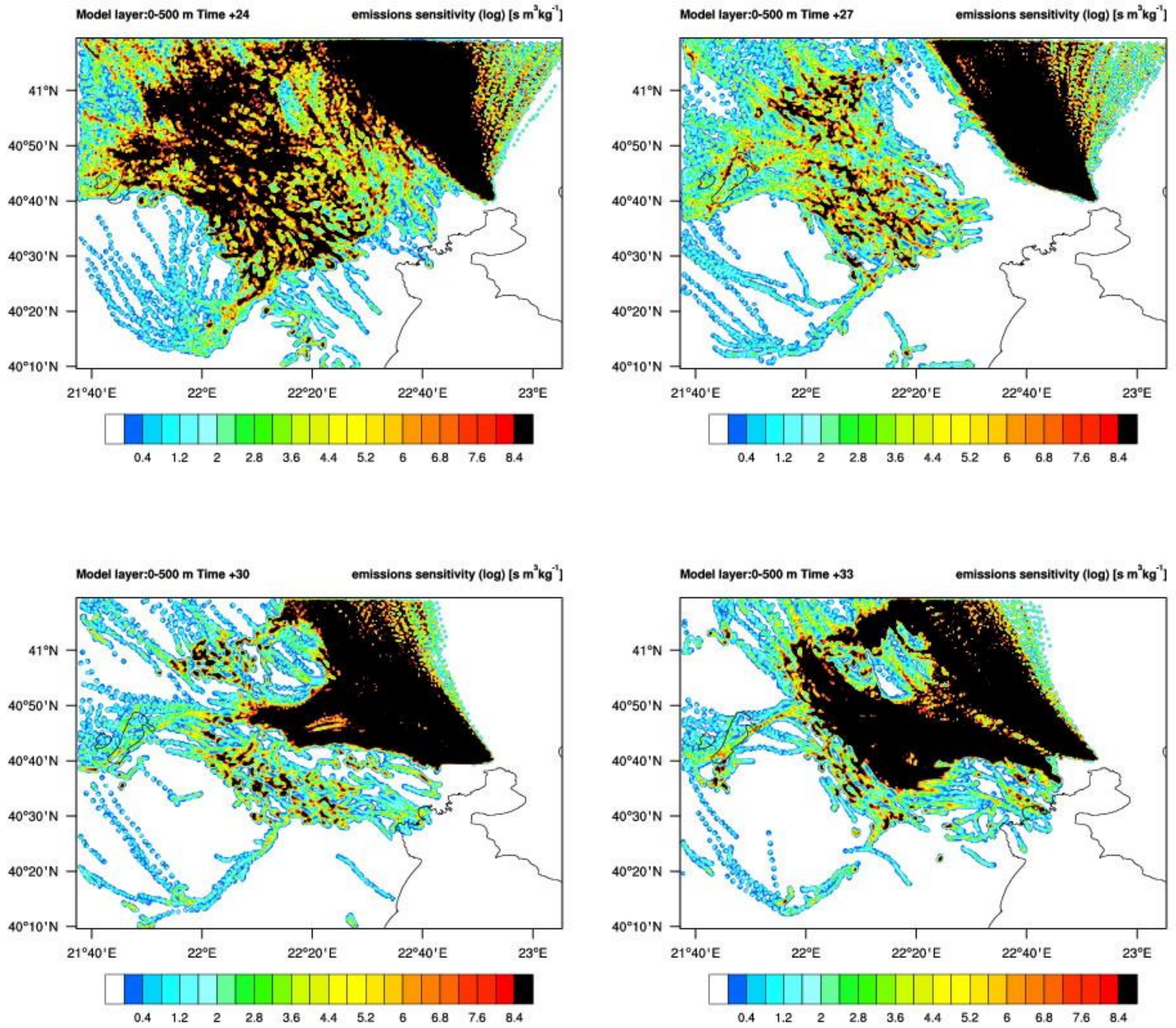

Figure 6.34. 11 to 13 February visualization of 3h output time-step based on Flexpart-WRF forward simulation from emitting site located West in the industrial area of the city initiation time 12:00 UTC.

6.9. Conclusions

It can be clearly observed from the visualized results of the Flexpart-WRF that the dispersion that resulted from the conveyance of pollutants is evident due to favoring meteorological conditions and from the emitting sources that contributed to the intensity of the phenomenon. The evolution and extension of the plume is related to the chemical and morphological analyses conducted that indicated increased concentrations of heavy metals. The impact on air quality is investigated for selected dates in 2012-2013 in the greater area of the city of Thessaloniki with the use of the Lagragian particle dispersion model FLEXPART driven by high resolution simulation of 0.6km for d3 with WRF model input. All our sampling locations indicated specific days with intensively high heavy metals concentrations, the simulations were made for 9-11January, 13-15January, 3January-2February, 3-5February and 11-13February. For AUTH - Aristotle University of Thessaloniki, located in the city center of Thessaloniki, the model run backwards and from our visualizations for the days of interest we can see the dispersion of the particles plume originating westerly from industrial area and northerly from specific industrial areas affecting our sampling site. This can be seen also with the forward runs, simulating releases from the emitting areas located westerly and northerly. For PORT - multi-storey parking lot located westerly near the commercial port of the city, the model run backwards indicating a more intensive contribution from industrial area located westerly due to the closest distance of the sampling location, without excluding the contribution of the northerly industries and the relocation of an amount towards the other sampling sites situated easterly from the location. Also forward runs originating from the possible emitting sites seem to affect that location as well, justifying the high concentration levels of analyzed heavy metals. Finally for KALAM – multi-storey apartments building located easterly in Kalamaria district it can be noted that there is a direct transfer from industrial area located westerly and northerly as well, with a partial part of the plume hovering above a part of Thermaikos gulf and transferring the plume to our eastern sampling location apart from the other sites and also from our forward runs for the possible emitting sites that show a quite intensive dispersion phenomenon affecting directly the eastern sampling location of Kalamaria. All the above visualizations from our simulations clearly depict and justify the transfer, from western and northern industrial areas towards our sampling sites, of dispersed polluted dust particles that we chemically and mineralogically analyzed resulting in high concentrations of toxic metals (as mentioned in previous chapter).

CHAPTER 7: CASE STUDY 5

7.1. Introduction

In chapter 7 the application of the FLEXPART-WRF system to verify model performance in a case study of a wildfire episode at mount Athos in August 2012 on the air quality of the city of Thessaloniki, is presented. This case study was implemented in order to verify the ideal set up for the use of the Flexpart-WRF in the previous chapter. Thus, a wildfire case was selected to be examined regarding the impact on the air quality of the city of Thessaloniki from an intense forest fire episode that occurred in the area of Mount Athos (Regional Unit of Halkidiki) during 8 to 13 August 2012 near the expanse of Chilandrinou Abbey in Monoxylites region. Forest fires burn considerable areas of the south European landscape with intensive occurrences during summer periods with most of the fire episodes taking place in the Mediterranean region. One of the several disturbing effects of forest fire smoke is that it has a significant impacts on air quality and human health since large amounts of pollutants are emitted into the atmosphere during the process. Smoke from forest fires includes significant amounts of carbon dioxide (CO_2), carbon monoxide (CO), methane (CH_4), nitrogen oxides (NOx), ammonia (NH_3), particulate matter (PM), non-methane volatile organic compounds (VOC’s), sulphur dioxide (SO_2) and other chemical species (Miranda et al. 2005). The effects of these emissions vary at different levels affecting from the contribution to the greenhouse effect to the occurrence of local atmospheric pollution episodes (Miranda et al. 1994, Borrego et al. 1999, Simmonds et al. 2005). In a changing climatic scenario forest fires may escalate triggering even larger sources of air pollutants to the atmosphere (Amiro et al. 2001, Carvalho et al. 2007). In order to identify and quantify the influence of the fire emitted particles and gases on the air quality of the city of Thessaloniki an integrated approach was applied using the mesoscale meteorological model WRF driven with analysis data from the ECMWF to provide the meteorological input data for the atmospheric dispersion model FLEXPART.

7.2 Data and Methodology

7.2.1 Data

Weather Research and Forecasting model (WRF) is a non-hydrostatic mesoscale numerical meteorological model with the Advanced Research dynamic solver (WRF-ARW Version 3.2.0, Skamarock et al. 2008, Wang et al. 2010) that was utilized in the numerical experiments. The ARW solves the fully compressible, non-hydrostatic Euler equations using a finite-difference scheme on an Arakawa C-grid staggering in the horizontal plane and a terrain-following, dry hydrostatic pressure vertical coordinate (Porter and Ashworth 2010).

Global data from the ECMWF was used as input into WRF to increase the resolution focusing on the local topography of the studied domain in order to provide output data to feed FLEXPART**.** ECMWF integrates vast number of synoptic observations from weather stations, meteorological balloons, satellites and feed them into a global model, which run continuously in forecast mode and also produces re-analysis of older data. WRF utilizes nested grids with different resolutions in order to get better predictions in the area of interest sustaining enough data for the surroundings as well.

FLEXPART, is a Lagrangian particle dispersion model designed for calculating the long-range and mesoscale dispersion of air pollutants from point sources (Stohl et al. 2010) capable of forward and backward trajectory simulations of particles (presented as infinitively small air parcels) released from point, line or volume sources. Different versions of the model enable the use of input data from global numerical weather prediction models from ECMWF, NOAA (GFS) as well as mesoscale models (MM5, WRF, COSMO). Removal processes incorporated into the model include radioactive decay, dry and wet deposition and OH reaction (Stohl et al. 2005).

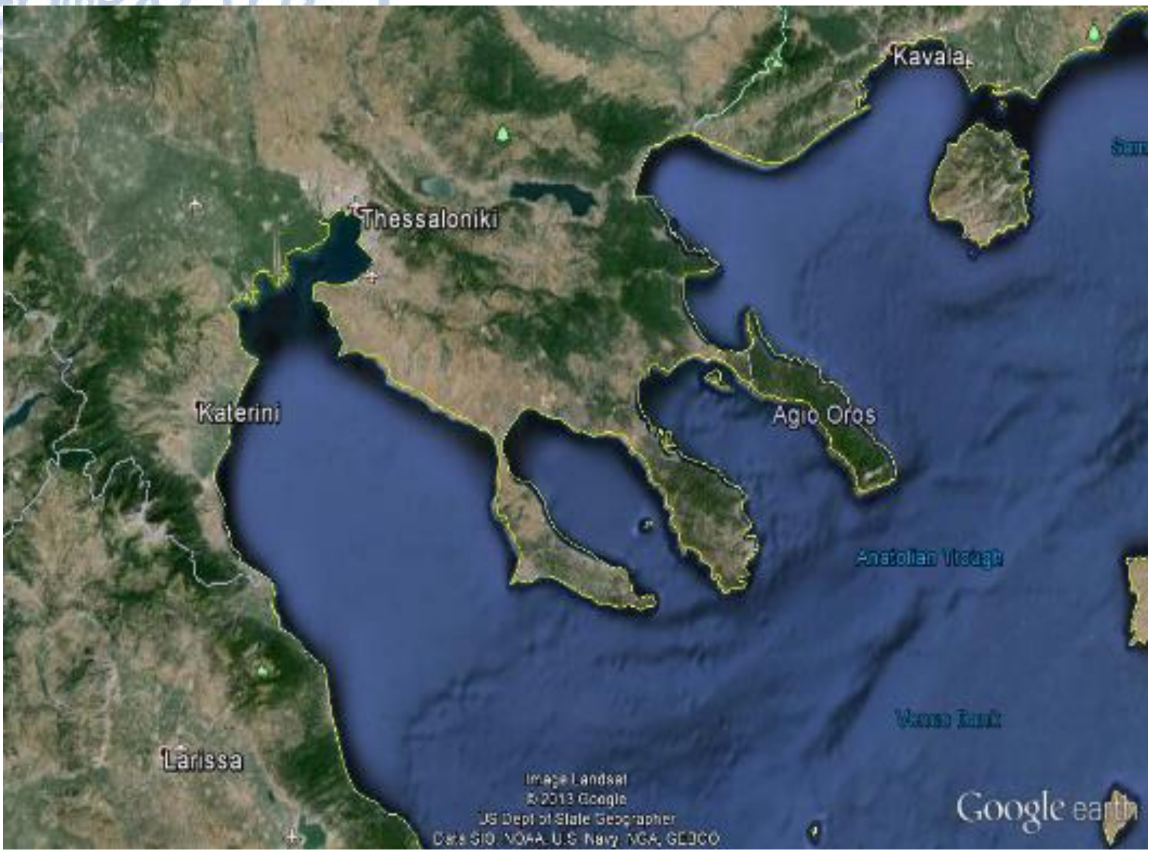

Figure 7.1. The high-resolution domain (d3) with a resolution of 1.3 km used for the WRF-ARW experiments.

7.2.2 Methodology

For WRF a one-way interactive model domains covering a part of eastern Europe, Greece and the major area of Central Northern Greece (Macedonia) at horizontal grid-spacing of 11.7 km x 11.7 km (d1) , 3.9 km x3.9 km (d2) and 1.3x1.3 km (d3) (Figure 7.1) have been used, utilizing the staggered Arakawa C grid. As initial and lateral boundary conditions for the coarse domain, ECMWF 6-hourly analyses were used .The analyses were available on a 0.125^o x 0.125^o regular grid. The necessary fields were retrieved at and near the surface and on the pressure levels of 1000, 950, 925, 900, 850, 800, 700, 600, 500, 400, 300, 250, 200, 150, 100, 70, 50, 30, 20, 10 mb. WRF was initialized in 08/08/12 at 00:00 and terminated in 13/08/2012 at 18:00 with output every180 min for d1 and 60 min for d2 and d3, respectively.

The d3 data output with 1.3 km resolution is utilized as input for FLEXPART for the period 08-13/08/2012. FLEXPART was set up to run forward and the particles were released in the area of the case study for 1h at pressure levels from 0-1 km at 08/08/2012 between 22:00 and 23:00 pm at 8 vertical levels starting from 1 km with 3h output and 180 min sampling rate.

7.3. Results

The Hovmöller diagram for near surface wind speed at 10 m from both ECMWF (Figure 7.2) and WRF (not shown) between 08 and 13/08/12 indicates that the day after the initiation of the forest fire there are easterly winds (6 m/s) that contributed to the resurgence and the escalation of the fire intensity that lifted the fire plume and made the dispersion even more intense. This is further evident from the output results of FLEXPART (Figure 7.3) which clearly indicates the plume formation and particle dispersion of the fire that affected southeastern Thessaloniki’s area. Finally the intensity of the forest fire phenomenon and the direction of the plumes at one point can be observed and clearly depicted in (Figure 7.4) from the satellite views from the NASA Earth Observing System Data and Information System (EOSDIS).The dispersion modeling experiment was also accompanied with measurements of particulate matter and gases from the network of air pollution monitoring stations of Thessaloniki district. From the analysis of the measurements an increase in particulate matter and CO concentrations were mainly observed at stations of eastern Thessaloniki. The dispersion modeling analysis indicated that the weather conditions were such that favored the transport and dispersion of pollutants emitted from the forest fire at the region of Monoxilitis Halkidiki and affected the greater area of Thessaloniki.

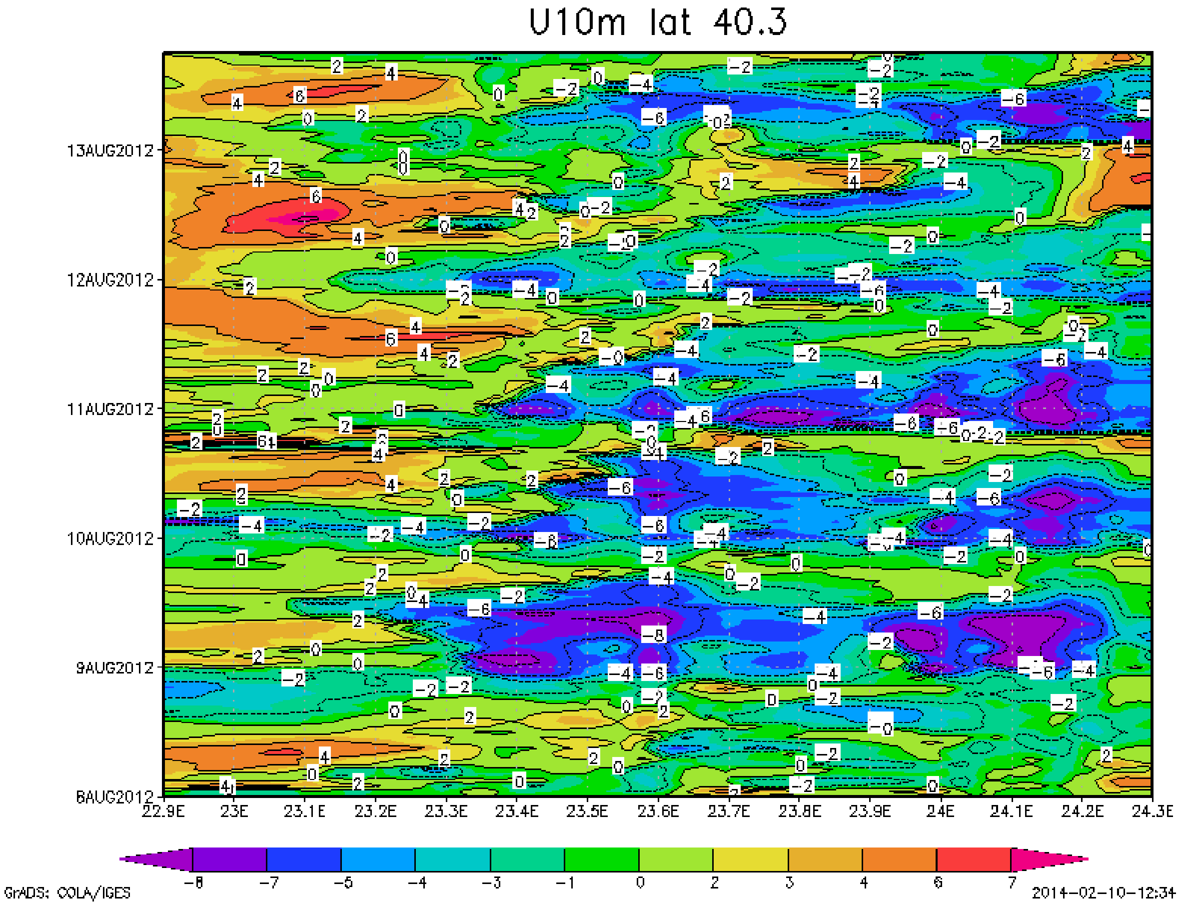

Figure 7.2. Hovmöller diagram (time versus longitude) for near surface wind speed at 10 m based on ECMWF. The area of the forest fire occurrence is located at longitude around 24.1 E.

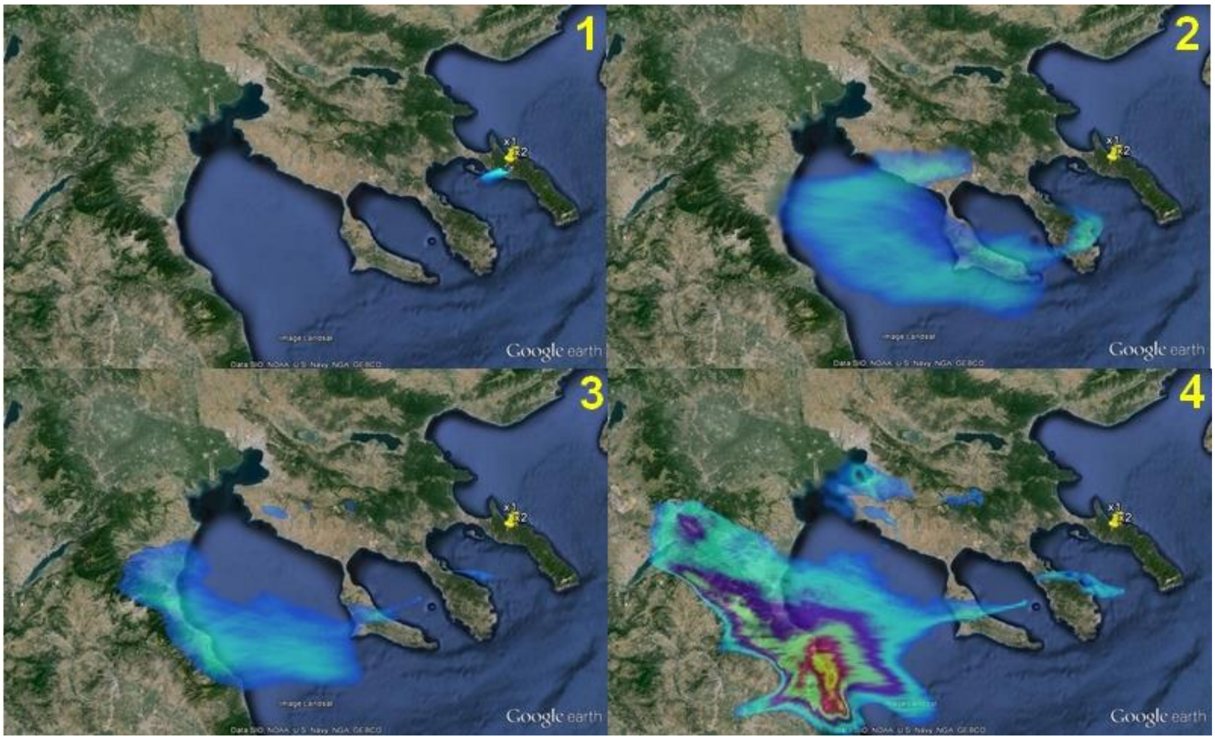

Figure 7.3. Visualized output of dispersion by FLEXPART -WRF on (1) 8/8/2012 at 22:00 UTC, (2) 9/8/12 at 02:00 UTC, (3) 9/8/12 at 03:00 UTC and (4) 9/8/12 at 04:00 UTC.

Figure 7.4. Nasa (EODIS) satellite photo on 09/08/2012.

7.4. Conclusions

This work focus is set in finding the ideal set up for Flexpart-WRF performance in order to implement the model to identify toxic metals possible emitting sources that resulted from mineralogical and chemical analyses of selected sampling sites in the city of Thessaloniki as mentioned in previous chapters.

To do so we investigated a forest fire episode that occurred in the area of Mount Athos (Regional Unit of Chalkidiki) from 08/08/12 to 13/08/12 and the impact on air quality of the greater area of the city of Thessaloniki with the use of the Lagragian particle dispersion model FLEXPART driven by high resolution simulation with WRF model. Our preliminary results indicate a satisfactory model's performance in capturing the evolution and the geographical extension of the plume which is further supported by satellite measurements from the NASA Earth Observing System Data and Information System as well as particulate matter and CO concentrations mainly at stations of eastern Thessaloniki.

CHAPTER 8: CONCLUSIONS

In a struggle to achieve better living standards for all we cannot be ill-informed of the space that surrounds us, also known as the environment. Nowadays modern life has intensive rhythms and demands, but nothing comes without a price. Since balance is a basic principle of nature the loss of that balance is now pretty easily observed. Uncontrolled pollution levels from industrial areas as well as other factors affected by the economic crisis that struck our daily life on local and global scale, offer a severe outcome to the environment with augmented levels of atmospheric pollution. Fortunately, European Union has set alert and alarm limits in accordance with rules - legislations and directives but in many cases, these are exceeded. Air pollution emissions and concentrations have increased in many areas worldwide, largely impacting health and ecosystems. In many European Union state members, air quality is still not adequately utilized in many aspects, despite reductions in emissions and ambient concentrations.

Greece being a state member of European Union is subjected to those rules and legislations. Thessaloniki is the second largest city of Greece and one of the most densely populated cities in Europe accounting for approximately 16,000 inhabitants per km^2. The city is surrounded by hills to the north and mount Hortiatis (1,200 m height) to the east. Numerous residential suburbs surround the city and several industrial activities (oil refining and petrochemical facilities, metal scrap incineration, iron and steel manufacturing, electrolytic MnO_2 production, cement and lime production, quarry works) are located at variable distances to the Western, Northwest and North parts of the city.

The present study analyzes the impact of atmospheric particle dispersion, as well as their chemical and mineralogical analysis in the wider region of Thessaloniki during 2012-2013. Regarding air pollutants, dust particles play an important role for PM concentrations which with favoring meteorological conditions play a key role to the dispersion of particles all over the city.

In order to analyze all the aspects, we decided to collect dust samples from roof top and street levels, from three (3) sampling locations surrounding the city's structural web. First sampling site (PORT - multi-storey parking lot building) located westerly near the commercial port and closer to the industrial area of the city. Second sampling site (AUTH - Aristotle University of Thessaloniki), located in the city center of Thessaloniki and finally, third sampling site (KALAM – multi-storey apartments building), located easterly in Kalamaria district. Sampling was carried out during the period June 2012 - May 2013, twice a month every 15 days. From each sample 50-150 g of powder was collected, wiping an area of 1 m^2 using sterilized collectible instruments. The samples were dried in an oven at 35 °C for 3 days. After that the <63 μm fraction was separated by sieving for further investigation.

Initially we investigated the case study of impact of uncontrollable burning of biomass for residential heating in the atmosphere of the city of Thessaloniki. Mineralogical, morphological and chemical analysis was conducted in precipitated falling dust samples collected from rooftop levels for out selected three sampling locations (Kalamaria, Aristotle University, and Port). By comparing powder samples collected from the same sites during September 2012 and December 2011, we found an increase in organic content, which was supported by the meteorological conditions, resulted in augmented pollution levels. The fallen dust mainly consists of inorganic origin components from the corrosion of building materials without excluding material contribution from air suspending fumes. This resulted in increased levels of pollutants mainly caused by the uncontrolled burning of biomass burners for domestic heating.

The findings of this research fired the main study plan which was to examine the annual variation of falling dust particles and their mineralogical, chemical composition and organic material in the city of Thessaloniki during 2012-2013 for a refined number of our total samples. Mineralogical analysis and organic material were conducted in the <63 μm fraction of falling dust samples collected from rooftop levels from our initial three sampling locations, East, Central and West Thessaloniki. This study indicated that calcite and quartz are the major inorganic constituents of the <63 μm fraction, with the latter being potentially dangerous for public health. The fallen dust mainly consists of inorganic origin components from the corrosion of building materials without excluding material contribution from air suspending fumes.

A significant increase in the organic load of dust samples had been observed for winter 2012-13 compared to the other seasonal sampling periods and to previous winter and autumn monthly periods. Additionally the chemical analysis indicated increased levels of toxic metals such as Ag (Silver), As (Arsenic), B (Boron), Ba (Barium), Be (Beryllium), Bi (Bismuth),Cd (Cadmium), Co (Cobalt), Cr (Chromium), Cu (Copper), Ga (Gallium), Hg (Mercury) La (Lanthanum), Mn (Manganese), Mo (Molybdenum), Ni (Nickel), Pb (Lead), Sb (Antimony), Sc (Scandium), Sr (Strontium), Te (Tellurium), Th (Thorium), Tl (Thallium), U (Uranium), V (Vanadium), W (Tungsten), Y (Yttrium), Zr (Zirconium) and Zn (Zinc).

From all the identified trace elements we chose those with the highest concentrations compared to mean average concentrations from continental crusts, soil levels and EU mean topsoil levels. Our findings indicated toxic heavy metals like As, Bi, Cd, Cr, Cu, Ni, Pb, Sb and Zn all having severe toxic effects to health and the environment when they re-suspend and inhaled via respiratory tract. These toxic metals capable of causing cancer, were monitored at such increased levels in the city of Thessaloniki definitely affecting the environment and augmenting the pollution levels at a very large magnitude. Possible emitting sources may be at one extent from road dusts contribution that mainly deprives from local building sites, pavements, tyres and braking systems wear, generating coarse particles that are either emitted directly to the air or being re-suspended on road dust surface depot. It should be taken into consideration that they are capable of disintegrating their initial coarse structure into that of a finer inhalable one due to passing vehicles contribution.

On another extent additional factors may contribute from the industrial sectors of the city with the aid of favoring meteorological conditions. In order to trace possible external sources apart from those already known to contribute from road dusts we implemented the atmospheric particle dispersion model FLEXPART with high resolution data from the numerical model WRF. FLEXPART-WRF system was thus utilized for a source-receptor approach of atmospheric particle dispersion in order to track down backward and forward in time the emitting sources that contribute to our results.

The atmospheric particle dispersion model run for selected dates of January and February 2013 for all of our sampling sites location taking under consideration possible emitting locations that are from the industrial zone situated westerly of the city and also industrial areas situated northerly on the city. For those possible emitting scenarios, the model run forward in order to identify possible contribution of the industrial areas to our sampling sites while for the sampling sites it run backward to track the origin of the emissions.

The evolution and extension of the plume is related to the chemical and morphological analyses we conducted that indicated increased concentrations of heavy metals. The impact on air quality is investigated for selected dates in 2012-2013 in the greater area of the city of Thessaloniki with the use of the Lagragian particle dispersion model FLEXPART driven by high resolution simulation of 0.6 km for d3 with WRF model input.

The results of the FLEXPART-WRF showed a clear contribution depriving from the two industrial areas located westerly and northerly of the city in both forward and backward runs identifying the contribution of re-suspended particles from the industrial areas, the dispersion that resulted from the conveyance of pollutants is evident due to favoring meteorological conditions and from the emitting sources that contributed to the intensity of the phenomenon.

ACKNOWLEDGEMENTS

I would like to express special thanks for the financial support during my PhD studies, under the scientific research projects, training courses and scholarships :

1. "Bioactivity of airborne particulates in relation with their size, morphology and chemical composition". Co-financed by the European Union (European Social Fund, ESF) and the Greek Ministry of Education through the Research Funding Program THALES (Project code/Title: MIS 377304). Duration 1/1/2012–30/9/2015.

2. "Excellence scholarship". A.U.TH Research Committee, Aristotle University of Thessaloniki, Greece, 2012.

3. "FLEXPART Training Course". Dept. of Meteorology and Geophysics, Univ. of Vienna, Vienna, Austria. Financial support by TOwer and surface Research Network for verification of Climate relevant emissions of Human origin in Europe (TTORCH) –European Science Foundations (ESF). Duration: 15/03/2013-17/03/2013.

4. "Assessment of the origin of chromium in the groundwater supply of the Municipal Districts of Akrini - Agios Dimitrios - Ryaki - Koilada of the Municipality of Kozani". Co-Financed by the Region of Western Macedonia, the Municipality of Kozani and the Water Supply & Sewerage Company (DEYA) of Kozani Municipality. Duration: 14/4/2014 - 25/9/2015.

5. "Study of the properties of chabazite zeolite in cementitious aqueous solutions". Financial support by ONDRAF/NIRAS, the Belgian Agency for Radioactive Waste and Fissile Materials (Agreement No CCHO 2016-0155/00/). Duration: 19/04/2016-18/04/2017.

6. "The Mediterranean Hot-Spot: Challenges and responses in a changing environment". Justus-Liebig-University Giessen and Aristotle University of Thessaloniki joint program (JLU-AUTh). Financial support by German Academic Exchange Service (DAAD-Deutscher Akademischer Austauschdienst). Duration: 19/06/2018-23/06/2018.

ΠΕΡΙΛΗΨΗ

Η παρούσα διατριβή αναλύει την επίδραση της διασποράς των ατμοσφαιρικών σωματιδίων και τη χημική και ορυκτολογική τους ανάλυση στην ευρύτερη περιοχή της Θεσσαλονίκης κατά την περίοδο 2012-2013. Συλλέχθηκαν δείγματα πίπτουσας σκόνης σε επίπεδο δρόμου και οροφής κτιρίου, από τρεις επιλεγμένες τοποθεσίες δειγματοληψίας ανατολικά (πολυώροφο κτίριο περιοχή Καλαμαριάς), κεντρικά (Αριστοτέλειο Πανεπιστήμιο - στέγη κτηρίου της Σχολής Θετικών Επιστημών) και δυτικά κοντά στο λιμάνι της Θεσσαλονίκης (πολυώροφος χώρος στάθμευσης).

Η δειγματοληψία πραγματοποιήθηκε για περίοδο ενός έτους (2012-13), σύμφωνα με τις επικρατούσες μετεωρολογικές συνθήκες, όπως η ταχύτητα του ανέμου και η βροχόπτωση. Από κάθε δείγμα συλλέχθηκαν 50-150 g σκόνης, σκουπίζοντας συνολική επιφάνεια 1 m^2 χρησιμοποιώντας αποστειρωμένα όργανα συλλογής. Τα δείγματα ξηράνθηκαν σε φούρνο στους 35 ° C για 3 ημέρες. Στη συνέχεια διήλθαν από κόσκινο διατομής βρογχίδας 63μm και παραλήφθηκε το κλάσμα διαμέτρου <63μm για περαιτέρω έρευνα.

Η αξιολόγηση της ορυκτολογικής σύστασης των δειγμάτων πραγματοποιήθηκε με τη μέθοδο της περιθλασιμετρίας ακτίνων X (XRD), ενώ η μελέτη της μορφολογίας και της χημείας των κόκκων σκόνης πραγματοποιήθηκε με τη μέθοδο ηλεκτρονικής μικροσκοπίας. Οι ανεξέλεγκτες εκπομπές καύσης βιομάζας για οικιακή θέρμανση στην ατμόσφαιρα της Θεσσαλονίκης τον Δεκέμβριο του 2012 εξετάστηκαν και εμφάνισαν επιπτώσεις με ρύπους οργανικής προέλευσης. Αυτό με συνεπικουρία των ευνοϊκών μετεωρολογικών συνθηκών, αποδίδεται στην εκτεταμένη και ανεξέλεγκτη καύση βιομάζας για οικιακή θέρμανση. Επιπλέον, εξετάστηκαν εποχιακές διακυμάνσεις της ορυκτολογικής σύνθεσης και του περιεχομένου οργανικής ύλης της πίπτουσας σκόνης στη Θεσσαλονίκη κατά τη διάρκεια του 2012-13 και έδειξαν ότι αποτελείται κυρίως από ανόργανα συστατικά προέλευσης από τη διάβρωση των δομικών υλικών χωρίς να αποκλείεται η συνεισφορά αέριων ρύπων ενώ ο ασβεστίτης και ο χαλαζίας ήταν η κύρια ανόργανη κρυσταλλική φάση που προσδιορίστηκε με την τελευταία να είναι δυνητικά επικίνδυνη για τη δημόσια υγεία. Αύξηση του οργανικού

φορτίου των δειγμάτων σκόνης παρατηρήθηκε κατά τη χειμερινή περίοδο του 2012-13 σε σύγκριση με τις άλλες εποχιακές περιόδους δειγματοληψίας και με προηγούμενες μηνιαίες περιόδους(χειμώνα και φθινοπώρου) λόγω της εκτεταμένης και ανεξέλεγκτης καύσης βιομάζας για οικιακή θέρμανση ως συνέπεια της οικονομικής κρίσης στην Ελλάδα και της υψηλής αξίας των τιμών καυσίμου (πετρελαίου) κατά τη διάρκεια αυτής της περιόδου.

Τέλος, αποφασίστηκε η ομαδοποίηση των δειγμάτων που εναποτέθηκαν υπό ξηρές συνθήκες που μεσολαβούσαν μεταξύ 2 επεισοδίων βροχόπτωσης, σε 14 δείγματα για την περιοχή δειγματοληψίας στην Καλαμαριά στο ανατολικό τμήμα της Θεσσαλονίκης, 18 δείγματα για την περιοχή δειγματοληψίας στο Αριστοτέλειο Πανεπιστήμια Θεσσαλονίκης στο κέντρο της Θεσσαλονίκης, και 16 δείγματα για την περιοχή δειγματοληψίας στην περιοχή κοντά στο λιμάνι στο δυτικό τμήμα της Θεσσαλονίκης. Συνολικά 48 δείγματα αναλύθηκαν χημικά και ορυκτολογικά. Η χημική ανάλυση των αναλυθέντων (48) ιχνοστοιχείων έδειξε αυξημένα επίπεδα συγκέντρωσης βαρέων μετάλλων όπως As, Zn, Mn, Co, Cr, Cu, Ba, Br, Hg, Mn, Ni, Pb, Sb, Tl κ.λπ. που με την εύνοια των μετεωρολογικών συνήθων εμφάνισαν αυξημένα επίπεδα ατμοσφαιρικής ρύπανσης.

Προκειμένου να εντοπίσουμε πιθανές πηγές εκπομπών και να επαληθεύσουμε σε τι βαθμό εξωτερικές παράμετροι επηρέασαν τα επίπεδα ρύπανσης των περιοχών μελέτης που εξετάσαμε τα δείγματα σκόνης, εφαρμόσαμε για επιλεγμένες ημερομηνίες, όπου είχαμε αυξημένες συγκεντρώσεων βαρέων μετάλλων, το λαγκρατζιανό μοντέλο ατμοσφαιρικής διασποράς Flexpart-WRF με ανάλυση πλέγματος 0,6 χμ. x 0,6 χμ. με εμπρόσθια χρονικά προσομοίωση για τις εν δυνάμει εκπομπές βιομηχανικών περιοχών που βρίσκονται βόρεια και δυτικά και οπισθόδρομη προσομοίωση για τις τρείς περιοχές της δειγματοληψίας μας. Για να ενισχύσουμε την απόδοσή του, έγινε τροφοδότηση δεδομένων υψηλής ανάλυσης, από το μη υδροστατικό αριθμητικό μετεωρολογικό μοντέλο μεσαίας κλίμακα WRF, που τρέχει σε υψηλή ανάλυση 0,6 km x 0,6 km με δεδομένα ανάλυσης από το ευρωπαϊκό κέντρο μετεωρολογικών προβλέψεων μεσαίας κλίμακας ECMWF. Η οπτικοποίηση των προσομοιώσεών μας για τις τρεις επιλεγμένες τοποθεσίες δειγματοληψίας, που βρίσκονται δυτικά, κεντρικά και ανατολικά έδειξαν μια άμεση επίδραση διασποράς όπου φαίνεται να προέρχεται από εν δυνάμει εκπομπές περιοχών που βρίσκονται δυτικά και βόρεια σε βιομηχανικές περιοχές της πόλης. Αυτό ενισχύει το αποτέλεσμα πιθανής συνεισφοράς των περιοχών αυτών στα αυξημένα επίπεδα τοξικών ρύπων που πήραμε από τις χημικές μας αναλύσεις, πέρα από άλλες ανθρωπογενείς και φυσικές παραμέτρους (φθορά δρόμων, δομικών υλικών, πέδησης οχημάτων κλπ.) που είχαν επιδράσει στην ενίσχυση αυτή.

ABSTRACT

The present thesis analyses the impact of atmospheric particles dispersion and their chemical and mineralogical analysis in the wider area of Thessaloniki during 2012-2013. Falling dust samples were collected at street-level and rooftop building level, from three selected sampling sites located East (Kalamaria District-multi-storey building), Central (Aristotle University- building roof of the Faculty of Sciences), and West near Thessaloniki's Seaport (multi-storey parking lot station). Sampling was conducted for a one year period (2012-13), according to prevailing meteorological conditions such as wind speed and precipitation. From each sample 50-150 g of powder was collected, wiping a total area of $1m^2$ using sterilized collectible instruments. The samples were dried in an oven at 35 °C for 3 days. After that they were passed through a bronchi sieve section of 63mm and received the fraction diameter <63 μm for further investigation.

The evaluation of the mineralogical composition of the samples was conducted by the method of X-ray diffractometry (XRD) while the study of the morphology and chemistry of the dust grains was performed by the method of electron microscopy.

Impact of uncontrolled emissions of burning of biomass for residential heating in the atmosphere of the city of Thessaloniki during December 2012 was examined and indicated impact in the atmosphere of Thessaloniki with pollutants of organic origin. This with favoring meteorological conditions, attributed to the extensive and uncontrolled burning of biomass for domestic heating. Additionally seasonal variations of the mineralogical composition and the organic matter content of falling dust in Thessaloniki during 2012-13 was examined and indicated that it mainly consists of inorganic origin components from the corrosion of building materials without excluding material contribution from air suspending fumes, while calcite and quartz were the major inorganic crystalline phase determined, with the latter being potentially dangerous for public health.

Increase in the organic load of dust samples had been observed for winter 2012-13 compared to the other seasonal sampling periods and to previous winter and autumn monthly periods due to the extensive and uncontrolled burning of biomass for domestic heating as a consequence of the economic crisis in Greece and the high value of petroleum fuel during this period.

Finally it was decided to group the samples that were deposited under dry conditions that mediated between 2 rain episodes to 14 bulk samples for sampling location Kalamaria in the east part of Thessaloniki, 18 bulk samples for sampling location AUTH campus in the center part of Thessaloniki, and 16 bulk samples for sampling location PORT in the west part of Thessaloniki, a total of 48 samples that we chemically and mineralogical analyzed. The chemical analysis of the analyzed (48) trace elements indicated increased levels of toxic metals such as As, Zn, Mn, Co, Cr, Cu, Ba, Br, Hg, Mn, Ni, Pb, Sb, Tl etc. which favored by the meteorological conditions, resulted in augmented air pollution levels. In order to identify possible emitting sources and to verify at what content, external parameters affected the pollution levels, of our study areas examined dust samples, we implemented for selected dates of increased heavy metals concentrations the FLEXible PARTicle dispersion model, Flexpart-WRF with grid spacing of 0.6 km x 0.6 km running backwards for the three sampling locations and forward for the possible industrial emitting sites. Augmenting its performance with high resolution data feedback from the non-hydrostatic mesoscale numerical meteorological model Weather Research and Forecasting Model (WRF) ruining at high analysis of 0.6 km x 0.6 km (with the advanced research dynamic solver-AWR) and with analysis data from the European Centre for Medium-Range Weather Forecasts (ECMWF). The visualization of our simulations for the three selected sampling sites located west, central and east indicated a direct effect of dispersion. Originating from possible emitting sites located west and north at industrial areas of the city resulting to the increased levels of toxic pollutants from our chemical analyses, apart from other anthropogenic and natural parameters (wear from pavements, vehicle tyres and braking systems).

REFERENCES

Agency for Toxic Substances and Disease Registry (ATSDR), 2004. Toxicological profile for Copper. Atlanta, GA: U.S. Department of Health and Human Service.

Agency for Toxic Substances and Disease Registry (ATSDR), 2005. Toxicological profile for Nickel. Atlanta, GA: U.S. Department of Health and Human Service.

Agency for Toxic Substances and Disease Registry (ATSDR), 2005. Toxicological profile for Zinc. Atlanta, GA: U.S. Department of Health and Human Service.

Agency for Toxic Substances and Disease Registry (ATSDR), 2007. Toxicological profile for Arsenic. Atlanta, GA: U.S. Department of Health and Human Service.

Agency for Toxic Substances and Disease Registry (ATSDR), 2012. Toxicological profile for Chromium. Atlanta, GA: U.S. Department of Health and Human Service.

Agency for Toxic Substances and Disease Registry (ATSDR), 2012. Toxicological profile for Cadmium. Atlanta, GA: U.S. Department of Health and Human Service.

Agency for Toxic Substances and Disease Registry (ATSDR), 2019. Toxicological profile for Lead. Atlanta, GA: U.S. Department of Health and Human Service.

Agency for Toxic Substances and Disease Registry (ATSDR), 2019. Toxicological profile for Antimony. Atlanta, GA: U.S. Department of Health and Human Service.

Amato, F., Cassee, F.R., van der Gon, H.A.C.D., Gehrig, R., Gustafsson, M., Hafner, W., Harrison, R.M., Jozwicka, M., Kelly, F.J., Moreno, T., Prevot, A.S.H., Schaap, M., Sunyer, J., and Querol, X., 2014. Urban air quality: the challenge of traffic non-exhaust emissions. *J. Hazard. Mater., 275, 31-36.*

Amiro, B.D, Stocks, B.J, Alexander, M.E, Flannigan, M., and Wotton, M., 2001. Fire, climate change, carbon and fuel management in the Canadian boreal forest. *International Journal of Wildland Fire 10:405–413.*

Barakat, M.A., 2010. New trends in removing heavy metals from industrial wastewater. *Arabian Journal of Chemistry, doi:10.1016/j.arabjc.2010.07.019.*

Barregard, L., Sällsten, G., Gustafson, P., Andersson, L., Johansson, L., Basu, S., and Stigendal, L., 2006. Experimental exposure to wood smoke particles in healthy humans: Effects on markers of inflammation, coagulation, and lipid peroxidation. *Inhalation Toxicology, 18(11): 845−853.*

Beljaars, A. C. M. and Holtslag, A. A. M., 1991. Flux parameterization over land surfaces for atmospheric models. *J. Appl. Meteor., 30, 327–341.*

Belzile, N., Chen, Y., and Filella, M., 2011. Human exposure to antimony: I. Sources and intake. *Crit Rev Environ Sci, 41: 1309-1373.*

Bentley, R., and Chasteen, T.G., 2002. Microbial methylation of metalloids: Arsenic, antimony, and bismuth. *Microbiol Mol Biol Rev 66(2):250-271.*

Berkowicz, R. and Prahm, L. P., 1982. Evaluation of the profile method for estimation of surface fluxes of momentum and heat. *Atmos. Environ., 16, 2809–2819.*

Borrego, C., Miranda, AI., Carvalho, AC., and Carvalho, A., 1999. Forest fires and air pollution: A local and a global perspective. In: Brebbia, C., Jacobson, M., and Power, H., eds. *Proceedings of the 7th International Conference on Air Pollution. WIT Press, Southampton, Boston, 741-750.*

Brioude, J., Angevine, W. M., McKeen, S. A., and Hsie, E.-Y., 2012. Numerical uncertainty at mesoscale in a Lagrangian model in complex terrain. *Geosci. Model Dev., 5, 1127–1136, 10 doi:10.5194/gmd-5-1127-2012.*

Brioude, J., Arnold, D., Stohl, A., Cassiani, M., Morton, D., Seibert, P., Angevine, W., Evan, S., Dingwell, A., Fast, J. D., Easter, R. C., Pisso, I., Burkhart, J., and Wotawa, G., 2013. The Lagrangian particle dispersion model FLEXPART-WRF version 3.1, *Geosci. Model Dev., 6, 1889-1904, http://doi.org/10.5194/gmd-6-1989-2013.*

Buck, B.J., Metcalf, R.V., Berry, D., McLaurin, B., Kent, D., Januch, J., and Goossens, D., 2015. Naturally Occurring Asbestos in the Southern Nevada Region: Potential for Human Exposure. *American Geophysical Union, Fall Meeting 2015, abstract id.A51U-05 ,2015AGUFM.A15U..05B*

Businger, J. A.,Wyngaard, J. C., Izumi, Y. and Bradley, E. F., 1971. Fluxprofile relationships in the atmospheric surface layer. *J. Atmos. Sci., 28, 181–189.*

Carvalho, A., Martins, V., Miranda, AI., and Borrego, C., 2007. Forest fire emissions under climate change: an air quality perspective. *4th International Wildland Fire Conference, 13-17 May, Seville, Spain.*

Chilvers, DC., and Peterson, PJ., 1987. Global cycling of arsenic. In: Hutchinson TC, Meema KM, eds. Lead, cadmium and arsenic in the environment. New York: John Wiley & Sons Ltd., 69-87.

Daher, N., Ruprecht, A., Invernizzi, G., De Marco, C., Miller-Schulze, J., Heo, J.B., Shafer, M.M., Shelton, B.R., Schauer, J.J., and Sioutas C., 2012. Characterization, sources and redox activity of fine and coarse particulate matter in Milan, Italy. *Atmospheric Environment, 49: 130−141.*

Dorling, S. R., Davies, T. D. and Pierce, C.E., 1992. Cluster analysis: a technique for estimating the synoptic meteorological controls on air and precipitation chemistry - method and applications. *Atmos. Environ., 26A, 2575–2581*

ECMWF, 1995. User Guide to ECMWF Products 2.1. *Meteorological Bulletin M3.2. Reading, UK*

EEA, 2018a. Air quality in Europe 2018, report. European Environment Agency (https://www.eea.europa.eu/publications/air-quality-in-europe-2018)

EEA, 2018b. Environmental pressures of heavy metal releases from Europe's industry. EEA briefing, European Environment Agency (https://www.eea.europa.eu/themes/industry/industrial-pollution-in-europe/heavymetal-pollution)

Emanuel, K. A., and Zivkovic-Rothman, M., 1999. Development and evaluation of a convection scheme for use in climate models. *J. Atmos. Sci., 56, 1766–1782.*

EU, 2004. Directive 2004/107/EC of the European Parliament and of the Council of 15 December 2004 relating to arsenic, cadmium, mercury, nickel and polycyclic aromatic hydrocarbons in ambient air. OJ L 23,26.1.2005, pp. 3-16 (http://eur-lex.europa.eu/LexUriServ/LexUriServ.do?uri=OJ:L:2005:023:0003:0016:EN:PDF)

EU, 2008. Directive 2008/50/EC of the European Parliament and of the Council of 21 May 2008 on ambient air quality and cleaner air for Europe. OJ L 152, 11.6.2008, p. 1-44 (http://eur-lex.europa.eu/LexUriServ/LexUriServ.do?uri=OJ:L:2008:152:0001:0044:EN:PDF)

EU, 2016. Directive 2016/2284/EC of the European Parliament and of the Council of 14 December 2016 on the reduction of national emissions of certain atmospheric pollutants, amending Directive 2003/35/EC and repealing Directive 2001/81/EC. OJ L 344, 17.12.2016,p. 1-31 (http://eur-lex.europa.eu/legal-content/EN/TXT/?uri= uriserv% 3AOJ.L_2016.344.01.0001.01.ENG)

European Commission, 2013. The Clean Air Programme for Europe. (http://ec.europa.eu/environment/ air/ clean_air/index.htm)

European Commission, 2017. Special Eurobarometer 468: Attitudes of European citizens towards the environment. (http://data.europa.eu/euodp/en/data/dataset/S2156_88_1_468_ENG).

European Commission, 2018. Communication from the Commission to the European Parliament, the Council, the European Economic and Social Committee and the Committee of the Regions. 'A Europe that protects: Clean air for all' (COM (2018) 330 final) (http://ec.europa.eu/environment/air/pdf/clean_air_for_all.pdf).

Fast, J. D. and Easter, R.C., 2006. A lagrangian particle dispersion model compatible with WRF. 7th Annual WRF User's Workshop.

Flocas, H., Kelessis, A., Helmis, C., Petrakakis, M., Zoumakis, N., and Pappas, K., 2009. Synoptic and local scale atmospheric circulation associated with air pollution episodes in an urban Mediterranean area. *Theor. Appl. Climatol. 95, 265-277.*

Foregs, 2005. Forum of the European Geological Survey Directors. Geochemical Atlas of Europe, Geological Survey of Finland, Espoo.

Goossens, D., and Buck, B., 2009. Dust emission by off-road driving: experiments on 17 arid soil types, Nevada, USA. *Geomorphology, 107, 118–138.*

Grund, SC., Hanusch, K., Breunig, HJ., and Wolf, H.U., 2012. Antimony and antimony compounds. In: Ullman's encyclopedia of industrial chemistry. *Hoboken, NJ: John Wiley & Sons, Inc., http://doi.org/10.1002/14356007.a03_055.pub2.*

Hanawalt, J.D., and Rinn, H.W., 1936. Identification off crystalline materials. *Ind. Eng. Chem. Anal. Ed. & 8:244-247.*

Hansen, L. J. and Hoffman, J. R., 2011. Climate savvy: adapting conservation and resource management to a changing world. Bainbridge Island, WA: Eco-adapt

HEI, 2018. State of global air 2018, Special Report, Health Effects Institute, Boston, MA (http://www.stateofglobalair.org/sites/default/files/soga-2018-report.pdf)

IARC, 1997. Silica, Some Silicates, Coal Dust and para-Aramid Fibrils. International Agency for Research on Cancer (IARC) Monographs, 68, pp.506.

IARC, 2013. Outdoor air pollution a leading environmental cause of cancer deaths. Press release No 221, International Agency for Research on Cancer

Iijima, A., Sato, K., Fujitani, Y., Fujimori, E., Saito, Y., Tanabe, K., Ohara, T., Kunihisa, D., and Furuta, N., 2009. Clarification of the predominant emission sources of antimony in airborne particulate matter and estimation of their effects on the atmosphere in Japan. *January 2009 Environmental Chemistry 6(2) DOI: 10.1071/EN08107*

Ikeda, M., Watanabe, T., Hayashi, H., and Tsunoda, A., 1986. Toxicological evaluation of quartz and silica contents in studded tire-generated dust in the city of Sendai. *Tohoku J Environ Med, 148: 207-211. http://doi.org/10.1620/tjem.148.207*

International Agency for Research on Cancer, 1997. Silica, Some Silicates, Coal Dust and para-Aramid Fibrils. International Agency for Research on Cancer (IARC) Monographs, 68, pp.506.

IPCC, 2013. Climate change 2013: the physical science basis, Contribution of Working Group I to the Fifth Assessment Report of the Intergovernmental Panel on Climate

Change. *Cambridge University Press, Cambridge, United Kingdom (https://dx.doi.org/10.1017/CBO9781107415324)*

Jackson, M.L., 1974. Soil chemical analysis. Adv. Coarse. Madison, Wisconsin, 690 pp.

Kabata-Pendias, A., 2011. Trace Elements in Soils and Plants. CRC Press. Boca Raton.

Kantiranis, N., Stergiou, A., Filippidis, A., and Drakoulis, A., 2004. Calculation of the percentage of amorphous material using PXRD patterns. *Bulletin of Geological Society of Greece, 36: 446-453.*

Karacostas, T. S., 2003. Synoptic, dynamic and cloud microphysical characteristics related to precipitation enhancement projects. 194–200. *In: Regional Seminar on Cloud Physics and Weather Modification. World Meteorological Organization, WMPNo. 42, WMO-TD No. 1227, (213 pp.).*

Karacostas, T., Kartsios, S., Pytharoulis, I., Tegoulias, I., and Bampzelis, D., 2018. Observations and modelling of the characteristics of convective activity related to a potential rain enhancement program in central Greece. *Atmospheric Research. 208, pp. 218-228. https://doi.org/10.1016/j.atmosres.2017.08.014.*

Kasischke, E. S., Hyer, E.J., Novelli, P.C., Bruhwiler, L. P., French, N.H.F., Ukhinin, A.I.S., Hewson, J.H., and Stocks, B.J., 2005. Influences of boreal fire emissions on northern hemisphere atmospheric Carbon and Carbon Monoxide. *Global Biogeochemical Cycles, 19, 1-16.*

Kazakis, N., Kantiranis, N., Kalaitzidou, K., Kaprara, E., Mitrakas, M., Frei, R., Vargemezis, G., Tsourlos, P., Zouboulis, A., and Filippidis, A., 2017. Origin of hexa-valent chromium in ground waters: The example of Sarigkiol Basin, Northern Greece. *Science of the Total Environment, 593–594: 552–566*

Kazakis, N., Kantiranis, N., Kalaitzidou, K., Kaprara, E., Mitrakas, M., Frei, R., Vargemezis, G., Vogiatzis, D., Zouboulis, A., and Filippidis, A., 2018. Environmentally available hexavalent chromium in soils and sediments impacted by dispersed fly ash in Sarigkiol basin (Northern Greece). *Environmental Pollution*, 235 (2018) 632-641.

Kazakis, N., Kantiranis, N., Kaprara, M., Mitrakas, M., Vargemezis, G., Voudouris, K., Chatzipetros, A., Kalaitzidou, K. and Filippidis, A., 2016. Potential toxic elements (PTEs) in ground and spring waters, soils and sediments: an in-terdisciplinary study in Anthemountas basin, N. Greece. *Bull. of the Geol. Soc. of Greece, 50(4), 2171-2181.*

Kazakis, N., Kantiranis, N., Voudouris, K.S., Mitrakas, M., Kaprara, E., and Pavlou, A., 2015. Geogenic Cr oxidation on the surface of mafic minerals and the hydrogeological conditions influencing hexavalent chromium concentrations in groundwater. *Science of the Total Environment, 514, 224-238.*

Kicińska, A., and Bożęcki, P., 2018. Metals and mineral phases of dusts collected in different urban parks of Krakow and their impact on the health of city residents. *Environ Geochem Health* **40,** 473–488.

Kjällstrand, J., and Petersson, G., 2001. Phenolic antioxidants in wood smoke. *Science of the Total Environment, 277(1−3): 69−75.*

Klug, H.P., and Alexander, L.E., 1974. X-Ray Diffraction Procedures: For Polycrystalline and Amorphous Materials. *2nd Edition. ISBN: 978-0-471-49369-3, 992 p.*

Kollias, P., Kantiranis, N., Samara, C., Zanis, P., and Pytharoulis, I., 2014. Impact of uncontrollable burning of biomass for residential heating in the atmosphere of the city of Thessaloniki during December 2012. *5th Environmental conference of Macedonia, Thessaloniki, March 14-16, 2014, e-Proc.*

Kourtidis, K., Ziomas, I., Zerefos, C., Kosmidis, E., Symeonidis, P., Christophilopoulos, E., Karathanassis S., and Mploutsos A., 2002. Benzene, toluene, O_3, NO_2 and SO_2 measurements in an urban street canyon in Thessaloniki, Greece. *Atmospheric Environment, 36: 5355-64.*

Legg, B. J., and Raupach, M. R. 1982. Markov-chain simulation of particle dispersion in inhomogeneous flows: the mean drift velocity induced by a gradient in Eulerian velocity variance. *Bound.- Layer Met., 24, 3–13*

Lewis, R.J., and Wiley J. Sr., 2007. Hawley's Condensed Chemical Dictionary. 15th ed. *Journal of the American Chemical Society. ISBN 978-0471-76865-4*

Lim, S.S., Vos, T., Flaxman, A.D., Danaei, G., Shibuya, K., Adair-Rohani, H., Amann, M., Anderson, H.R., Andrews, K.G., Aryee, M., Atkinson, C., Bacchus, L.J., Bahalim, A.N., Balakrishnan, K., Balmes, J., Barker-Collo, S., Baxter, A., Bell, ML., Blore, J.D., Blyth, F., Bonner, C., Borges, G., Bourne, R., Boussinesq, M., Brauer, M., Brooks, P., Bruce, N.G., Brunekreef, B., Bryan-Hancock, C., Bucello, C., Buchbinder, R., Bull, F., Burnett, R.T., Byers, T.E., Calabria, B., Carapetis, J., Carnahan, E., Chafe, Z., Charlson, F., Chen, H., Chen, J.S., Cheng, A.T., Child, J.C., Cohen, A., Colson, K.E., Cowie, B.C., Darby, S., Darling, S., Davis, A., Degenhardt, L., Dentener, F., Des Jarlais, D.C., Devries, K., Dherani, M., Ding, E.L., Dorsey, E.R., Driscoll, T., Edmond, K., Ali, S.E., Engell, R.E., Erwin, P.J., Fahimi, S., Falder, G., Farzadfar, F., Ferrari, A., Finucane, M.M., Flaxman, S., Fowkes, F.G., Freedman, G., Freeman, M.K., Gakidou, E., Ghosh, S., Giovannucci, E., Gmel, G., Graham, K., Grainger, R., Grant, B., Gunnell, D., Gutierrez, H.R., Hall, W., Hoek, H.W., Hogan, A., Hosgood, H.D. 3rd., Hoy, D., Hu, H., Hubbell, B.J., Hutchings, S.J., Ibeanusi, S.E., Jacklyn, G.L., Jasrasaria, R., Jonas, J.B., Kan, H., Kanis, J.A., Kassebaum, N., Kawakami, N., Khang, Y.H., Khatibzadeh, S., Khoo, J.P., Kok, C., Laden, F., Lalloo, R., Lan, Q., Lathlean, T., Leasher, J.L., Leigh, J., Li, Y., Lin, J.K., Lipshultz, S.E., London, S., Lozano, R., Lu, Y., Mak, J., Malekzadeh, R., Mallinger, L., Marcenes, W., March, L., Marks, R., Martin, R., McGale, P., McGrath, J., Mehta, S., Mensah, G.A., Merriman, T.R., Micha, R., Michaud, C., Mishra, V., Mohd Hanafiah, K., Mokdad, A.A., Morawska, L., Mozaffarian, D., Murphy, T., Naghavi, M., Neal, B., Nelson, P.K., Nolla, J.M., Norman, R., Olives, C., Omer, S.B., Orchard, J., Osborne, R., Ostro, B., Page, A., Pandey, K.D., Parry, C.D., Passmore, E., Patra, J., Pearce, N., Pelizzari, P.M., Petzold, M., Phillips, M.R., Pope, D., Pope, C.A. 3rd, Powles, J., Rao, M., Razavi, H., Rehfuess, E.A., Rehm, J.T., Ritz, B., Rivara, F.P., Roberts, T., Robinson, C., Rodriguez-Portales, J.A., Romieu, I., Room, R., Rosenfeld, L.C., Roy, A., Rushton, L., Salomon, J.A., Sampson, U., Sanchez-Riera, L., Sanman, E., Sapkota, A., Seedat, S., Shi, P., Shield, K., Shivakoti, R., Singh, G.M., Sleet, D.A., Smith, E., Smith, K.R., Stapelberg, N.J., Steenland, K., Stöckl, H., Stovner, L.J., Straif, K., Straney, L., Thurston, G.D., Tran, J.H., Van Dingenen, R., van Donkelaar, A., Veerman, J.L., Vijayakumar, L., Weintraub, R., Weissman, M.M., White, R.A., Whiteford, H., Wiersma, S.T., Wilkinson, J.D., Williams, H.C., Williams, W., Wilson, N., Woolf, A.D., Yip, P., Zielinski, J.M., Lopez, A.D., Murray, C.J., Ezzati, M., AlMazroa, M.A., Memish, Z.A., 2012. A comparative risk assessment of burden of disease and injury attributable to 67 risk factors and risk factor clusters in 21 regions, 1990-2010: a systematic analysis for the Global Burden of Disease Study 2010. Lancet. 2012 Dec 15;380(9859):2224-60. doi: 10.1016/S0140-6736(12)61766-8.

Manoli, E., Voutsa, D., and Samara, C., 2002. Chemical characterization and source identification/apportionment of fine and coarse air particles in Thessaloniki, Greece, *Atm. Environ., 36, 949-961.*

Marley, A., and Frederick, J.E., 2008. Formation and Effects of Smog. Environmental and Ecological Chemistry – vol. ii – ©Encyclopedia of Life Support Systems (EOLSS).

Mason, B., and Moore, C.B., 1982. Principles of geochemistry. 4th Edition, John Willey & Sons, New York.

Matschullat, J., 2000. Arsenic in the geosphere - a review. *Sci Total Environ 249:297-312.*

McCracken, J.P., Smith, K.R., Diaz, A., Mittleman, M.A., and Schwartz J., 2007. Chimney stove intervention to reduce long-term wood smoke exposure lowers blood pressure among Guatemalan women. *Environmental Health Perspectives, 115(7): 996−1001.*

McNider, R. T., Moran, M. D. and Pielke, R. A. 1988. Influence of diurnal and inertial boundary layer oscillations on long-range dispersion. *Atmos. Environ., 22, 2445–2462.*

Miranda, A.I., Borrego, C., Sousa, M., Valente, J., Barbosa, P., Carvalho, A., 2005. Model of Forest Fire Emissions to the Atmosphere. *Deliverable D252 of SPREAD Project (EVG1-CT-2001-00043). Department of Environment and Planning, University of Aveiro AMB-QA-07/2005, Aveiro, Portugal, 48 pp.*

Miranda, A.I., Coutinho, M., Borrego, C., 1994. Forest fires emissions in Portugal: a contribution to global warming? *Environmental Pollution 83, 121-123.*

Misaelides, P., Samara, C., Noli, F., Kouimtzis, T., & Anousis, I., 1993. Toxic element concentrations in airborne particulate matter in the area of Thessaloniki, Greece. *Sci Total Environ, 130/131: 139–146.*

Moore, D. M., & Reynolds, R. C. Jr., 1997. X-Ray Diffraction and the Identification and Analysis of Clay Minerals. *2nd ed. xviii + 378 pp. Oxford, New York: Oxford University Press*

Morrow, H., 2001. Cadmium and cadmium alloys. In: Kirk-Othmer encyclopedia of chemical technology. *John Wiley & Sons, Inc., 471-507. http://www.mrw.interscience.wiley.com/ emrw/9780471238966/kirk/article/cadmcarr.a01/current/pdf hd= All%2Ccadmium. April 29, 2008.*

Mousiopoulos, N., 2013. Impact of biomass burning and wood in air quality: Measurements and simulations. *Greek International University workshop titled: Economic Crisis and Energy Mix: Societal and Health Impact of Biomass and Wood Burning, Thessaloniki, 16/12/2013.*

Noyes, P. D., McElwee, M. K., Miller, H.D., Clark, B.W., Van Tiem, L. A., Walcott, K.C., Erwin, K.N., and Levin, E.D., 2009. The toxicology of climate change: environmental contaminants in a warming world. *Environment International 35, 971-86.*

Orozco-Levi, M., Garcia-Aymerich, J., Villar, J., Ramirez-Sarmiento, A., Anto, J. M., and Gea J., 2006. Wood smoke exposure and risk of chronic obstructive pulmonary disease. *European Respiratory Journal, 27(3): 542−546.*

Pacyna, J.M., 1987. Atmospheric emissions of arsenic, cadmium, lead and mercury from high temperature processes in power generation and industry, and their atmospheric transport. *In: Lead, Mercury, Cadmium and Arsenic in the Environment, Ed. By T.C. Hutchinson and K.M. Meema. Chichester, John Wiley.*

Pacyna, J.M., Pacyna, E.G., 2001. An assessment of global and regional emissions of trace metals to the atmosphere from anthropogenic sources worldwide. *Environ Rev 9(4):269-298. http://doi.org/10.1139/a01-012.*

Pagano, L. E., 2010. A Comparative Study between FLEXPART-WRF and HYSPLIT in an Operational Setting: Analysis of Fire Emissions across complex geography using WRF. *Department of Marine, Earth and Atmospheric Sciences North Carolina State University, Raleigh, NC.*

Pechinger, U., Langer, M., Baumann, K., and Petz, E., 2001. The Austrian emergency response modeling system tamos. *Physics and Chemistry of the Earth, Part B: Hydrology, Oceans and Atmosphere, 26 (2), 99-103.*

Petrakakis, M.J., Kelessis, A.G., Tzoumaka P.N., and Samara, C., 2013. Levels of suspended particulate matter before and after the economic crisis in Thessaloniki, Greece. *17th International MESAEP Symposium Istanbul/Turkey.*

Porter, A.R., and Ashworth, M., 2010. Configuring and Optimizing the Weather Research and Forecast Model On the Cray XT. *In: Cray User Group Proceedings.*

Pye, K., 1987. Aeolian Dust and Dust Deposits. *Academic Press, San Diego, Calif, USA.*

Pytharoulis, I., Tegoulias, I., Kotsopoulos, S., Bampzelis, D., Karacostas, T., and Katragkou, E., 2014. Evaluation of the operational numerical weather predictions of the WaveForUs project. *In: Proc. 12th Int. Conf. of Meteorology, Climatology and Physics of the Atmosphere. Heraklion, Greece, 28-31 May, 96-101.*

Rastigejev, Y., Park, R., Brenner, M. P., and Jacob, D. J., 2010. Resolving intercontinental pollution plumes in global models of atmospheric transport. *J. Geophys. Res., 115, D02302, doi:10.1029/2009JD012568..*

Reimann, C., and de Caritat, P., 1998. Chemical Elements in the Environment. Factsheets for the Geochemist and Environmental Scientist. *ix+398 pp. Berlin, Heidelberg, New York, London, Paris, Tokyo, Hong Kong: Springer-Verlag.*

Saffari, A., Daher, N., Samara, C., Voutsa, D., Kouras, A., Manoli, E., Karagkiozidou, O., Vlachokostas, C., Moussiopoulos, N., Shafer, M.M., Schauer J.J., and Sioutas C., 2013. Increased biomass burning due to the economic crisis in Greece and its adverse impact on wintertime air quality in Thessaloniki. *Environmental Science & Technology, 47(23): 13313-20.*

Samara, C., Argiropoulos, A., Grigoratos, T., Kantiranis, N., and Papadopoulou, L., 2011. Chemical and mineralogical composition of particulate matter PM10 in Thessaloniki. *Proc. of the 21st Pahellenic Chemistry congress, Thessaloniki, e-proc., 6p.*

Samara, C., Kantiranis, N., Kollias, P., Planou, S., Kouras, A., Besis, A., Manoli, E., and Voutsa, D., 2016. Spatial and seasonal variations of the chemical, mineralogical and morphological features of quasi-ultrafine particles ($PM_{0.49}$) at urban sites. *Science of The Total Environment 553:392-403 DOI: 10.1016/j.scitotenv.2016.02.080.*

Samara, C., Kouimtzis, Th., Tsitouridou, R., Kanias, G., and Simeonov, V., 2003. Chemical mass balance source apportionment of PM_{10} in an industrialized urban area of Northern Greece. *Atm. Environ., 37, 41-54.*

Seibert, P. and Frank, A., 2004. Source-receptor matrix calculation with a Lagrangian particle dispersion model in backward mode. *Atmos. Chem. Phys., 4, 51–63*.

Seibert, P., Kruger, B. and Frank, A., 2001. Parametrisation of convective mixing in a Lagrangian particle dispersion model. *Proceedings of the 5th GLOREAM Workshop, Wengen, Switzerland, September 24–26.*

Seinfeld, J. H., and Pandis, S. N., 1998. Atmospheric Chemistry and Physics from air pollution to climate change. *John Willey and Sons, Incorporated, Willey-Interscience Publication.*

Shevchenko, V., Lisitzin, A., Vinogradova, A., and Stein, R., 2003. Heavy metals in aerosols over the seas of the Russian Arctic. *Sci Total Environ 306:11-25.*

Simmonds, P.G., Manning, A.J., Derwent, R.G., Ciais, P., Ramonet, M., Kazan, V., and Ryall, D., 2005. A burning question. Can recent growth rate anomalies in the greenhouse gases be attributed to large-scale biomass burning events. *Atmosphere and Environment, 39, 2513-2517*.

Skamarock, W.C., Klemp, J.B., Dudhia, J., Gill, D.O., Barker, D.M., Duda, M.G., Huang, X.Y., Wang, W., and Powers, J.G., 2008. A description of the Advanced Research WRF Version 3. *Tech. Note, NCAR/TN-475+STR. National Center for Atmospheric Research, Boulder.*

Slinn, W. G. N. 1982. Predictions for particle deposition to vegetative canopies. *Atmos. Environ., 16, 1785–1794.*

Solomos, S., Amiridis, V., Zanis, P., Sofiou, F., Herekakis, T., Brioude, J., Stohl, A., Kahn, R., and Kontoes, C., 2015. Improving smoke dispersion modeling over a complex terrain with the use of high-resolution meteorology and satellite observations, *Atmospheric Environment, 119, 348-361.*

Soukup, D., Buck, B.J., Goossens, D., Teng, Y., and Baron, D., 2011. Mineralogical composition of soil samples in the nellis dunes recreation area. *In: Goossens D., Buck B.J., editors. Assessment of Dust Emissions, Chemistry, and Mineralogy for Management of Natural and Disturbed Surfaces at Nellis Dunes Recreation Area, Nevada. Final Report to Bureau of Land Management for Task Agreement Number FAA010017. pp. 171–187.*

Spichtinger, N., Wenig, M., James, P., Wagner, T., Platt, U. and Stohl, A., 2001. Satellite detection of a continental-scale plume of nitrogen oxides from boreal forest fires, *Geophys. Res. Lett., 28, 4579–4582.*

Staudt, A., Leidner, A., Howard, J., Brauman, K., Dukes, J., Hansen, L.J., Paukert, C. P., Sabo, J.L., and Solrzano, L.A., 2013. The added complications of climate change: understanding and managing biodiversity and ecosystems. *Frontiers in Ecology and the Environment 11(9), pp. 494- 501 (https://doi.org/10.1890/120275).*

Stohl, A. and Thomson, D. J., 1999. A density correction for Lagrangian particle dispersion models. *Bound.-Layer Met., 90, 155–167.*

Stohl, A. and Trickl, T., 1999. A textbook example of long-range transport: Simultaneous observation of ozone maxima of stratospheric and North American origin in the free troposphere over Europe. *J. Geophys. Res., 104, 30,445–30,462.*

Stohl, A., Cooper, O. R., Damoah, R., Fehsenfeld, F. C., Forster, C., Hsie, E.-Y., Hbler, G., Parrish, D. D., and Trainer, M., 2004. Forecasting for a Lagrangian aircraft campaign. *Atmos. Chem. Phys., 4, 1113–1124.*

Stohl, A., Eckhardt, S., Forster, C., James, P., Spichtinger, N., and Seibert, P., 2002. A replacement for simple back trajectory calculations in the interpretation of atmospheric trace substance measurements. *Atmos. Environ., 36, 4635–4648.*

Stohl, A., Forster, C., Frank, A., Seibert, P., and Wotawa, G., 2005. Technical Note The Lagrangian particle dispersion model FLEXPART version 6.2. *Atmos. Chem. Phys. 5, 2461-2474.*

Stohl, A., Hittenberger, M., and Wotawa, G., 1998. Validation of the Lagrangian particle dispersion model FLEXPART against large scale tracer experiment data. *Atmos. Environ., 32, 4245–4264.*

Stohl, A., Sodemann, H., Eckhardt, S., Frank, A., Seibert, P., and Wotawa, G., 2010. Technical Note The Lagrangian particle dispersion model FLEXPART version 8.2.

Stohl, A., Wotawa, G., Seibert, P., and Kromp-Kolb, H., 1995. Interpolation errors in wind fields as function of spatial and temporal resolution and their impact on different types of kinematic trajectories. *J. Appl. Meteor., 34, 2149–2165.*

Stull, R. B., 1988. An Introduction to Boundary Layer Meteorology. Kluwer Academic Publishers, Dordrecht.

Tossavainen, M. and Forssberg, E., 1999. The potential leachability from natural road construction materials. *Science of Total Environment, 239: 31–47.*

UNEP, 2014. United Nations Environment Assembly of the United Nations Environment Programme First session, Resolution 7 on Air Quality, (http://wedocs.unep.org/handle/20.500.11822/ 17135).

UNEP, 2017. United Nations Environment Assembly of the United Nations Environment Programme Third session, Resolution 8 on Preventing and reducing air pollution to improve air quality globally (https://papersmart.unon.org/resolution/uploads/k1800222.english.pdf).

USDI, 2009. Mineral commodity summaries. USGS. http://minerals.usgs.gov/mineral

Verma, V., Polidori, A., Schauer, J.J., Shafer, M.M., Cassee, F.R., and Sioutas, C., 2009. Physicochemical and toxicological profiles of particulate matter in Los Angeles during the October 2007 Southern California wildfires. *Environ Sci Technol 43(3): 954−960. doi:10.1021/es8021667.*

Vogelezang, D. H. P., and Holtslag, A. A. M., 1996. Evaluation and model impacts of alternative boundary-layer height formulations. *Bound.-Layer Met., 81, 245–269.*

Wang, W., Bruyere, C., Duda, M., Dudhia, J., Gill, D., Lin, H-C, Michalakes, J., Rizvi, S., and Zhang, X., 2010. ARW Version 3 Modelling System's User Guide. NCAR-MMM, pp. 312.

Wenig, M., Spichtinger, N., Stohl, A., Held, G., Beirle, S., Wagner, T., Jahne, B., and Platt, U., 2003. Intercontinental transport of nitrogenoxide pollution plumes. *Atmos. Chem. Phys. Discuss., 2, 2151-2165.*

WHO, 2000. Air quality guidelines for Europe. World Health Organization, Regional Office for Europe, Copenhagen (http://www.euro.who.int/__data/assets/pdf_file/0005/74732/E71922.pdf).

WHO, 2006. Air quality guidelines: global update 2005 — particulate matter, ozone, nitrogen dioxide and sulphur dioxide. World Health Organization, Regional Office for Europe, Copenhagen.

WHO, 2013. Review of evidence on health aspects of air pollution - REVIHAAP Project, Technical Report. World Health Organization, Regional Office for Europe, Copenhagen.

WHO, 2014. Burden of disease from ambient air pollution for 2012 - summary of results. World Health Organization (http://www.who.int/phe/health_topics/utdoorair/databases/AAP_BoD_results_March2014.pdf).

WHO, 2016a. Ambient air pollution: a global assessment of exposure and burden of disease. World Health Organization (http://apps.who.int/iris/bitstream/handle/10665/250141/9789241511353-eng.pdf?sequence=1).

WHO, 2016b. WHO expert consultation: available evidence for the future update of the WHO Global air quality guidelines (AQGs). World Health Organization Regional Office for

Europe, Copenhagen, (http://www.euro.who.int/__data/assets/pdf_file/0013/301720/Evidence-futureupdate- QGs-mtg-report-Bonn-sept-oct-15.pdf?ua=1)

Wotawa, G. and Stohl, A., 1997. Boundary layer heights and surface fluxes of momentum and heat derived from ECMWF data for use in pollutant dispersion models – problems with data accuracy. *In: Gryning, S.-E., Beyrich, F. and E. Batchvarova (editors): The Determination of the Mixing Height – Current Progress and Problems. EURASAP Workshop Proceedings, 1-3 October 1997, Risø National Laboratory, Denmark.*

Wotawa, G. and Trainer, M., 2000. The influence of Canadian forest fires on pollutant concentrations in the United States. *Science, 288.*

Wotawa, G., Stohl, A. and Kromp-Kolb, H., 1996. Parameterization of the planetary boundary layer over Europe - a data comparison between the observation based OML preprocessor and ECMWF model data. *Contr. Atmos. Phys., 69, 273–284.*

Zheng, M., Salmon, L.G., Schauer, J.J., Zeng, L., Kiang, C.S., Zhang, Y., and Cass, G.R., 2005. Seasonal trends in PM2.5 source contributions in Beijing, China. *Atmos Environ 39(22): 3967−3976.doi:10.1016/j.atmosenv.2005.03.036*

Zheng, M., Salmon, L.G., Schauer, J.J., Zeng, L., Kiang, C.S., Zhang, Y., and Cass, G.R., 2005. Seasonal trends in PM2.5 source contributions in Beijing, China. *Atmospheric Environment, 39(22): 3967−3976.*

Online Sources

European Chemicals Agency (ECHA- echa.europa.eu)

Nasa (EODIS) satellite, https://worldview.earthdata.nasa.gov/

©2006 Yahoo! Inc - Imagery © 2006 i-cubed, GeoEye